NUMERICAL MODELS OF CRUSTAL DEFORMATION

Thesis by

Dan Douglas Kosloff

In Partial Fulfillment of the Requirements
for the Degree of
Doctor of Philosophy

California Institute of Technology
Pasadena, California

1978

(Submitted September 30, 1977)

ACKNOWLEDGEMENTS

During my tenure as a graduate studying at Caltech, I have benefited considerably from my relationship with Dr. Ron Scott. From his original, and incisive approach to earth problems, I have learned much.

Dr. C. B. Archambeau was most instrumental in the developing of the basic concepts which underlie this work. Dr. G. Frazier introduced me to the Finite Element method.

To the faculty of the Seismo Lab and in particular to Dr. Harkrider, Dr. Helmberger, Dr. Kanamori, and Dr. Minster, I owe the complete scientific freedom which I was allowed in my work there. I have also enjoyed the research atmosphere of the Lab.

The work for Chapter Three of this thesis was performed jointly with Dr. Hsi Ping Liu, who was responsible for conceiving the research topic. Mr. Jim Scranton and Mr. Dennes Allen from the City of Long Beach assisted in the collection of the data for the second chapter, and have always been most cooperative. Discussions with Dr. Tom Hughes were very helpful in the numerical aspects of this work. There were also numerous helpful discussions with students at the Seismo Lab, and in particular I would like to mention Dave Cole, Robert Geller, and Tai Lin Hong.

I want to thank Mrs. Marla Turner for doing an exceptional job of typing the manuscript. The figures were coordinated and drafted by Mr. Joe Galvan and Mr. Laszlo Lenches. The computations for chapter two were performed with the help of the City of Long Beach.

I have also received help from my family; from my wife in drafting some of the figures, and from my mother, Jean Kosloff, in the editing of the manuscript.

This work was supported by the National Science Foundation under contracts DES75-15013 and EAR76-22624.

Abstract

Several tectonic features in Southern California cannot be directly explained by the plate tectonic interpretation for the region. In particular, both the existence of the Transverse Ranges and the geometry of the San Andreas fault imply a stress pattern deviating from the simple horizontal shear, which parallels the spreading between the Pacific and North American plates. A number of possible mechanisms responsible for this anomalous stress field, are examined quantitatively in the light of seismicity and other tectonic observations, and in particular to the Palmdale uplift which was reported to have occurred between the years 1960-1965.

The subsidence in the Wilmington oil field in Long Beach has long been a source of concern, as its economic consequences were disastrous. An area of approximately 20 mi has been affected by the subsidence, which in 1965 reached a value of 29 ft in the center of a bowl shaped pattern. The subsidence was accompanied by horizontal displacements of up to 12 feet. A series of shallow earthquakes, with hypocentral depths between 500 to 600 meters took place in the years 1947, 1949, 1952, 1955, and 1961. The slip planes were within a thin shale layer above the producing zones of the Wilmington field. It is now agreed upon that the subsidence was caused by the pore fluid pressure reduction resulting from oil production in the field. Indeed, after a repressurization program had been initiated, the subsidence was virtually stopped in all areas of the field. The subsidence, and subsequent rebound are simulated with the aid of the Finite Element calculation method. Pressure data compiled from records of individual oil wells are converted to input data for the numerical calculation. The simulations reproduce synthetically the field observations of vertical movements, horizontal movements, and collar count survey data. For the material rheology of the formations of the Wilmington field, first a layered linearly elastic approximation is used. However, it is found that not all observations can be reproduced with this material model, and in particular, the size of the subsidence pattern is overestimated by the linear models. Therefore, a more complete elastic-plastic cap model is incorporated into the simulations. With the aid of the nonlinear material characterization, the field observations can be reproduced in a satisfactory manner. It is demonstrated that the stress, prior to the onset of oil production in the Wilmington field, can have a dominant influence on the size and shape of the subsidence pattern. Accordingly, the final, and most successful, simulation includes a horizontal extensional stress component which is added to the overburden stresses at points lying in the vicinity of the center of subsidence.

The lithosphere in the vicinity of island arcs and seamounts can be modeled as a plate which overlies an invicid fluid of asthenosphere material. It has been recognized that bathymetry profiles in such areas resemble the mathematical solutions of certain plate bending problems. This study attempts to improve on previous models by incorporating a lithosphere rheology based on rock deformation data for Dunn-Mountain Dunite. The material behavior is approximated to be as strain rate dependent elastic-plastic. The rheological approximation is converted into a moment-curvature relation for the lithosphere, which in turn is incorporated into a Finite Element algorithm for solving von Karman's plate bending equations. The complete formulation is tested in matching gravity and bathymetry in a profile in the vicinity of the island of Molukai of the Hawaiian-Emperor seamount chain. It is shown that the model can match the observations, while avoiding the excessive fibre stresses which have been produced in previous models.

TABLE OF CONTENTS

Introduction

This thesis contains three numerical modeling studies of tectonic processes in the lithosphere. Chapter one describes a numerical simulation of the tectonics of Southern California; chapter two presents a model for the subsidence in the Wilmington oil field; while chapter three contains a study on the flexure of the lithosphere from loads such as seamounts and island arcs, which is applied to an example in the Hawaiian-Emperor island chain. Although the three problems are on different dimension and time scales, the common feature is the use of the Finite Element method to solve the partial differential equations of equilibrium. Details of the numerical algorithms used in this study are given in the appendices.

The problem of modeling tectonic processes in the Earth is a very difficult one because of the lack of reliable data for the boundary conditions, material response, and initial conditions. Whereas the seismic structure of the Earth is known to a high degree of precision, the knowledge on the state of stress in the lithosphere, or on the forces responsible for tectonic deformation is at best crude. Furthermore, the material response of the crust and upper mantle as a function of depth is not known precisely, and questions such as what is the mechanical nature of faults beyond a depth of a few kilometers?, cannot be answered in a satisfactory manner.

In view of these problems, the approach of this thesis has been to choose problems where it is felt that there is some control on the data, and to limit the study to those aspects of these problems, where it appears that meaningful conclusions can be reached.

In the problem of the tectonics of Southern California, the faulting pattern in the region and certain aspects of the Geology, are incorporated in the model. The study is based on a fault model which is often used by Geophysicists, and it attempts to draw inferences from it on the mechanisms responsible for the formation of the Transverse Ranges and the Palmdale uprise.

The Long Beach subsidence problem presents a study on a very small scale in comparison. In this problem the deformations took place in an accessible region of the crust, and there is relatively good data control on the forces responsible for the Earth movements. Therefore, the Long Beach subsidence problem presents a test case for the numerical techniques used in all the thesis. Indeed, the fit between data and observation obtained in the Long Beach study gives confidence in the ability to simulate accurately tectonic processes whenever good data are available.

The third study is an attempt to construct a realistic moment-curvature relation for the lithosphere in the vicinity of seamounts and island arcs. The rheological model is based on laboratory results for the deformation of Dunite at various strain rates and temperatures. The material model is incorporated into a Finite Element code and the method is tested in fitting a bathymetric profile in the vicinity of Oahu. Although flexure problems are non-unique, the success in fitting profiles by using a material model based on experimental data, demonstrates that there is no paradox between laboratory deduced rock deformation properties and global observations. In particular, the third study shows that the excessively high stress levels which were encountered in previous plate flexure models are not necessary for explaining observed morphological features.

The Finite Element technique used in the three studies in this thesis appears suitable for modeling other tectonic processes in the Earth, whenever data is available. Indeed, it would seem that since the advent of numerical codes capable of solving fully 3-D continuum problems including a realistic material rheology prescription, very often the main obstacle in constructing models lies not in the numerical method, but rather in the data.

Chapter One: NUMERICAL SIMULATIONS OF TECTONIC PROCESSES IN SOUTHERN CALIFORNIA

1.1 Introduction

Several tectonic features in Southern California do not fit easily into the simple plate tectonic model for the region. According to the simple model, the boundary between the North American plate and the Pacific Plate, lies in California, trending in a SE-NW direction (e.g., Atwater, 1970; Minster et al., 1974). The San Andreas fault is a transform fault, along which a large portion of the motion between the two plates occurs. The simple model explains the gross recent tectonic motion which is of a right lateral shear, parallel to the relative velocity vectors between the Pacific plate and North American plate (Minster, et al., 1974). However, it does not explain the existence of the big bend in the San Andreas fault between Taft and San Bernardino, nor the nature of faulting in the Transverse Ranges, nor the Garlock fault, a major feature (Davis and Burchfiel, 1973) (Figure 1.1).

The Transverse Ranges and the area of the White Wolf fault (Figure 1.1) represent narrow zones in which there is a considerable thrust component in the faulting. This indicates a major change in the type of stresses which are responsible for the faulting, since in all other areas of Southern California the faulting is predominantly of the strike-slip type. A number of investigators (Rogers and Chinnery, 1973; Scholtz, 1973) have suggested that the difference

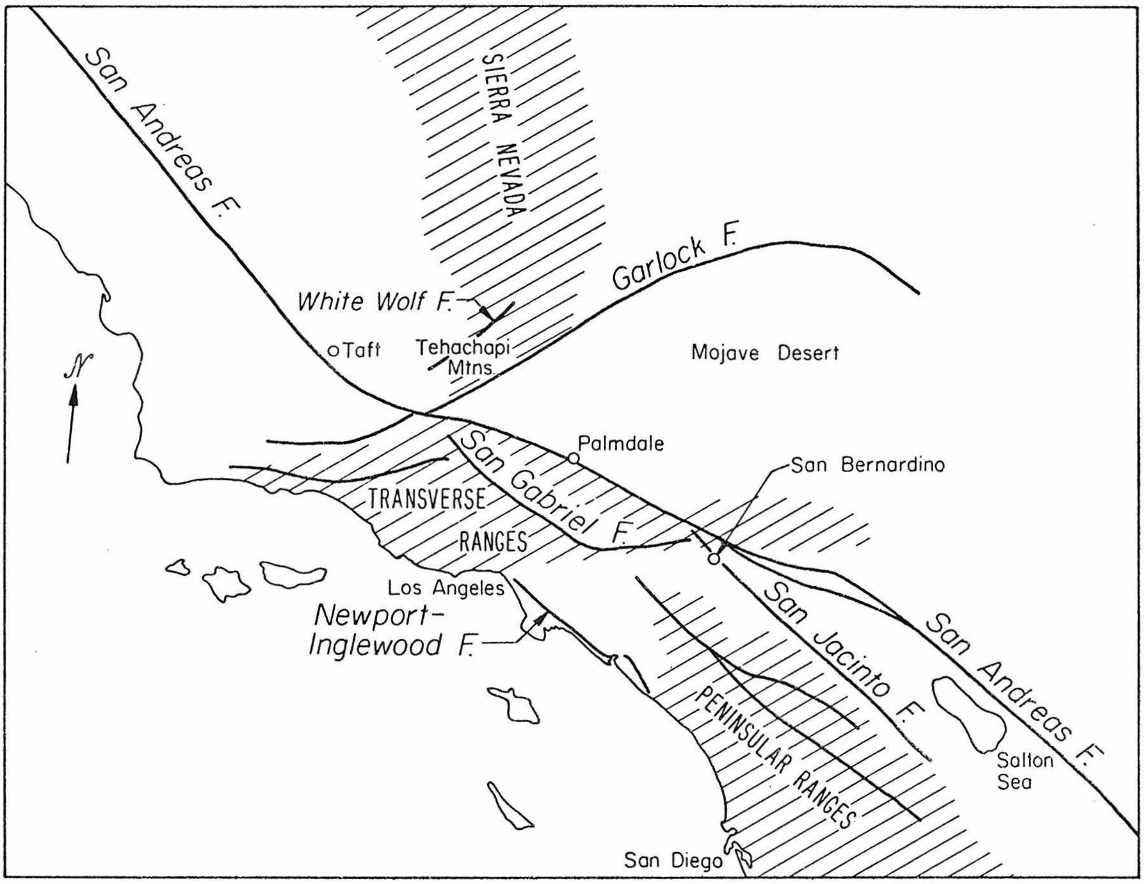

Figure 1.1 Map of the main tectonic features in Southern California.

in fault pattern has been caused by the geometry of the San Andreas fault at the big bend. However, it has not been demonstrated quantitatively that fault geometry can indeed produce such effects, nor does such an hypothesis explain the asymmetry in topography and faulting between the Mojave desert and the San Gabriel Mountains, which lie on opposite sides of the San Andreas fault in the region of the bend.

Interest in the area of the Transverse Ranges gained momentum after the observation of ground upheavals of about 23 cm in the Palmdale area, between the years 1960-1965 (Castle et al., 1976). The observation raised the question of the responsible mechanism for such large displacements, and whether they are related to an impending large earthquake.

This study presents a method of simulating various intra-plate tectonic processes numerically. The method is applied in the region of Southern California in an attempt to explain its topographic and tectonic features. In principle, the availability of computer codes which are capable of solving three dimensional continuum problems with a wide range of material rheologies make it possible to solve deformations in a given region, once boundary and initial conditions and a prescription of its material properties have been specified. In practice, however, the available data in most cases are insufficient to pose these problems. In tackling numerical tectonic simulations therefore for the values of the parameters for the boundary conditions, and for the material rheologies, one must resort to making simplifying assumptions.

Most of the assumptions in this study are based on the notion that on a gross scale the plate tectonic model for Southern California is correct, and various perturbations in it have been considered in order to explain and reproduce the observed anomalous intraplate features.

For the posing of initial conditions in setting up the models, a point requiring attention concerns the time scale to be covered. The present available data suggest that the current tectonic regime in Southern California, has been in existence for about the past four and one half million years (Atwater, 1970). However, the historical record of earthquakes and deformations extends back only a few hundred years at best, and does not give enough data to verify all the results of a simulation of the movements prior to the data's collection. On the other hand, simulations of present or future motions do depend on past history.

A possibility of resolving the difficulty is to assume that mechanisms in the San Andreas fault behave in a cyclical manner (Wallace, 1970), with each cycle consisting of a series of large earthquakes such as the Fort Tejon earthquake of 1857 or the San Francisco earthquake of 1906, followed by numerous smaller events in other segments of the San Andreas fault, and in other faults of the region. With this assumption only one cycle needs to be simulated rather than the full history. Since, according to the slip rate between the Pacific and North American plates and seismicity, the time scale of a cycle in California is on the order of a few hundred years, the configuration of the region would not change appreciably after a few cycles. The use of the infinitesimal continuum theory in simulating motion during each cycle therefore appears justified. Obviously this approach can be used only to approximate motion in the last hundreds, or perhaps thousands, of years, so that processes like the evolution and change of the tectonic regime with time cannot be simulated.

An additional important factor is the choice of material rheology for the lithosphere in Southern California. It is assumed that most nonlinear behavior occurs around faults, and consequently a nonhomogeneous linear elastic prescription has been used to simulate the lithospheric response. Fault segments which undergo creep at certain depths are approximated by narrow zones with a very low shear modulus. As long as the loading of such a creep zone proceeds in the same direction, the approximation resembles an elastic plastic material with a Von-Mises yield criterion (Fung, 1965). Although it is not expected that the approximation of material properties will reproduce correctly causal sequences of events, the existence, or possibility, of stress concentrations and surface uplifts resulting from fault motion, can be reproduced correctly. Thus, the creep event of the Palmdale uplift (Castle et al., 1976), for example, is reproduced, but the modeling cannot determine the exact time that it happened, or when it will produce another event in the future.

1.2 Modeling Procedure

In most of the models tested for the study, a region of Southern California surrounding the Transverse Ranges, has been modeled as a block of continuum material (Figure 1.2). According to the assumptions

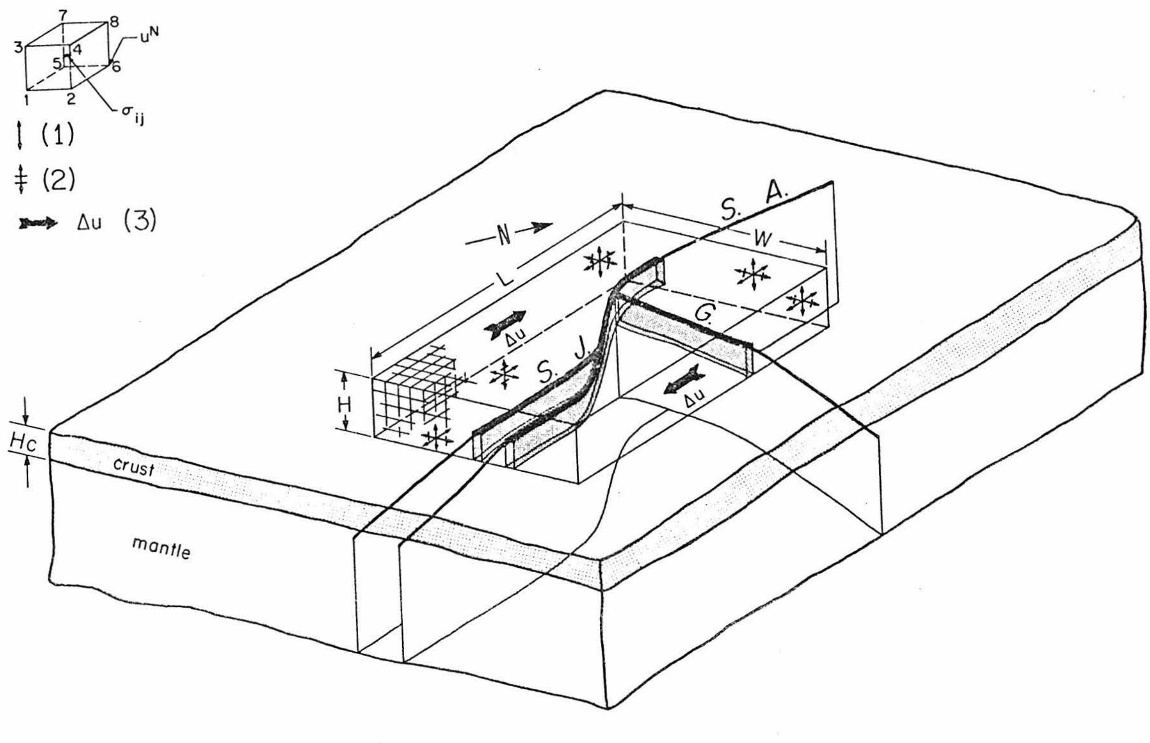

Figure 1.2 A sketch of a typical tectonic model configuration. The large block depicts a portion of the crust and upper mantle in Southern California and the interior brick shape region represents the portion covered by the Finite Element grid. In the upper left corner a single 3-D element is shown where the displacements U_i^N refer to its eight nodes and the stresses σ_{ij} are related to the element centroid. Below the various symbols of the plot are shown where, (1) denotes a boundary condition of a specified traction component in the direction of the arrows, (2) denotes a displacement specified boundary condition, and (3) gives the magnitude of the specified displacement.

made for each model, various regions are assigned different material properties, and a set of displacement or traction boundary conditions are posed on the outer surfaces. The deformations of the region are calculated by a Finite Element method, after approximating the continuum by a three dimensional grid (Figure 1.2). The Finite Element calculations produce three components of displacements at each node of the grid, and six stress components at the centroids of each element (Figure 1.2).

Since the Finite Element mesh approximates only a finite portion of the entire earth, it is important to minimize the effect of this finiteness on the calculations. To achieve this the Eastern and Western boundaries of the FE mesh are chosen far enough away from the surroundings of the San Andreas fault to lie in regions where, according to the plate tectonic postulate, it is justified to assume that the rigidity of the plates holds. (This assumption can be questioned on the east where Basin and Range faulting and other tectonic deformations occur.) The Northern and Southern boundaries of the mesh traverse the San Andreas fault and other active faults so that it is necessary to pose the boundary conditions in a manner that will not affect the validity of the calculated results. It is found that this can be achieved by constraining the horizontal component of motion which is tangential to these boundaries, but allowing free motion in the two remaining directions (Figure 1.2).

The bottom boundary is usually taken at a depth well below the crust-Moho transition, which is about 30 km deep in Southern California (Kanamori and Hadley, 1975). Since it is assumed that little vertical motion takes place below this depth on the bottom boundary, the vertical displacements are constrained to be zero. The horizontal displacements on this boundary are not constrained in the two models discussed in this study, and no tractions are applied there either. (In other models combinations of drag forces of various signs are applied on the bottom boundary).

For the present study, two of the tested models have been chosen for presentation, a model of a straight and long transform fault, and a model for a region containing a major transform with a bend.

1.3 A Model of a Straight and Long Transform Fault

The first model tested is of a straight and long transform fault surrounded by a homogeneous medium. It serves to establish a background deformation pattern, upon which contributions from the various complications in the tectonics of Southern California can be superimposed in later models. Since the results can be interpreted readily, it also serves to insure that the computations are not artificially influenced by the configuration of the Finite Element mesh.

The model consists of a crustal block 435 km long, 300 km wide and 60 km deep (Figure 1.3a). A vertical weak zone, 20 km wide is situated in the middle of the block between the depths of 30 km and 60 km (Figure 1.3a). It represents the unlocked portion of the transform fault undergoing creep. The choice of these depths is based on the observation that all hypocentral depths in Southern California, so far, have been shallower than 20 km (Hileman *et al.*, 1973), and on the assumption that fault motion is totally aseismic a few kilometers beyond that

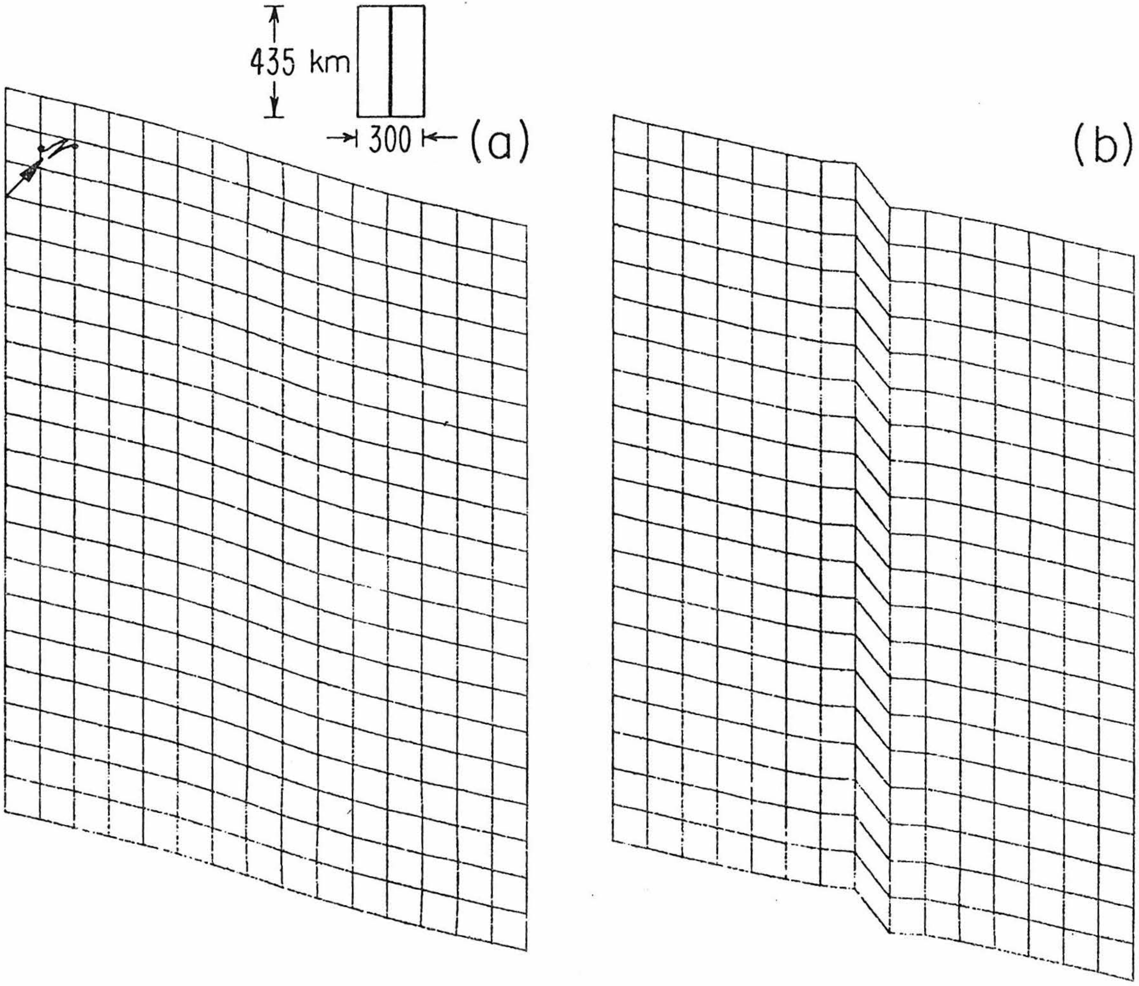

Figure 1.3 (a) A horizontal cross section of the Finite Element grid of the first model, which gives the horizontal dimensions and the fault geometry. The material parameters for regions outside the faults were a density of 2.8 gr/cm3 and P and S velocities of 6 km/sec and 3.464 km/sec respectively. The fault zones were assigned a density of 2.8 gr/cm3 and P and S velocities of 4.4726 km/sec and 0.14 km/sec respectively. (b) A plot of the horizontal displacements at the free surface. (c) A plot of the horizontal displacements at a depth of 45 km.

depth. (In a later section we discuss the implications of fault creep at shallower depths than 25-30 km with regard to the shape of the Palmdale bulge.) On the lower boundary, the block is allowed to slide freely in the horizontal directions, but is prevented from moving vertically. Hence this boundary is considered a decoupling zone at the bottom of the plate. The model tested the hypothesis that the main tectonic driving force in regions around transform faults is caused by drag from the sides by the two plates which meet at the fault. Consequently, a displacement increment of ±3 meters in opposite directions is applied to the Eastern and Western boundaries, corresponding to approximately one hundred years of plate motion (spreading) in California (Savage and Burford, 1973; Brune, 1968). It should be noted that for a given displacement increment, the width of the block will determine the magnitude of the strains, with the results seeming to depend on the choice of block width. However in the absence of heterogeneities and faults, the boundary conditions in this example approximately produce a state of constant shear strain, and thus conclusions concerning stress concentration factors over the homogeneous case, or the perturbations of displacement patterns, are still considered valid for this model.

The horizontal displacement at the free surface is given in Figure 1.3b, in which at each node a product of the horizontal displacement and a constant scale factor are added to the coordinate. The plot shows a rather diffuse displacement pattern, while the trace of the weak zone at depth is not distinct. The general pattern is of horizontal shear which extends to the boundary, with no noticeable adverse distortions (such as twisting where the fault contact the boundary). Figure 1.3c displays the displacements at a depth of 45 km. It can be seen that a large portion of the strains are taken up on the fault.

The vertical displacement contours at the free surface are given in Figure 1.4. In the central portion of the plot, the vertical displacement values are within the resolution limits of the contour plot, and are practically zero. Only where the creep zone intersects the Northern and Southern boundaries of the Finite Element mesh are there noticeable vertical displacements.

Figures 1.5a, 1.5b, 1.5c and 1.5d give lower hemisphere stereographic projections of stresses at chosen points in four horizontal layers, at depths of 7.5 km, 22.5 km, 37.5 km and 52.5 km respectively. In these plots, the radius of each circle is linearly proportional to the difference between the maximum and minimum principal stresses at the center point. Such plots display the orientation of the principal stresses, as well as give some information about their values. A similar stereographic projection method is often used to display focal mechanisms of earthquakes. Hence, for fracture models in which the fracture plane is close to a maximum shear plane, these plots can predict and display the focal mechanism for an earthquake which will be caused by the stresses. The derivations used to construct these plots are given in appendix F.

Figure 1.5a and 1.5b show that in the two upper layers the stresses are essentially of horizontal shear with a large stress concentration at points directly above the creep zone. In the lower layers, the

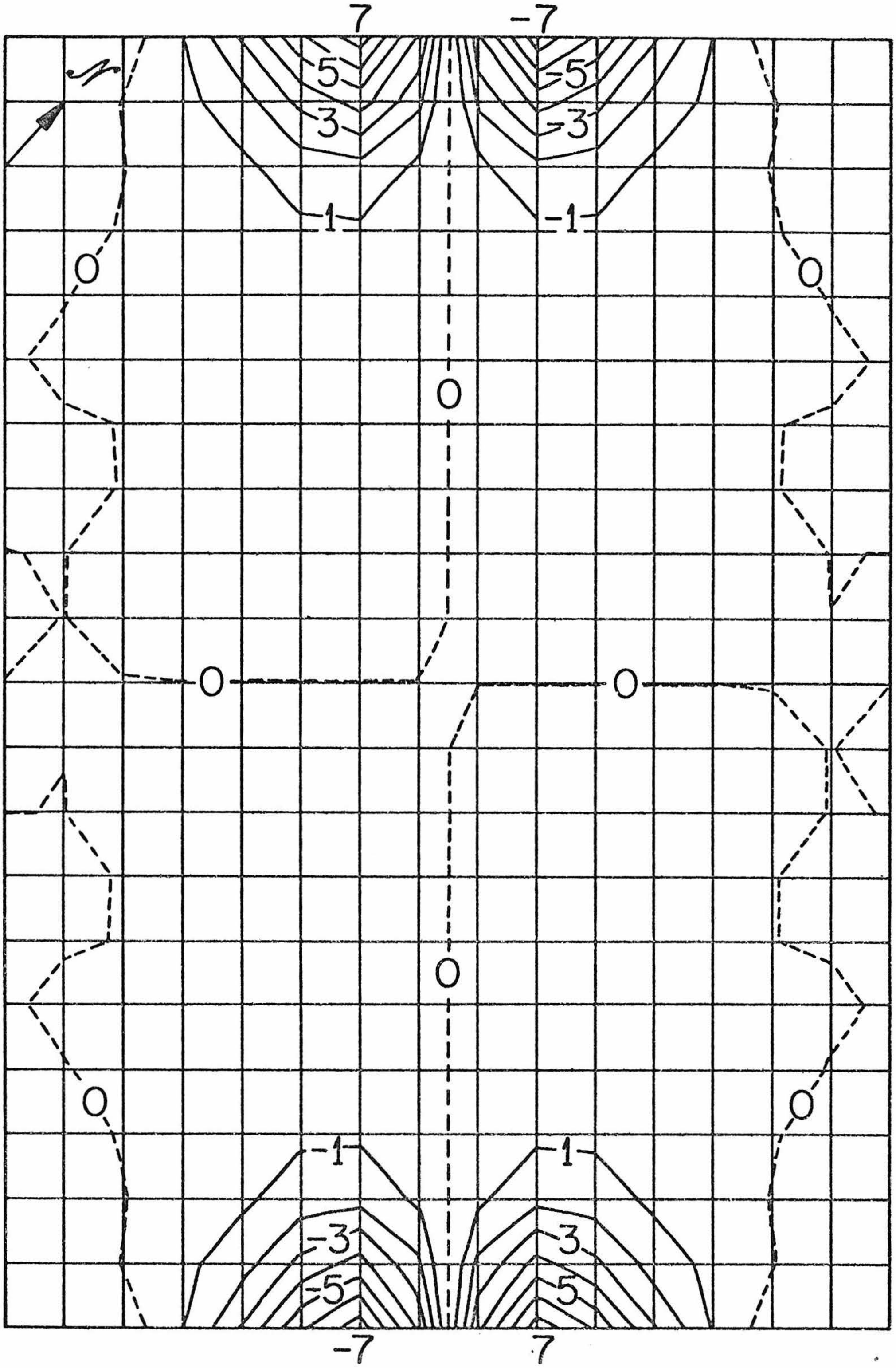

Figure 1.4 Vertical displacement contours in centimeters on the free surface for the first model.

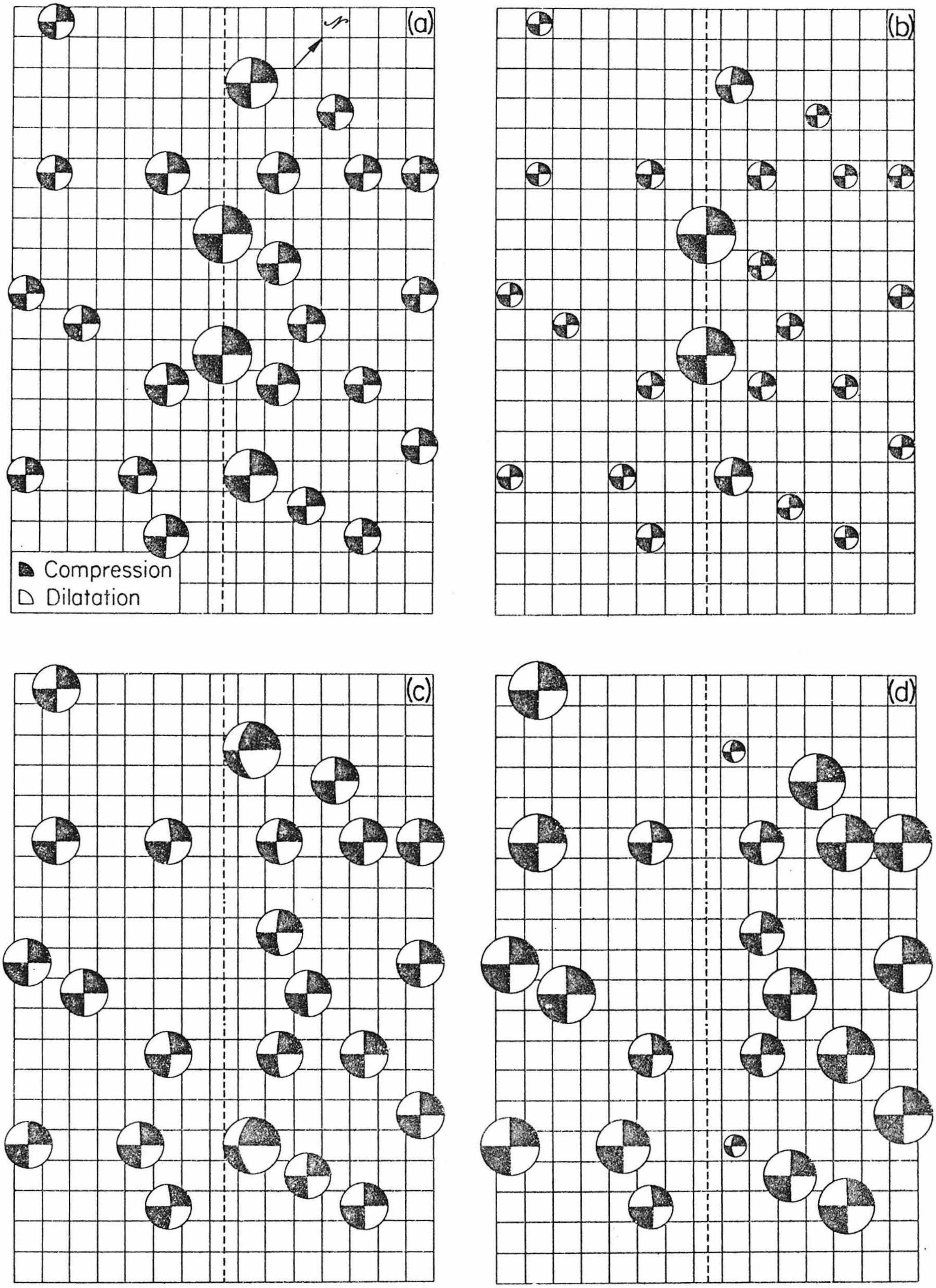

Figure 1.5 Stereographic projections of stresses at selected points on horizontal sections at various depths (a) d=7.5 km, $|\sigma_1-\sigma_3|_{max}$ = 19.1 bar. (b) d=22.5 km, $|\sigma_1-\sigma_3|_{max}$ = 27.0 bar. (c) d=37.5 km, $|\sigma_1-\sigma_3|_{max}$ = 14.0 bar. (d) d= 52.5 km, $|\sigma_1-\sigma_3|_{max}$ = 11.4 bar.

stresses are lower and more uniform. Adjacent to the fault zone, one of the two maximum shear planes is rotated towards the fault. In all the layers the stresses vary only as a function of distance from the Eastern or Western boundary and not in the N-S direction. This again shows that the boundary conditions can be used to approximate the effect of the surrounding media on the region under study, except toward its edges.

An additional class of models, in which the driving forces are supplied by tractions on the lower boundaries as opposed to a displacement specification, also have been tested. In general, the results for these models do not differ in nature from the results of models with the displacement specification. For example, one model uses the grid configuration of Figures 1.3a and 1.3b, and has a driving mechanism of two uniform tractions applied respectively on the Eastern and Western halves of the lower boundary of the grid. These tractions are equal in magnitude, but opposite in sign in a right lateral sense. The calculated displacement and stress patterns for this model are very similar to the patterns in Figures 1.3, 1.4, and 1.5; the only significant difference is a somewhat higher stress and strain concentration above the creep zone.

1.4 A Model for a Region Containing a Major Transform Fault with a Bend

In seeking an explanation for some of the major physical processes in Southern California, a model has been set up which consists of a lithospheric plate decoupled from below, containing a transform fault with a pre-existing bend in it (Figure 1.6a). According to this model, between major earthquakes, motion along the fault is restricted to creep at lower depths until the stress buildup in the locked zone exceeds the strength of its material. It is then that the rupture will occur. Variations on this model have been proposed by a number of investigators (Allen, 1968; Rogers and Chinnery, 1973; Scholtz, 1973; Barker, 1976), while some researchers put forth the suggestion that the Transverse Ranges have been caused because the bend in the San Andreas fault does not allow the material to be displaced freely, and it becomes compressed (Scholtz, 1973; Rogers and Chinnery, 1973).

The model has been tested numerically by simulating motion at intervals between large earthquakes along the segment of the San Andreas fault between San Bernardino and Taft (Figure1.1). This particular example considers creep at depth only along the San Andreas and San Jacinto faults. Other examples which have been tested consider also creep along other faults, including the Garlock fault and the Newport-Inglewood fault.

In this model the upper portion of the San Andreas fault above 30 km, is considered to be locked. However, in the upper layers, the San Jacinto fault is approximated by a zone with a shear modulus reduced to about one third of the shear modulus of the crust, thus attempting to account for the higher level of seismicity on this fault (Hileman et al., 1973).

Figure 1.6a gives the grid configuration, as well as other pertinent parameters for the calculations in the model. The vertical dimension

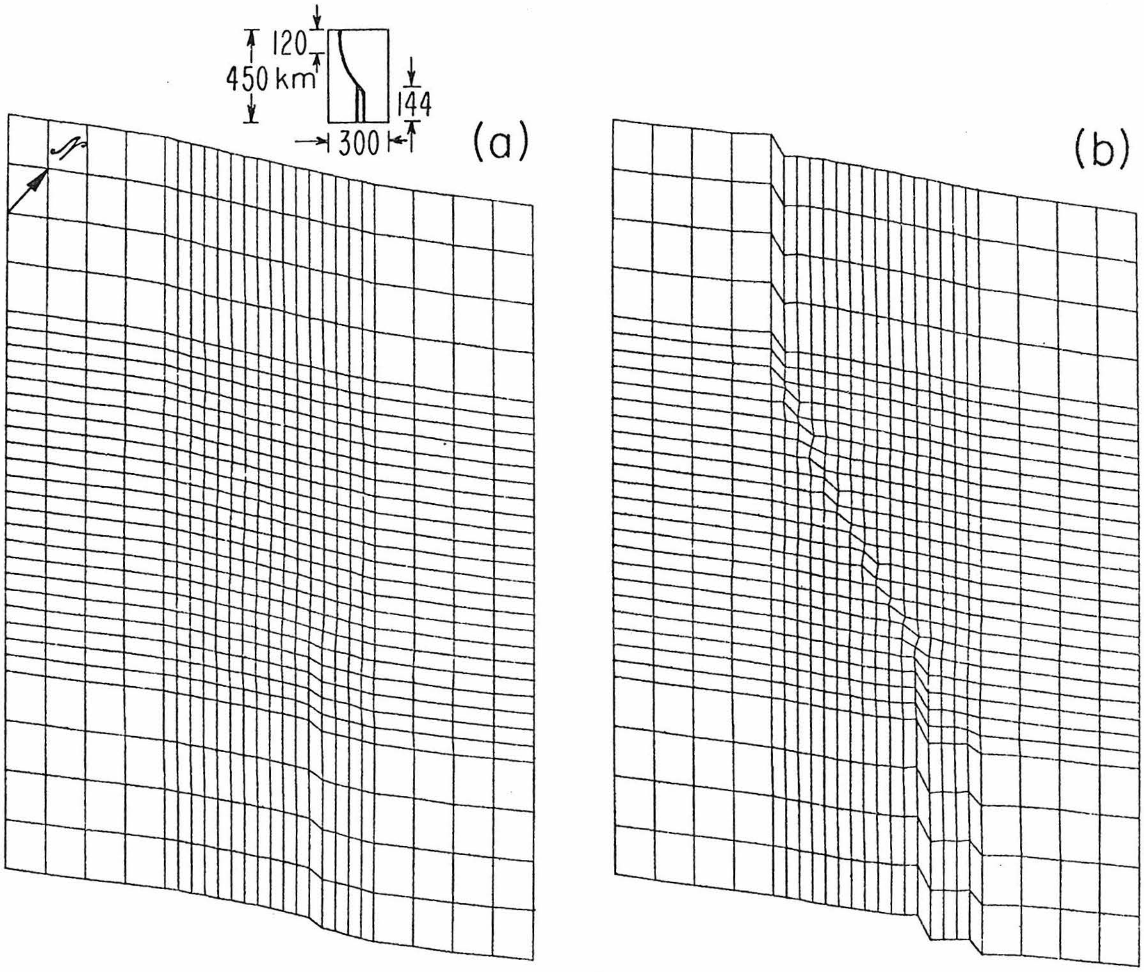

Figure 1.6 (a) A horizontal cross section of the Finite Element grid of the second numerical model. (b) Horizontal displacements at the free surface. (c) Horizontal displacements at a depth of 45 km.

of the lithospheric block is 60 km. This depth has been chosen to correspond roughly to the thickness of oceanic plates, but it is obvious that there is need for data on whether such a decoupling zone exists at such a depth in Southern California. However, we have not experienced significantly different results in a model with a plate thickness of 70 km. The fault zones are 7.5 km wide (one element), in segments which are parallel to the grid, and are slightly wider in the region of the bend (e.g. Figure 1.8). The material constants chosen to represent the lithosphere, correspond to a P velocity of 6 km/sec, an S wave velocity of 3.464 km/sec and a density of 2.8 gr/cm^3. These values are close to values often quoted for granite. However, it is questionable whether these parameters accurately represent the response of the lithosphere to long term loads, and they are used only as an approximation. The creep zones of the faults are assigned P and S velocities of 4.4726 km/sec and 0.14 km/sec respectively with a density of 2.8 gr/cm^3. These velocities correspond to a shear modulus three orders of magnitude smaller than the modulus of crustal material. The upper layers of material along the San Jacinto fault have P and S velocities of 5.03 km/sec and 2. km/sec respectively, and a density of 2.8 gr/cm^3. A displacement boundary condition of $\mp$ 3 meters is applied on the Eastern and Western boundaries of the grid. The calculations use a 30 X 24 X 4 grid totaling 2880 elements and 3875 nodes. At points corresponding to the region where higher accuracy is required, the mesh is finer.

The calculated horizontal displacements at the free surface and at a depth of 45 km are shown in Figure 1.6b and 1.6c respectively. As in the previous example (Figures 1.3b and 1.3c), the faults are not very noticeable on the free surface, and the strain is distributed over a wide zone. In the deeper layers where the faults are not locked, most of the strain is concentrated on the faults. The traces of the San Andreas fault and the San Jacinto fault can be easily distinguished there.

Figure 1.7 gives the calculated vertical displacements at the free surface. The striking feature in the plot is the surface uplift above the bend in the creep zone. The contours resemble the so-called "Palmdale uplift" which, as reported by Castle et al. (1976), occurred between the years 1968-1965. (This uplift does not appear in the previous model of a straight fault; that it appears here must be a consequence of the bend in the fault geometry.)

The stereographic projections of stresses at selected points in the four layers of elements, are given in Figures 1.8 a, b, c and d. In the first two layers, which are above the creep zones, the stresses are dominated by horizontal shear. The main effect of the unlocked portions of the faults in the lower layers is to produce stress concentrations above them, and to rotate the maximum shear planes in the upper layers of the bend segment toward alignment with the fault trace. In the two lower layers, the stresses are low along the faults. Adjacent to them, one of the maximum shear planes is tilted.

In regard to a possible mechanism for producing the Transverse Ranges, the stresses in the plots of the two upper layers nowhere appear to be conducive to thrust faulting. Basically, both the maximum and minimum principal stresses there are horizontal, while

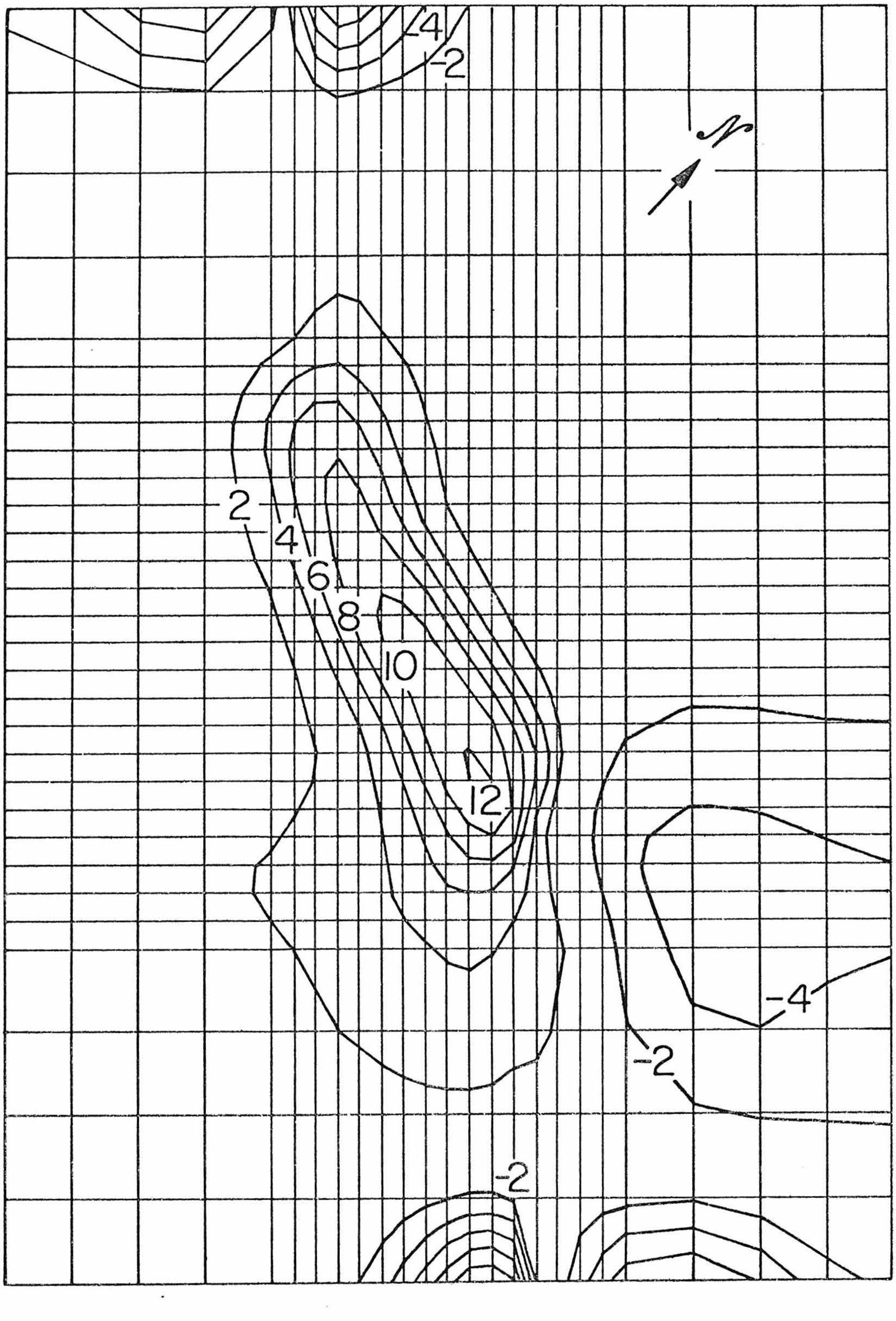

Figure 1.7 Vertical displacements contours in cm at the free surface for the second tectonic model.

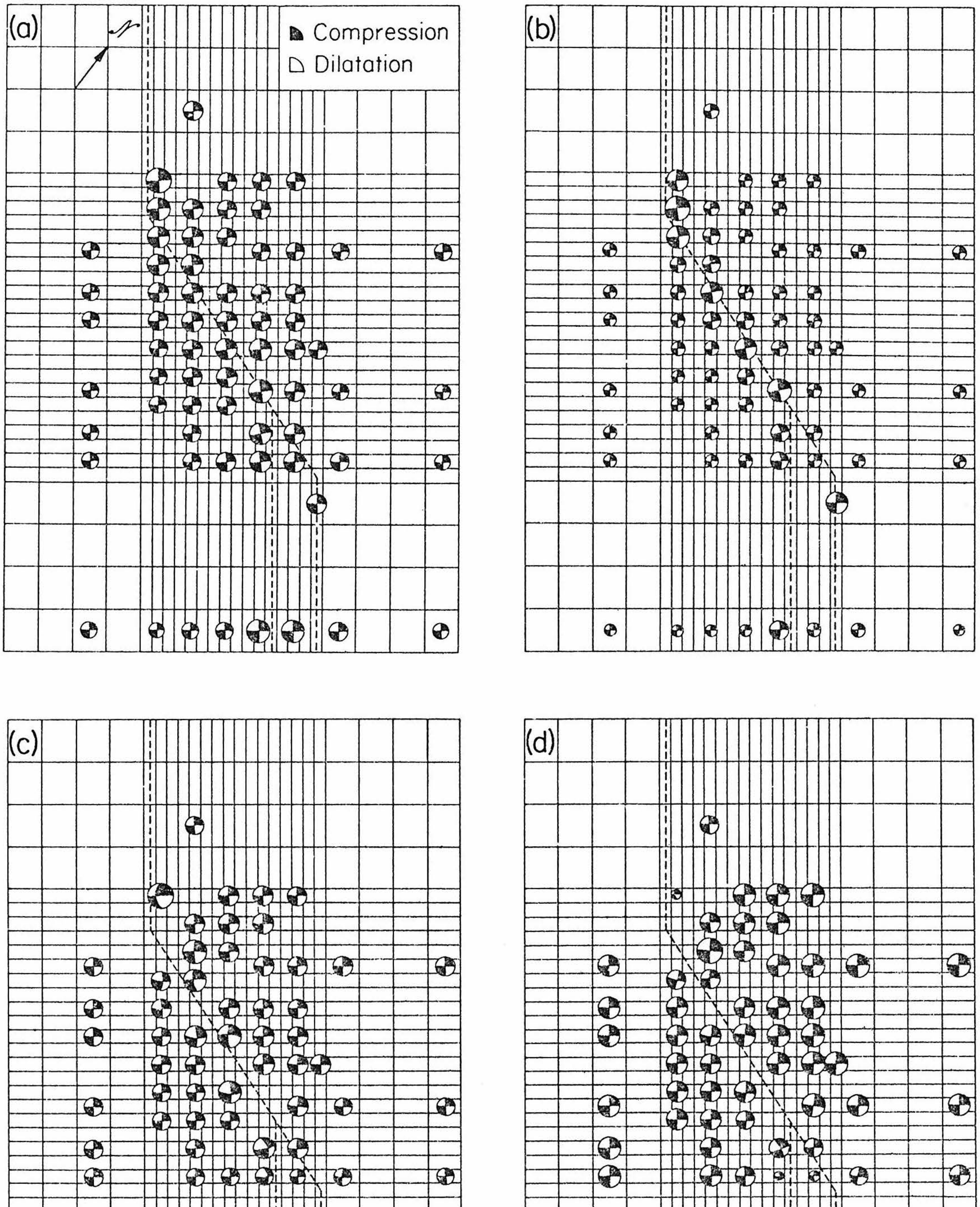

Figure 1.8 Stereographic projections of stresses at different depths for the second model (a) d=7.5 km, $|\sigma_3 - \sigma_1|_{max}$ = 17.2 bars. (b) d=22.5 km, $|\sigma 3 - \sigma 1|_{max}$ = 22.4 bars. (c) d=37.5 km $|\sigma_3\ \sigma_1|_{max}$ = 15.5 bars. (d) d=52.5 km $|\sigma_3 - \sigma_1|_{max}$ = 13.4 bars.

for thrust faulting, in most fracture models, the minimum principal stress has to be close to vertical. Other models have been tested as mechanisms for the Transverse Ranges. These include features such as crustal heterogeneities, creep on other faults including the Garlock fault, or a driving mechanism of drag on the plate bottom. The results also do not produce significantly different stress patterns. A model based on dislocation theory in a half space, in which displacement discontinuities are prescribed along the faults, again does not produce stress patterns conducive to thrust faulting. On the other hand, the stresses can be modified by introducing localized forces or obstacles which resist motion on the bottom boundaries. It appears therefore, that if the Transverse Ranges are produced only as a result of material heterogeneities in the crust, or by the geometry of the San Andreas fault, the rate of strain release by thrust faulting must be slower than the rate of release of horizontal shear strain by right lateral motion.

In order to clarify further this point, we have considered the stress tensor $\sigma_{ij}^{(1)}$, which is obtained by subtracting from the stresses shown in Figure 1.8a and Figure 1.8b, a uniform shear stress $\sigma_{ij}^{(0)}$, of magnitude 6.56 bars, and an orientation parallel to the sides of the grid. To a good approximation, these uniform stresses are produced in a homogeneous model which does not contain faults, and has the same dimensions as the model of this section. This is because the strains in such a model, essentially consist of horizontal shear, equal in magnitude to the ratio between the absolute values of the specified displacements on either of the two sides of the grid, and the width of the mesh. Physically, the uniform stresses, $\sigma_{ij}^{(0)}$, build up during periods in which the faults are inactive, as the lithosphere then behaves approximately like a homogeneous block. When certain faults become activated by creep at depth, a new stress pattern is produced, which in the model of this section is the pattern of Figures 1.8a, b, c and d. Thus the stresses of $\sigma_{ij}^{(1)}$ are the perturbation to the stresses of the homogeneous model caused by the inception of creep on faults.

The perturbation stresses $\sigma_{ij}^{(1)}$ for the two upper layers are plotted in Figure 1.9a and 1.9b respectively. In these plots, the stresses directly above the creep zone are still predominantly of horizontal shear. The rotation of the maximum shear planes toward the direction of the trace of the San Andreas fault is very apparent. In the regions of the grid corresponding to the Transverse Ranges province, the minimum compressive stress axis is close to vertical. These stress perturbations, therefore, are conducive to thrust faulting. The feature is asymmetric, and in the region corresponding to the Mojave desert is less apparent. Apparently this is the result of the existence of the San Jacinto fault in the model. Indeed, with a model containing an additional fault at depth (Figures 1.9c and 1.9d) in the vicinity of the Newport-Inglewood fault, this characteristic is further enhanced (especially since the numerical values of the stresses there are higher than in Figures 1.9a and 1.9b). These results may give a clue to the cause of the Transverse Ranges by suggesting a model in which for some particular reason the right lateral faults to the west of the San Andreas fault and south of the Transverse Ranges cannot continue throughout this province. The right lateral motion along

Figure 1.9 Perturbation stresses $\sigma_{ij}^{(1)}$ at selected points (a) Stresses for the second model at a depth of 7.5 km, $|\sigma_3^{(1)} - \sigma_1^{(1)}|_{max} = 5.4$ bars. (b) Stresses for the second model at a depth of 22.5 km, $|\sigma_3^{(1)} - \sigma_1^{(1)}| =$ 10.1 bar. (c) Stresses for a model which included the Newport-Inglewood fault at a depth of 7.5 km $|\sigma_3^{(1)} - \sigma_1^{(1)}|_{max} = 6.3$ bars. (d) Stresses for a model which included the Newport-Inglewood fault at a depth of 22.5 km, $|\sigma_3^{(1)} - \sigma_1^{(1)}|_{max} = 13.5$ bars.

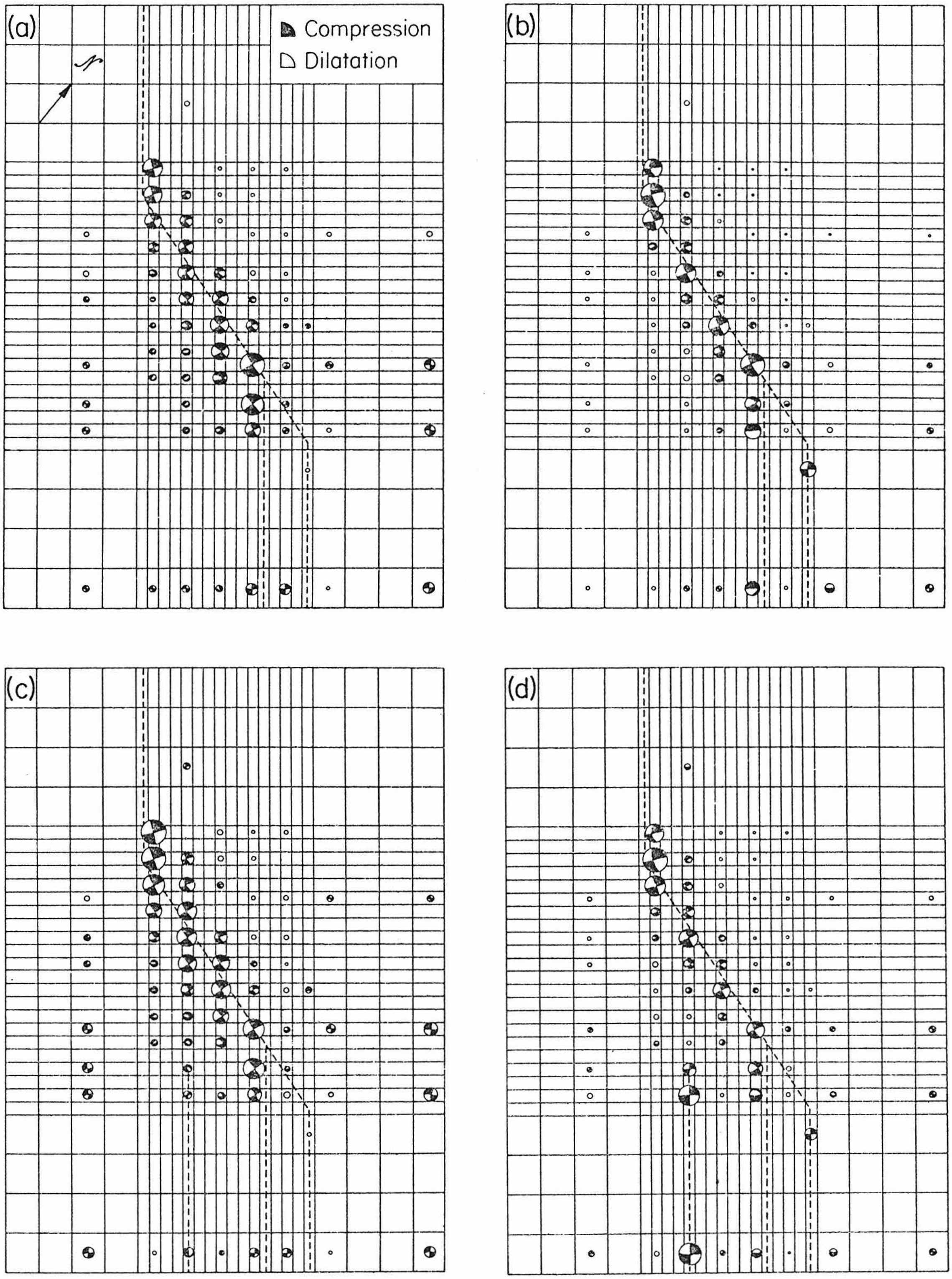
(a)
Compression
Dilatation
(b)
(c)
(d)

them, therefore, concentrates stresses which are conducive to thrust faulting. Other alternative explanations could involve local forces on the bottom of the plate below the Transverse Ranges, but at the moment the amount of data available on their values may render an attempt at calculation premature.

1.5 The Palmdale Uplift

Figure 1.7 shows that a tectonic model of Southern California which includes the San Andreas fault with a creep zone at depth, produces a vertical displacement pattern similar to the so-called Palmdale uplift as reported by Castle et al. (1976). This explanation of the Palmdale uplift invokes a shear stress buildup in the region of the bend in the San Andreas fault. Thus, after one or a number of such events, when the stresses will exceed the strength of the material, the locked zone of the fault ruptures. In this section, the main implications of this model in the formation of Palmdale uprise will be summarized.

(a) According to the model of Figures 1.6a and 1.6b, the Palmdale uprise has been caused by creep at depth on a weak zone of finite width on the San Andreas fault in the region of the bend. In this area, the trace of the San Andreas fault is at an angle to the predominant NW-SE shear stress plane in Southern California. Consequently, weak material in the creep zone which is squeezed, pushes the material above it upward, resulting in a bulge on the surface.

(b) From the results of calculations in a number of cases, it appears that in order to form an uplift pattern which resembles the Palmdale uprise, the creep zone must begin at a depth of at least 25 km and extend to depths of 50-60 km. This is because for shallower depths the uplift would be much narrower than observed.

(c) For a creep zone 7.5 km wide and a deep fault, the ratio between fault dislocation at the bottom of the creep zone and the surface uplift is between five to one to ten to one. Thus the observed uplift of around 23 cm around Palmdale, corresponds to about 1-2 meters of creep on the fault at depth.

(d) In this explanation, creep on the Garlock fault could not have taken place during the formation of the Palmdale uprise, because models which include the fault produce totally different contours.

(e) The numerical model predicts that uprises of the type of the Palmdale uplift will be accompanied by a horizontal shear strain parallel to the trace of the San Andreas fault in the region of the bend. From Figure 1.9a and Figure 1.6c these strains are on the order of 10^{-5}.

According to this explanation, during periods in which the faults are inactive at all depths, the lithosphere in Southern California behaves like a uniform block subjected to a shear stress rate field parallel to the spreading vector between the North American and Pacific plates. When the San Andreas fault in the bend area becomes active at depth, the stress rates in the vicinity of the fault will accelerate and rotate in a counter clockwise direction with respect to their previous orientation (as in Figures 1.9a and 1.9b).

1.6 Conclusion

This study has attempted to shed some light on the mechanism responsible for producing the Transverse Ranges. It has found that in the plate tectonic interpretation of Southern California, their existence cannot be directly attributed to the geometry of the San Andreas fault, nor to crustal heterogeneities, nor to the existence of the Garlock fault. In models which account for creep on the San Jacinto fault, as well as on some other right lateral faults in Southern California, a very small stress component conducive to thrust faulting is observed in the region of the Transverse Ranges. Because this component is very small, it appears that either the rate of stress release by thrust faulting in the Transverse Ranges is much smaller than the rate of release by right lateral strike slip faulting on the San Andreas fault, or that there is a separate mechanism which is responsible for the formation of the Transverse Ranges.

The study also shows that a region containing creep zones of a finite width, under certain circumstances, can experience surface upheavals similar to the Palmdale uplift.

References

Allen, C. R., 1968. The tectonic environment of seismically active and inactive areas along the San Andreas fault system. Stanford Univ. Publ. Geol. Sci., VXI, p. 70.

Atwater, T., 1970. Implications of plate tectonics for the Cenozoic evolution for Western North America, Bull. Geol. Soc. Amer., V. 81, p. 3513-3536.

Barker, T. G., 1976. Quasistatic motions near the fault zone, Geophys. J. R. Soc., 45, p. 689-705.

Brune, J. N., 1968. Seismic moment, seismicity and rate of slip along major fault zones. J. Geophys. Res., V. 73, p. 777.

Buchanan-Banks, J. M., 1975. Elevation changes in the central Transverse Ranges near Ventura, California, Tectonophysics, 29, p. 113-125.

Castle, R. O., Church, J. P., and Elliot, M. R., 1976. Aseismic uplift in Southern California, Science V. 192, p. 251-253.

Davis, G. A., and Burchfiel, B. C. 1973. Garlok fault: An intra-continental transform structure, Southern California, Geol. Soc. Amer Bull., 84, p. 1407-1422.

Fung, Y. C., 1965. Foundations of solid mechanics, Prentice Hall.

Hileman, J. A., C. R. Allen and J. M. Nordquist (1973), Seismicity of the Southern California region, January 1932 to 31 December 1972, Seismological Laboratory, California Institute of Technology, 487 p.

Jahns, R. H., 1973. Tectonic evolution of the Transverse Ranges province as referred to the San Andreas fault system. In Kovach, R. L. and Nur, A. eds: Proceedings of the Conference on tectonic problems of the San Andreas fault system, Stanford Univ. Pubs. Geol. Sc., V. 13, p. 149-170j.

Kamb, B., Silver, L. T., Abrams, M. J., Carter, B. A., Jordan, T. H., and Minster, J. B., 1971, Pattern of faulting and nature of faulting movement in the San Fernando earthquake, U. S. Geol. Survey Prof. paper 733, p. 41-54.

Kanamori, H. and Hadley, D., 1975. Crustal structure and temporal velocity changes in Southern California, Pure and App. Geophys. V. 113, p. 257-280.

Minster, J. B., T. H. Jordan, Haines, E., 1974. Numerical modeling of instantaneous plate tectonics, Geophys. J. R. Astr. Soc., 36, 541-576.

Rogers, P. A. and Chinnery, M. A., 1973. Stress accumulation in the Transverse Ranges, Southern California, in Kovach, R. L. and Nur, Amos, eds, Proceedings of the Conference on tectonic problems of the San Andreas fault system, Stanford Univ. Publs. Geol. Sci. 13.

Savage, J. C., and Burford, R. O., 1973. Geodetic determination of relative plate motions in central California, J. Geophys. Res., 78, p. 832-845.

Scholtz, C. H., 1973. A comparison of the San Andreas fault with the Alpine fault, in Kovach R. L. and Nur, Amos, eds, Proceedings of the Conference on problems of the San Andreas fault system, Stanford Univ. Pubs. Geol. Sci., 13.

Smith, S. W. and W. Van de Lint, 1969. Strain adjustments associated with earthquakes in Southern California, Seism. Soc. Amer. Bull., 59, p. 1569.

Wallace, R. E., 1970. Earthquake recurrence intervals on the San Andreas fault, Geol. Soc. Am Bull., 81, p. 2875-2890.

Chapter Two: SUBSIDENCE IN THE WILMINGTON OIL FIELD

2.1 Location and Subsidence History

The Wilmington oil field is situated in the Western part of the Los Angeles basin in the Long Beach harbour area (Figure 2.1). The field extends lengthwise approximately 18 Km in a SE-NW direction. The width is about 5 Km in the SW-NE direction. Production in the field began in 1936. Cumulative production through 1967 was 1156 billion barrels of oil, and 840 million ft^3 of gas (Mayuga, 1970).

The subsidence in the field began in 1937 (Gilluly and Grant, 1949, p. 479), but was first definitely recognized in 1941, when the U.S. Coast and Geodetic Survey releveled lines between San Pedro and Long Beach which had been previously run in 1933-34. Subsequent releveling showed an increasing maximum subsidence of 8 feet in 1947, 13 feet in 1951, 20 feet in 1954, 26 feet in 1958, until the maximum of 29 feet in 1965. Figure 2.2 shows the subsidence contours for the year 1958. Their pattern has roughly an elliptic shape, and most of the subsidence occurred in areas lying above fault blocks II, III, and IV (e.g. Figure 2.5).

The subsidence was also accompanied by large horizontal displacements which reached a maximum of about 12 feet (Allen, 1973). In general, the horizontal displacement vectors pointed roughly towards the center of the subsidence bowl.

Although most of the subsidence and horizontal motion took place in a continuous manner, in a number of instances abrupt strain release

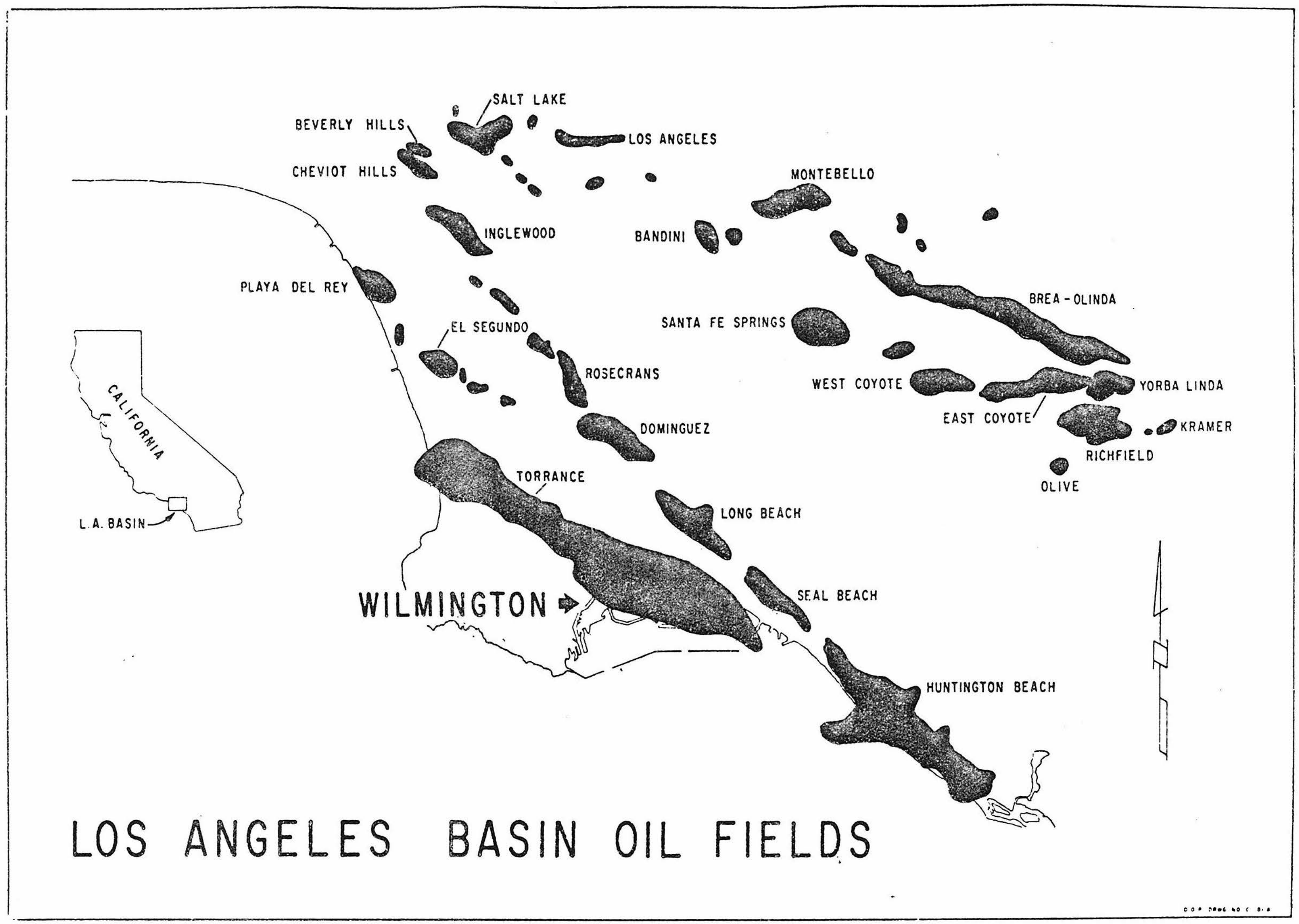

Figure 2.1 Los Angeles basin oil fields (after Mayuga, 1970).

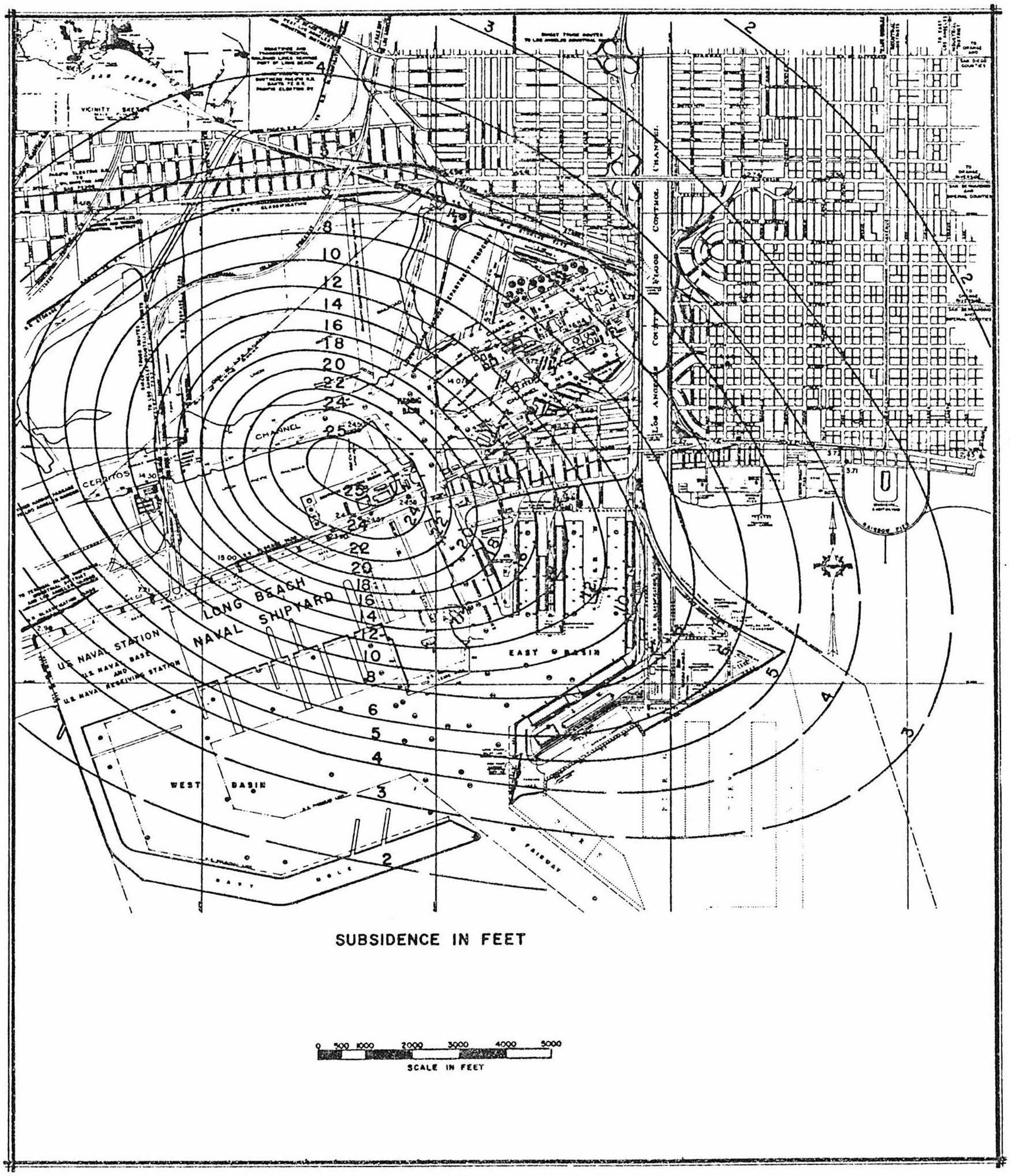

Figure 2.2 Observed subsidence in feet for 1958 (Courtesy of City of Long Beach).

also happened in the form of small earthquakes. These events occurred in the years 1947, 1949, 1952, 1955, 1961 and have not been observed since (Richter, 1958; Poland, 1969). The hypocenters were at shallow depths between 450 to 550 meters in bedded shale formations (Figure 2.3). The fault planes were always close to horizontal (Richter, 1958; Mayuga, 1965; Kovach, 1974). The epicentral locations were as shown in Figure 2.3. Because of their shallow depths, the earthquake events produced unique seismograms in Pasadena and Riverside, which consisted essentially of surface waves (Kovach, 1974; Richter, 1958).

The Wilmington oil field subsidence caused considerable damage in the port of Long Beach. Extensive remedial measures were required to prevent flooding of lands and structures, primarily in the form of construction levees, retaining walls, fills, etc. (Poland, 1969). In order to prevent further major subsidence, a repressurization program by water injection was initiated in 1958. By 1962, the subsidence rate had decreased appreciably, while in certain areas there was a rebound to a maximum of about 1.5 feet (Allen, 1973).

In 1965, after it had become apparent that the subsidence could be checked by repressurization, an offshore extension of the field was developed. In order to prevent the recurrence of subsidence, and its associated effects, in the new extension area, a pressure maintenance program was initiated at the onset of production. The present study is concerned with the subsidence, and with the subsequent rebound in the area of the field exploited until 1965. In the absence of major pressure changes in the new area which has been exploited since 1965, it is very unlikely that its development affected elevation

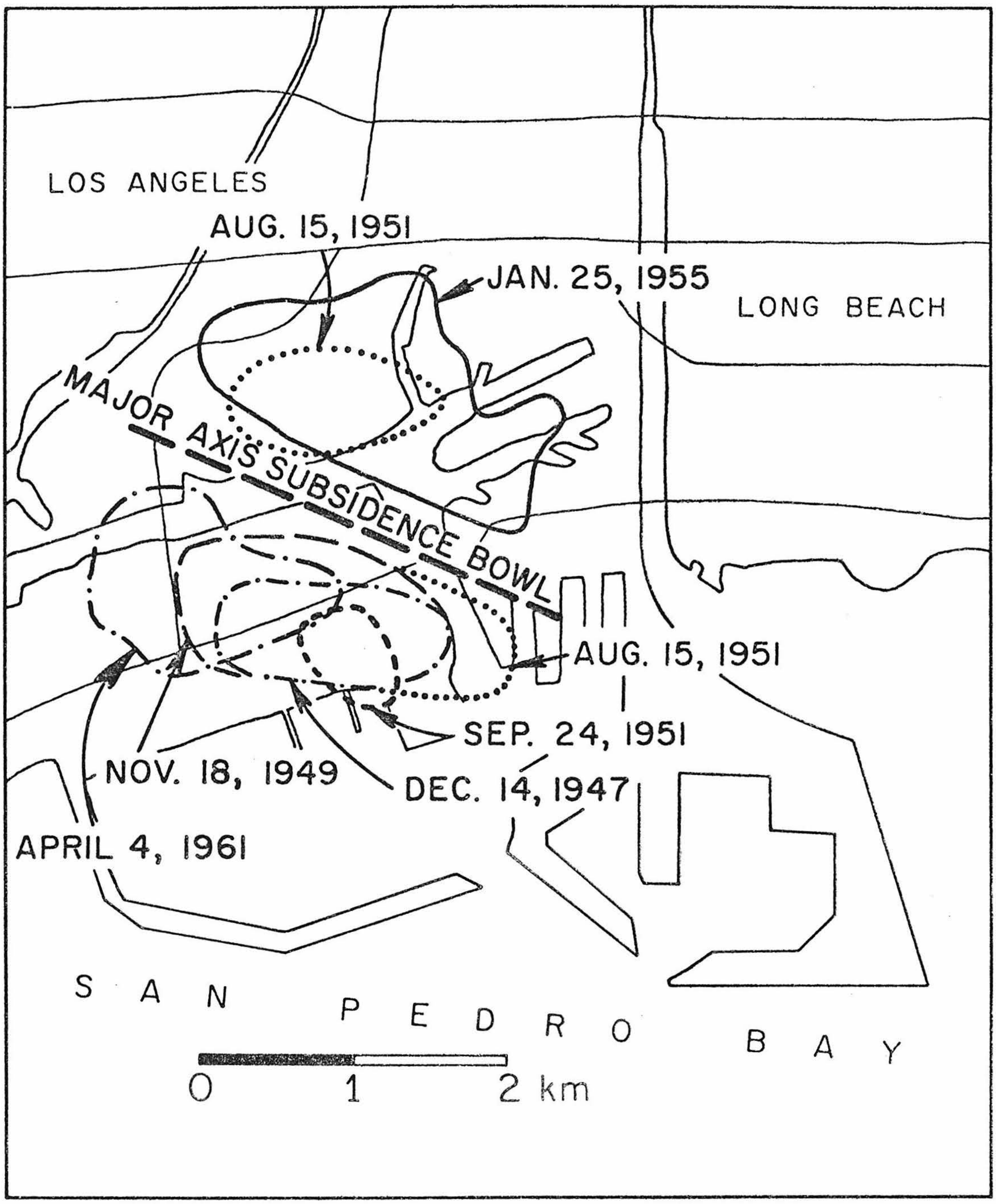

Figure 2.3 Epicentral locations and slip planes of subsidence earthquakes.

changes in the older area.

Further details on the various aspects of the subsidence and rebound in the Wilmington oil field may be found in the references (Allen and Mayuga, 1969; Mayuga, 1965; Mayuga, 1970, Allen, 1973; Poland, 1969; Gilluly and Grant, 1949).

2.2 Geological Structure

Oil in the Wilmington field has been produced between depths of approximately 600 to 2000 meters in seven producing zones of sedimentary rock, namely; Tar, Ranger, Upper Terminal, Lower Terminal, Union Pacific, Ford and 237 (Figure 2.4). In the following discussion the last three zones will be considered together and referred to as the "deep" zones. The oil bearing formations are of Pliocene and Miocene age, and include the Puente and Repetto formations which are found throughout the LA basin. The producing zones overlie unconformably a schist Cretacious basement. The sediments are composed predominantly of sands and siltstones, with interbedding of shale layers. The sediments tend to be rather loose and unconsolidated in the upper layers, and become more consolidated and cemented with increasing depth. The percentage of sand in the several zones ranges from 23% to 70%, and the average porosity ranges from 24 to 34 percent (Poland, 1969).

The Wilmington field is a gently plunging anticline trending in a SE-NW direction. The old portion of the field is divided into six main structural blocks by five faults, namely: "Wilmington", "Ceritos", "Powerline", "Harbour Ave", and "Daisy Ave" (Figure 2.5).

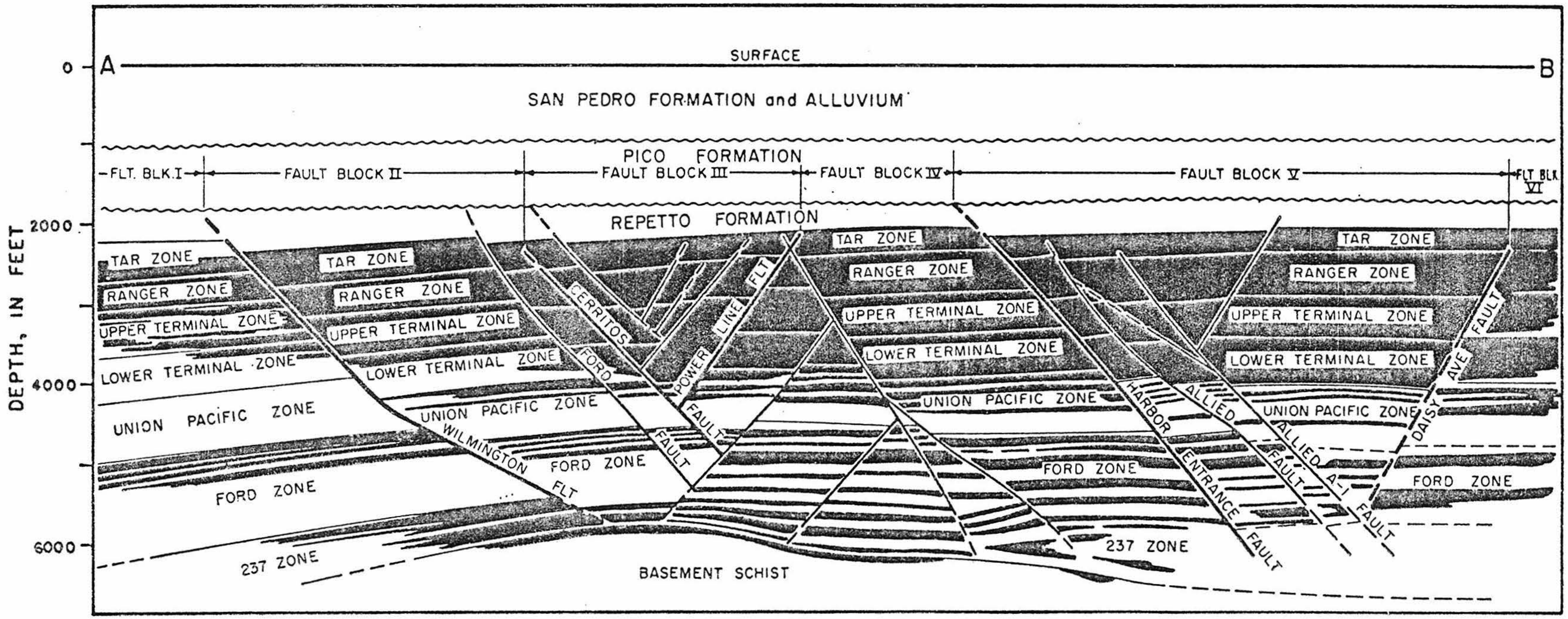

Figure 2.4 Geological section parallel to the major axis of subsidence at the Wilmington oil field (after Poland and Davis, 1969).

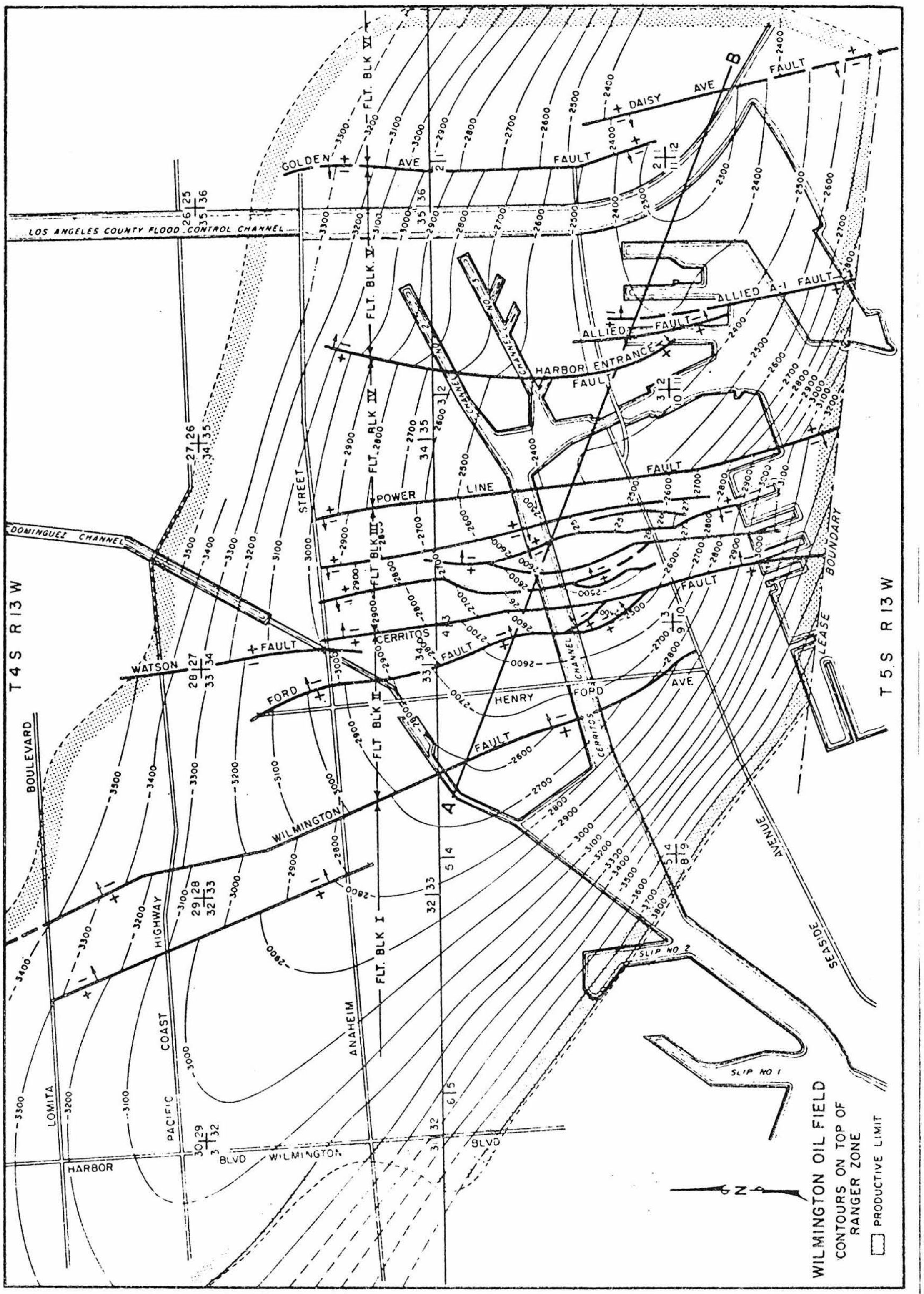

Figure 2.5 Structural contour map at Wilmington oil field (after Poland and Davis, 1969).

All the faults have a 50°- 60° Eastward dip, except the Powerline and Daisy Ave faults, which dip Westward (Figure 2.4). The faults terminate at the unconformity at the top of the Repetto formation, at depths of approximately 600 meters. They therefore appear to be inactive at the present time. The faults restrict fluid flow between the blocks, but their effectiveness as barriers is highly variable (Poland, 1969).

2.3 Cause Of Subsidence

In the beginning, the cause of subsidence in the Wilmington oil field was debatable. Among the reasons, other than oil withdrawal, which had been proposed to explain the subsidence were: (1) increased loading due to surface structures and fill deposit on the surface; (2) crustal changes from tectonic origin; (3) lowering of the water table in shallow water bearing formations; (4) vibration incident to land use (Mayuga, 1965). However two reports by Harris and Harlow (1947), and Gilluly and Grant (1949), both based on consultation work performed in 1945, concluded that the subsidence was caused by a compaction of the oil bearing strata, which in turn resulted from a decrease in reservoir pressures due to production in the field. The collar count method, introduced in 1948-1949, left little doubt about oil withdrawal being the main subsidence cause. In the collar count method, vertical distances between well casing joints are measured periodically. The lengthening or shortening patterns of the joints give a good indication of the vertical compaction or stretching in the formations around the individual wells although the actual amount of collar shortening must not be interpreted too seriously. Figure 2.6 is an example of results of collar count surveys, taken in different years, for a typical well in the region of large subsidence. It is apparent from the figure that the bulk of the compaction occurred between depths of 650 to 1100 meters.

There have been a number of attempts to explain the Wilmington subsidence in quantitative terms. The problem can be described in terms of volumetric changes in a nonhomogeneous half space. The regions of volume change and the amounts are not definitely known, and the behaviour of the soil and rock material at the stress levels developed is nonlinear and hysteretic. Such a complex situation is difficult to reduce to simple models, so that early attempts to describe the behaviour were unsatisfactory. Assuming that the regional response could be taken to be linearly elastic, G. D. McCann and C. H. Wilts (1951) performed a mathematical analysis of the subsidence. Their study was based on the tension center concept, introduced by Carillo (1950). This involved representing the producing zones by a number of spherical regions, whose volume was reduced to correspond approximately to the estimated volume changes in those zones. The general picture of ground deformations was reasonably reproduced by the model, considering its limitations and the computational methods available at the time. Grant (1954) proposed explaining the subsidence by modelling the formations above the producing zones as a beam subjected to a distributed load underneath. Although such a model can match some characteristics of the subsidence, it is obviously somewhat arbitrary, since the beam analog does not permit simulating a 3-D

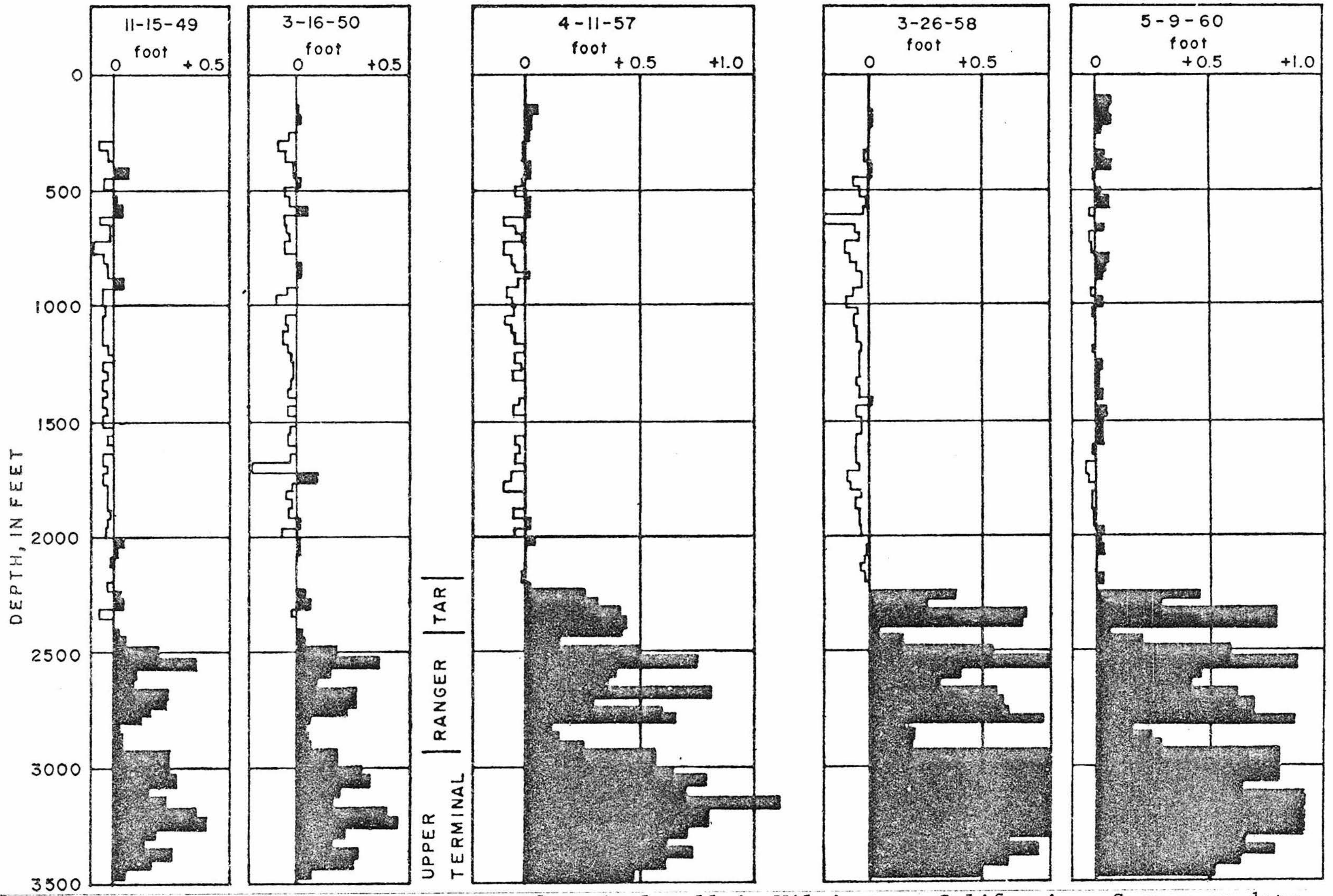

Figure 2.6 Casing collar counts surveys of typical well in Wilmington, California. Survey on data indicated compared to casing tally of 9/26/45; elongation due to tension shown to left of zero reference; shortening due to compaction shown to right (shaded), length of casing joints 41-44 feet in general (after Poland and Davis, 1969).

continuous medium, such as the Wilmington field. A more recent series of attempts to model the Wilmington subsidence was made by Jungels (1973), and Archambeau (1975). In addition to considering the deformations in the solid medium, they considered and solved the problem of fluid diffusion in the producing zones of the field. To do this, they performed a series of 2-D axisymmetric subsidence simulations, and were able to match the time history of the maximum subsidence, and to reproduce roughly the shape of the subsidence bowl, as well as to provide an explanation for the cause of the shallow earthquakes in the field.

2.4 Outline Of Study

The purpose of the present study has been to simulate numerically the Wilmington subsidence, in order to explain the mechanics of the observed deformations, and to provide a model for the effects of future fluid withdrawals and injections. The Finite Element method has been chosen, enabling fully three dimensional simulations to be performed. Having obtained a satisfactory fit to the data, it is now possible to use the developed numerical capability for predicting future displacements, given appropriate reservoir pressure programs.

The important observations used for the fitting included the subsidence contour maps of given years (e.g. Figure 2.2), horizontal displacement maps, and internal data such as collar counts and the location of earthquake epicenters. Each simulation is arranged to produce the first three observations synthetically for ease of comparison. The study enables an identification of the influence of the input parameters of the simulations on the observed quantities. In particular, certain aspects of nonlinear material behaviour are examined and shown to have a definite and interesting influence on the subsidence process.

2.5 Basic Equations in Poroelasticity

Quantitative simulations of the subsidence and subsequent rebound in the Wilmington oil field area involve the mechanics of a fluid saturated porous medium. Biot (1941) developed the theory for the mechanics of an elastic porous medium containing a fluid, which is now known as "the theory of poroelasticity". In his derivation, Biot considers the stresses and strains in the solid matrix and in the fluid as well. The basic assumptions are, first that a strain energy function exists for the fluid-matrix system, and second that the relation between stresses and strains is linear. The first study dealt with media undergoing small deformations, but in later works (Biot, 1956; Biot, 1962; Biot, 1972) the theory was extended to treat finite deformations and to consider time dependent viscoelastic behaviour. Whereas Biot's approach is empirical, there have been more recent attempts to derive the equations of poroelasticity theoretically from the theory of interacting continua (Garg and Nur, 1973), according to which the solid and the fluid are viewed as a solution of two elastic substances. However, the main drawback in these types of derivations is that they do not consider the role of matrix structure, or of grain shape and size distribution in determining the mechanical properties of the solid-fluid composite.

This section presents a brief summary, based on Biot's derivation, of the theory of poroelasticity for small deformations in an isotropic medium. It is assumed that the system is under isothermal equilibrium and thus temperature effects can be ignored. Section 2.12 contains an extension of the theory to the case of a matrix with an elastic-plastic rheology.

Let $u_i(\underline{x})$ denote the three Cartesian displacement components at point $\underline{x}$ in the solid matrix, and $U_i(\underline{x})$ denote the displacement components in the fluid. The strains in the matrix are given by;

$$(2.1) \qquad e_{ij} = \frac{1}{2}\left(\frac{\partial u_i}{\partial x_j} + \frac{\partial u_j}{\partial x_i}\right), \qquad i,j = 1 \ldots 3,$$

where x_i is a set of chosen cartesian coordinates. The fluid dilatation is given by,

$$(2.2) \qquad \varepsilon = \frac{\partial U_i}{\partial x_i} .$$

The volume of fluid ξ which enters a unit volume of porous material during deformation is given by,

$$(2.3) \qquad \xi = n(e_{kk} - \varepsilon),$$

where n is the porosity.

The stresses are conveniently divided into three types namely: (a) those from which the total forces on a unit cube of solid and matrix can be derived; (b) those from which the forces on the solid part of the cube phase can be derived; (c) those from which the forces on the fluid part of the cube phase can be derived. We denote these stresses by τ_{ij}, σ_{ij} and σ respectively. These stresses are related to each other by,

$$\tau_{ij} = \sigma_{ij} + \sigma\delta_{ij} , \qquad i,j = 1 \ldots 3 . \tag{2.4}$$

The fluid stresses can be expressed in terms of the pore fluid pressure P_f, according to,

$$\sigma = -n P_f . \tag{2.5}$$

In a linear poro-elastic medium, the relation between the stresses and the strains can be written,

$$\tau_{ij} + \alpha P_f \delta_{ij} = 2\mu e_{ij} + \lambda e_{kk} \delta_{ij} , \qquad j,i = 1 \ldots 3 \tag{2.6a}$$

and,

$$\xi = \frac{1}{\mu} P_f + \alpha e . \tag{2.6b}$$

In the above equations, λ and μ are respectively Lame's constant and the shear modulus of the solid phase. The coefficient α is empirical. It appears in both equations (2.6a), (2.6b), as a consequence of the assumption that the fluid-solid system possesses a strain energy function (Biot and Willis, 1957). In the same paper Biot demonstrates that the factor $(1 - \alpha)$ equals the ratio between the unjacketed compressibility and the jacketed compressibility of a sample of fluid-saturated porous material. In loose porous materials α is usually very close to unity (Nur and Byerlee, 1971; Brace, 1968).

Under conditions of static equilibrium, the total stress components must satisfy the three equilibrium equations,

$$(2.7) \qquad \frac{\partial \tau_{ij}}{\partial x_j} + \rho g_i = 0 , \qquad i = 1, \ldots 3,$$

where g_i is the ith component of the gravitational acceleration, ρ is the mass per unit volume of fluid-solid composite. The equilibrium in the fluid is expressed by the equation of hydrostatics which reads,

$$(2.8) \qquad \frac{\partial}{\partial x_i} \left(\frac{P_f}{\rho_f} \right) + g_i = 0 , \qquad i = 1, \ldots 3,$$

where ρ_f is the fluid density.

In the Wilmington subsidence problem, as well as in many hydraulic problems, the medium is not under static equilibrium, as there is a continuous flow of fluid through the pores. In most of these problems, however, inertial effects are negligible. When a dissipation function for the composite exists, the balance of forces on the fluid is given by Darcy's law,

$$(2.9) \qquad \mathring{\xi} = - \kappa \left(\frac{\rho_f}{\eta} \right) \frac{\partial}{\partial x_i} \left(\frac{P_f}{\rho_f} \right) + g_i ,$$

which replaces (2.8). κ is the permeability coefficient and η represents the fluid viscosity.

After specification of the appropriate boundary and the initial conditions with reference to a given volume of porous material, equations (2.6a), (2.6b), (2.7) and (2.9) completely determine the mechanical evolution of the system in time.

2.6 The Boundary and Initial Conditions for the Wilmington Field

There are two possible approaches to model subsidence in oil fields each involving a different specification of boundary and initial conditions.

The first approach is to solve the complete system of equations (2.6a), (2.6b), (2.7) and (2.9). This involves the isolation of a region which includes the oil field. The unknowns are chosen to be the three displacement components in the matrix, plus the pore fluid pressure. The boundary conditions include a specification on the outer surfaces of the displacement or the traction time history, and a specification of the pressure history. Alternatively, the boundary conditions include a specification of the pressure gradient history or the flow rate as a function of time. The producing wells in the field are considered as part of the boundary on which either the pressure or fluid withdrawal rate is specified. The initial conditions for a subsidence simulation are zero displacement everywhere, and a given initial pressure. As was stated previously, in the Wilmington field the initial well pressures were approximately equal to the hydrostatic head. The solution of the above mentioned transient equations gives the time history for the displacement and the pore fluid pressure in the field. This approach can be used for predicting future displacements and pressures when a well production program for the field exists. The technique was used by Jungels (1973), and Archambeau (1975) for a series of axi-symmetric models for the Wilmington subsidence.

The second method is based on the fact that if the pore fluid time history is known, and therefore considered as data, the displacement history can be obtained by solving static equations (2.6a), (2.1) and (2.7) at different times. The boundary conditions include a specification of displacements or tractions on the boundaries of the region under consideration. The input body forces are equal to the product of α times the gradient of the pore fluid pressure. This approach can be applied in developed oil fields, such as the Wilmington field, where there is a large number of wells which can be used as pressure data points. The method can be used for matching past observed displacements, as well as for predicting future displacements, when a pressure program for the management of the oil reservoir exists.

The main advantage of the first approach is that it permits calculation of pore fluid pressure profiles and displacement histories simultaneously, whereas in the second approach, only displacements can be calculated. The main drawback of this approach lies in the uncertainties in permeability values. Whereas most of the material constants of the various porous formations in an oil field do not vary usually more than one order of magnitude, the constant of permeability can vary over a few orders of magnitude (e.g. shale vs sand), and is often a highly nonlinear function of strains.

In this study, the second approach was chosen because of the existence of good pressure data for the Wilmington field. Input for a simulation of the subsidence includes a specification of the material rheology as a function of space, and pressure data for points in the producing zones of the field. The output consists of the displacement solutions. In practice, equations (2.6a), (2.1), and (2.7) cannot be solved analytically for realistic material parameter variation in space, and numerical methods must be employed.

In this study the Finite Element method has proven most suitable for subsidence simulations, because of its flexibility in incorporating nonhomogeneous material parameter variations and various boundary conditions.

2.7 Construction of Input Parameters for Subsidence Simulations

In a Finite Element simulation, a region of the Earth's crust surrounding and including the Wilmington field is isolated and represented by a Finite Element mesh as shown in Figure 2.7. The input parameters include a specification of the material properties for all elements, and the pressure reduction values in those elements which lie in regions corresponding to portions of the producing zones of the field. The output of a simulation includes displacement components at the nodes of the grid, and stresses at the centroids of the elements.

Ideally the boundaries of the grid should correspond to points far enough removed from the limits of the oil field so as not to artificially affect the calculated results. In the case of the Wilmington field, however, there are additional fields in the area, and it

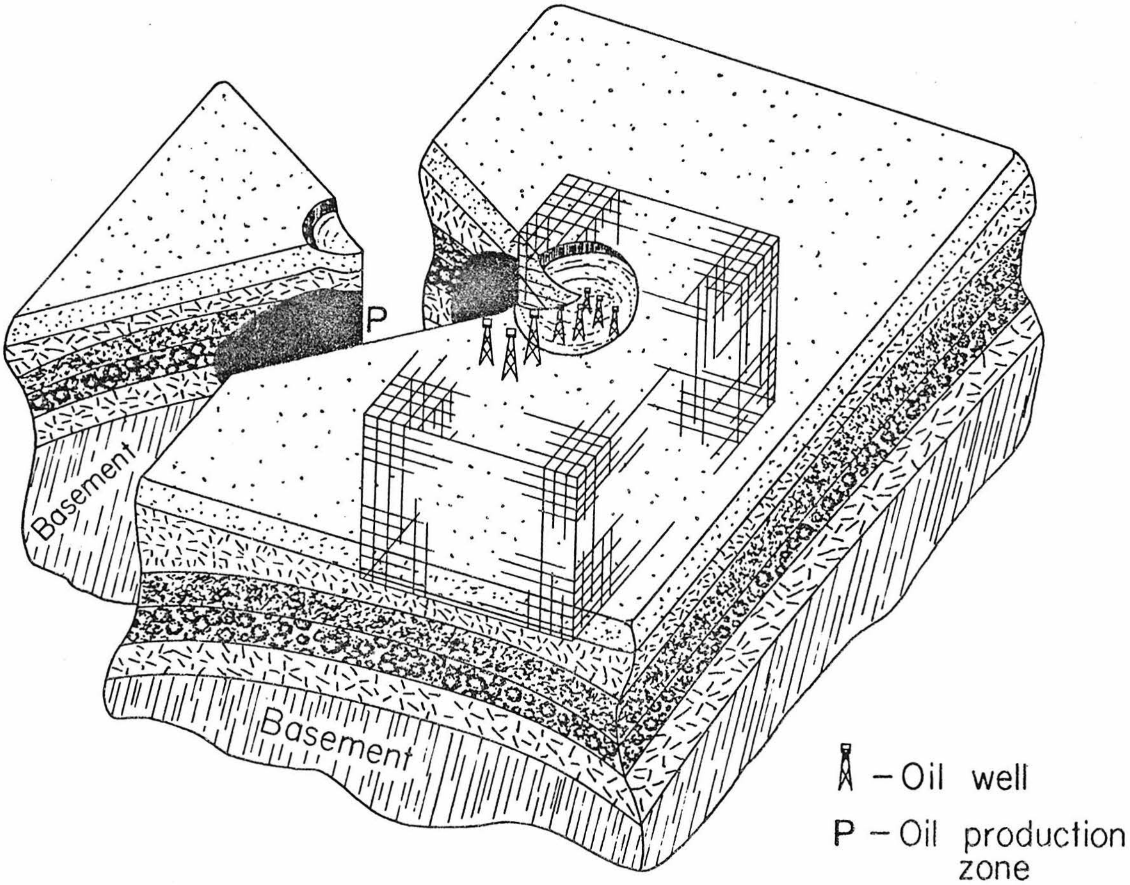

Figure 2.7 A sketch of a typical Finite Element subsidence model configuration.

is difficult to find an "undisturbed" region at which to locate the grid boundaries. It has been found that by placing the boundaries at a distance of 6 km from the production limits, the displacements in the central portion of the mesh do not appear to be too sensitive to the boundary conditions. This has been partially verified by comparing an analytic displacement solution for an axisymmetric pressure reduction zone in a homogeneous isotropic elastic halfspace (Geertsma and Kepel, 1973), to a FE displacement solution obtained with the mesh shown in Figure 2.8a. The analytic and FE displacement solutions at the earth's surface are compared in Figure 2.8b. The agreement between the solutions is close up to a radius of 3 Km, beyond which the FE solution becomes stiffer as a result of the fixed displacement boundary condition at the outer radius of the grid.

With regard to the mechanical properties of the geological layers of the Wilmington field, the information is not as detailed as is ideally desirable. Only a few samples were tested in the original investigation 25-30 years ago, and these were subjected mostly to one dimensional tests. However, in recent years a number of investigations have been performed on the behaviour of soils at high confining pressures (Vesiĉ and Clough, 1968), and the results can be employed to fill in gaps in the data.

The first series of 3-D subsidence simulations has used a linearly elastic nonhomogeneous model to represent the material response of the geologic formations in the Wilmington field. The model is based on the experimental results of Vesiĉ and Clough (1968) for sands. Each layer of elements of the FE mesh is assigned an elastic modulus which

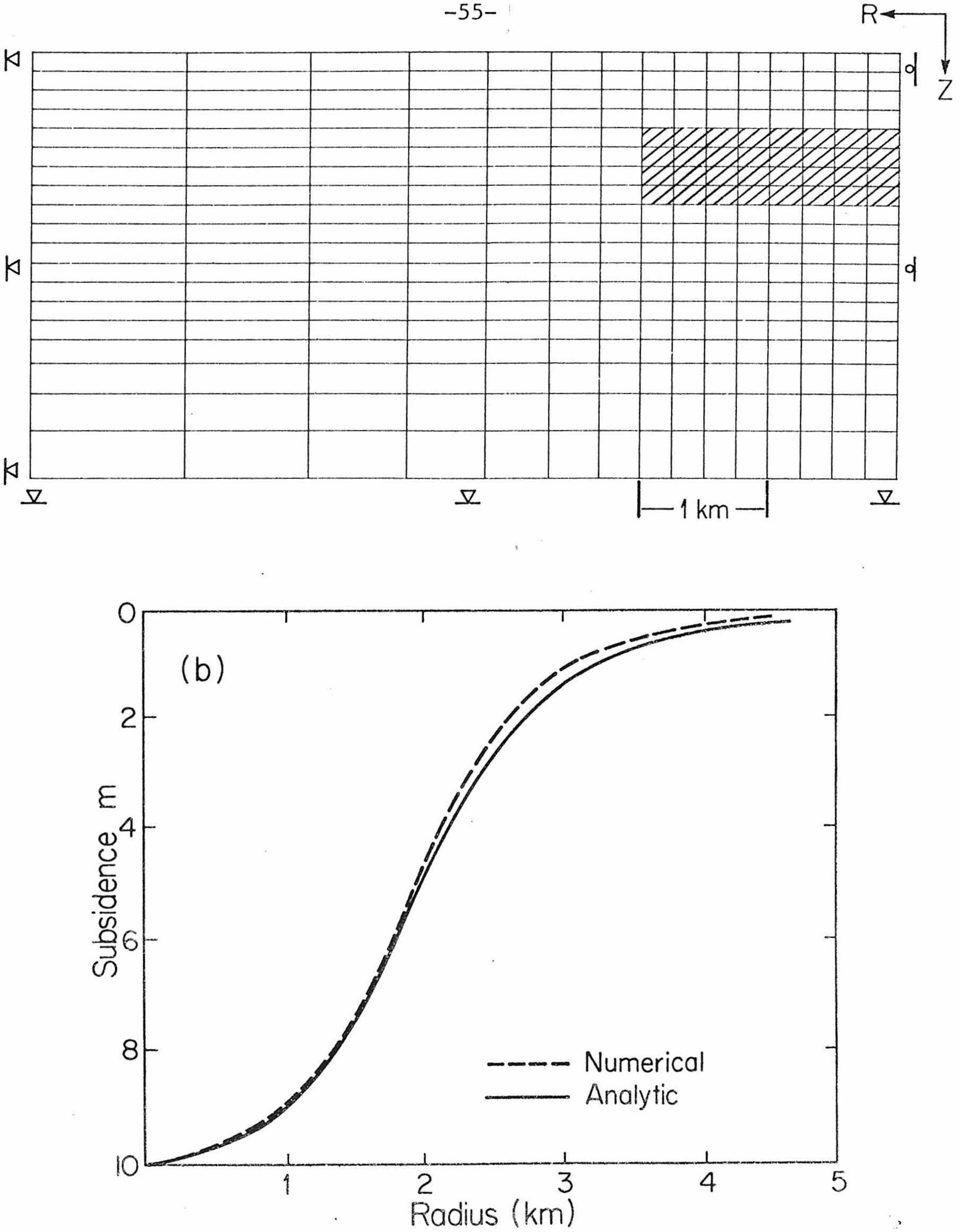

Figure 2.8 (a) Finite Element grid for axi-symmetric calculation. Shaded elements represent region where pore pressure was reduced. nodes constrained to move only parallel to boundary totally constrained nodes. (b) Comparison between numerical and analytical solutions for axi-symmetric subsidence problem.

equals the modulus derived by Vesiĉ and Clough at a pressure equal to the lithostatic confining pressure at the center of the layer. In this rheological approximation, the material properties are not related directly to the geological structure but rather are assigned only on the basis of depth of burial by the overburden. This prescription appears justified in the case of the Wilmington oil field, in which no major change in material properties, other than in the degree of compaction or cementation,can be observed between geologic formations (Muyuga, 1965; Mayuga, 1970 . A density of 2.0 gr/cm^3 is assumed for the material in every layer. Table 2.1 lists the material coefficients at a number of representative depths. The values of the parameters in this material approximation are within a factor of two of soil test results for the formations of the field (McCann and Wilts, 1951; Scranton, personal communications, 1977), and are also within an order of magnitude for measured results on shales and clays (Rieke and Chilingarian, 1974).

It is interesting to note that the seismic wave velocities shown in Table 2.1 are much lower than velocities derived from surface wave dispersion (Kovach, 1974; Archambeau, 1975), or from in situ ultrasonic measurements (Scranton, personal communications, 1977). This can be attributed to the fact that the elastic constants derived from static tests correspond to larger strains than those encountered during seismic wave propagation, and the assumption of linear elasticity is an approximation to be used only in a limited range of strain variation.

The second class of input data are the pore fluid pressure values in the producing zones of the field, at given times. The initial reservoir pressures in the oil producing zones were approximately equal to the pressure of a column of sea water extending from sea level to the individual zone (Gilluly and Grant, 1949, p. 464 and p. 479). Reservoir pressure values at subsequent times are obtained by compiling the pressure records of individual wells. The calculated displacements are measured in this study from the state of the field before production began. The input pressure, P_f, for equation (2.6a) is equal to the difference between the pore pressures at the end of the time interval of the simulation and the pressures at the beginning of the interval. Ideally, the size of the time intervals for the subsidence calculations should be small. However, in this study, because of the overwhelming amount of pressure data involved, we choose two relatively large time intervals, one between the years 1936 to 1958, a period in which most of the subsidence took place, and one interval between 1958 to 1975, when the rebound occurred. The pore pressure values for 1936 are approximated to be equal to the hydrostatic head, and the values for 1958 and 1975 are obtained from well data. In simulations which use a linear elastic rheology the calculations are path independent and the calculated subsidence for a given year does not depend on the number of time intervals. On the other hand, for subsidence models which employ a nonlinear material rheology, the size of the time intervals may somewhat affect the accuracy of the results. However, we feel that considering the accuracy of the available pressure and material property data, little can be gained by a finer division in time.

For the FE calculations, the pore pressure data from the field has been converted into input data at the centroids of the elements. The standard grid shown in Figure 2.9 is used in all the simulations. The data reduction process involves the following steps;

(a) Compilation of structural data; refer to Figure 2.10 which is a horizontal section of the grid shown in Figure 2.9. The numbering system, $1 \leq I \leq 18$, $1 \leq J \leq 13$, is used to locate elements in the shaded region of the figure. The coordinate system in feet defines the correspondence between points in the oil field (on the earth's surface) and points in the figure. The depth to the top of each of the producing zones and to the basement are compiled from logs of representative wells in the field. Each element in Figure 2.10 is then assigned six depths, which are equal to the average vertical distance from the center of the element (on the earth's surface) to the five producing zones and the basement beneath the element (because of the correspondence between points in Figure 2.10 and points in the oil field, we refer loosely to points in the figure as points in the field (the more precise, but cumbersome, definition is to refer to points in the field as images of points in the figure);

(b) calculation of initial pore fluid pressure values for the year 1936 in the producing zones of the field. For each element in the shaded area in Figure 2.10, the initial pore fluid pressures in the portions of the producing zones located directly beneath the element are calculated from,

$$P_n^i = \rho g h_n \ ,$$

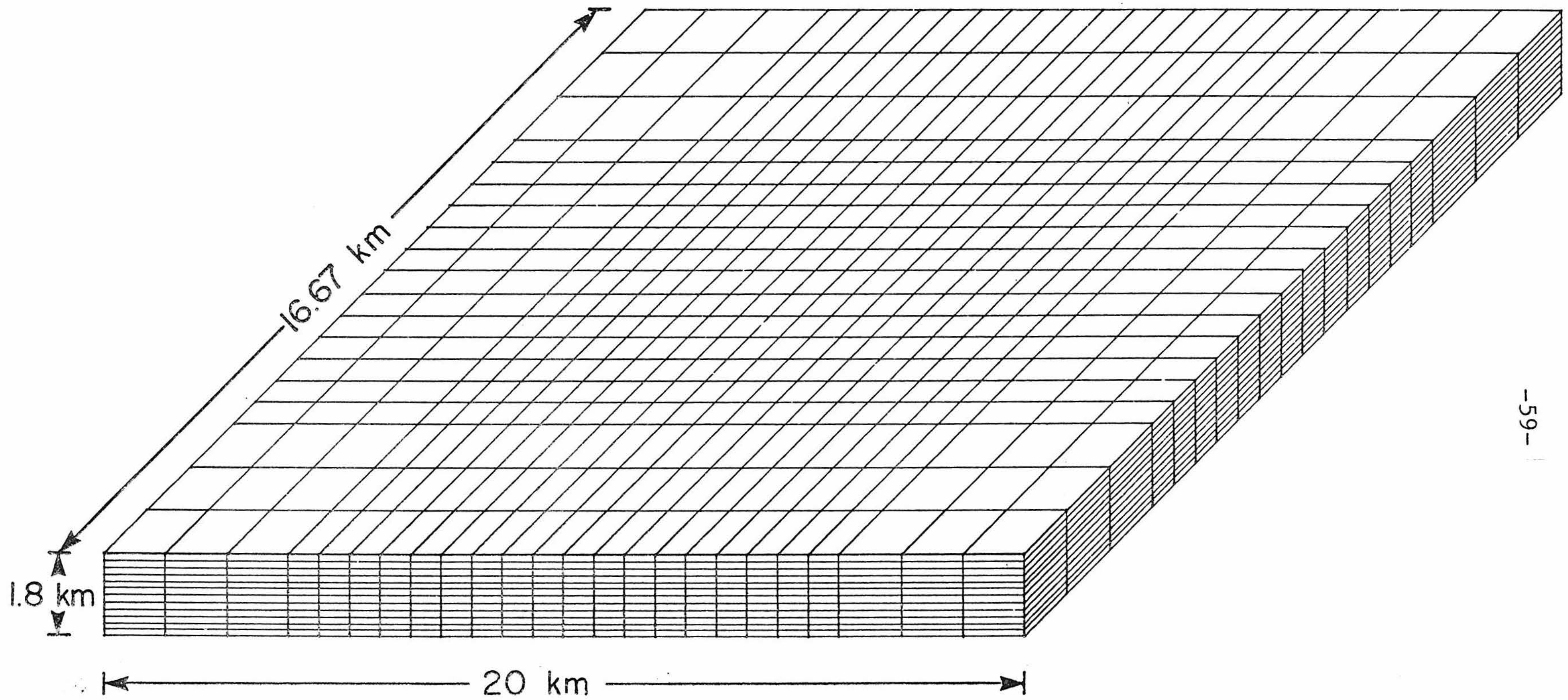

Figure 2.9 Spatial configuration of 3-D Finite Element grid for subsidence calculations.

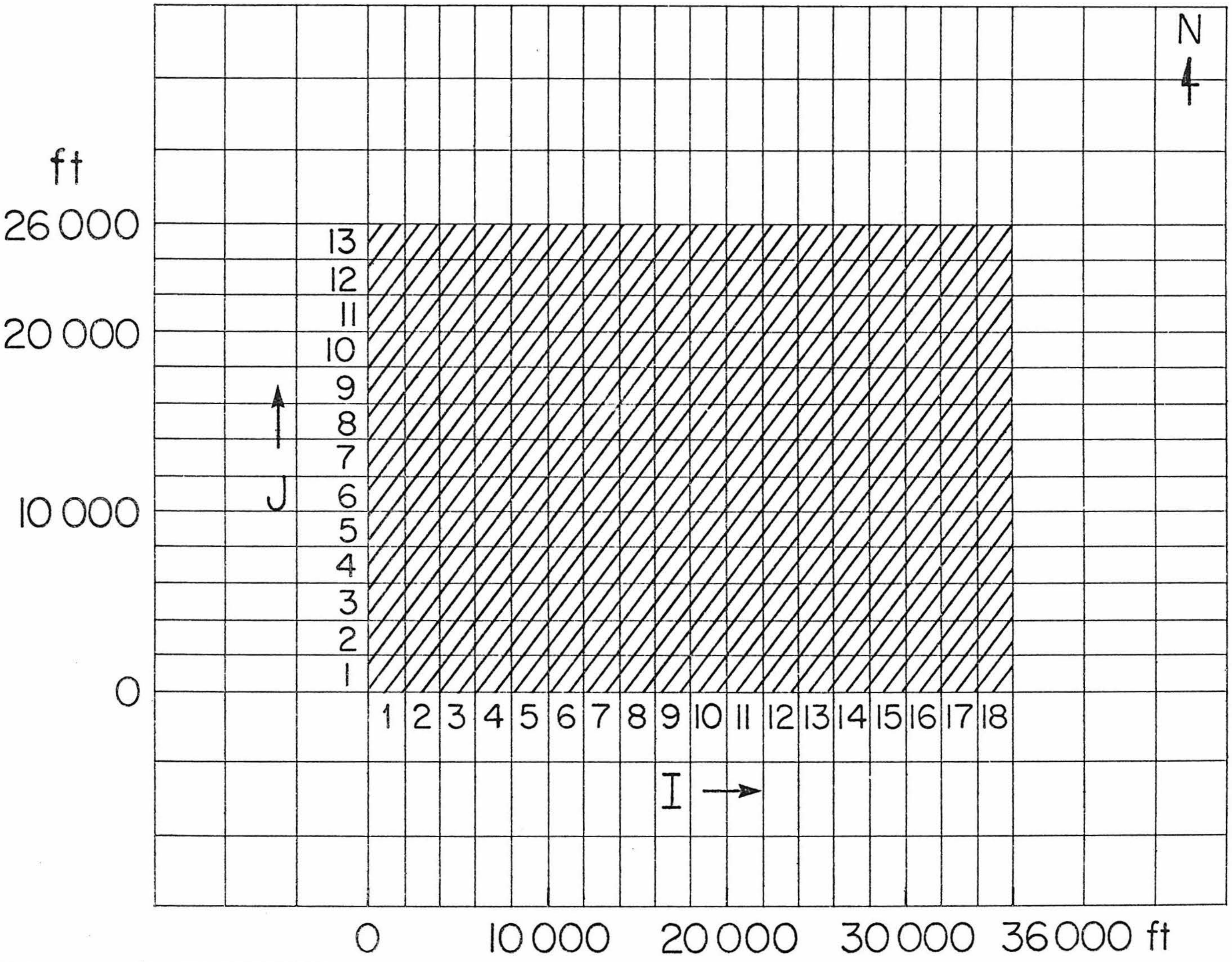

Figure 2.10 Horizontal section of the 3-D grid in Figure 2.9 showing the element numbering system and the coordinate system in feet for the data reduction.

where P_n^i is the initial pore fluid pressure in the nth zone, ρ is the water density, g is the gravitational acceleration, and h_n is the average between the depth to the top of the nth zone, obtained according to (a), and the depth to the bottom of the zone;

(c) Projection of measured pressure values for given years into the elements in the shaded area of Figure 2.10. Each element in the figure is assigned five pressure values for each one of the producing zones, which are equal to the pore fluid pressure at the given year at the portion of the zone directly beneath the element;

(d) Calculation of pressure reduction values for specified time intervals. The value of the pressure reduction is simply equal to the difference between the pore fluid pressures at the end of the interval and the pressure values at the beginning of the interval. For time intervals which begin in the year 1936, the pressures at the beginning of the interval are calculated according to (b). In all other years the pore fluid pressures are obtained according to (c);

(e) Construction of element pressure reduction input values. The elements in the 3-D grid shown in Figure 2.9 are scanned one by one, and tested, on the basis of the data in (a), to see if they contain a volume portion which corresponds in the field to a volume portion of one or more of the producing zones. In cases when an element contains such a volume, it is assigned a pressure reduction value equal to,

$$P = \sum_{i=1}^{5} W_T^i \quad P_i ,$$

where P_i is the pressure reduction value in the volume portion of the element which contains part of the ith producing zone, and W_T^i is a weighting factor equal to the ratio of the thickness of the zone in the element to the total zone thickness in the vertical section containing the element.

The element pressure values obtained in (e) are supplied to the Finite Element program as input data.

The specification of material parameters and pressure reduction values covers the required data for a Finite Element simulation. The remaining input parameters are used in defining the Finite Element mesh and for various other bookkeeping purposes. The next stage involves the actual Finite Element calculation of displacements and stresses.

2.8 Evaluation of Data for the Comparison Between the Subsidence Simulations and Field Observations.

Before discussing the subsidence simulations it is appropriate to examine the observational data which are available for comparing the calculations to.

The first set of data consists of surface observations of vertical and horizontal ground movements. For both observations, the data are compiled from surveys of movements of benchmarks which are distributed throughout the Wilmington field. The horizontal movements are surveyed once in every four years (Allen, 1977, personal communications). The data are presented in vector plot maps which show the displacement and magnitude of horizontal movements between survey dates (see Figure

2.13). The plots display the horizontal movements, as they are measured, without much personal interpretation. The vertical displacements are surveyed twice a year (Allen, 1977, personal communications). The data are displayed in contour plots which usually show vertical movements between specified years. The contour maps are based on some smoothing and personal interpretation of the investigator. In particular the rebound contours are subject to some uncertainties, as the vertical displacements associated with the settlement of land fill can often have magnitudes similar to the rebound magnitude. Furthermore, the total rebound maps do not refer to a specific time interval, but rather, they display the rebound which occurred at each point from the largest subsidence value which was ever attained there. Since different points have attained their maximum subsidence at different times, it is impossible to compare accurately the observed rebound maps with subsidence simulations, which always refer to a specific time interval.

The next type of observations include the collar count survey data which give the lengthening or shortening of well casing joints between specified survey dates. These observations give some picture of the vertical strains in the vicinity of the oil wells, but it is not assured that the deformations in the metal casings and in the surrounding medium are always the same. The collar count method is useful in establishing the regions where the majority of the compaction took place, but the numerical values of a single collar count survey are not to be taken literally.

The subsidence earthquakes are a transient phenomenon which is not covered by the quasistatic analysis used in this study. However, the epicentral locations and the shear planes could be mapped accurately by observing the depths at which oil wells were damaged. This information can then be used in comparing the stresses which are predicted by the simulations at the epicentral depths, and quoted failure strengths for the type of shales present in the earthquake slip planes.

2.9 A Linear Elastic Subsidence Calculation for the Year 1958

The first numerical subsidence simulation uses a linear elastic approximation to material response, and covers the time interval 1936-1958. In this period, well pressures were monotonically decreasing in most parts of the field,as the effects of the repressurization program were not yet noticeable. The subsidence during this time followed the trend of the pressure reduction, and was progressing continuously. In 1958, a maximum subsidence of 26 feet was observed (Figure 2.2).

For constructing the input data for the numerical calculations, the procedure outlined in Section 2.7 is used. As the beginning of the time interval coincided with the onset of production in the Wilmington field, the initial pressures are taken to be equal to the hydrostatic head (see Section 2.7). The material parameters for the calculations are listed in table 2.1; the Finite Element grid is shown in Figure 2.9. In order to compare calculations and observations, the results are displayed graphically in a series of plots, whose description occupies the remainder of this section.

Figure 2.11 shows the calculated vertical displacements at the

Table 2.1 Elastic Constants of the Axisymmetric Layered Model.

Layer Number	Depth to Base Km	Shear Modulus Kbars	Bulk Modulus Kbars
1	0.3	0.8000	1.5943
2	0.6	0.9946	2.0080
3	0.9	1.2301	2.5544
4	1.2	1.6589	3.4618
5	1.5	2.0352	4.4628
6	1.8	2.4781	5.3845
7	2.1	2.8426	6.4599
8	2.522	3.2805	7.4360
9	3.639	3.6295	8.6636

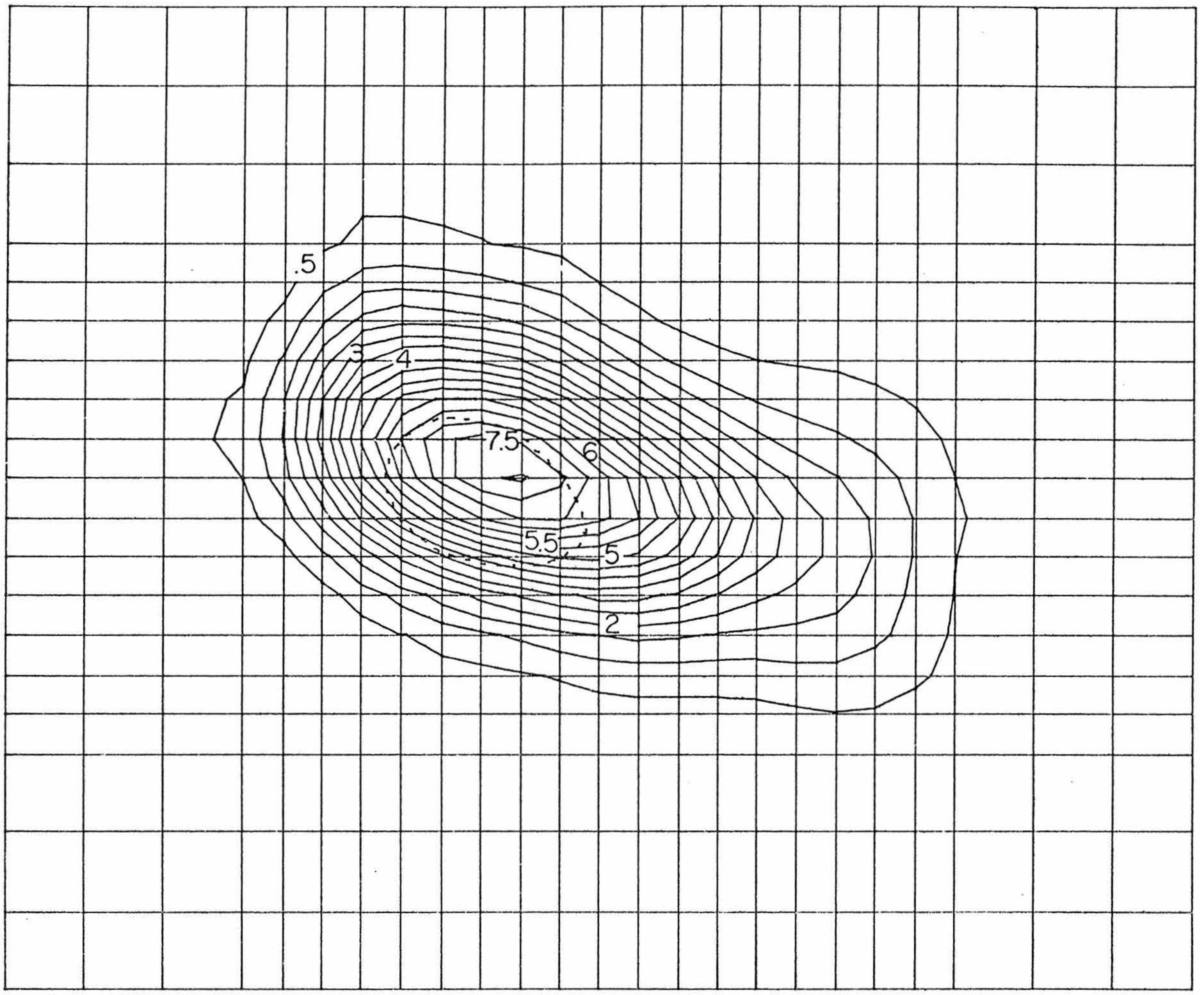

Figure 2.11 Contours of calculated vertical subsidence in meters. Elastic subsidence model.

earth's surface for the year 1958. For comparison the 4 meter subsidence contour observed in the same year (denoted by the dashed line) is included in the figure. The maximum calculated subsidence in the center of the subsidence bowl has a value of approximately 8 meters, in fair agreement with observations. The main discrepancy, however, between calculation and observation, is that although the shape and location of the subsidence bowl are very similar in both cases, the calculated subsidence ellipse is two to three times larger than that of the observed bowl (Figure 2.11). As the following text shows, this discrepancy appears consistently in all comparisons of this material model with observations, and therefore is an important motivation for considering more complex material rheological models.

The calculated horizontal displacements at the earth's surface are shown in Figure 2.12a. Each arrow in the figure points in the direction of the displacement at the node from which it originates, and its length is scaled in proportion to the displacement magnitude. The pattern is roughly of convergence towards the center of subsidence, but is neither symmetric nor strictly radial. The maximum calculated horizontal displacement is about 6 meters, which is somewhat larger than the 3-4 meters which was observed (Allen, 1973). The calculated vertical displacements at a depth of 900 m are shown in Figure 2.12b. This figure resembles Figure 2.12a; however a slightly smaller displacement decay with distance from the center of subsidence in Figure 2.12b appears to be responsible for the slight visual difference between the two figures. For comparison, the observed surface horizontal displacements are shown in Figure 2.13 (a) - (f). The broken arrows in this

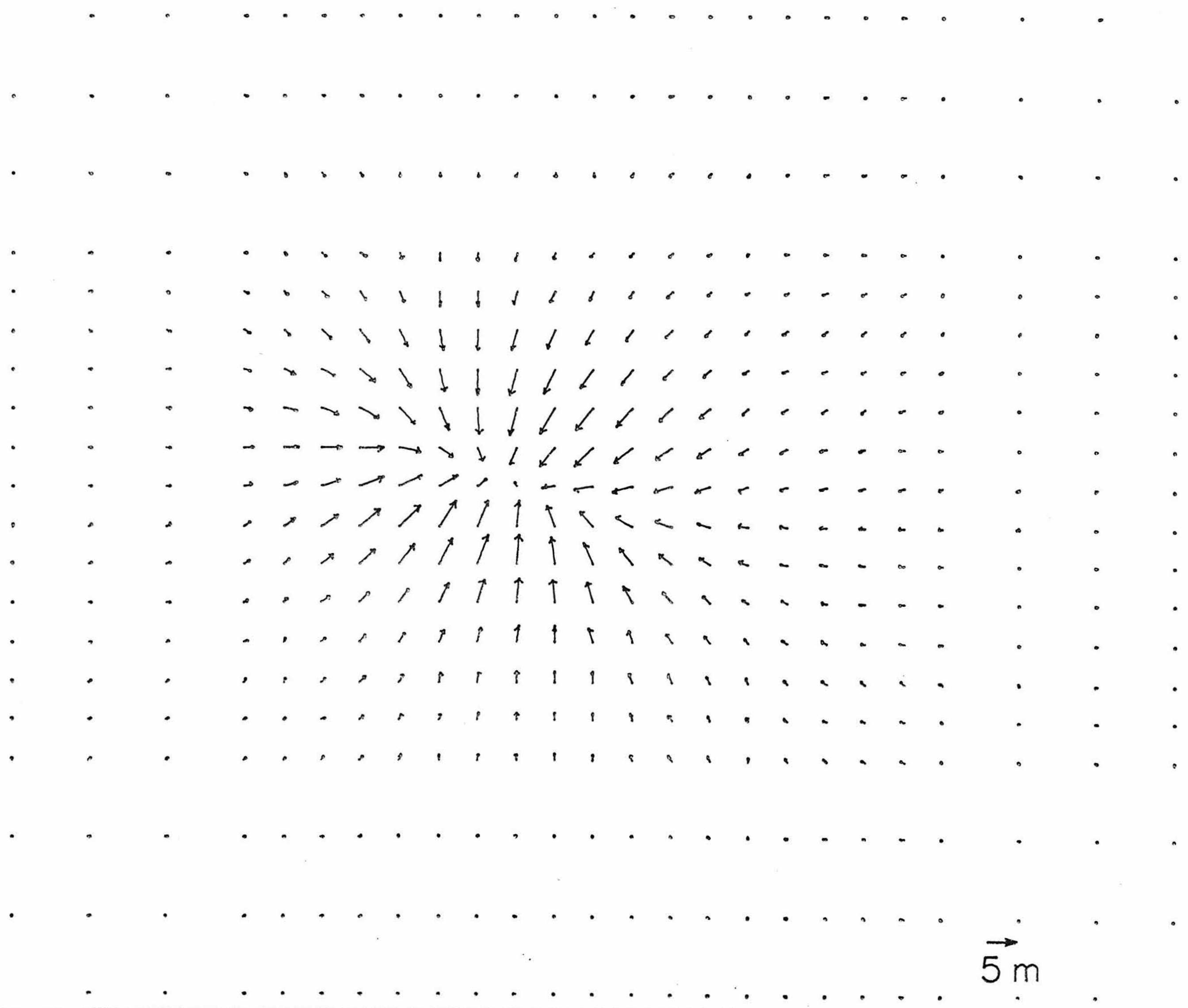

Figure 2.12 (a) Calculated horizontal displacements at the earth's surface. Elastic subsidence model.

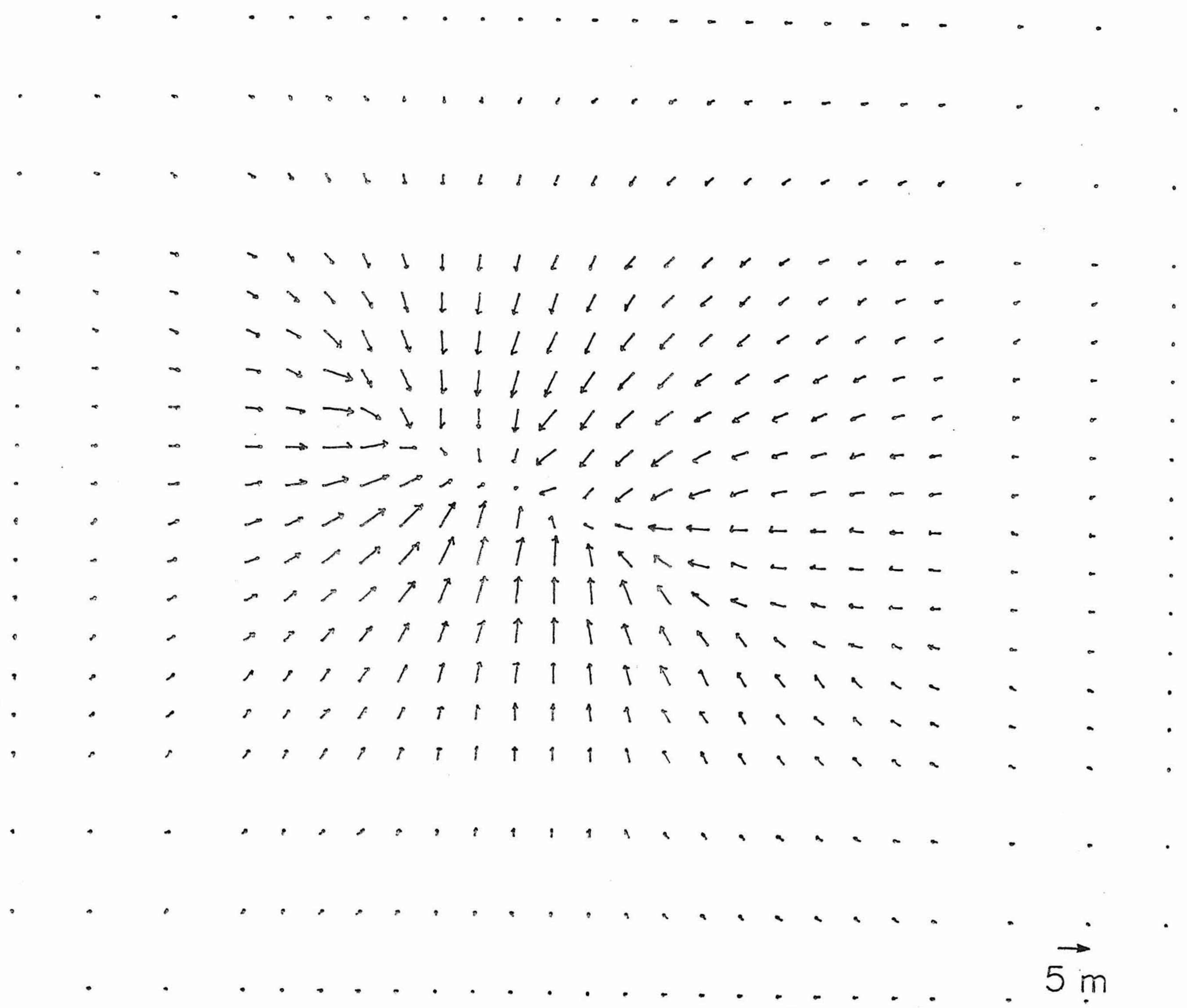

Figure 2.12 (b) Calculated horizontal displacements at a depth of 900 m. Elastic subsidence model.

figure represent the horizontal displacement history at the point from which they initiate. Each segment represents the displacement between the years which are marked on its ends. The pattern of these figures is very similar to the calculated results shown in Figure 2.12a. However, as with the vertical displacements, the calculated horizontal displacements form a wider pattern than the observed one .

In order to provide a picture of the variation of subsidence with depth, a series of synthetic collar count plots was constructed (Figure 2.14 (a)-(d)). Each figure represents a vertical column from the earth's surface to a depth of 1.8 Km (where the lower boundary of the Finite Element grid lies). The coordinate where each column intersects the earth's surface is marked in feet on the left part of each figure (see Fig. 2.10). The twelve layers of the Finite Element mesh are defined in the figures by solid lines, whereas the top of each (observed) producing zone is denoted by a dashed line. The shortening or lengthening of each section of the column (which corresponds to a layer in the Finite Element mesh) is printed on the right side of the column. From these figures, it is apparent that most of the calculated shortening occurred in the four upper producing zones. This is in general agreement with observations (Allen, 1968; see also Figure 2.6), although the synthetic collar counts produce slightly more shortening than that observed in the Tar and Lower Terminal zones. The synthetic values show a small amount of compaction in the deep zones, a point which was neither verified nor refuted by the measurements. This coincides with the observation that material in the deep zones appears stiffer and more cemented than material in the four upper zones, and therefore

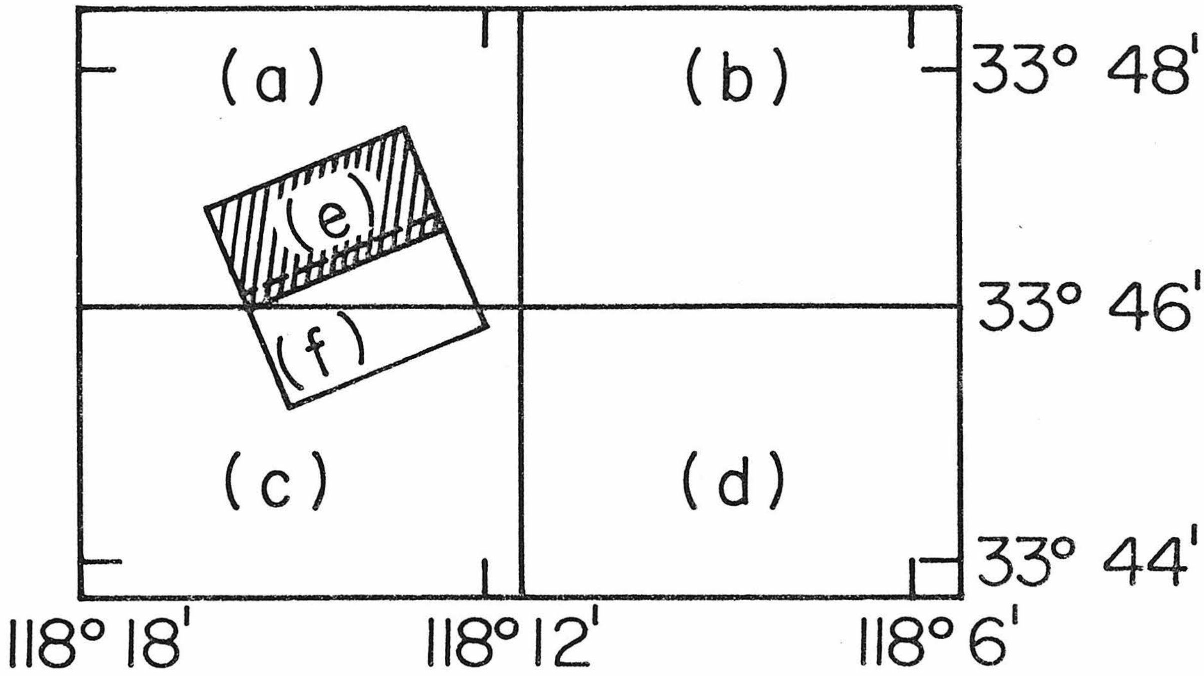

Figure 2.13 Index of maps of observed horizontal displacements shown in Figure 2.13 (a) - (e).


MATCH LINE SURVEY DIVISION FILE MAP NO 19-112-2
LOS ANGELES
CITY OF LOS ANGELES
DOMINGUEZ CHANNEL
CERRITOS CHANNEL
EAST BASIN
TURNING BASIN
CHANNEL
MATCH LINE SURVEY DIVISION FILE MAP NO 19-112-3
SURVEY DIVISION FILE MAP NO 19-112-5
N
0
2000 ft

Figure 2.13(a)

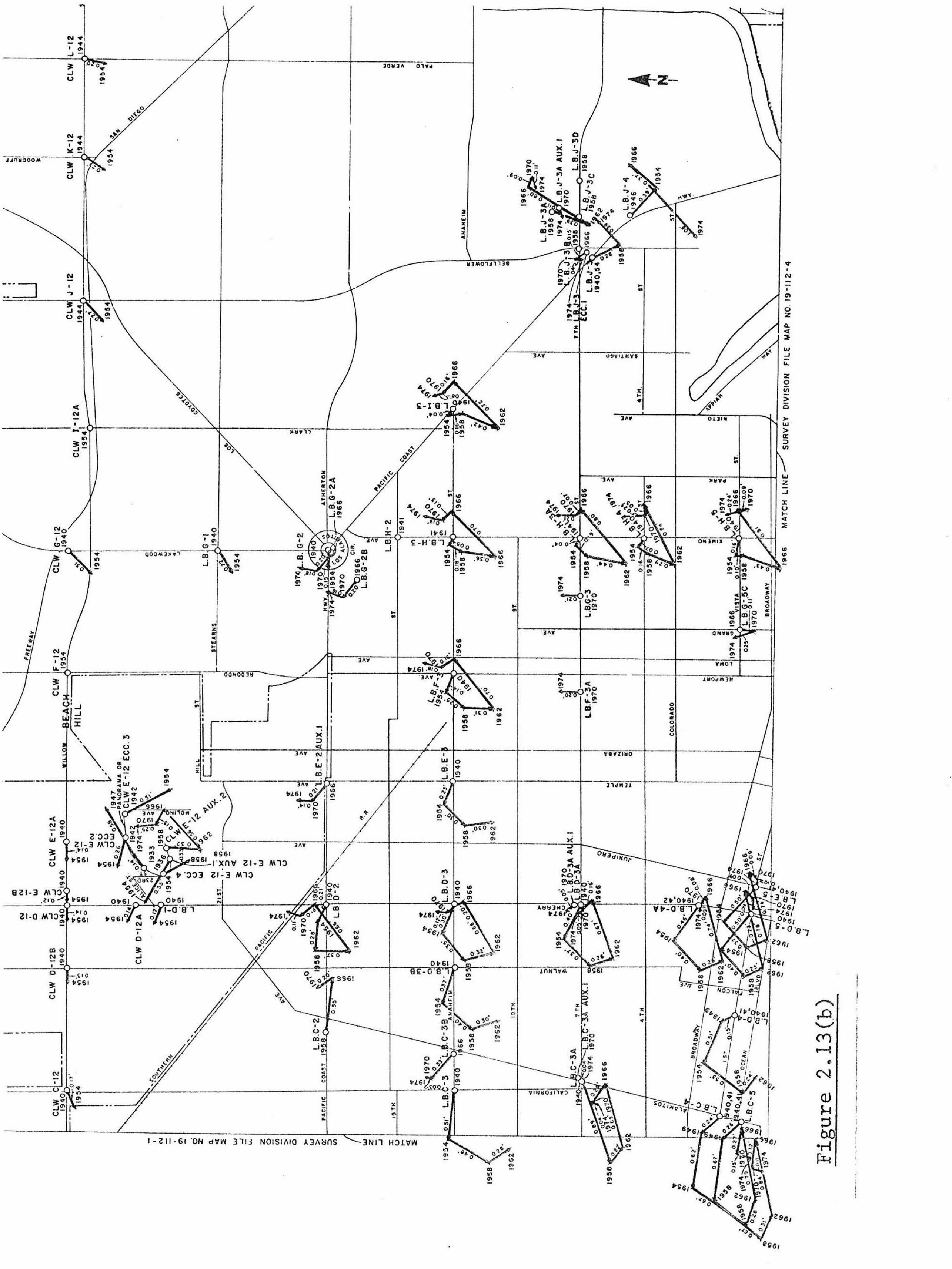
N
PALO VERDE
WOODRUFF
SAN DIEGO
BELLFLOWER
ANAHEIM
CLARK
COYOTES
LOS
LAKEWOOD
ATHERTON
PACIFIC COAST HWY
STEARNS
REDONDO
FREEWAY
WILLOW
BEACH HILL
HILL ST
PANORAMA DR.
MOLINO AVE
TEMPLE
ORIZABA
JUNIPERO
CHERRY
WALNUT
10TH
7TH
4TH
CALIFORNIA
ALAMITOS
1ST
OCEAN
BROADWAY
FALCON AVE
GRAND
NEWPORT
LOMA
COLORADO
XIMENO
PARK
NIETO
APPIAN WAY
SANTIAGO
SOUTHERN PACIFIC
R.R.
21ST
15TH
CLW L-12
CLW K-12
CLW J-12
CLW I-12A
CLW G-12
CLW F-12
CLW E-12A
CLW E-12B
CLW D-12
CLW D-12B
CLW C-12
CLW D-12A
CLW E-12 ECC. 2
CLW E-12 ECC. 3
CLW E-12 ECC. 4
CLW E-12 AUX. 1
CLW E-12 AUX. 2
L.B.G-1
L.B.G-2
L.B.G-2A
L.B.G-2B
L.B.H-2
L.B.H-3
L.B.I-3
L.B.J-3
L.B.J-3A
L.B.J-3A AUX. 1
L.B.J-3B
L.B.J-3C
L.B.J-3D
L.B.J-4
L.B.J-3 ECC. 1
L.B.H-4
L.B.H-5
L.B.G-5
L.B.G-5C
L.B.F-3A
L.B.F-4
L.B.E-2 AUX. 1
L.B.E-3
L.B.D-1
L.B.D-2
L.B.D-3
L.B.D-3A
L.B.D-3A AUX. 1
L.B.D-3B
L.B.D-4A
L.B.D-5
L.B.E-5
L.B.C-2
L.B.C-3
L.B.C-3A
L.B.C-3A AUX. 1
L.B.C-3B
L.B.C-4
L.B.C-5
MATCH LINE — SURVEY DIVISION FILE MAP NO. 19-112-4
MATCH LINE — SURVEY DIVISION FILE MAP NO. 19-112-1

Figure 2.13(b)

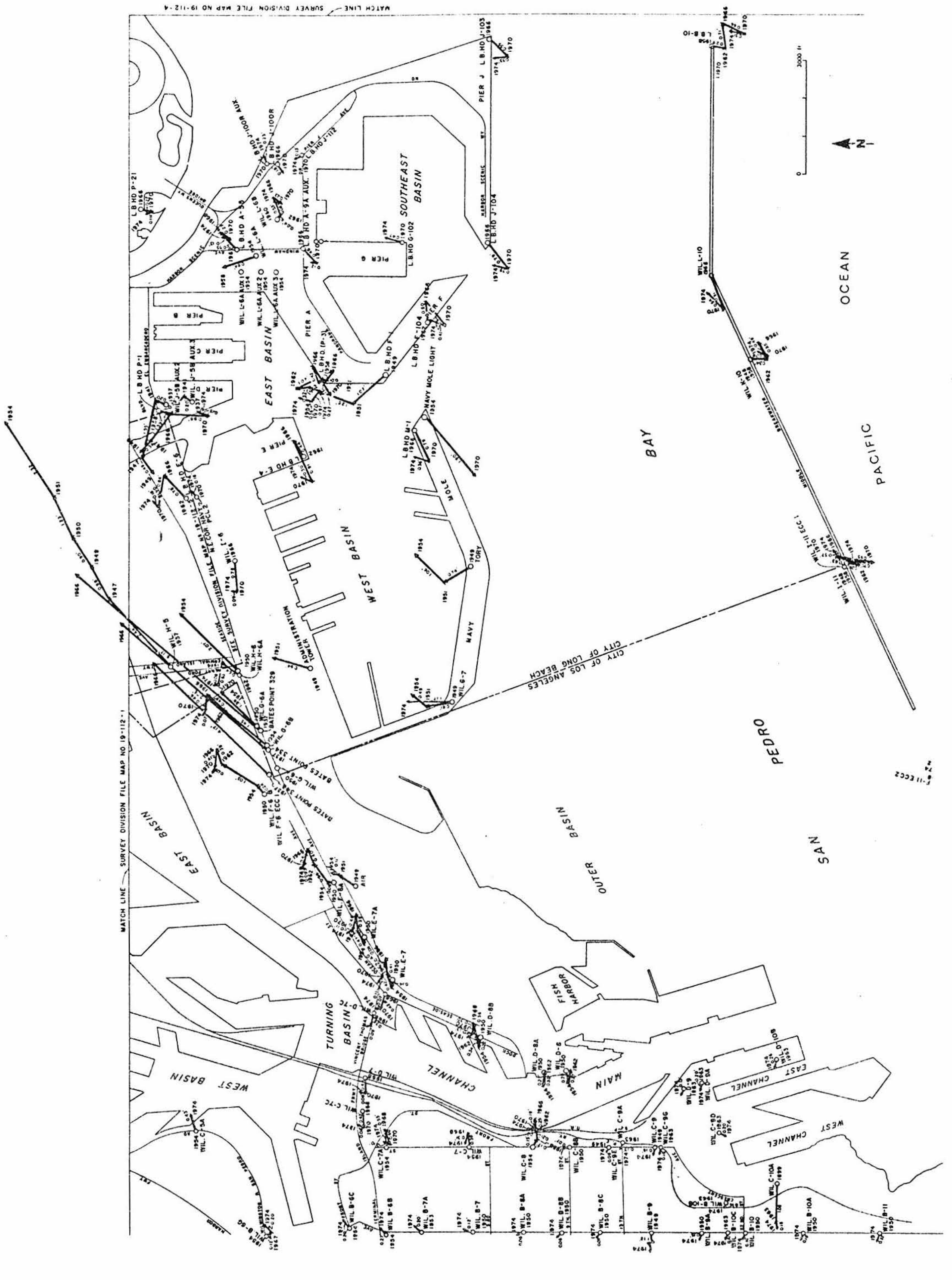
MATCH LINE — SURVEY DIVISION FILE MAP NO 19-112-4
MATCH LINE — SURVEY DIVISION FILE MAP NO 19-112-1
SOUTHEAST BASIN
PIER G
PIER A
PIER B
PIER C
PIER D
PIER E
PIER F
PIER J
EAST BASIN
WEST BASIN
NAVY MOLE
NAVY MOLE LIGHT
ADMINISTRATION TOWER
BATES POINT 329
BATES POINT 330
BATES POINT 331
CITY OF LONG BEACH
CITY OF LOS ANGELES
OUTER BASIN
FISH HARBOR
TURNING BASIN
MAIN CHANNEL
EAST CHANNEL
WEST CHANNEL
SAN PEDRO BAY
PACIFIC OCEAN
N
2000 ft

Figure 2.13(c)

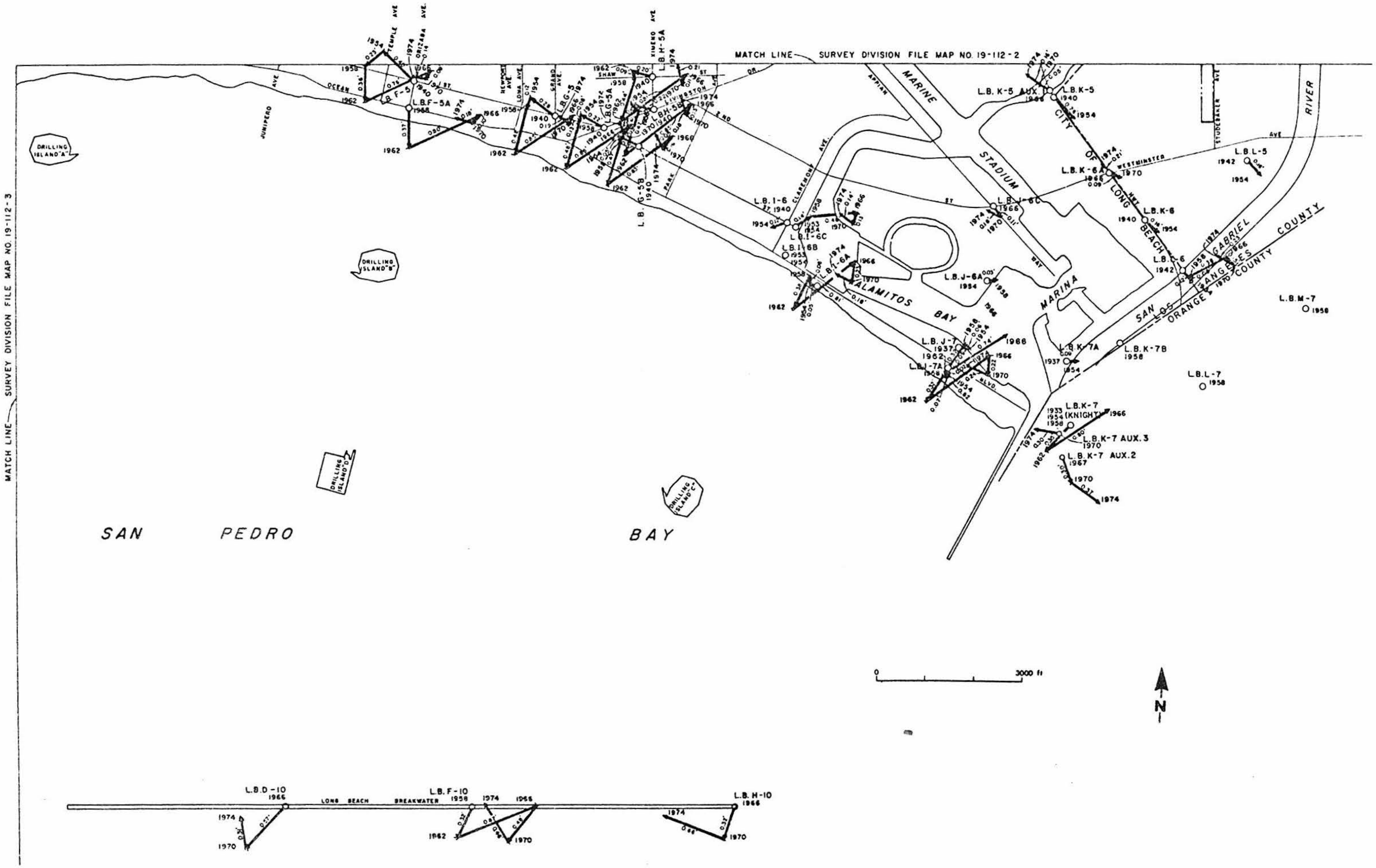
MATCH LINE — SURVEY DIVISION FILE MAP NO. 19-112-2
MATCH LINE — SURVEY DIVISION FILE MAP NO. 19-112-3
SAN PEDRO BAY
ALAMITOS BAY
MARINA
MARINE STADIUM
CITY OF LONG BEACH
SAN GABRIEL RIVER
LOS ANGELES COUNTY
ORANGE COUNTY
DRILLING ISLAND "A"
DRILLING ISLAND "B"
DRILLING ISLAND "C"
DRILLING ISLAND "D"
OCEAN BLVD
TEMPLE AVE
ORIZABA AVE
NEWPORT AVE
LOMA AVE
GRAND AVE
XIMENO AVE
JUNIPERO AVE
CLAREMONT AVE
APPIAN WAY
WESTMINSTER AVE
STUDEBAKER AVE
PARK
2 ND ST
L.B. F-5
L.B. F-5A
L.B. G-5
L.B. G-5A
L.B. G-5B
L.B. H-5A
L.B. I-6
L.B. I-6A
L.B. I-6B
L.B. I-6C
L.B. J-6A
L.B. J-6C
L.B. J-7
L.B. J-7A
L.B. K-5
L.B. K-5 AUX
L.B. K-6
L.B. K-6A
L.B. K-7 (KNIGHT)
L.B. K-7A
L.B. K-7B
L.B. K-7 AUX. 3
L.B. K-7 AUX. 2
L.B. L-5
L.B. L-6
L.B. L-7
L.B. M-7
L.B. D-10
L.B. F-10
L.B. H-10
LONG BEACH BREAKWATER
0
3000 ft
N

Figure 2.13(d)

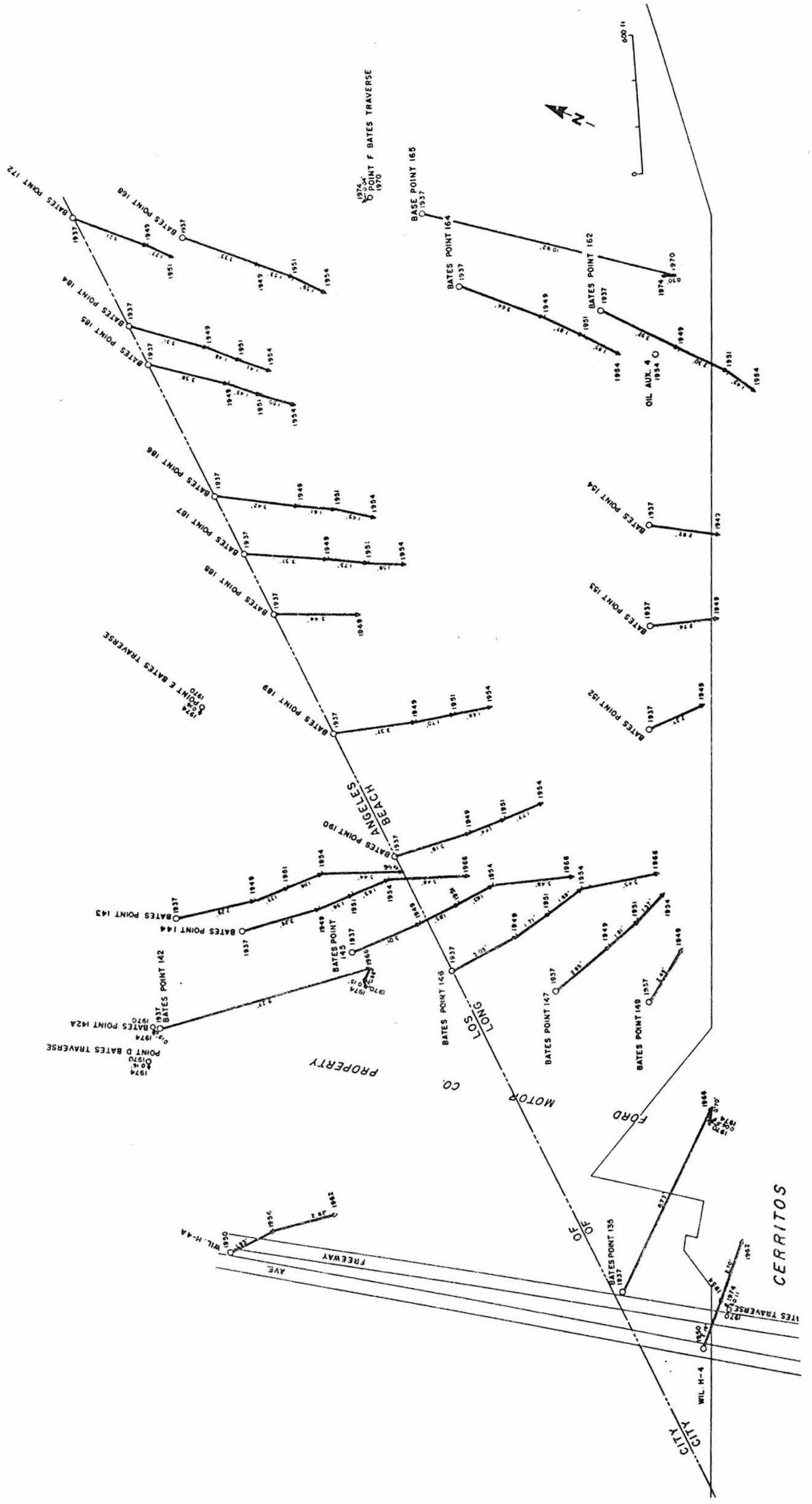
N
0
600 ft
BATES POINT 172
BATES POINT 168
POINT F BATES TRAVERSE
BASE POINT 165
BATES POINT 164
BATES POINT 162
OIL AUX. 4
BATES POINT 184
BATES POINT 185
BATES POINT 186
BATES POINT 187
BATES POINT 188
BATES POINT 154
BATES POINT 153
POINT E BATES TRAVERSE
BATES POINT 189
BATES POINT 152
BATES POINT 190
BATES POINT 143
BATES POINT 144
BATES POINT 145
BATES POINT 142
BATES POINT 142A
POINT D BATES TRAVERSE
BATES POINT 146
BATES POINT 147
BATES POINT 148
BATES POINT 135
BATES TRAVERSE
WIL H-4A
WIL H-4
CITY OF LOS ANGELES
CITY OF LONG BEACH
FORD MOTOR CO. PROPERTY
FREEWAY
AVE.
CERRITOS

Figure 2.13(e)

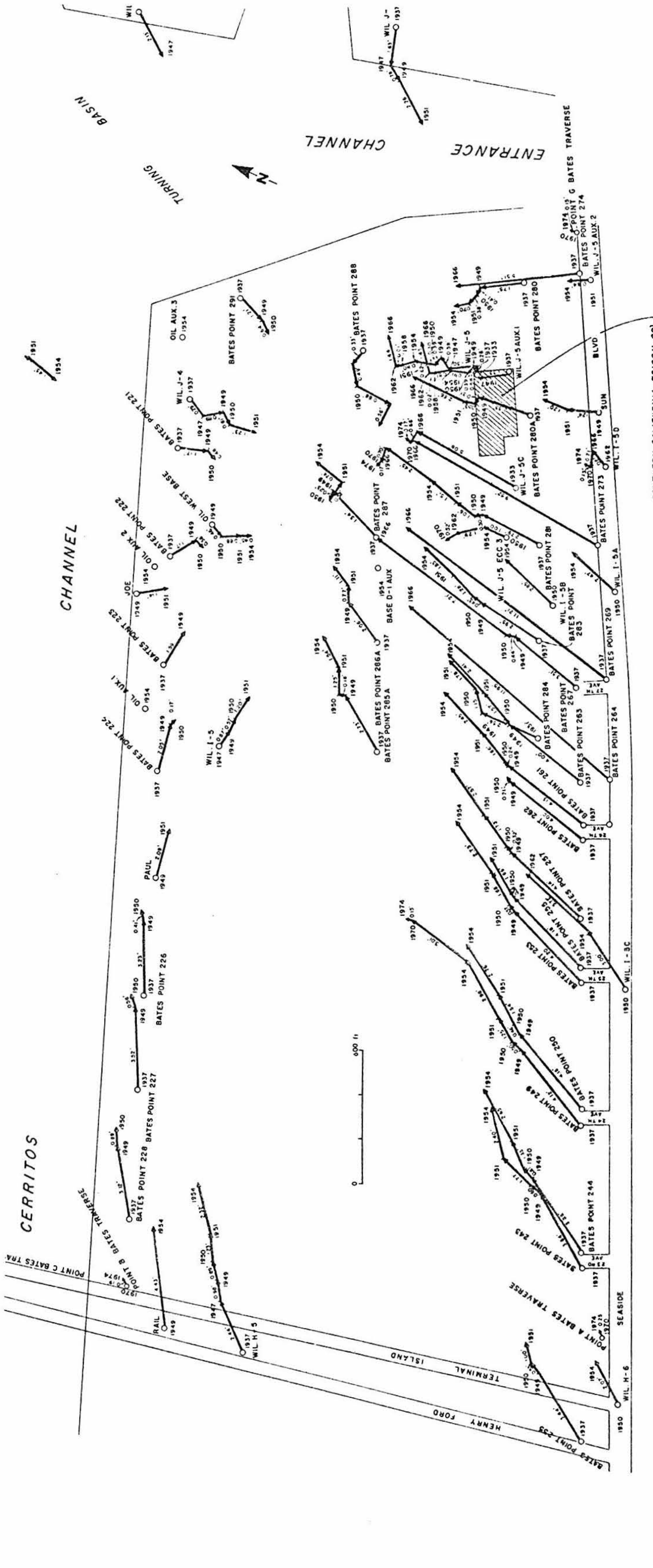
CERRITOS CHANNEL
TURNING BASIN
ENTRANCE CHANNEL
N
SOUTHERN CALIFORNIA EDISON CO. STEAM PLANT NO. 2
TERMINAL ISLAND
HENRY FORD
SEASIDE BLVD
POINT A BATES TRAVERSE
POINT B BATES TRAVERSE
POINT C BATES TRA.
POINT G BATES TRAVERSE
BATES POINT 274
WIL J-5 AUX 2
BATES POINT 288
BATES POINT 280
BATES POINT 280A
BATES POINT 291
OIL AUX 3
WIL J-4
BATES POINT 221
OIL WEST BASE
BATES POINT 222
OIL AUX 2
JOE
BATES POINT 223
OIL AUX 1
BATES POINT 224
WIL I-5
PAUL
BATES POINT 226
BATES POINT 227
BATES POINT 228
RAIL
WIL H-5
WIL H-6
BATES POINT 235
BATES POINT 243
BATES POINT 244
BATES POINT 248
BATES POINT 250
BATES POINT 253
BATES POINT 252
BATES POINT 257
BATES POINT 262
BATES POINT 261
BATES POINT 263
BATES POINT 264
BATES POINT 267
BATES POINT 284
BATES POINT 285A
BATES POINT 286A
BASE D-1 AUX
BATES POINT 287
BATES POINT 283
BATES POINT 269
WIL I-5A
WIL I-3C
WIL I-3D
BATES POINT 281
WIL J-5 ECC 3
WIL J-3C
WIL J-5
WIL J-5AUX 1
BATES POINT 273
SUN
WIL I-5D
WIL J-
WIL
0
600 ft

Figure 2.13(f)

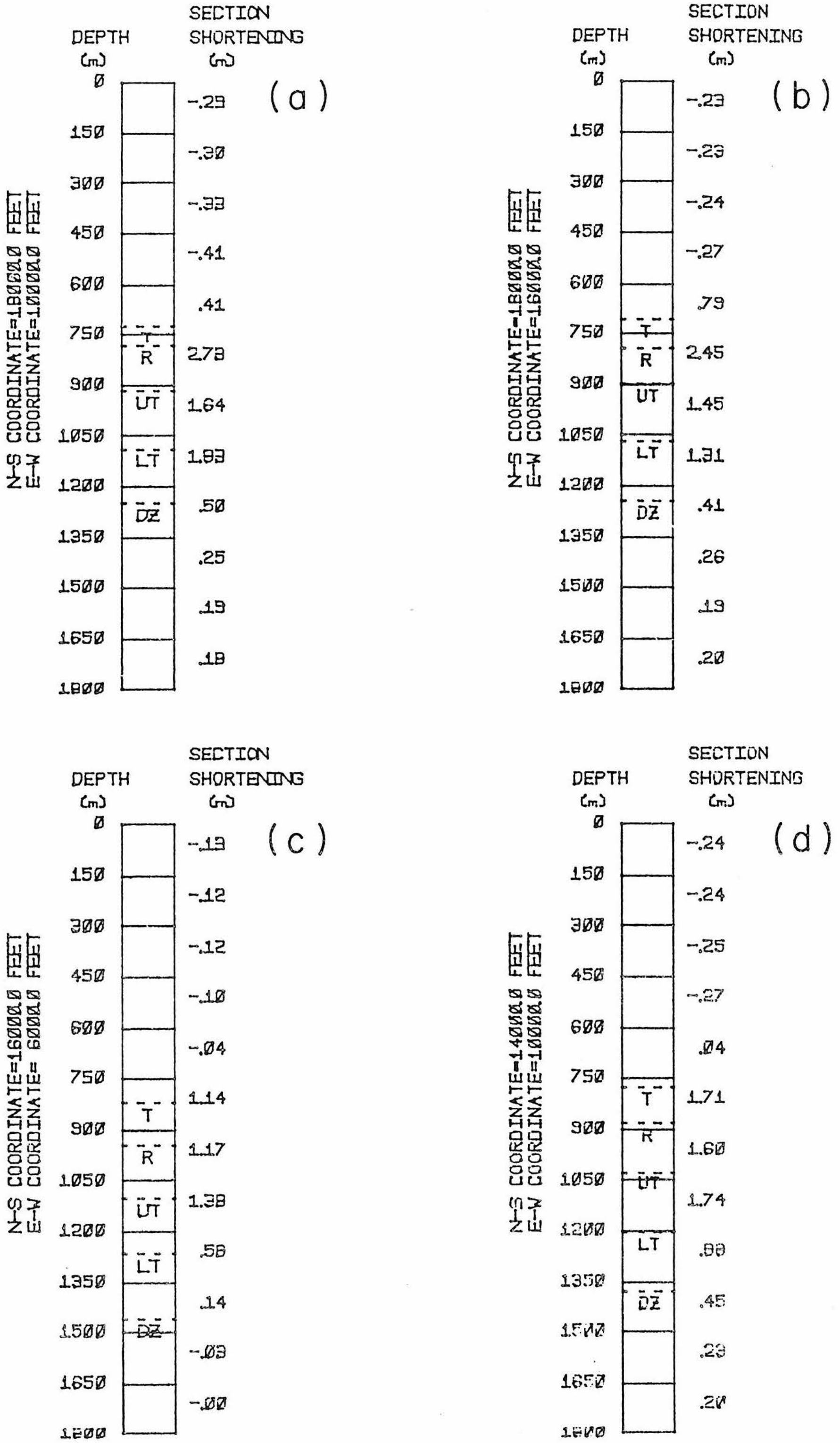

Figure 2.14 (a) - (d) Synthetic collar counts for elastic subsidence model.

may need a separate rheological prescription including much stiffer elastic moduli (Allen, personal communications, 1977; Mayuga, 1970). All the plots show a small amount of extension above the producing zones, in agreement with suggestions from some investigators based on observed behaviour (Allen and Mayuga, 1968).

It is instructive to compare the calculated collar counts in Figure 2.14 (a) - (d) with one dimensional subsidence calculations (Allen, 1968). In the 1-D method, the subsidence at a point on the surface is calculated by a formula of the type;

$$\Delta W = \frac{\Delta P}{E} \cdot \Delta Z \ , \tag{2.10}$$

where E is an assumed elastic modulus, ΔW is the subsidence, ΔZ is the combined thickness of the producing zones, and ΔP is the average pressure reduction in the zones. Applying this formula to the compaction in the four upper zones in Figure 2.14 (d), which represents a section approximately below the center of subsidence, we obtain (using $E = \lambda + 2\mu = 4.5$ kbar (Table 2.1), $\Delta P = 0.09$ kbar (a typical value for the upper producing zones), $\Delta Z = 0.5$ km) a compaction value of 8.5 meters, which roughly agrees with Figure 2.14 (a). However, when the formula is applied to the section in Figure 2.14 (c), the resulting compaction is larger than the total compaction (of about 4.5 meters) in the four upper zones of this figure. This is in spite of the fact that inspection of the pressure reduction data has shown that the sections in Figure 2.14 (a) and in Figure 2.14 (c) lie in regions with similar pressure reduction values. This indicates that the one dimensional calculation can be used only for approximating compaction in the vicinity of the center of subsidence, and that three dimensional effects become important for points lying away from the center.

The calculated stresses on horizontal sections at depths of 75m, 225m, 375m, and 525m are shown in Figure 2.15 (a) - (d) respectively. The stresses at selected points in each layer are represented stereographically. The center of each circle is located at the point where the stress is calculated, and the radius of each projection circle is scaled linearly with the difference between the maximum and minimum principal stresses. The complete details of the construction of the stereographic stress plots are given in Appendix F.

The stresses in the two upper layers of the Finite Element mesh (Figure 2.15 (a), (b)), show a general pattern of horizontal compression pointing towards the point of maximum subsidence in the region of the center of the subsidence bowl, and horizontal extension on the flanks. The magnitude of the absolute value of the largest difference between the maximum principal stress and the minimum principal stress is 11.8 bar for the first layer (d=75m), and 11.6 bar for the second layer (d=225m). The magnitude of the strains which are associated with the stresses is on the order of 10^{-3}. It should be noted that whereas in the region of the center of the bowl the extension axis is vertical, on its flanks both the extension axis and the compressive axis are horizontal.

The stresses at depths of 375m and 525m (Figure 2.15 (c) and Figure 2.15 (d) respectively), show a general pattern which resembles that of the shallower layers (Figure 15 (a) and (b)). However, in

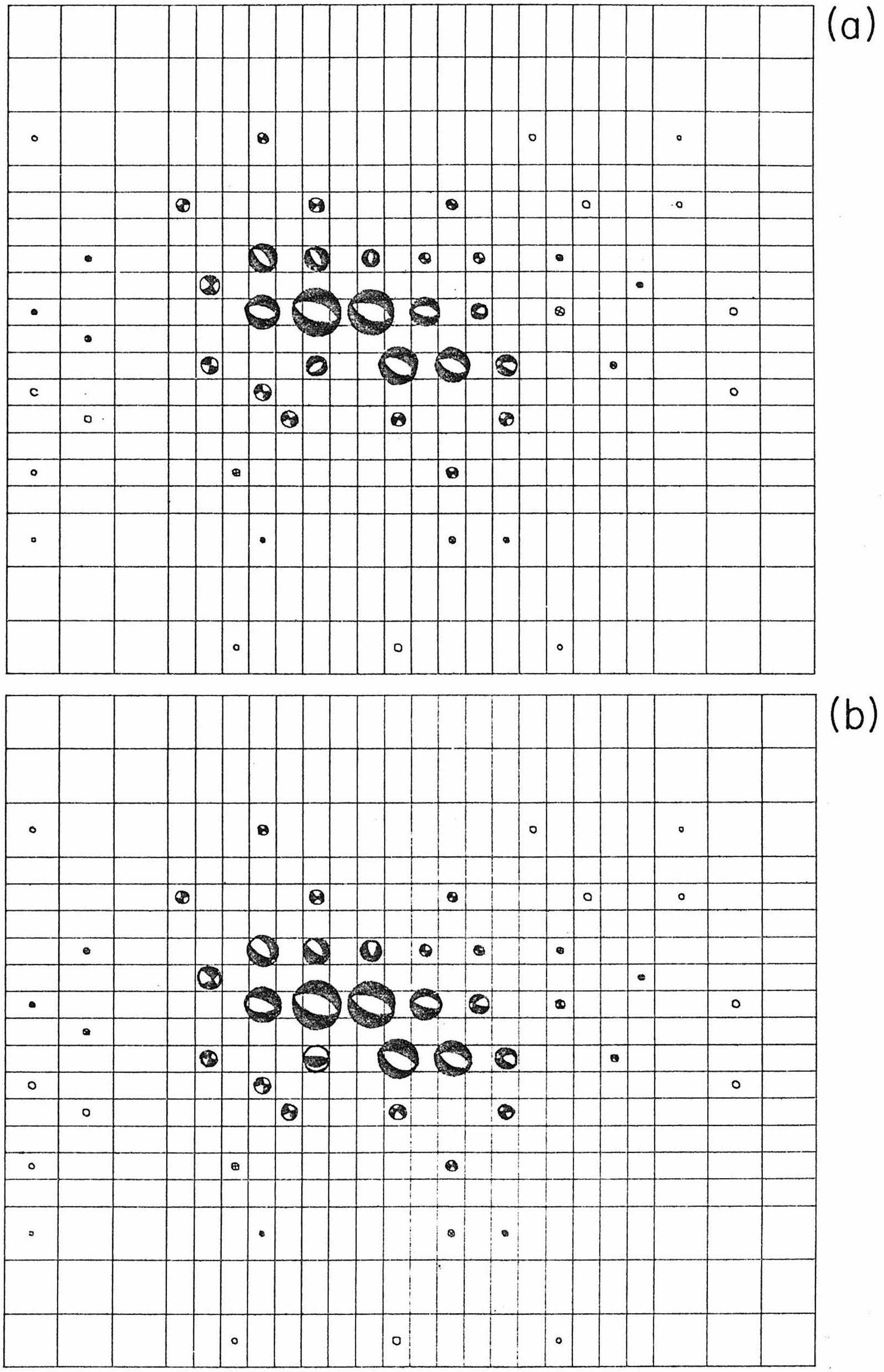

Figure 2.15 Stereographic projection of calculated stresses at different depths. (a) d = 75m, $|\sigma_1 - \sigma_3|_{max}$ = 11.8 bars; (b) d = 225m, $|\sigma_1 - 3|_{max}$ = 11.6 bars.

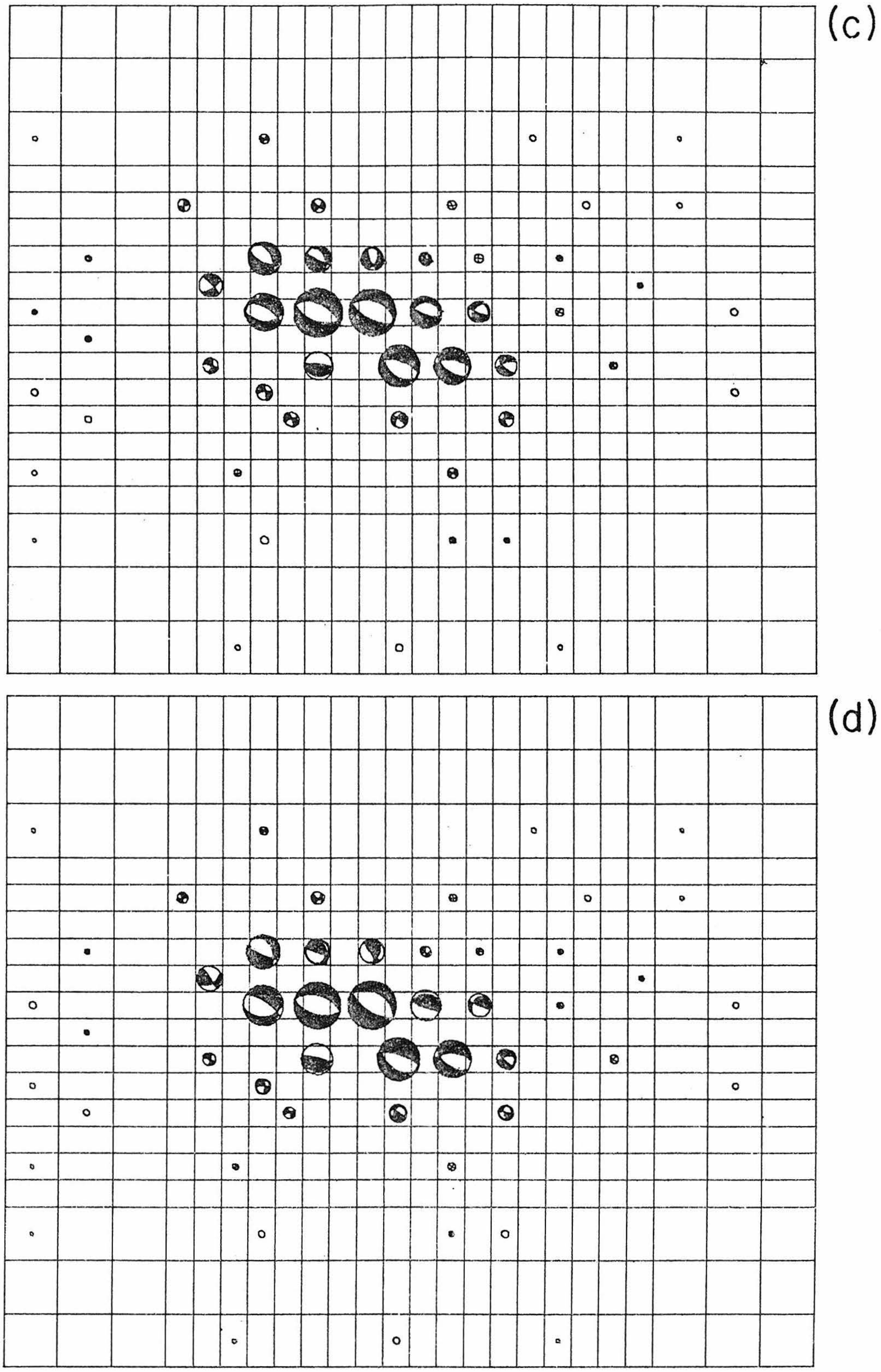

Figure 2.15 (c) d = 375m, $|\sigma_1 - \sigma_3|_{max}$ = 14.9 bars; (d) d = 525m, $|\sigma_1 - \sigma_3|_{max}$ = 17.4 bars.

regions corresponding to the Southern and Northern flanks of the anticlinal trough of the structure of the field, the stresses essentially represent horizontal shear (Figure 2.15 (c) and (d)). These regions correspond to the parts of the Wilmington field which gave rise to small earthquakes deduced to be associated also with horizontal shear mechanisms. The magnitude of the absolute value of the largest difference between the maximum principal stress and the minimum principal stress is 14.9 bar for the third layer of the Finite Element mesh (d=375m), and 17.4 bar for the fourth layer (d=525m). Thus, according to the present model, these values imply that the magnitude of the horizontal stress which caused the earthquakes was less than ten bars. It is interesting to note that the subsidence earthquakes did not take place where the Finite Element calculations predict the largest stress differences, but rather in regions where the stresses are essentially of horizontal shear. This perhaps can be attributed to the fact that the earthquake slip always occurred along thin shale beds (e.g. Kovach, 1974) which were more conducive to slippage than any other possible plane in the region above the producing zones.

In conclusion, the elastic model succeeds in reproducing most of the observed phenomena which were associated with subsidence in the Wilmington oil field. Its main shortcoming is that the calculations produce a wider deformation pattern than was observed. Also, as will be apparent in later sections, the amount of rebound observed in the field after the repressurization program was initiated, was much smaller than that predicted with the elastic model used in this section. To match rebound, it is evident that a different set of elastic constants needs to be employed, a fact which emphasizes the nonlinearity of the mechanical response of the material in the Wilmington field.

2.10 A Need for a More Complete Characterization of Material Response

As already noted, the linearly elastic subsidence model produces a deformation pattern wider than the observed deformation. Furthermore, even without going into detailed calculations, it is apparent that the type of elastic model used in the previous section gives rise to an excessive amount of rebound. This is because the maximum observed rebound in 1975 was only on the order of 1-2 feet, whereas the pressures at that time in certain areas in the field were above the hydrostatic head (Scranton, personal communications, 1977) (i.e. higher than at the time of field development). In this section we will attempt to demonstrate that the shortcomings of the elastic model cannot easily be overcome, and that a more complete characterization of material response is required in order to explain the observations.

The most straightforward explanation for the apparent small extent of observed surface deformations, would be to postulate a change in material properties as a function of horizontal distance from the center of subsidence. If the material were stiffer towards the flanks of the oil field, most of the subsidence would be limited to the center of the field. Unfortunately, field evidence from core samples does not support this hypothesis, and there does not appear to be any consistent spatial variation in material properties in the field, although on a local scale, material properties often vary, depending on the percentage of sand in the formations (Allen, personal communications, 1977).

Moreover, core samples extracted from formations in the Wilmington field, are very similar in appearance to samples from adjacent fields, and are typical of sediments in the L.A. basin area in general (Allen, personal communications, 1977). For these reasons, it does not appear that lateral material heterogeneities can explain the confined horizontal extent of the observed displacement and strain patterns.

It also does not appear that material anisotropy can be responsible for the size of the subsidence bowl. This is because the horizontal extent of the pressure reduction zone is much larger than the size of the subsidence bowl, and thus anisotropy alone could not confine the subsidence to only a limited portion of the area above the region where pressure reduction took place.

Finally, the small amount of observed rebound suggests that the material in the Wilmington field behaves differently upon loading and unloading. This type of response cannot be reproduced in an entirely elastic material, and thus at best, a different set of elastic moduli would be required for the subsidence and rebound phases respectively.

The above mentioned shortcomings of the elastic subsidence models suggest that a more complete material response characterization is in order. The construction of such a model, in the framework of the theory of plasticity, is the topic of the next section.

2.11 Construction of a Nonlinear Material Response Model for the Formations in the Wilmington Field

Most of the theoretical and experimental work which has been done so far on the mechanical properties of sands and other soils has been related to the civil engineering structural problems. Consequently the stress levels of interest in these undertakings were on the order of a few bars, far below the lithostatic overburden stresses present in the earth beyond a few hundred meters of depth. Since most of the Wilmington subsidence and related effects appear to be controlled by the mechanical properties of the producing zones, most of the results of previous work cannot be applied directly to the subsidence problem. Therefore, it was necessary to construct the parameters of a nonlinear model which would be relevant to the stress range encountered in the formations of the Wilmington field. As in previous sections, the work of Vesiĉ and Clough (1968) on sands, which did cover a wide range of pressure variation, serves as the main laboratory or experimental basis for constructing the nonlinear model. The parameters of the model are further constrained by field observations.

The rheological model used in this study is a variant of the cap model, elements of which first appeared in Gibson et al. (1957), and was further developed by DiMaggio and Sandler (1971), and Sandler et al., 1976. The model covers important effects in sands which include the existence of a failure surface in stress space, and the appearance of non-recoverable plastic volumetric strains, even under hydrostatic compaction conditions. The experimental work of Vesiĉ and Clough, (1968) did not cover stress paths other than hydrostatic loading, triaxial loading, and octahedral shear loading, and therefore phenomena such as the appearance of yielding while unloading, or the effect of varying the stress trajectories during the experiment could not be elucidated. However, it is felt that the material model developed in this study covers the most important nonlinear effects in the Wilmington field, which are, the size of the subsidence bowl and the small amount of rebound (relative to subsidence) observed after the initiation of the repressurization program. The model does, in addition, shed light on various internal processes in the deforming zones, which are not accessible by direct observation.

A point which requires attention in plasticity simulations is the role of prestress. It may be recalled that in the elastic simulation the coordinate system in the calculations refers to the configuration of the field prior to production. The subsequent displacements are determined by the change in pore fluid pressure during production, and there is no need to consider prestress in the field. Conversely, in plastic simulations the material response depends on the initial stresses, and therefore the prestress, which is caused mainly by gravity loading, must be considered. However, the plastic simulations can still employ the same coordinate system as used in the elastic simulations in which the change in strains and stresses are defined with respect to the initial state of the field, prior to production. The use of an infinitesimal deformation theory is justified for this choice of coordinates, since the maximum strain changes during the subsidence are only on the order of one to two percent (see for example Fig. 2.14). Thus the initial prestrain (which is finite) does not enter the equations of equilibrium, and only appears as a hardening parameter in the stress-strain relations.

2.12 Properties of the Cap Model

This section summarizes the main features of the cap model used in the present study. Additional details on the fitting of the cap model to experimental data are given in appendix G.

The cap model belongs to the class of isotropic elastic-plastic strain hardening material models. The model assumes that nonlinear material behavior can be described by the two stress invariants J_1 and J_2' which are given by;

$$J_1 = \sigma_{ii} \tag{2.11}$$

$$J_2' = \frac{1}{2} \sigma_{ij}' \sigma_{ij}' ,$$

where, as in previous sections, σ_{ij}' denotes the stress deviator. The model contains two yield surfaces whose equations are given by, (Fig. 2.16)

$$\text{(2.12)} \qquad \text{(a)} \quad F_1 = \sqrt{J_2'} + \alpha J_1 + \beta$$

and

$$\text{(b)} \quad F_2 = (J_1 - \ell)^2 + R^2 J_2' - (x - \ell)^2 \ .$$

Equation (2.12a) is a generalization of the Mohr-Coulomb failure criterion.

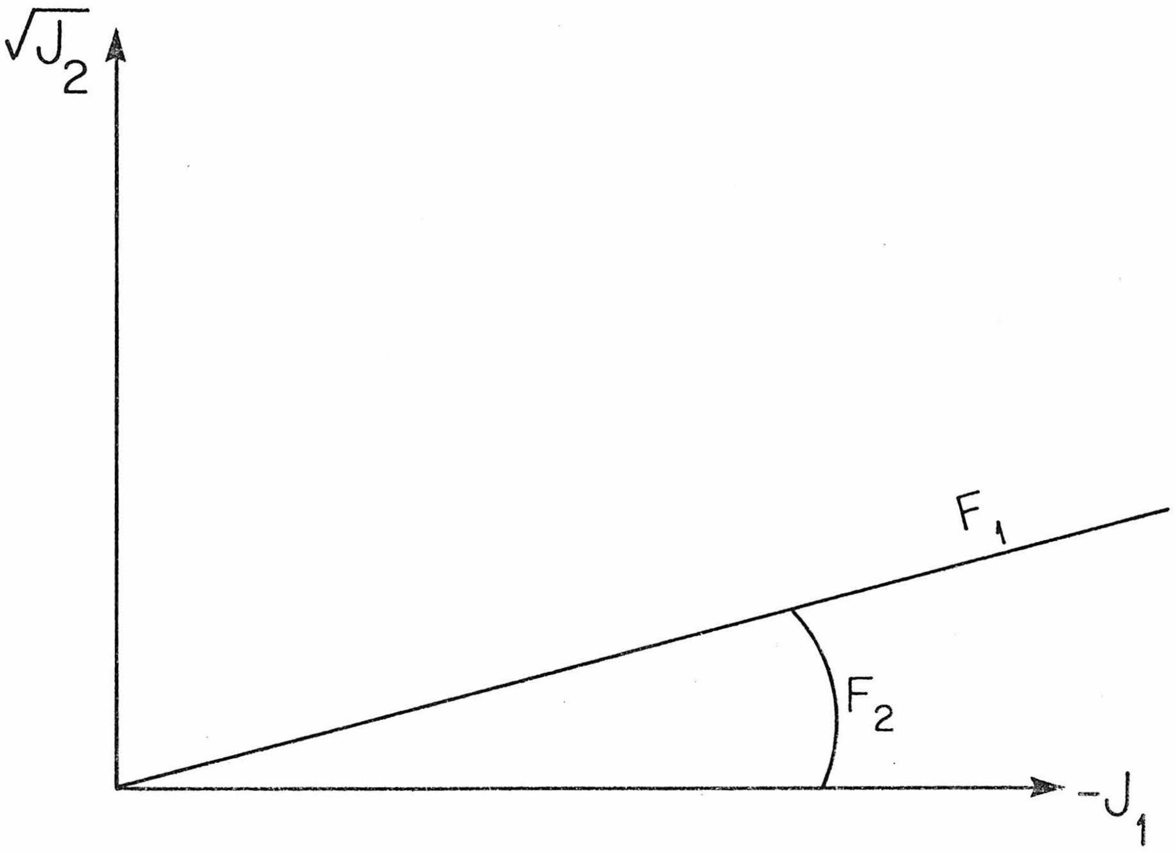

Figure 2.16 Sketch of the yield surfaces of the cap model in $-J_1 - \sqrt{J_2'}$ space.

In axial compression and extension soil tests for which $\sigma_1 = \sigma_2$, the criterion is often written in terms of the shear angle ϕ which is defined by,

$$(2.13) \qquad \sin\phi = \frac{\sigma_3 - \sigma_1}{\sigma_3 + \sigma_1}$$

(e.g. Vesiĉ and Clough, 1968). The experimental work of Vesiĉ and Clough indicates that in triaxial and octahedral shear tests, to a good approximation, the sample fails at a value of ϕ between 30^o-40^o, even at confining pressures on the order of one kilobar, and the cohesion is very small. This translates in equation (2.12)(a) to $\alpha \simeq 0.25$ and $\beta \simeq 0$. The yield surface in (2.12)(a) differs from the yield surface proposed by DiMaggio and Sandler (1971), in that it does not approach a Von-Mises yield surface at large hydrostatic stresses. Their claim that sands reach a fluid state at large confining pressures, does not seem to be justifiable, at least for pressures on the order of one kilobar or less (Vesiĉ and Clough, 1968).

The second yield surface describes an ellipse in $-J_1 - \sqrt{J_2'}$ space. This surface accounts, among other things, for the irreversible volume change due to pore collapse, which is exhibited by sands during hydrostatic compression. The yield surface, F_2, does not remain stationary for most loading paths, and its movement is determined in a hardening law which writes;

$$(2.14) \qquad x = \frac{1}{D} \ln\left(\frac{e_p}{W} + 1\right) ;$$

D and W are material parameters and e_p is a measure of plastic volumetric strain which is given by,

$$(2.15) \qquad e_p = \ell n\ (1 + \frac{\Delta v^p}{v_o})\ ,$$

where v_o is the initial bulk unit volume of the material, and Δv^p is the total nonreversible (plastic) volume change undergone during the deformation. According to the choice of the coordinate system made in this study, the change of e_p from its value at the prestressed state, is equal to the (infinitesimal) plastic volumetric strain change undergone by the material.

The rheological model contains material parameters which include the elastic bulk modulus and the shear modulus, and the plastic parameters α, β, D, and R which appear in (2.12a), (2.12b) and (2.14). These parameters are selected in order to produce a response similar to the results of Vesiĉ and Clough at the stress levels which exist in the producing zones in the Wilmington field. It should be emphasized that the comparison is for different types of stress paths, since the experimental values are derived from standard triaxial compression tests and octahedral shear tests, whereas the theoretical results are effective for tests under hydrostatic compression and uniaxial strain (rigid confinement). Details of the procedure for fitting the cap model to the data are given in appendix G. The equations of equilibrium for an elastic plastic material are given by,

$$(2.16) \qquad \frac{\partial \delta\sigma_{ij}}{\partial x_j} + \delta f_i = 0$$

where $\delta\sigma_{ij}$ and δf_i respectively denote the change in stress and change in body forces from the initial prestressed state. The stresses and coordinates x_j are measured in the prestressed configuration of the body. Equation (2.16) must be supplied with the customary boundary conditions of prescribed displacements or prescribed tractions.

For the case of an elastic-plastic saturated porous medium, equations (2.12), (2.13), (2.14), and (2.16) are still applicable when the stresses are replaced by the effective stresses $\sigma^*_{ij} = \sigma_{ij} + \alpha P_f \delta_{ij}$ (see equation 2.5). The justification of this assumption, as in poroelasticity, is empirical. Moreover, some of the evidence which is quoted to justify the theory of poroelasticity, deals with materials which are similar to the formations in the Wilmington field, and thus, in essence, justifies the applicability of the theory for the type of nonlinear rheology which this study is attempting to model.

2.13 Stress Changes During Production in the Wilmington Field on the Basis of the Cap Model

The Wilmington subsidence and its associated effects originated in a medium which was in a prestressed state. The main causes of the prestress were the overburden weight of the formations of the field, and the loading of the region by tectonic processes in the vicinity of the field. Since the latter, as in most crustal tectonic problems, are difficult to evaluate, at first the tectonic prestress will not be considered here, and will be incorporated only after it becomes apparent that the observations cannot be explained without it.

For a saturated medium containing a material with bulk density ρ, pore fluid density ρ_f, and porosity n, the vertical gravitational total stress component at a point below the surface is given by,

$$\sigma_{33} = -g(\rho + n\rho_f)z , \tag{2.17}$$

where z is the vertical depth of the point, and g is the gravitational acceleration. It is assumed that the medium is saturated at all depths.

The horizontal total stress components σ_{11} and σ_{22} are given by,

$$\sigma_{11} = \sigma_{22} = K_o \sigma_{33} , \tag{2.18}$$

where K_o is the confinement factor.

The effective prestress is calculated by algebraically adding the pore fluid pressure to the total prestress. As the original pore fluid pressure in the field was approximately equal to the hydrostatic head (e.g. section 2.7), it can be calculated from,

$$P_f = \rho_f g z. \tag{2.19}$$

Thus the initial effective stresses in the field are given by,

$$\sigma^*_{33} = -g(\rho + (n-1)\rho_f)z \tag{2.20a}$$

$$\sigma^*_{11} = \sigma^*_{22} = K^*_o \sigma^*_{33} , \tag{2.20b}$$

with,

$$K_o^* = \frac{-(\rho + n\,\rho_f)\,K_o + \rho_f}{-(\rho + (n-1)\,\rho_f)} \quad .$$

In general $K_o^* \leq K_o$, since the pore fluid pressure causes the effective stress to be farther away from the hydrostatic state. In most cases K_o^* varies between unity (hydrostatic state) and one third (rigid confinement of a Poisson solid). For a uniform K_o^* at all depths, the effective stresses in (2.20a) and (2.20b), plot as a straight line through the origin in $-J_1 - \sqrt{J_2'}$ space (Fig. 2.17). This line cannot lie above the F_1 yield surface, which therefore defines the lower bound for K_o^*. For a shear angle of 30°, this limit is approximately one-third. The construction does not determine whether the initial effective stresses lie on the cap yield surface or not. If only gravitational loading is present, the effective prestress will plot on the F_2 yield surface, but effects like erosion and ground vibration, as well as viscous effects (not included in the plasticity model), would tend to put the initial point slightly inside, in the elastic region (Fig. 2.17, point (a)). The subsidence history of the Wilmington field indicates that, in the beginning, the subsidence rate was rather low, causing the researchers at the time to underestimate the amount of ultimate subsidence. This can perhaps be attributed to the possibility that the initial effective stress was not on the yield surface so that the first subsidence strain increments were purely elastic (line AB in Fig. 2.17). The simulations of this study have tested various initial cap surface positions, and, as will be discussed later, these positions have a strong effect on the total amount of

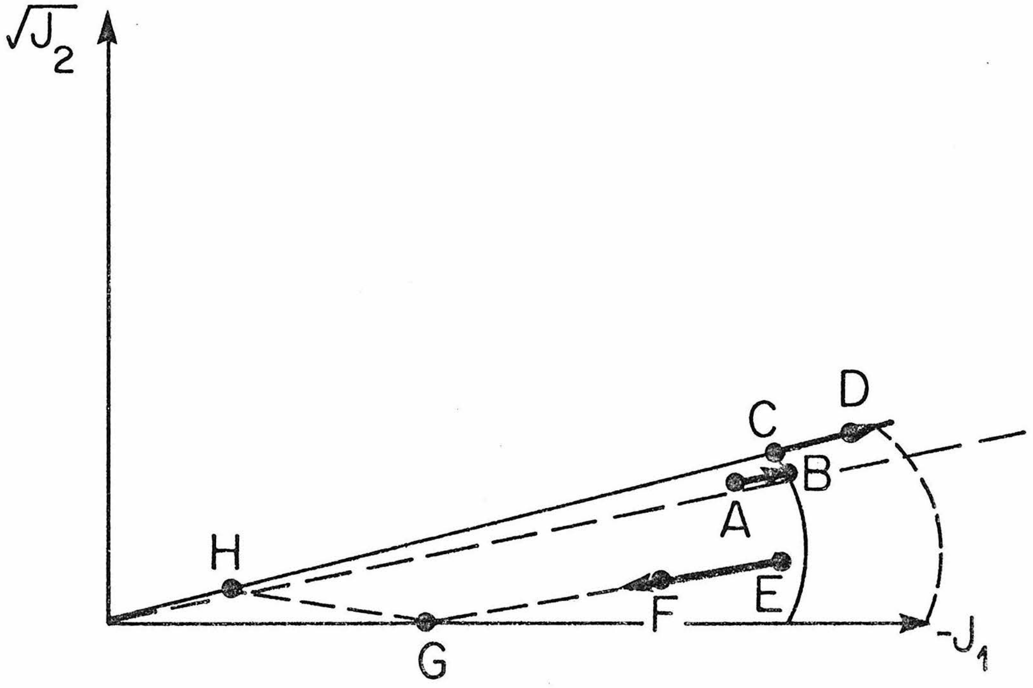

Figure 2.17

subsidence.

During the production stage, the effective stresses plot a trajectory in $-J_1 - \sqrt{J_2'}$ space. In general, stress paths which constantly lie on the yield surface have correspondingly low tangent material coefficients (Fig. 2.17, line CD), whereas trajectories which lie inside the elastic region (Fig. 2.17, line EF) have corresponding material coefficients which are equal to the elastic constants. This suggests the explanation, which will be tested later, that during the rapid subsidence phase, most of the region in the producing zones followed effective stress paths which lay on the yield surface, and therefore the subsidence was rather large. During the repressurization phase, most of the stress trajectories were progressing in the general direction of the origin (Fig. 2.17, line EF), and the material then behaved elastically. This explains why there was a relatively small amount of rebound after the field was repressurized. By this line of reasoning, the observed amount of rebound is used for fitting the elastic moduli of the cap model (section 2.14).

Conceivably, if unloading by repressurization were allowed to progress far enough, certain points in the field could experience second yielding (Fig. 2.17 line EFGH), and a large rebound would suddenly occur. There are indications that this may have occurred locally in regions surrounding repressurization wells, in which water was injected at very high pressures (Allen, 1977, personal communications). However, judging by the small amount of observed rebound, it appears that on a large scale the rebound is essentially elastic.

After a specification of the material parameters and the prestress, the data reduction and analysis of results for nonlinear simulations follow the same steps as in the elastic case.

The following section deals with the rebound phase which served to establish the elastic parameters of the material in the formations on the Wilmington field. The section is followed by sections which describe the results of non-linear subsidence simulations.

2.14 Construction of Elastic Coefficients by Matching Observed Rebound

The analysis of the previous section shows that, excluding local effects, the rebound in the Wilmington field was a result of elastic unloading caused by repressurization in the producing zones. This enables the calculation of the elastic moduli of the cap model to be made by first simulating the rebound with arbitrary coefficients and then taking into account the linearity by scaling the moduli in order to fit the observed data.

The nonlinear material approximation which was adopted in this study contains uniform material coefficients at all points in the field. The variation of material response in space is brought about through the prestress condition. Thus, mathematically, the rebound problem is a problem of deformation in a uniform elastic halfspace. The scaling method consists of assigning a fixed value to the Poisson's ratio, and varying the bulk modulus of the halfspace to produce the correct amount of rebound. Ideally, the data should be able to detect the value of Poisson's ratio as well, however, it is found from simple axi symmetric test models that the deformation pattern is extremely insensitive to values of Poisson's ratio in a reasonable range between

0.25 and 0.33. Therefore, this study does not attempt to obtain Poisson's ratio from the observations, and a value of 0.25 has been assigned to that parameter.

The pressure data for the rebound consist of the difference in well pressures in the field between the years 1958 and 1975. Unfortunately, the pressure data for 1975 are not as complete as for 1958, since production in certain areas of the field had been terminated by that time (wells were capped), and some well pressures are not available (Scranton, 1977, personal communication). In such cases it is assumed that no pressure change took place in the time interval under consideration. This assumption is made for lack of a better alternative and is likely inaccurate, as it is expected that formation pressures would recover in regions where production has ceased. Because of this underestimation of the pressure difference, the calculated rebound is expected to be conservative.

In addition to the above mentioned difficulties, there are the uncertainties listed in section 2.8 as to what portion of the measured elevation changes between 1958-1975 is a genuine result of the repressurization in the producing zones.

For these reasons it is not expected that numerical simulation will accurately reproduce the elevation changes between the years 1958-1975 (whose values are not readily available as discussed in section 2.8). The main objective of the rebound simulation is to obtain a pattern which grossly resembles the observation, and which has a maximum rebound of about 40 cm (1.3 feet). In order to obtain a more accurate rebound simulation, pressure values would need to be sampled in nonproductive wells, as well as in active wells.

The initial elastic moduli selected for the rebound calculation were a bulk modulus of 4.73 kbar, and a Poisson's ratio of 0.25.

The calculated surface elevation changes during the time interval 1958-1975 are shown in Fig. 2.18, in which the contour values are given in meters. The maximum surface uplift in the figure is about 2 meters, compared to the maximum of 40-50 cm of rebound which was observed. This indicates that with a value of 20 kbars for the bulk modulus, the measured amount of observed rebound can approximately be reproduced. Consequently, this value for the bulk modulus has been adopted for the cap model.

The observed rebound for 1975 is shown in Fig. 2.19. When the figure is compared to Fig. 2.18, it becomes apparent that the calculation resembles the observation only in the gross features of the rebound pattern. This may be partly due to the limited resolution of the FE mesh, but it appears to be primarily due to the limitation of the pressure data and surface observations as noted above. In fact, the Western rebound "hill" in Fig. 2.19 could not be reproduced because the pressure data was absent there.

After obtaining the elastic coefficients, the remaining cap model parameters are obtained by the procedure outlined in appendix G.

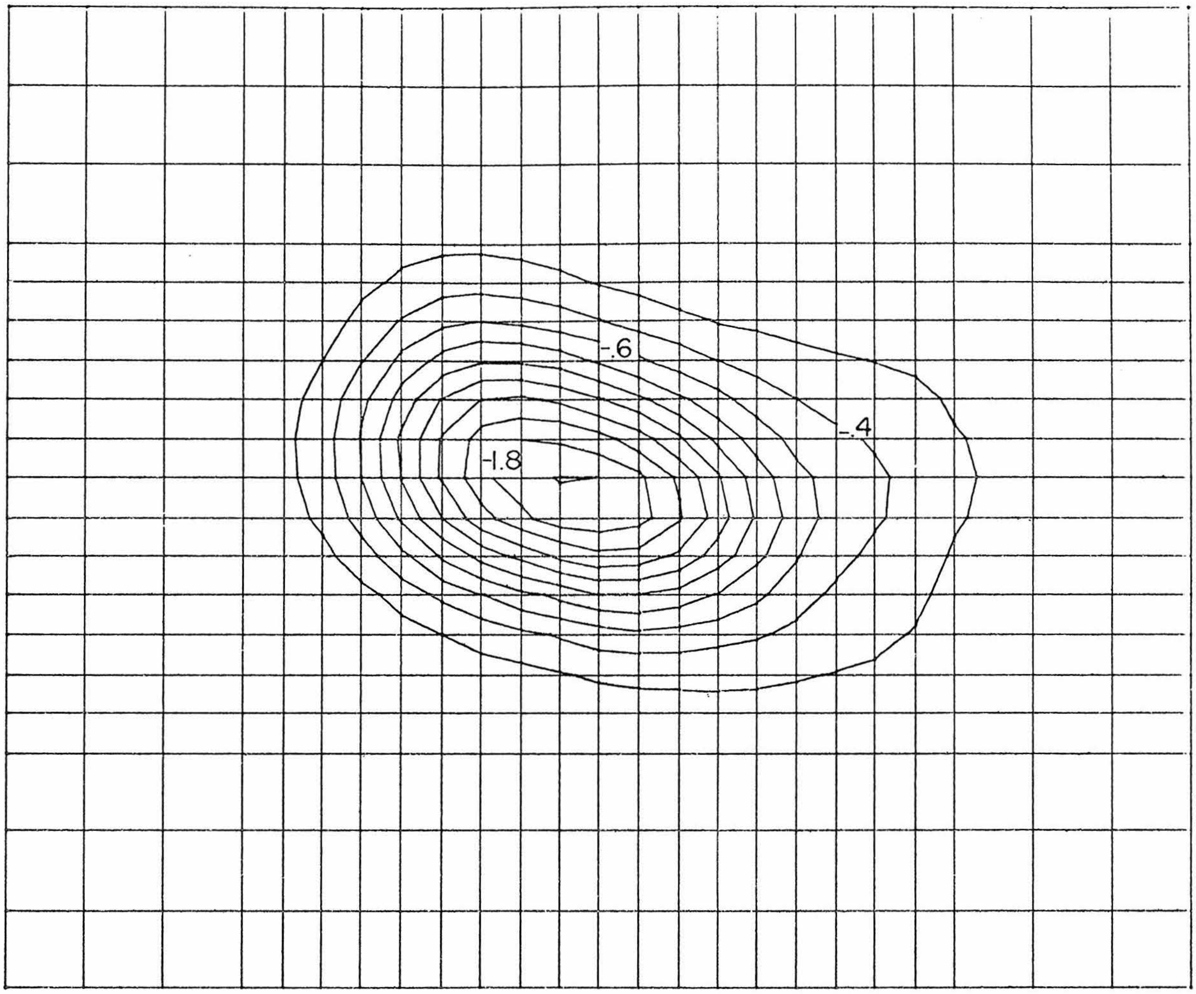

Figure 2.18 Calculated rebound in meters for 1975.

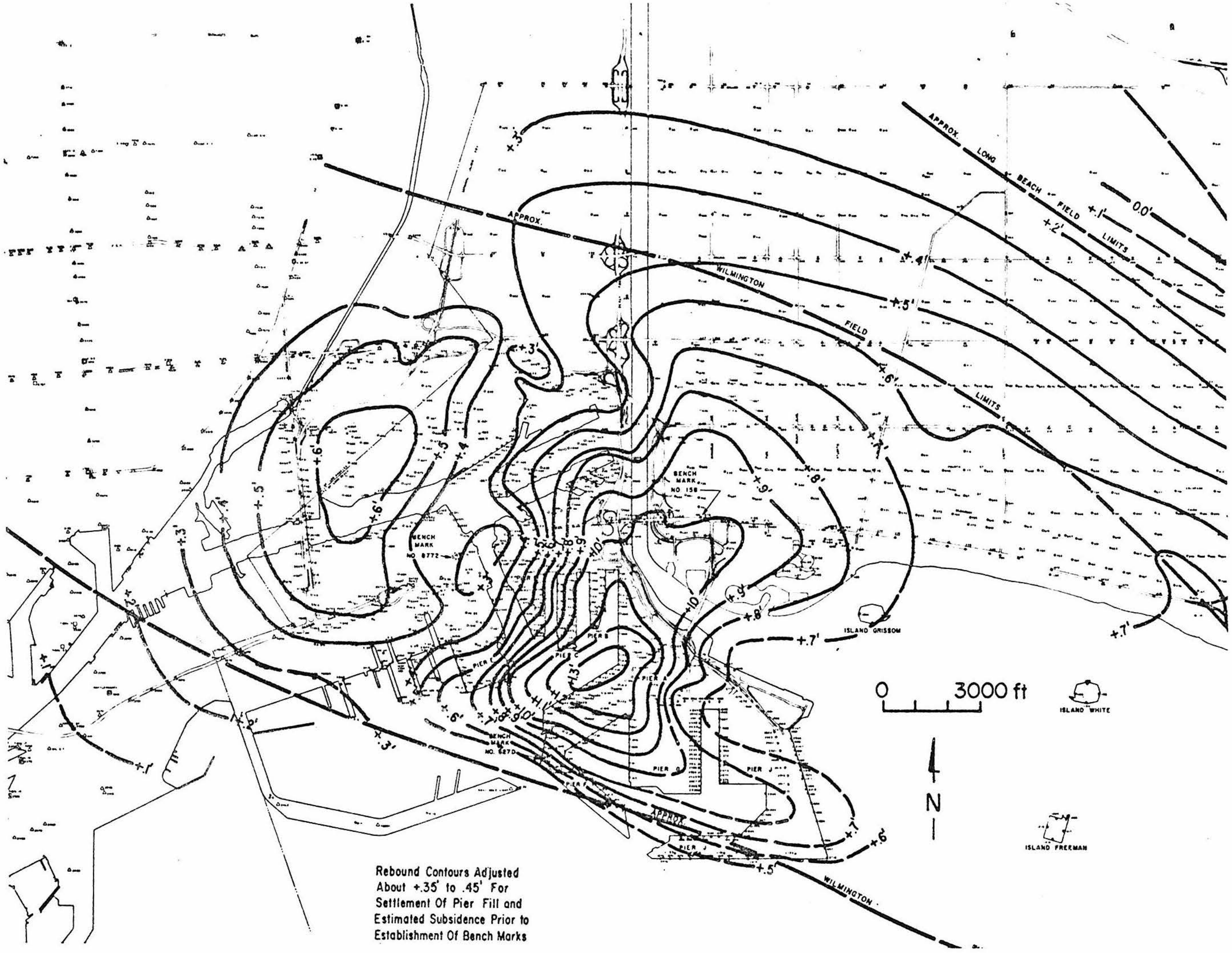

Rebound Contours Adjusted
About +.35' to .45' For
Settlement Of Pier Fill and
Estimated Subsidence Prior to
Establishment Of Bench Marks

Figure 2.19 Observed rebound in feet for 1975.

2.15 An Elastic Plastic Subsidence Model for 1958, I

The first nonlinear subsidence calculation includes lithostatic overburden as prestress, but does not account for possible stresses arising from tectonic origins. The initial stresses are taken to be slightly inside the yield surface ($J_1= 0.9x$). This is done because processes like surface erosion or dynamic ground shaking cause the stresses to be lower than yield, although by precisely how much, is unknown (a dramatic example of such a situation was reported by Bishop et al., 1965; who found in London clay a ratio of 3.4 between the lateral stresses and the vertical stress. They attributed this fact to the removal of glacial loads). The cap parameters are a Poisson's ratio of 0.25, a bulk modulus of 20 kbar, and A=0.25, D=0.7143 kbar^{-1}, R=1.227, W=0.27 (see section 2.12 and appendix G for meaning of variables). The volumetric stress-volumetric strain curve, and the variation of the tangent moduli with confining pressure, for the above choice of parameters, are shown respectively in Fig. G.2 and Figure G.3 in appendix G. The remaining input parameters are the same as in the elastic model (described in section 2.8).

The calculated vertical surface displacements are shown in Fig. 2.20. When the figure is compared to Fig. 2.11 of the elastic calculation, it becomes apparent that this nonlinear model also produces too wide a subsidence bowl, and therefore the model does not improve significantly on the elastic model in this sense. The maximum calculated subsidence in the present model is slightly more than 7 meters, in fair agreement of the observed value of slightly more than 8 meters.

The calculated horizontal displacements which are shown in Fig.

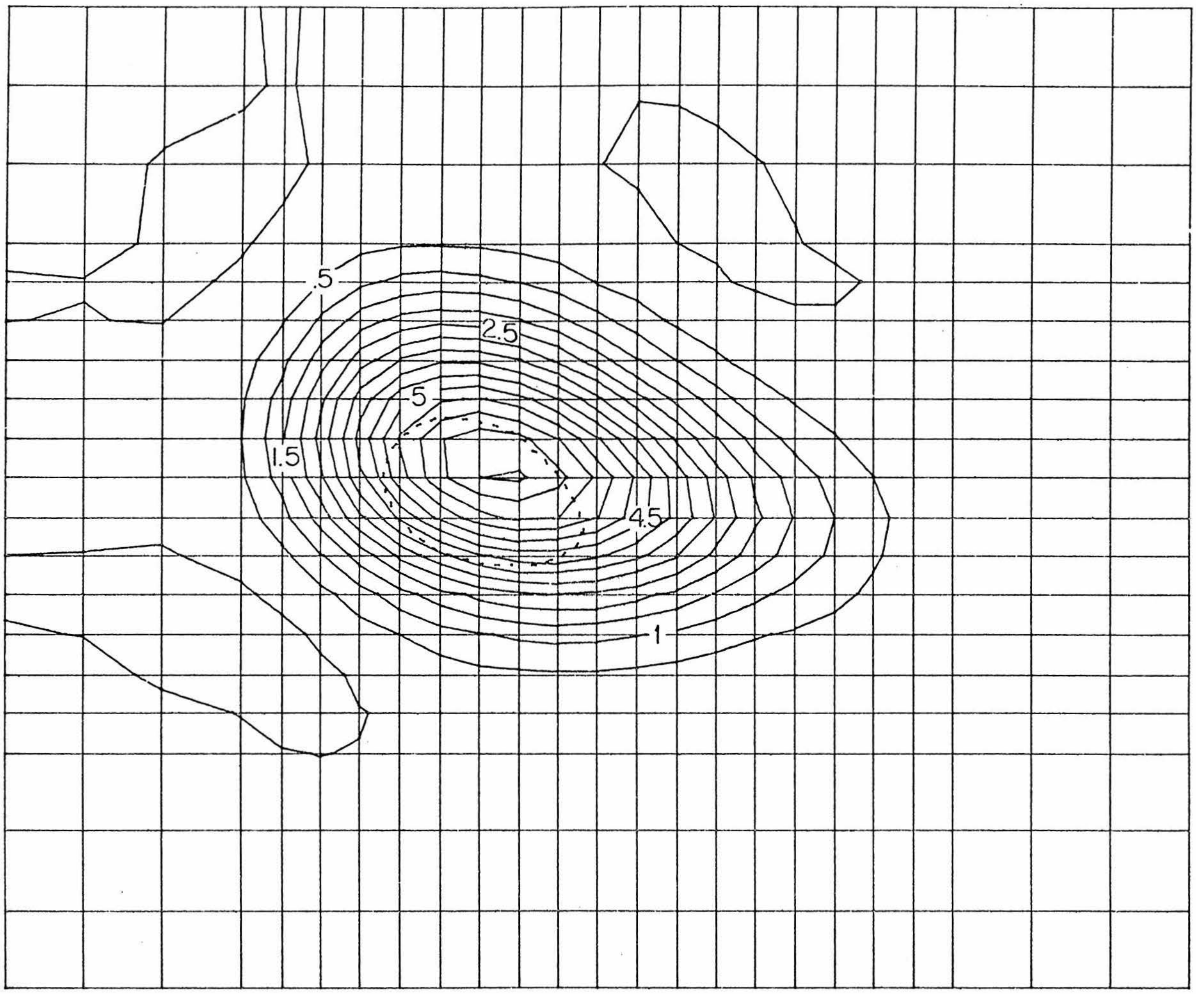

Figure 2.20 Calculated subsidence in meters for 1958. Elastic-plastic subsidence model with horizontally uniform prestress.

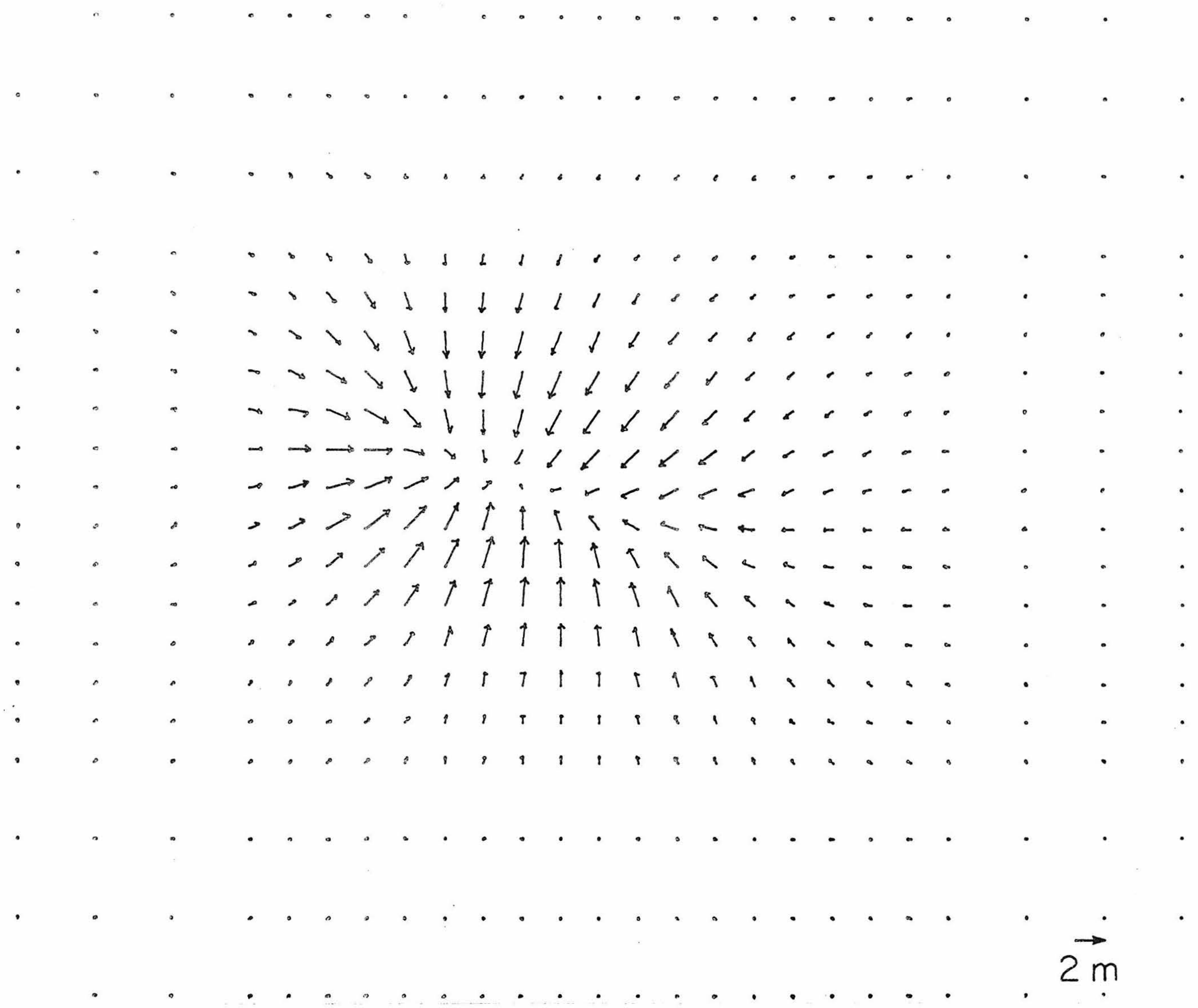

Figure 2.21 (a) Calculated horizontal displacements at the earth's surface. Elastic plastic subsidence model with horizontally uniform prestress.

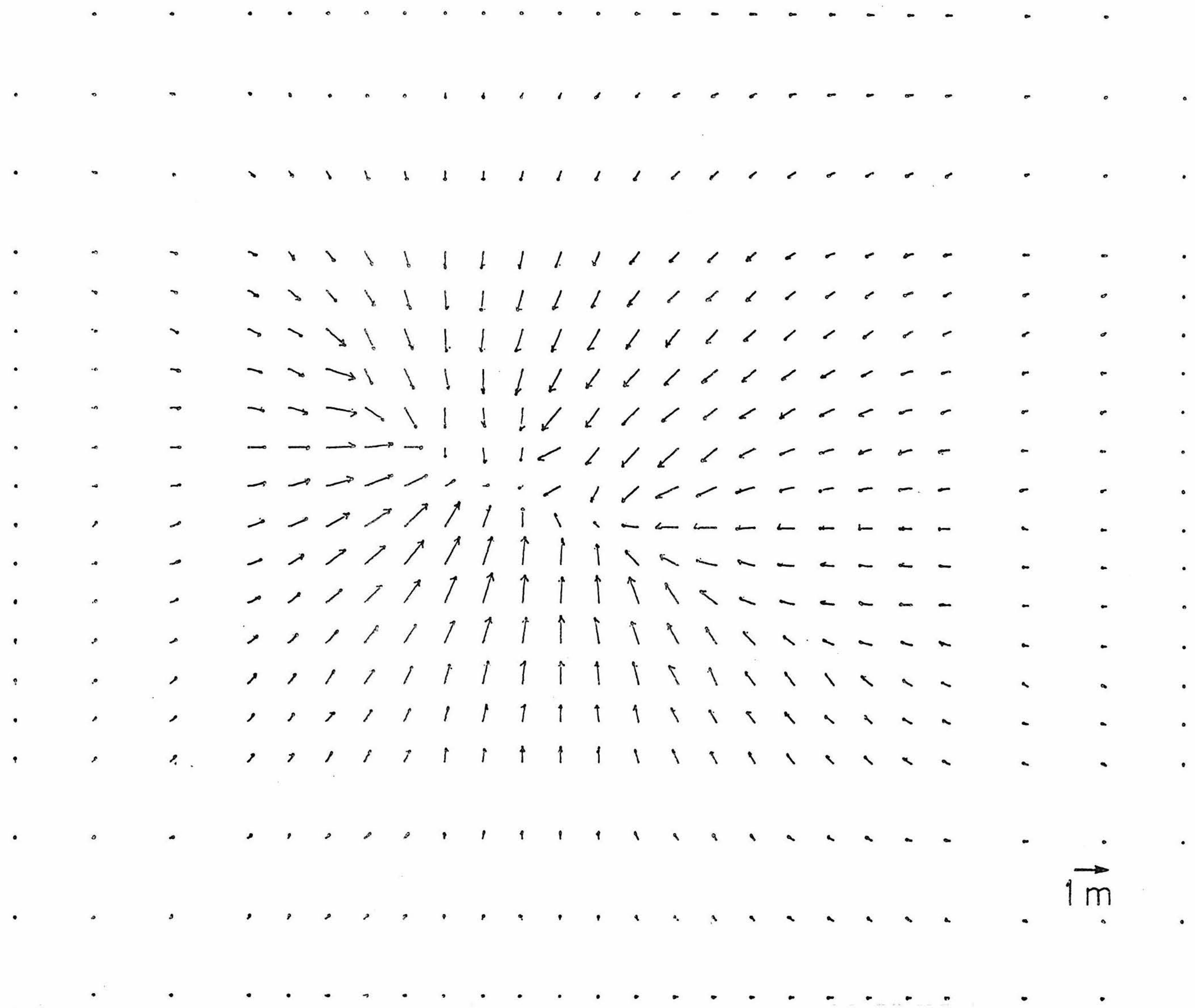

Figure 2.21 (b) Calculated horizontal displacements at a depth of 900 m. Elastic-plastic subsidence model with horizontally uniform prestress.

2.21 (a), (b), for the depths of 0 and 900 meters respectively, form a similar pattern to the one of the elastic simulation. However, the displacement magnitude is about two times smaller, with a maximum magnitude on the surface of 2-3 meters. When this value is compared to the observed magnitude of 14 feet in 1965 (Allen, 1973), (probably less in 1958), it is apparent that the present plastic model somewhat underestimates the horizontal displacement magnitude, whereas the elastic model slightly overestimates it.

The synthetic collar counts are shown in Fig. 2.32 (a)-(d). The noticeable differences between this figure and Fig. 2.14 (a)-(d) for the elastic simulation in section 2.9, are the smaller amount of compaction in the deep zones, and the smaller amount of stretching above the producing zones. The former appears to be in agreement with the observation that little compaction took place in the deep zones.

Finally, the stresses at depths of 75m, 225m, 375m and 525m are shown in Fig. 2.23 (a)-(d) respectively. The general pattern is almost identical to the elastic case. However, in the nonlinear case, the stress difference magnitude is more than twice as large, with a maximum stress difference of 18.3, 35.2, 47., and 51.7 bar respectively for the four layers. This is probably due to the fact that the region above the producing zones is in extension (e.g. Fig. 2.22 (a)-(d)), and therefore the material there undergoes unloading and behaves elastically. Thus, the nonlinear model with high elastic moduli produces high stress differences. This perhaps also explains why there is less stretching above the producing zones in the present

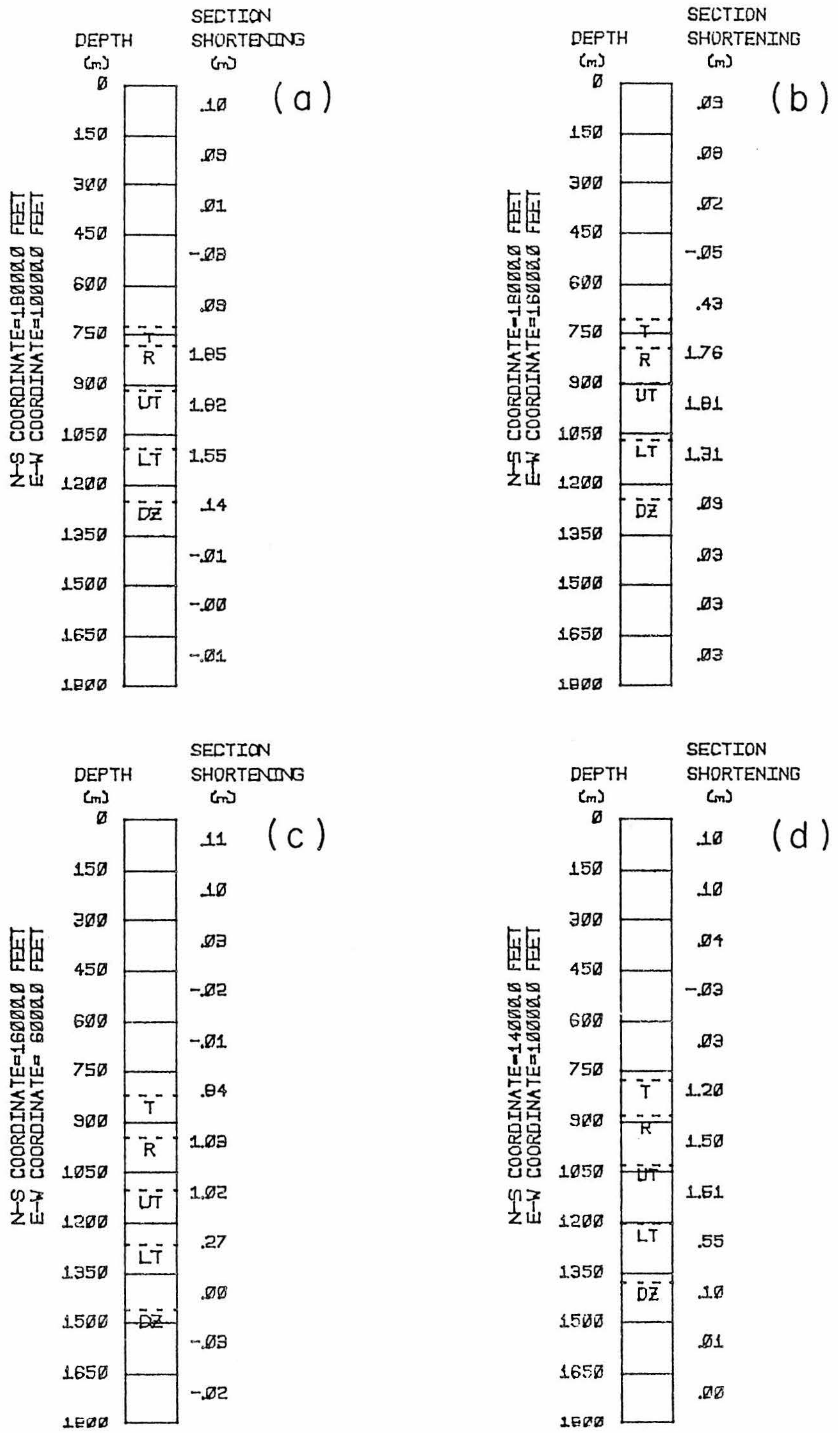

Figure 2.22 (a) - (d) Synthetic collar counts for elastic-plastic subsidence model with horizontally uniform prestress.

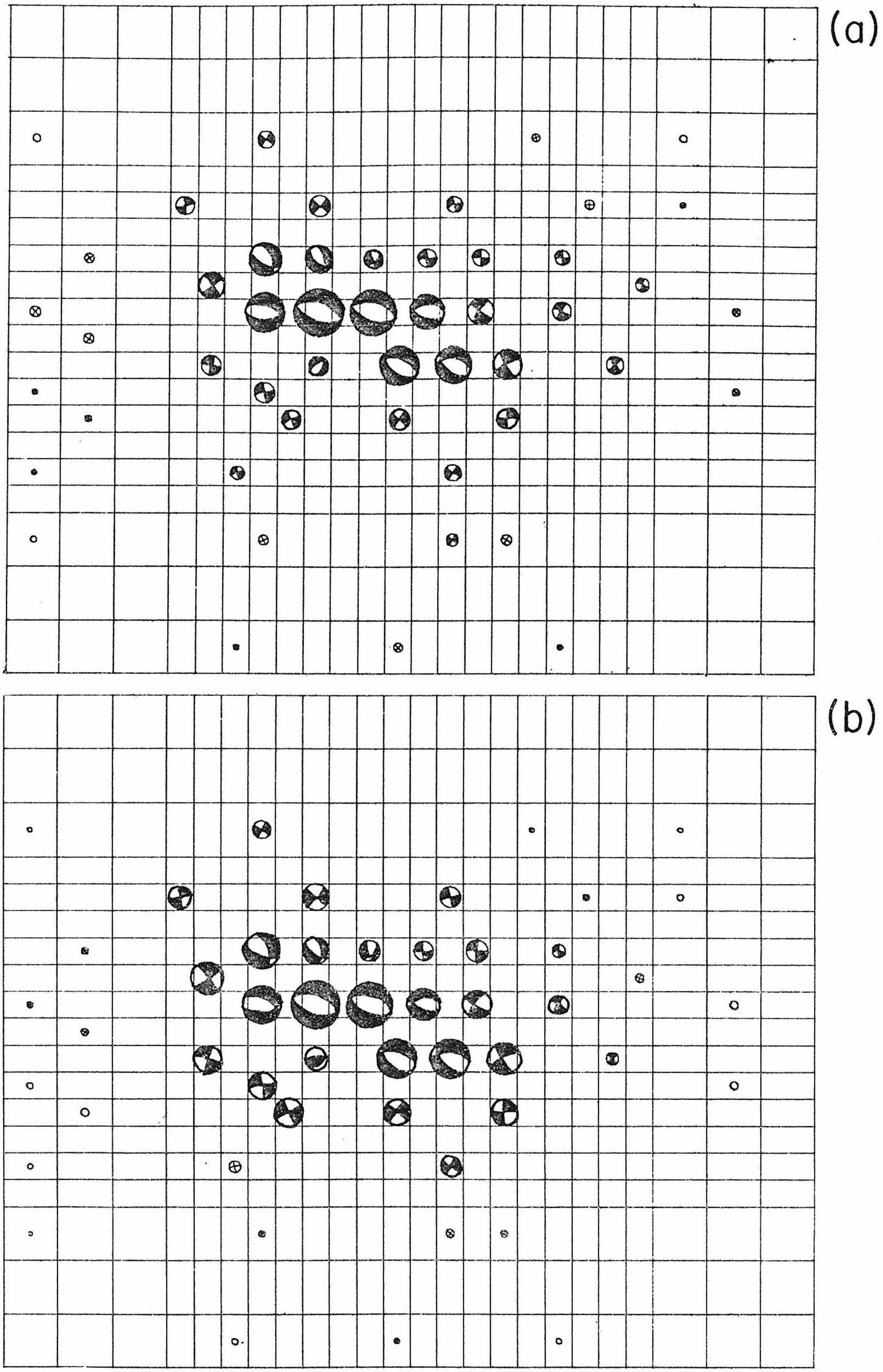

Figure 2.23 Stereographic projection of calculated stresses at different depths. Elastic-plastic subsidence model with horizontally uniform prestress. (a) d = 75m, $|\sigma_1 - \sigma_3|_{max}$ = 16.8 bars; (b) d = 225m, $|\sigma_1 - \sigma_3|_{max}$ = 29.2 bars.

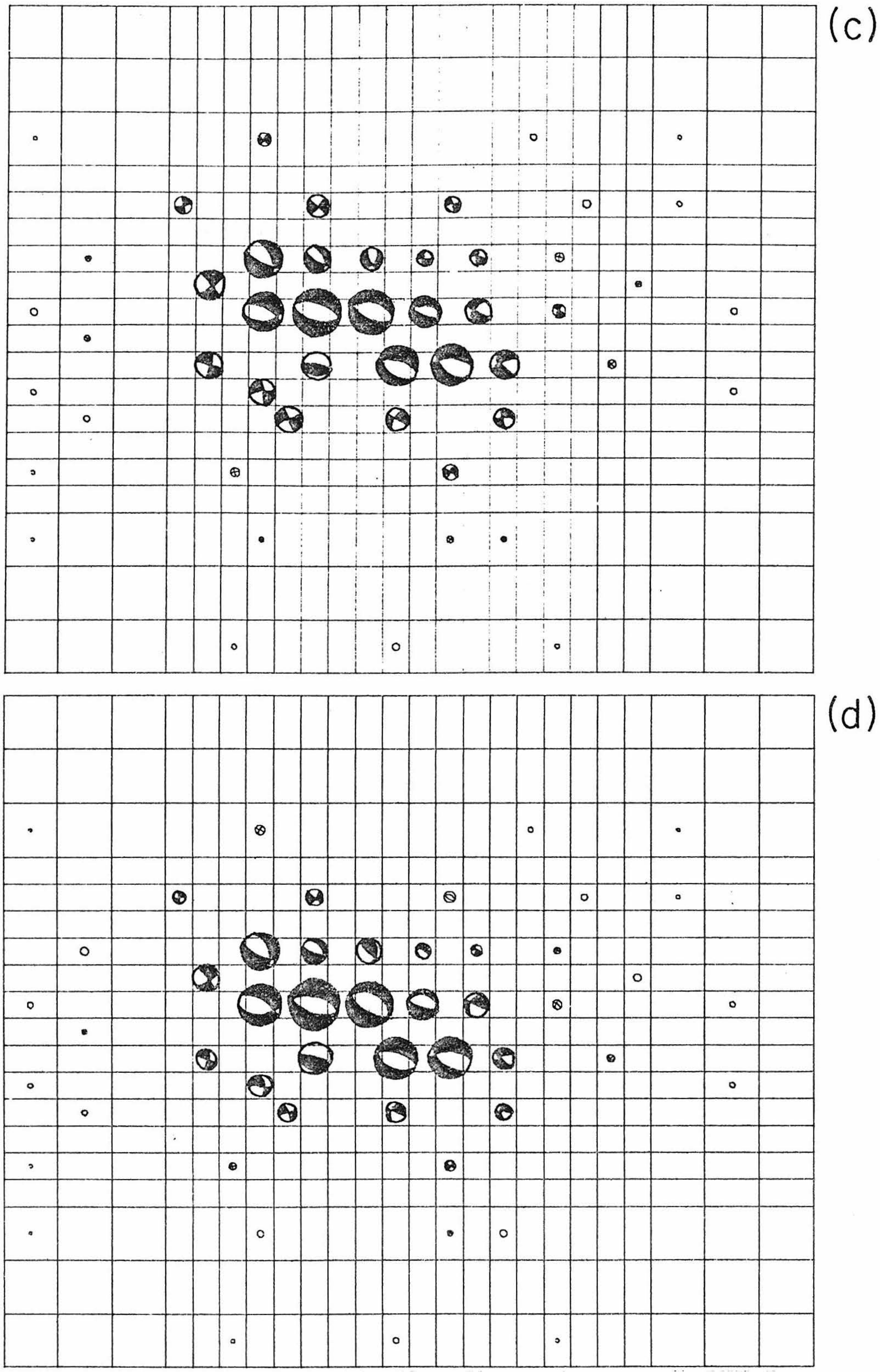

Figure 2.23 (c) d = 375m, $|\sigma_1 - \sigma_3|_{max}$ = 36.3 bars; (d) d = 525m, $|\sigma_1 - \sigma_3|_{max}$ = 43.6 bars.

model, than in the linear model, since the high moduli tend to resist deformation. From a physical viewpoint, the nonlinear model appears more satisfying, since the linear model behaves in the same manner both upon loading and unloading, contradicting both the experimental data and common sense.

In regard to the mechanism responsible for the subsidence earthquakes, the conclusions reached for the elastic simulation are still valid for the nonlinear model, except that the stress differences responsible for the events must be scaled upwards. It is instructive to compare the calculated stress differences, in both the linear and nonlinear models,with experimental results on the strength of shale (the type of material which failed in the subsidence earthquakes). The experimental work of Peterson et al. (1960) on the strength of hard Bearpaw shale indicated that for a normal stress of 55 bars (which is the stress at a depth of 550 m with an effective density of 1 gr/cm^3), the shear strength is approximately 32 bars. As the maximum shear, in any stress state, is equal to half the difference between the largest and least principal stresses, the stress differences in the nonlinear model are closer in value to the experimental results of Peterson et al. (1960), than those in the elastic model. Furthermore, the work of Peterson et al. (1960) showed that the strength of the shale could be reduced by as much as 50% when the tests were carried out with a total loading time on the order of a year, instead of the short loading times commonly used in laboratory tests. If this rate dependence is present in the shale formations in the Wilmington field, the subsidence earthquakes did not necessarily take place at the time of peak stress differences, but rather they took place after moderate stress differences were present for a sufficiently long time for the material to fail.

In conclusion, the present model, though capable of effecting some improvements over the elastic model of section 2.9 in a few details, is still not capable of reproducing the correct size of the subsidence pattern in the Wilmington field. The next section will investigate the influence of tectonic prestress on the subsidence pattern, and will show that it can explain the discrepancy.

2.16 An Elastic-Plastic Subsidence Model for 1958, II

This model examines the role of tectonic prestress in determining the size and shape of the subsidence pattern.

A number of past investigators have raised the question of why the subsidence in the Wilmington oil field was much larger than in other oil fields. Although part of the answer to the question may lie in the fact that the Wilmington oil field is situated in a populated area in the proximity of the coast, where vertical displacements are always noticeable, there are other fields which occupy similar locations which did not evidence the same degree of subsidence.

A second important observation is that most of the subsidence in the Wilmington field took place above fault blocks III and IV, in spite of the fact that the horizontal extent of the region of pressure reduction in the field was much larger than the area covered by these blocks. This fact is the reason why the numerical simulations discussed so far have failed to reproduce the observed size of the subsidence pattern, since the size of the subsidence bowl in these simulations has been on the same order as the horizontal extent of the pressure reduction zone.

A mechanism which may explain the above observations invokes a horizontal tensile stress component being added to the prestress in the region of the producing zones in fault blocks III and IV. The tensile stress, according to this explanation, was caused by the flexure of the crest of the structural anticline of the Wilmington field. As a result of the material being in extension, the region of fault block III and IV became weakened, thus causing a large subsidence there. The high density of normal faults in fault block III (e.g. Fig. 2.4) supports this hypothesis. This explanation has been proposed by past investigators (Mayuga, 1970; Allen, personal communication, 1977), but has not yet been put into quantitative terms.

Mathematically, when horizontal extension is added to the overburden stress system, the difference between the vertical stress and the horizontal stresses increases, and therefore the J_2' stress invariant increases as well. This puts the initial prestress closer to the F_1 yield surface in comparison with the stress state without the tension. The present model attempts to account for this situation by assigning a prestress localized on the corner of the yield surfaces (point A in Fig. 2.24) in elements which are situated beyond a depth of 0.6 Km (5th layer and on), and which satisfy the criteria, $8<I<13$ and $|14 - (J - 4) \cdot 7/16| < 1$ (for reference see Fig. 2.10). For the remaining elements, the assigned prestress lies below the two yield surfaces (point B, Fig. 2.24), to satisfy the relation $J_1=0.75x$. The

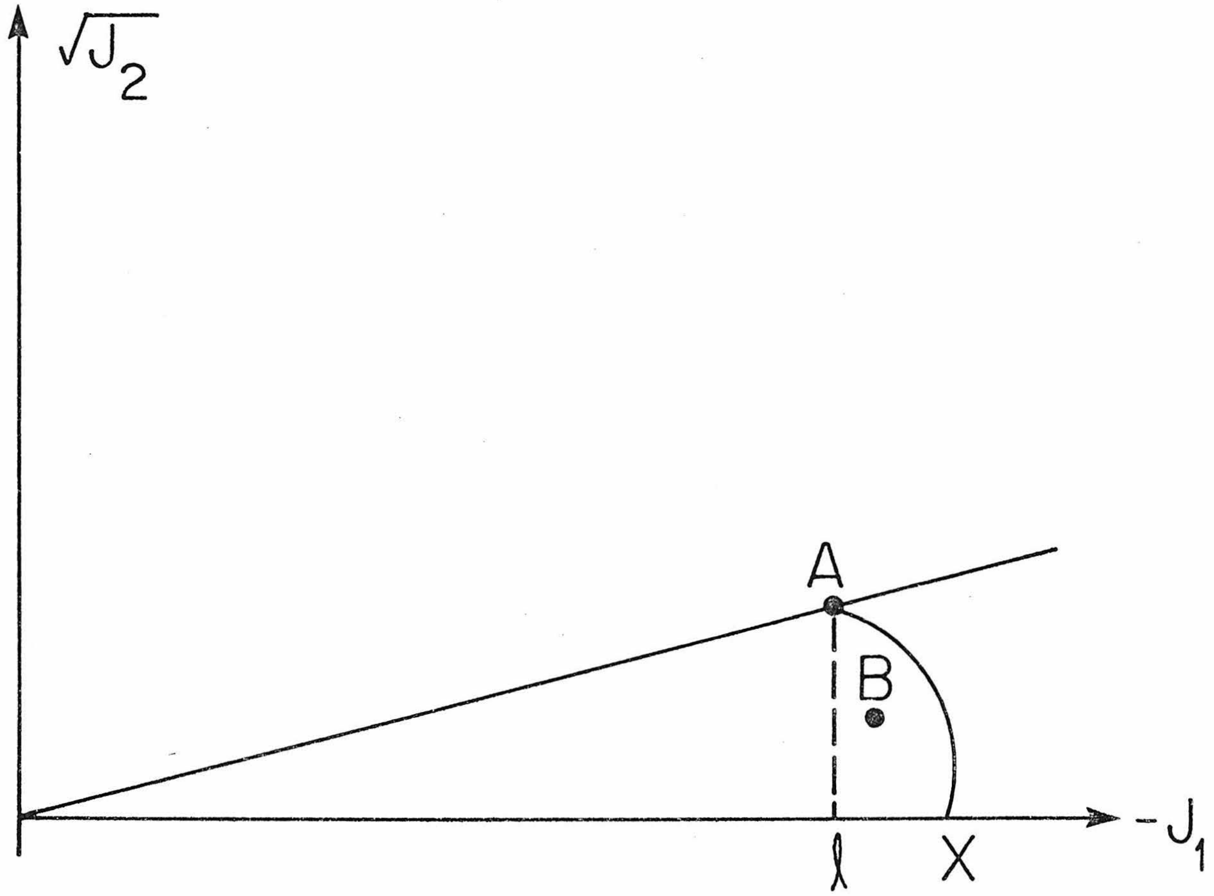

Figure 2.24 Initial stress points for subsidence calculation with horizontally varying prestress.

other parameters are identical to those of the model in the previous section.

The calculated vertical surface displacements for the present model are shown in Fig. 2.25. The maximum subsidence is about 6 meters, which is approximately 25% lower than the observation. However, considering the uncertainties in the material model, it is not felt that the discrepancy is fundamental. From a two dimensional simple model, it is found that the difference can be removed by increasing the W parameter by about 20%. As regards the size of the subsidence pattern, the agreement between observation and calculation is far better than in the previous model (the 4m observed contour (dashed line), which represents the contour of half the maximum subsidence, should be compared with the 3m calculated subsidence contour). Thus, this model proves the plausibility of explaining the small size of the observed subsidence bowl by the existence of an additional tensile stress components at the crest of the structural anticline of the field. This tensional stress also provides an explanation why the subsidence in the Wilmington field was larger than in other fields. Without the tension, all points in the field would have a prestress which plots below the yield surfaces. Thus a large portion of the pressure reduction would create elastic strains only, until the loading had progressed far enough for those points to reach the yield surfaces.

The remaining figures for this model do not contain major features which have not appeared in previous models. However, they show, as do the vertical displacements, a narrower deformation pattern

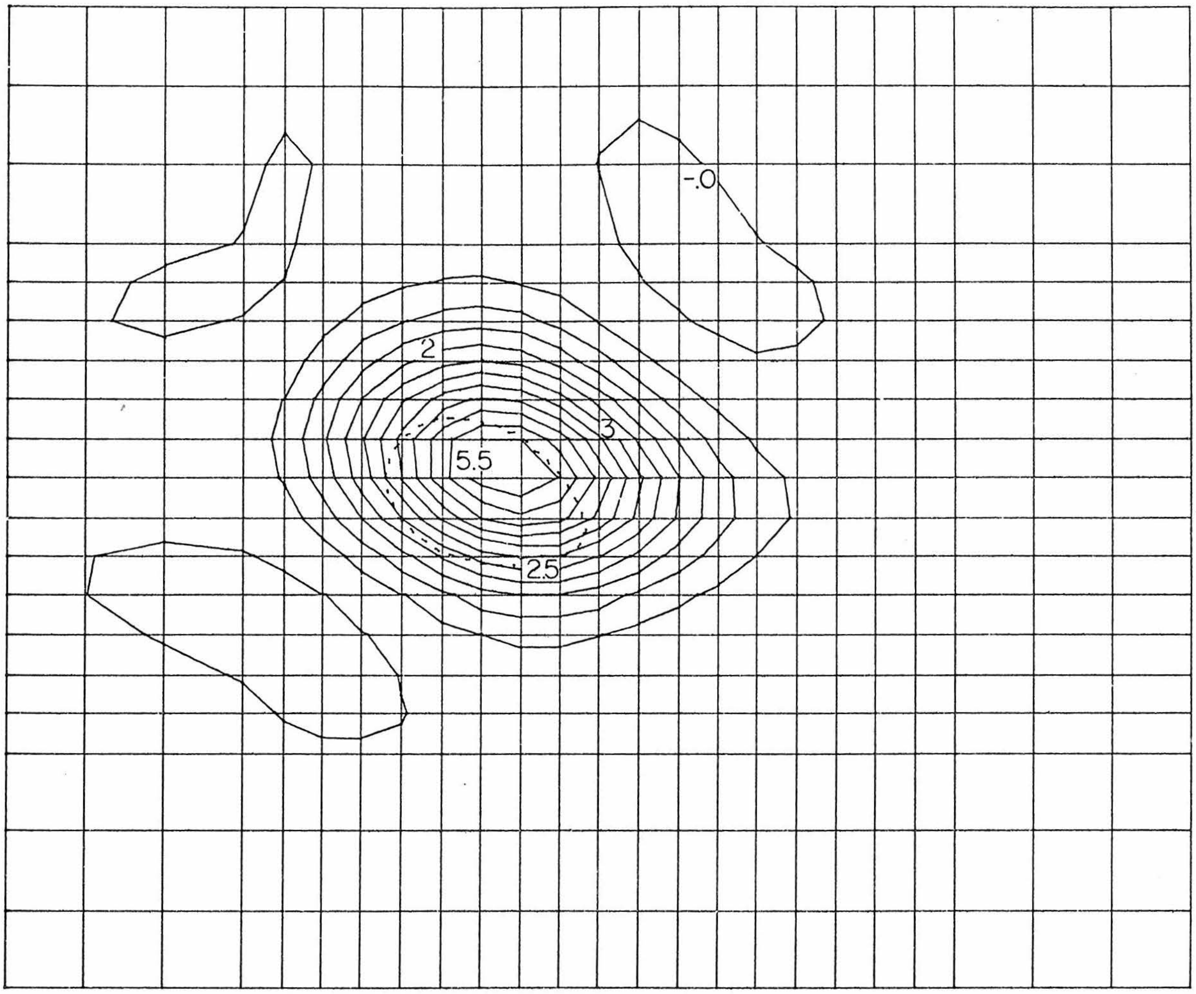

Figure 2.25 Calculated subsidence in meters. Elastic-plastic subsidence model with horizontally varying prestress.

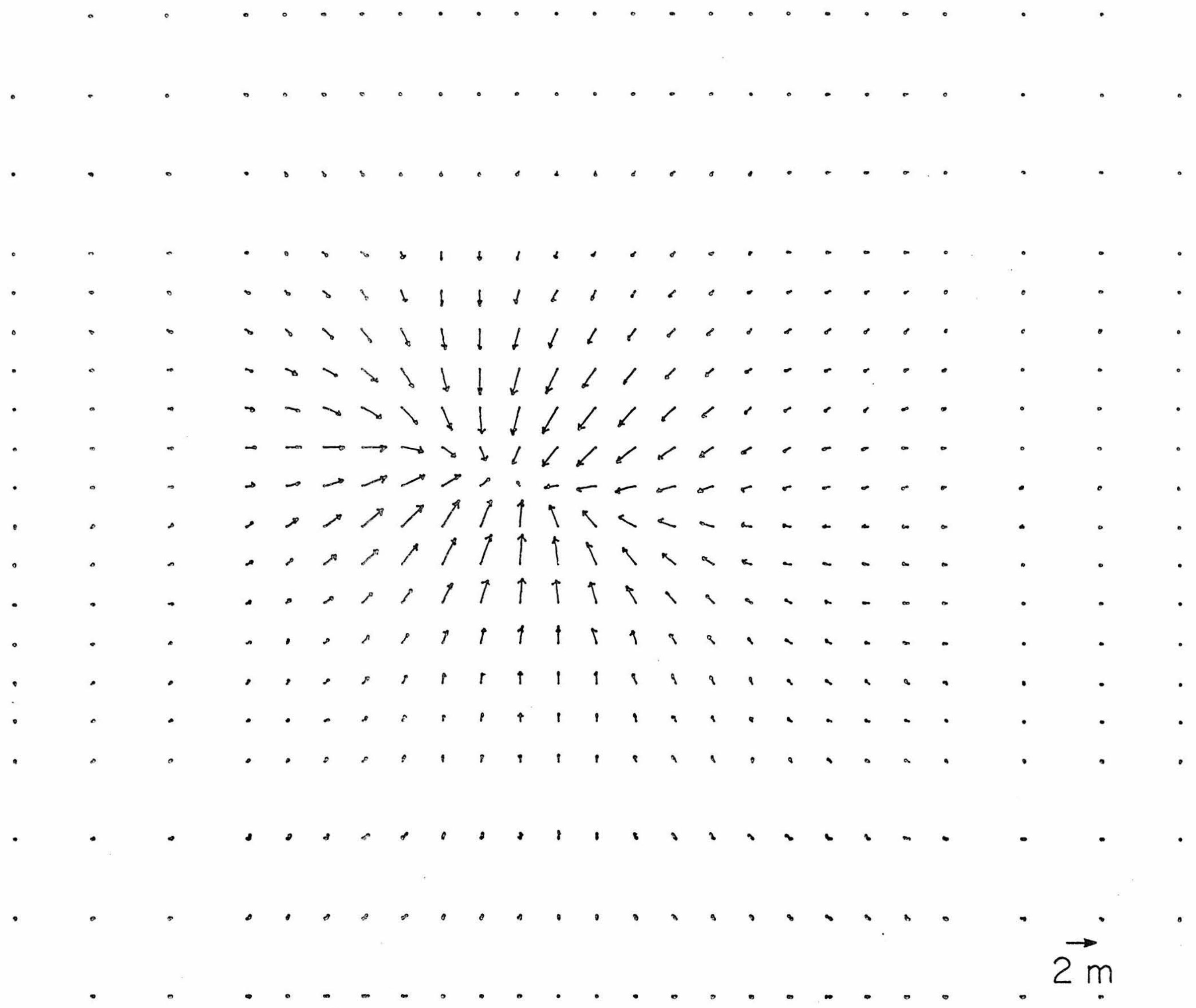

Figure 2.26 (a) Calculated horizontal displacements at the earth's surface. Elastic-plastic subsidence model with horizontally varying prestress.

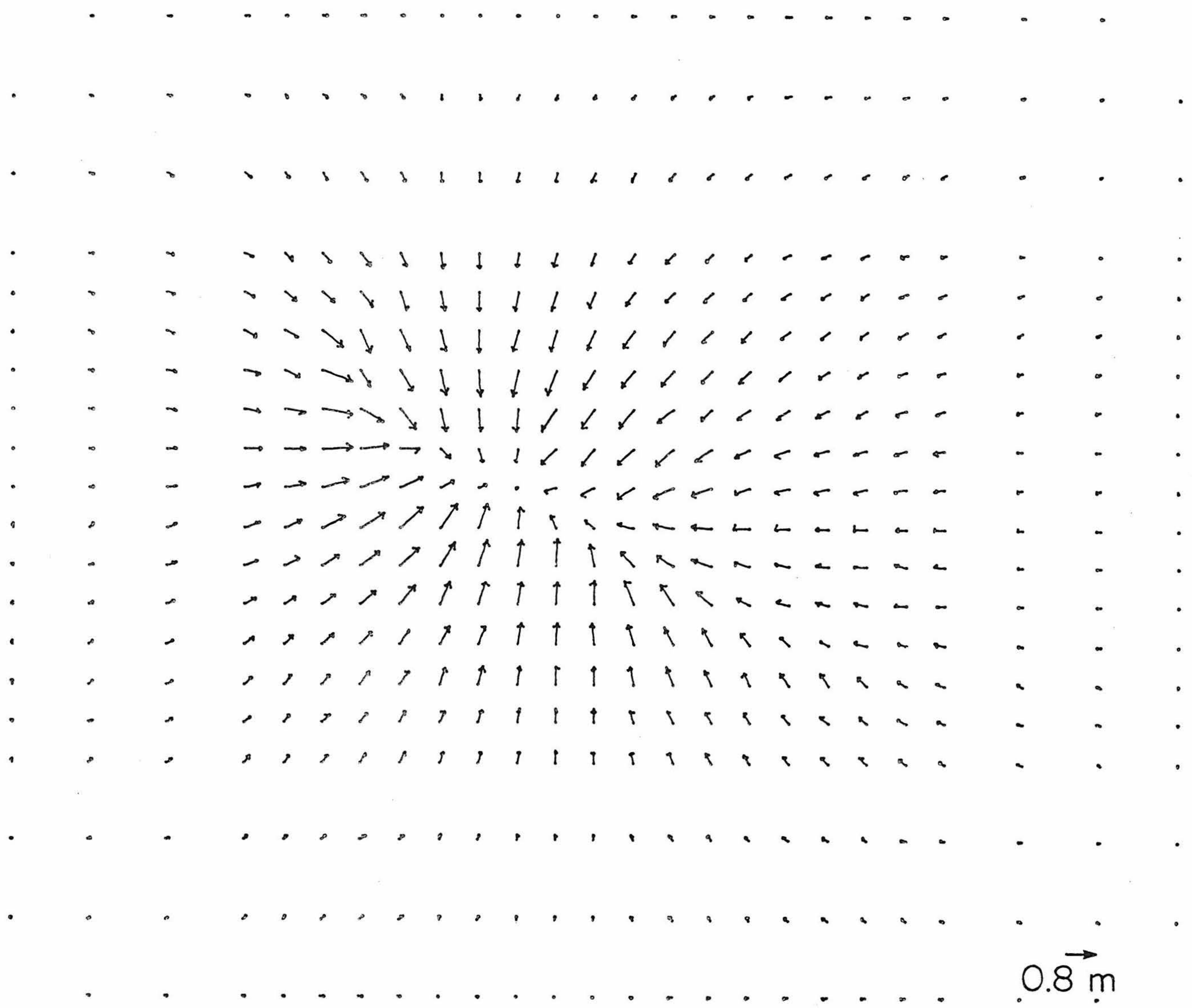

Figure 2.26 (b) Calculated horizontal displacements at a depth of 900 meters. Elastic plastic subsidence model with horizontally varying prestress.

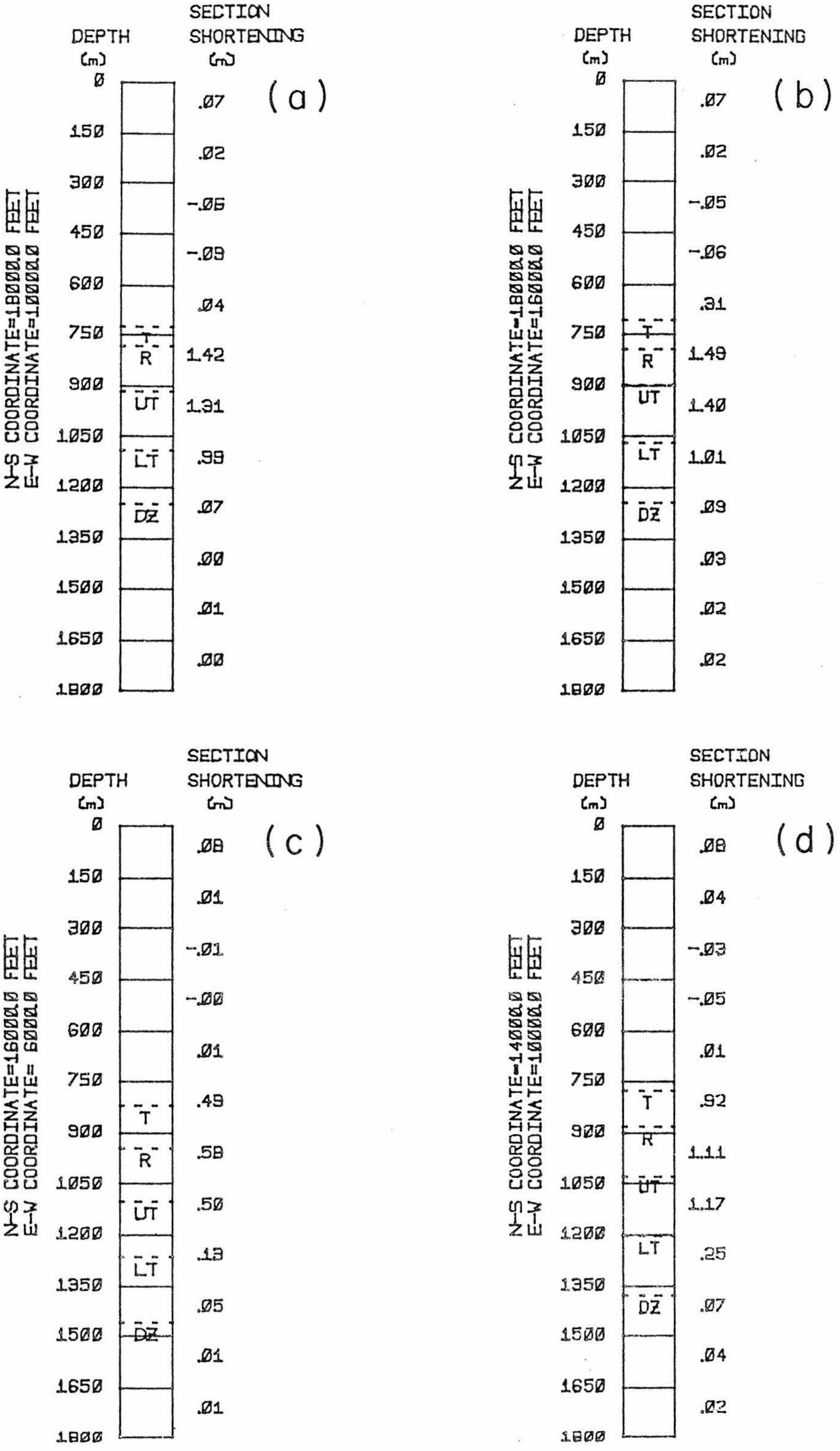

Figure 2.27 (a) - (d) Synthetic collar counts for elastic-plastic subsidence model with horizontally varying prestress.

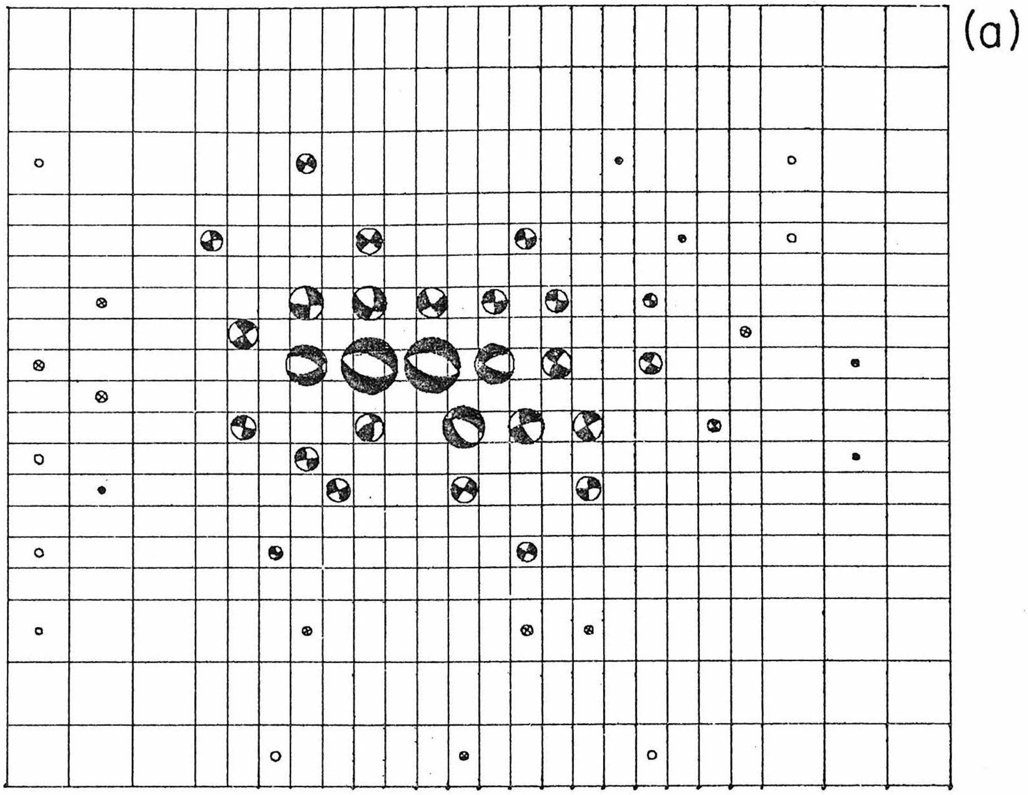

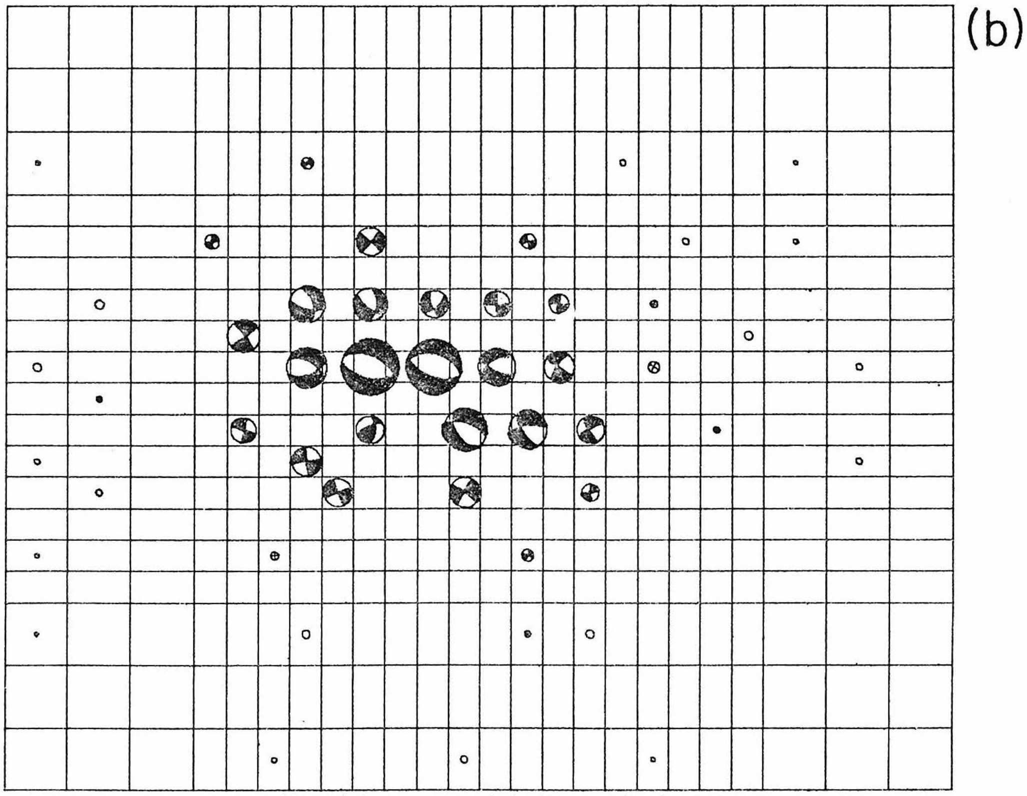

Figure 2.28 Stereographic projection of calculated stresses at different depths. Elastic plastic subsidence model with horizontally varying prestress. (a) d = 75 m, $|\sigma_1 - \sigma_3|_{max}$ = 18.3 bars; (b) d = 225 m, $|\sigma_1 - \sigma_3|_{max}$ = 35.2 bars.

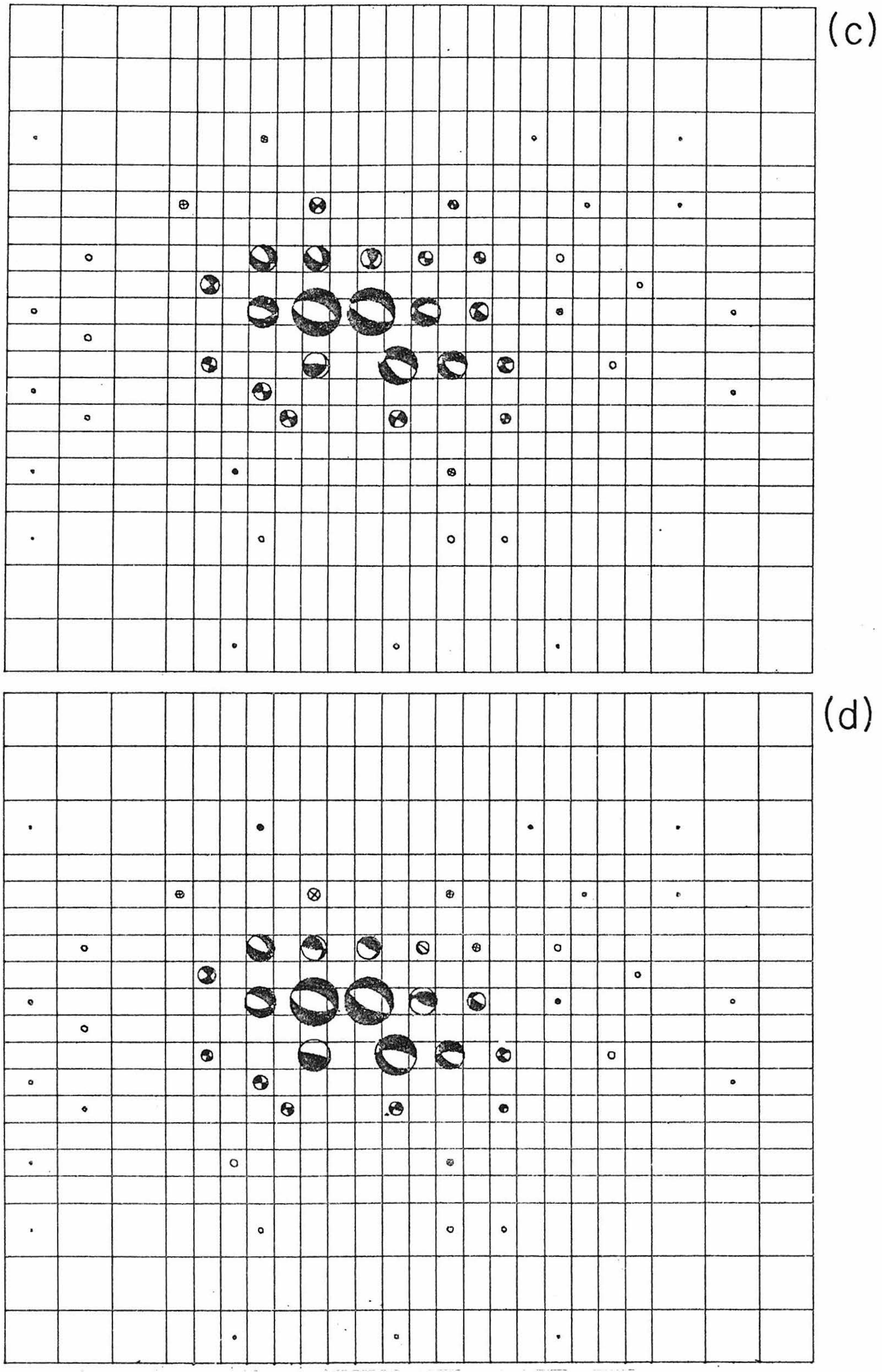

Figure 2.28 (c) d = 375 m, $|\sigma_1 - \sigma_3|_{max}$ = 47.0 bars; (d) d = 525 m, $|\sigma_1 - \sigma_3|_{max}$ = 51.7 bars.

than their previous counterparts. For brevity, we chose not to repeat the previous discussion, but to merely present the figures for the sake of completeness.

2.17 Conclusion

The Wilmington subsidence has presented a unique opportunity to study a tectonic problem with relatively good data. The numerical simulations of the subsidence have provided quantitative explanations for the surface displacement observations, as well as for the collar count survey data. They have also shed some light on the process which was responsible for the subsidence earthquakes. The success of this study, which also serves as a reduced scale test case for larger tectonic problems, gives confidence in the ability of the numerical techniques used to simulate other tectonic processes, whenever good data are available. It can also be used as a predictive tool in areas evidencing subsidence problems for which a fluid pressure maintenance program exists.

References

Allen, D. R., 1968. Physical properties of reservoir properties caused by subsidence and repressuring operations; J. Petrol. Technol. 20, pp. 23-29.

Allen, D. R., and Mayuga, M. N., 1969. The mechanics of compaction and rebound, Wilmington oil field, Long Beach, California, U.S.A., Assoc. Intern. d'Hydrologie Scientifique.

Allen, D. R., 1973. Subsidence rebound and surface strain associated with oil producing operations, Long Beach, California; Assoc. Eng. Geologists, special publications.

Archambeau, C. B., 1975; unpublished report; California Institute of Technology.

Biot, A. A., 1941. General theory of three dimensional consolidation; J. Appl. Phys., Vol. 12, pp. 155-165.

Biot, M. A., 1956. Theory of deformation of a porous visco-elastic anisotropic solid, J. Appl. Phys., vol. 27, pp. 459-467.

Biot, M. A., and Willis, D. G., 1957. The elastic coefficients of the theory of consolidation, J. Appl. Mech., 24, pp. 594-601.

Biot, M. A., 1962. Mechanics of deformation and accoustic propagation in porous media; J. Appl. Phys., 33, pp. 1482-1498.

Biot, M. A., 1972. Theory of finite deformations of porous solids; Indiana University Mathematics Journal, Vol. 21. No. 7.

Brace, W. F., and Martin, R. J. III, 1968. A test of effective stress laws for crystaline rocks of low porosity, Int. J. of Rock Mechanics, Miner. Sci. 5, p. 415.

Carrillo, N., 1950. Report on the subsidence in the Long Beach San Pedro area, Stanford Research Institute, p. 67.

DiMaggio, F., and Sandler, I., 1971. Material model for granular soils, J. of Eng. Mech. Div., ASCE, Vol. 97, pp. 935-950.

Garg, S. K., and Nur, A., 1973. Effective stress laws for fluid saturated porous rocks; JGR, 78, pp. 5911-5921.

Geertsma, J., and Ksepel, P., 1973. A basic theory of subsidence due to reservoir compaction, the homogeneous case; in "The analysis of surface subsidence resulting from gas production in the Gronigen area, the Nederland, pp. 43-62.

Gilluly, J., and Grant, U. S. 4th, 1949. Subsidence in the Long Beach harbor area, Geol. Soc. of Amer., Vol. 60, pp. 461-530.

Grant, U. S. 4th, 1954. Subsidence of the Wilmington oil field, California; Div. Mines and Geology Bull., 170, pp. 19-24.

Harris, F. M., and Harlow, E. W., 1947. Subsidence in the Long Beach Terminal Island area, California; ASCE Proc., V. 73, No. 8, pp. 1197-1218.

Jungels, P., 1973. Ph.D. Thesis, California Institute of Technology.

Kovach, R. L., 1974. Source mechanisms for Wilmington oil field, California subsidence earthquakes; BSSA, Vol. 64, pp. 699-711.

Mayuga, M. N., 1965. How subsidence affects the city of Long Beach; Landslides and Subsidence, Geologic hazards conference, The Resources Agency, State of California.

Mayuga, M. N., 1970. Geology and development of California giant; the Wilmington oil field; in Geology of Giant Petroleum Fields, Am. Assoc. Petrol. Geol. Mem., 14, pp. 158-184.

McCann, G. D., and Wilts, C. Y., 1951. A mathematical analysis of the subsidence in the Long Beach-San Pedro area; California Institute of Technology, Pasadena.

Nur, A., and Byerlee, J. D., 1971. An exact effective stress law for elastic deformation of rocks and fluids; JGR, Vol. 76, pp. 6414-6419.

Peterson, R., Jasper, J. L., Rivard, P. J., Iverson, N. L., 1960. Limitations of laboratory shear strength in evaluating stability of highly plastic clays; Research conference on shear strength of cohesive soils, ASCE soil Mechanics and Foundations Division.

Poland, J. F., and Davis, G. H., 1969. Land subsidence due to withdrawal of fluids; in Reviews in Engineering Geology, Vol. I, USGS, Varnes, D., and Kiersch, G., Editors.

Richter, C. F., 1958. Elementary Seismology; W. H. Freeman and Company.

Rieke, H. H. III, and Chilingarian, G. V., 1974. Compaction of argillaceous sediments, Elsevier Scientific Publishing Company.

Sandler, I., Di Maggio, F., and Baladi, G. Y., 1976. Generalized cap model for geological materials, J. Geotech. Engin. Div., ASCE, Vol 102, No GT7, pp..683-700.

Vesiĉ, A. S., and Clough, G. W., 1968. Behaviour of granular soils under high stresses, ASCE, Soil Mech. and Foundations Div., pp. 661-687.

Chapter 3: FLEXURE OF THE LITHOSPHERE IN THE VICINITY OF ISLAND CHAINS AND SUBDUCTION ZONES

3.1 Introduction

The mechanical model of plate tectonics, where strong lithospheric plates float on a weak layer asthenosphere, is supported by evidence from seismology (Gutenberg, 1960; Anderson, 1962; Kanamori and Press, 1970), from gravitational observations (e.g. Gunn,1943; Vening Meinesz, 1941) and from petrological considerations (Green, 1972). The relaxation time on the order of 2 X 10^3 years for vertical movements in shield areas unloaded by late Quaternary ice sheets (e.g. O'Connell, 1971) suggests that the asthenosphere can be modelled as an inviscid fluid for loading times exceeding 10^6 years. The lithosphere is often modeled as an elastic sheet (Gunn, 1943; Walcott; 1970a; Hanks, 1971; Watts and Cochran, 1974; Watts and Talwani, 1974), or as a viscoelastic sheet (Walcott, 1970b) to explain the departure from isostasy near seamounts and trenches as well as to explain observed surface morphology in the vicinity of the structures.

Such a mechanical model, while capable of obtaining an agreement between observed and computed gravity anomalies and between observed and computed bathymetry near some trenches, fits only in a general way moho displacements as well as the surface morphology of mid oceanic seamounts and islands, such as those of the Hawaiian archipelago. Some other problems are encountered in the employment of such an elastic or viscoelastic plate model. These are:

(1) Lateral thrust was not included in the computations for gravity anomalies or for bathymetry in the interior of the Pacific Plate (e.g. Watts and Cochran, 1974; Walcott, 1970a). Lateral thrust was included in the plate calculations near the trenches by Hanks (1974) but was considered to be not essential by Parsons and Molnar (1976). However, lateral thrust has a strong influence on the wavelengths of flexure and cannot be ignored in most realistic situations (e.g. Le Pichon et al., 1973).

(2) The extreme fibre stress associated with the elastic or visco-elastic plate bending models is on the order of several kilobars in fitting the trench or the seamount chain data (e.g. Walcott, 1976). The strength of possible mantle rocks near the base of the lithosphere (at about 60 Km depth), on the other hand, is on the order of 50 bars, as inferred from laboratory rock deformation experiments on a geologic time scale (e.g. Carter, 1976). The high stresses deduced from the elastic or visco-elastic plate models therefore cannot be sustained by the inferred strength of the rocks in the lower lithosphere.

(3) The flexure rigidity obtained from an elastic or viscoelastic plate model in fitting the trench or seamount chain data implies too thin a plate thickness for the lithosphere, even a reasonable difference between seismic and static deformation moduli is allowed for. For example, Watts, Talwani, and Cochran (1976), in summarizing their earlier work, gave flexure rigidity of 3×10^{29} dyne-cm for the Pacific plate near the trenches, and 5×10^{29} dyne-cm (for a continuous sheet), and 2×10^{30} dyne-cm (for a broken half sheet) for the interior of the Pacific plate. Walcott (1970a) obtained 3.6×10^{30} dyne-cm for the

interior of the Pacific plate (broken half sheet). If we adopt for the relaxed elastic moduli a 10% reduction from their seismic values (Liu et al., 1976), the above rigidity values would imply a plate thickness of 13 Km, 15 Km, 24 Km, and 29 Km respectively. These values are too low compared with plate thickness values obtained from seismology (e.g. Kanamori and Press, 1970). Indeed, Watts, Talwani and Cochran (1976) emphasized that the flexure rigidity used in the elastic plate calculations should be regarded as "effective flexure rigidity" and not as the actual flexure rigidity.

The above discussions suggest that the elastic or viscoelastic model, while capable as a first approximation to explain certain features of the plate deformation near some trenches and seamount chains, leads to some difficulties when compared with the seismological and rock deformation data.

This study attempts to improve on the elastic or viscoelastic plate models by presenting a strain rate dependent elastic-perfectly plastic plate bending model. The rheological model for the lithosphere is deduced from laboratory results on the deformation of Dunite at temperatures and pressures which are pertinent to the upper mantle. From this material model, the flexural response of the lithosphere as whole is derived, and put in a form of moment-curvature relations. These in turn are combined with a Finite Element code which is designed for solving Von-Karman's plate equation with nonlinear moment curvature relations. The complete formulation is finally applied to the fitting of bathymetry and gravity profiles in the vicinity of the Hawaiian island chain.

3.2 Equilibrium Equations of the Plate Theory Approximation

The theory of large deflection of plates, due to v̌on Karman, is an extension of the theory of small deflection of plates which also considers the dominant finite strain effects (e.g. Fung, 1965). Implicit in the theory are the following assumptions;

a) The plate thickness is much smaller than the typical plate dimension.

b) The magnitude of the deflection w is of the same order as the thickness of the plate, but small compared to the typical plate dimension.

c) The slope is everywhere small, i.e. $\left|\frac{\partial w}{\partial x}\right| << 1$ and $\left|\frac{\partial w}{\partial y}\right| << 1$.

d) The tangential displacements u, v are infinitesimal. In the strain displacement relation, only those terms which depend on $\frac{\partial w}{\partial x}$ and $\frac{\partial w}{\partial y}$ are to be retained.

e) Kirchhoff's hypotheses holds, e.g. tractions on surfaces parallel to the middle surface of the plate are negligible, while strains vary linearly within the plate thickness.

v̌on Karman's theory uses the Lagrangian description in which displacements, strains, and stresses refer to the underformed configuration. In the following, x, y, z will denote a coordinate system with the z axis extending vertically downward, and with the x and y axis extending horizontally. w will denote the vertical deflection of the neutral surface and u and v will denote the horizontal displacements. The z coordinate of the top of the plate will be denoted by Z_t, and of the bottom of the plate by Z_b.

After combining assumptions (a) - (e) listed above with the continuum mechanics equations of force balance, the plate theory equilibrium equations are obtained (e.g. Fung, 1965);

(3.1) $$\frac{\partial^2 M_x}{\partial x^2} + 2\,\frac{\partial^2 M_{xy}}{\partial x \partial y} + \frac{\partial^2 M_y}{\partial y^2} = -q - \frac{\partial m_x}{\partial x} - \frac{\partial m_y}{\partial y} - N_x \frac{\partial^2 w}{\partial x^2} -$$

$$- 2 N_{xy} \frac{\partial^2 w}{\partial x \partial y} - N_y \frac{\partial^2 w}{\partial y^2} + f_x \frac{\partial w}{\partial x} + f_y \frac{\partial w}{\partial y} ,$$

where,

(3.2) $$M_x = \int_{z_t}^{z_b} S_{xx}\, \zeta\, d\zeta ,$$

(3.3) $$M_{xy} = \int_{z_t}^{z_b} S_{xy}\, \zeta\, d\zeta ,$$

(3.4) $$M_y = \int_{z_t}^{z_b} S_{yy}\, \zeta\, d\zeta ,$$

(3.5) $$N_x = \int_{z_t}^{z_b} S_{xx}\, d\zeta ,$$

(3.6) $$N_{xy} = \int_{z_t}^{z_b} S_{xy}\, d\zeta ,$$

(3.7) $$N_y = \int_{z_t}^{z_b} S_{yy}\, d\zeta ,$$

(3.8) $$q = \left(S_{zz} + S_{zx} \frac{\partial w}{\partial x} + S_{zy} \frac{\partial w}{\partial y} \right|_{z_t}^{z_b} + \int_{z_t}^{z_b} Z d\zeta ,$$

(3.9) $$m_x = \frac{(z_b - z_t)}{2} \left(S_{zx}(z_b) - S_{zy}(z_t) \right) + \int_{z_t}^{z_b} \zeta X \, d\zeta ,$$

(3.10) $$m_y = \frac{(z_b - Z_t)}{2}\left(S_{zy}(z_b) - S_{zy}(z_t)\right) + \int_{z_t}^{z_b} \zeta Y \, d\zeta ,$$

(3.11) $$f_x = S_{zx}(z_b) - S_{zx}(z_t) + \int_{z_t}^{z_b} X \, d\zeta ,$$

(3.12) $$f_y = S_{zy}(z_b) - S_{zy}(z_t) + \int_{z_t}^{z_b} Y d\zeta .$$

X, Y, Z respectively denote the body forces in the x, y, z directions, S_{ij} denotes the Kirchhoff stress tensor which, by assumptions (a) to (e) above, is equal, to first order, to the Lagrangian stress tensor which is measured in the deformed configuration of the plate. For many tectonic problems the horizontal body forces are zero, and the plate is overlain by ocean water and underlain by the asthenosphere which is considered as an inviscid fluid. In such problems, the shear stresses S_{xz} and S_{yz} are approximately zero. When in addition, flexure occurs only parallel to one vertical plane (as in the case of the Hawaiian emperor seamont chain problem discussed in section 3.7), equation (3.1) to (3.12) simplify considerably to read,

(3.13) $$\frac{d^2 M_x}{dx^2} = -q - N_x \frac{d^2 w}{dx^2} ,$$

(3.14) $$M_x = \int_{z_t}^{z_b} S_{xx} \, \zeta d\zeta ,$$

$$N_x = \int_{z_t}^{z_b} S_{xx}\, dz \;, \tag{3.15}$$

$$\bar{q} = S_{zz}(z_b) - S_{zz}(z_t) + \int_{z_t}^{z_b} Z d\zeta \;. \tag{3.16}$$

For a complete posing of plate bending problems, equations (3.1) to (3.12), or (3.13) to (3.16) must be supplemented by appropriate boundary conditions at the ends of the plate (see Appendix B) and a rheological prescription which relates moments to curvature. The latter can be constructed readily once the full continuum theory stress-strain relation is known. For the linear elastic plane strain case the moment curvature relation writes,

$$M_x = -D \frac{\partial^2 w}{\partial x^2} \quad , \tag{3.17}$$

where D is the flexural rigidity (Fung, 1965). By substituting equation (3.17) into the plate equation (3.13), a fourth order ordinary differential equation is obtained, the solutions of which have been used in the elastic plate flexure studies by previous investigators (Walcott, 1970a; Hanks, 1971; Watts and Cochran, 1974; Watts and Talwani, 1974). The main object of this study has been to replace (3.17) by a more realistic moment curvature relation, based on rock mechanics data, to produce plate models which are capable of explaining and matching geodetic, gravimetric, and seismic data.

The term N_x in equations (3.13) and (3.15), represents the stress resultant across a section of the plate. In tectonic problems, prior to the existence of the flexure causing loads, the variable is equal to the integral of the horizontal prestress over the lithosphere thickness. After application of the loads, a horizontal fibre stress is added to the prestress but, as will be demonstrated in the following sections, by reasons of maintaining mechanical equilibrium, the value of N_x remains unchanged after the activation of the flexural loads.

This study uses the Finite Element method for solving the plate equations. In plane strain, this entails the construction of a one dimensional grid (see Figure B.1 in Appendix B), in which each node possesses two degrees of freedom of the displacement w and the slope $\frac{dw}{dx}$. The input consists of (a) nodal boundary conditions on the ends of the grid which may include a specification of the deflection or of the moment, and a specification of the slope or of the shear traction; (b) prestress values, (c) values for the variable q in equation (3.16), which in tectonic flexural problems usually consists of bouyancy forces from the asthenosphere, and the ocean water load. Details of the derivation of the Finite Element method are given in Appendix B.

3.3 An Elastic Plastic Model for Lithospheric Response Based on Experimental Data

Rock deformation experiments under lithospheric temperature and confining pressure have been carried out extensively (e.g. Carter, 1976, for a review). The loading stress strain curve for Dun-Mountain dunite at 800° C, at a confining pressure of 5 Kb and a strain rate of 5×10^{-4} s^{-1} is illustrated in Figure 3.1 (after Griggs, Turner and Heard, 1960). The curve is typical of dunite deformation at temperatures greater than

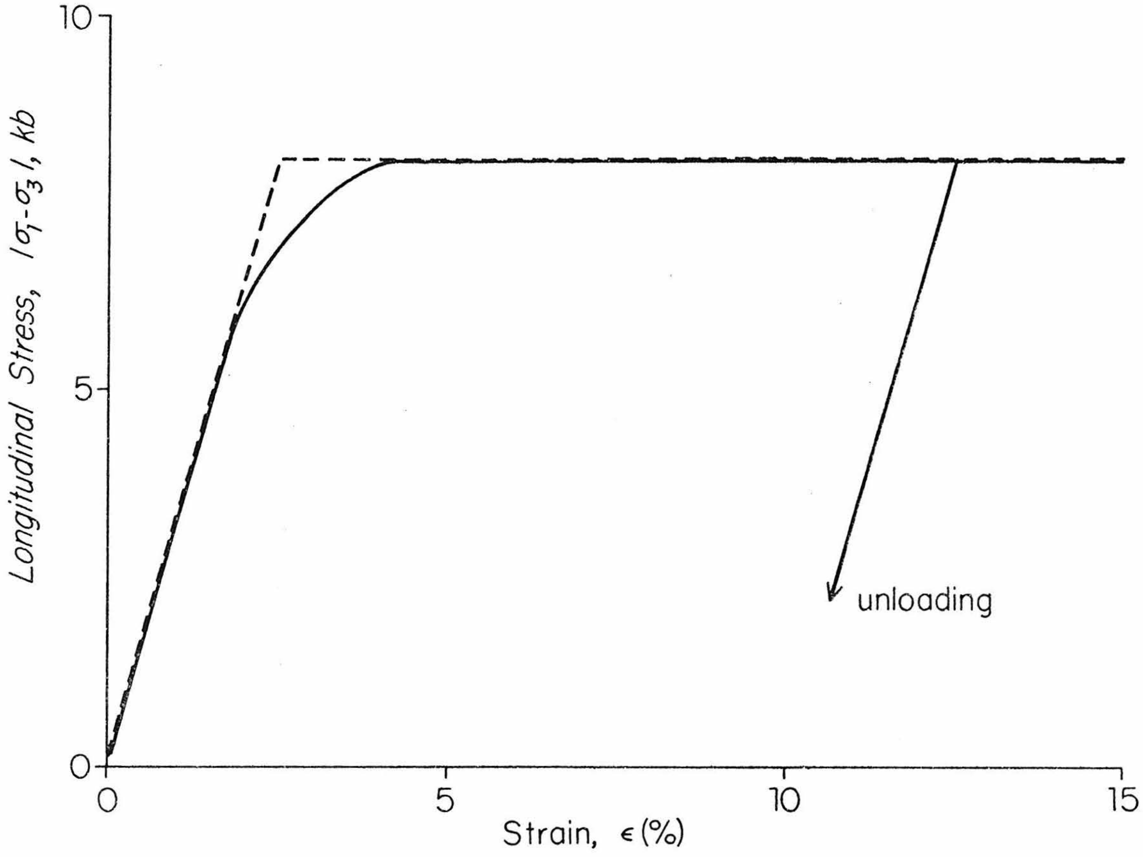

Figure 3.1 Stress-strain curve of Dun-Mountain dunite at 5 Kb confining pressure, T = 800°C, $\dot{e} \approx 5 \cdot 10^{-4}$ s^{-1} (after Griggs et al., 1960).

300° C as well as for the behavior of Basalts and Pyroxenites (Griggs et al., 1960). At low temperatures, dunite exhibits brittle behavior. Figure 3.1 represents, therefore, a typical stress-strain curve for lithosphere type materials at depths beyond the first few kilometers in the crust (Carter, 1976).

The stress-strain curve of Dunite is both temperature dependent and strain rate dependent. For fixed temperature and strain rate the stress vs strain curve initially has a sharp slope (Figure 3.1). Afterwards the slope approaches a zero value. To a good approximation the curve can be replaced by the two dashed straight line segments shown in the figure. The material can thus be modeled as elastic-perfectly plastic with the first segment in Figure 3.1 representing an elastic (strain rate dependent) loading curve, and the segment with zero slope representing yielding at the yield stress value. The strain rate dependence of the elastic parameters is generally known as visco-elasticity. Unfortunately, reliable values for the elastic parameters at low strain rates, are presently not available. However, as demonstrated by Liu et al. (1976), for a constant Q of 220, the material moduli decrease at lower strain rates by 2% per three decades of strain rate. Consequently, the elastic parameters in this study are chosen at 90% of their seismically determined values. As for the plastic part of the stress-strain curve, the yield function was taken to be a Tresca yield condition of the form,

$$f(S_1, S_2, S_3) = |S_1 - S_3| - K , \tag{3.18}$$

where S_1 and S_3 denote the largest and least principal stresses and K is the yield value. Whether or not this yield condition truly describes yielding in Dunite for all possible load paths cannot be determined by triaxial tests alone. However, the Tresca yield condition has been used extensively to describe yielding in certain metals (e.g. Martin, 1974), and since it appears that for the strain rates of concern in this study, yielding in rocks, as in metals, is controlled by dislocation motion, equation (3.18) seems to be a reasonable approximation.

The dependence of the yield stress on the strain rate and temperature fits well an activation energy type formula of the form (Carter, 1976),

$$(3.19) \qquad \sigma_Y = \left(\frac{\dot{e}}{A} \right)^{1/n} \exp(Q/RT \cdot 10^{-3}\, n) \ ,$$

where $\dot{e}$ is the strain rate in s^{-1}, A is a material constant, n is a positive numerical constant, σ_Y is the yield stress in kb, Q is an activation energy in kcal/mole, R is the gas constant and T is the temperature in K^o. The yield stress in (3.19) does not depend on the confining pressure. The constant n usually has values between two and nine for rocks, with a value of about three for Dunite (Carter, 1976). The application of equation (3.19) to the modeling of tectonic processes implies the assumption that laboratory results obtained at strain rates on the order of 10^{-6} to 10^{-7} or faster, can be extrapolated to the slower geologic rates.

3.4 State of Stress in the Lithosphere Prior to Flexing

In plate bending models which contain a nonlinear stress-strain prescription for the material response, the state of stress in the lithosphere, prior to the existence of the flexure causing forces, has a significant influence on the bending properties of the plate. Unfortunately, the value of the prestress in the lithosphere is presently known only crudely, and as in similar instances in this thesis, the recourse has been to a number of assumptions concerning its magnitude.

Consider the portion of the lithosphere shown in Figure 3.2 which contains a crust with density ρ_c, a portion of the upper mantle with density ρ_m, and which is overlain by ocean water with density ρ_w. The vertical overburden stress component at a depth z below the ocean surface is given by,

$$S_1^{(P)} = \begin{cases} -\rho_w g Z_t - \rho_c g(z - Z_t), & \text{for } Z_t \le z \le Z_2 \\ -\rho_w g Z_t - \rho_c g(Z_2 - Z_t) - \rho_m g(z - Z_2), & \text{for } Z_2 \le z \le Z_b \,. \end{cases} \tag{3.20a}$$

When the vertical stress consists only of the overburden component, the horizontal stress is given by,

$$S_3^{(P)} = S_{30} + \beta(z)\, S_1^{(P)} \,, \tag{3.20b}$$

where $\beta(z)$ is the confinement factor, and S_{30} is a stress component from tectonic origins. It will be assumed in the following that the value of the S_2 component lies between the values of S_1 and S_3, and

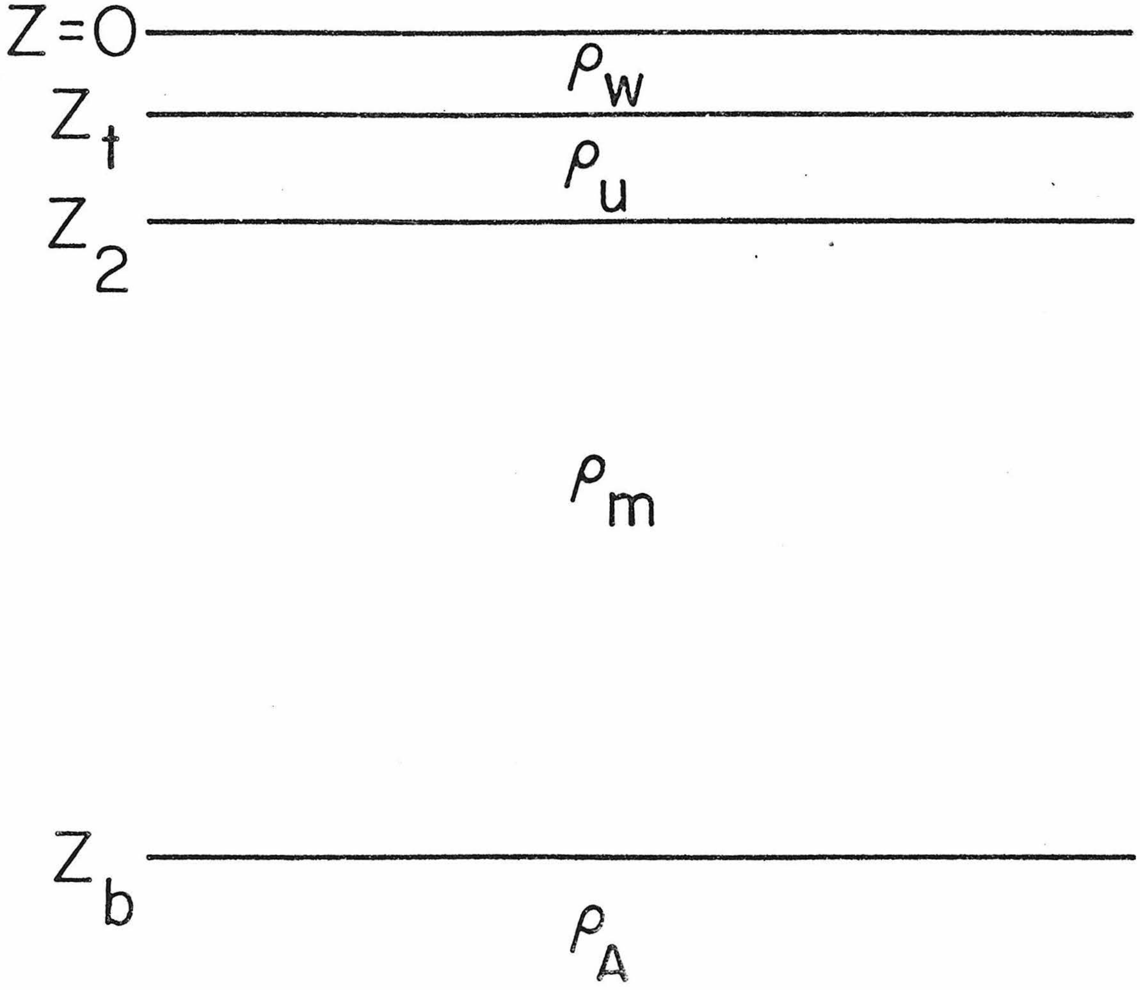

Figure 3.2 Sketch of an undeformed portion of lithosphere.

that the subsequent plate bending will take place in the xz plane.

The confinement factor $\beta(z)$ depends on the manner in which the material in the lithosphere is emplaced, and the amount of stress relaxation which the plate has undergone since the emplacement. In the parts of the lithosphere which are removed from plate margins and which are not undergoing significant deformations, by symmetry, the material must be in a state which resembles rigid horizontal confinement. As dislocation motion does not involve volume changes, and in the absence of horizontal strains, in the rigid confinement case there can be no contribution from dislocations to the vertical strain component. As no strain components from dislocations can exist, it appears that the stresses in a material which is rigidly confined, either cannot relax in time towards a hydrostatic stress state, or at most can relax at a much lower rate than when the material is in a state where flow can take place freely.

For lack of more accurate data, therefore, it will be assumed in the following that the β factor is constant at all depths, and that its value lies between one third (as in uniaxial compression of a Poisson-solid) to unity (total relaxation).

3.5 Construction of A Moment Curvature Relation for the Lithosphere

According to the fifth postulate of von Karman's plate theory (Section 3.2), tractions on planes parallel to the mid-surface of the plate are negligible, and strains vary linearly within the plate thickness. Mathematically this statement writes, (e.g. Fung, 1965),

$$e_3^f = -K(z - Z_3) , \tag{3.21a}$$

where e_3^f is the horizontal fibre strain, z is the depth to the observation point, Z_3 is the depth to the neutral surface, and the curvature, K, is given by,

$$K = \frac{d^2w}{dx^2} . \tag{3.21b}$$

The plate moment-curvature relation is constructed under the assumption that the flexure process takes place at a constant strain rate. Accordingly, the flexural strain rate is given by,

$$\dot{e}_3^f = - \frac{K(z - Z_3)}{t} , \tag{3.22}$$

where t is the loading time of the plate. Although, the accuracy of the above assumption is questionable, it will be used only in the yield stress vs strain rate relation, a relation very insensitive to inaccuracies in the strain rate.

After the plate becomes flexed, certain portions of it will undergo plastic deformation whenever the condition,

$$\left|S_1 - S_3\right| \geq \left(\frac{\dot{e}_3^{P\ell}}{A}\right)^{1/n} \exp(Q/R \cdot T(z) \cdot 10^{-3} n) , \tag{3.23}$$

is met. $\dot{e}_3^{P\ell}$ denotes the horizontal plastic strain rate. Equation (3.23) is written as an inequality rather than as an equality such as

(3.19), as in certain confinement conditions in which material flow is restricted, the value of $|S_1 - S_3|$ can be higher than the yield value according to (3.19), which applies to triaxial tests. However, except at points along the neutral axis whose length is unchanged by the flexure, plastic flow can take place in the plate as the flexure progresses and eventually the stresses will adjust to render (3.21) an equality. Thus, plastic flow will be excluded from occurring in a very narrow strip surrounding the neutral axis, but will be allowed in all other regions of the plate whenever the yield condition is met.

The plastic strain rate $\dot{e}_3^{P\ell}$ can be decomposed into a flexural plastic strain rate, and a plastic strain rate which is present prior to flexure. For convenience, the subsequent derivations will be for the case where the initial plastic strain rate is zero. This situation approximately exists when the lithosphere is in a state of rigid confinement. The generalization of the equations to other confinement conditions is straightforward.

After substituting (3.22) for the plastic strain rate in (3.23), one obtains the yield condition,

$$(3.24) \qquad |S_1 - S_3| \geq \left|\frac{K(z - Z_3)}{At}\right|^{1/n} \exp(Q/R\ T(z) \cdot 10^{-3}\ n)\ .$$

As the factor n has a numerical value of about 3 (Carter, 1976), and as the temperature variation in the lower lithosphere is approximately linear (Sclater and Francheteau, 1970), the exponential term varies most rapidly on the right side of equation (3.24). The term $K(z - Z_3)$ can therefore be replaced by its average over the yielded part of the plate, $K(\overline{z - Z_3})$, without causing significant error.

For clarity, we now discuss separately the derivation of the moment-curvature relation for negative plate curvature and positive plate curvature.

(A) Moment-Curvature relation for negative plate curvature.

According to the convention in which the z axis points from the surface of the Earth downwards, the plate curvature is negative when the lower part is under tension and the upper part is under compression.

The horizontal stress in the plate can be factorized into,

$$(3.25) \qquad S_3 = S_3^P + S_3^f$$

where S_3^P is the horizontal prestress and S_3^f is the fibre stress. The yield condition, (3.24), can now be rewritten in terms of a fibre yield stress,

$$(3.26) \qquad S_3^Y = \begin{cases} 0, \text{ if } \left|S_1^P - S_3^P\right| > \left|\dfrac{K(\overline{z - Z_3})}{At}\right|^{1/n} \exp(Q/RT(z) \cdot 10^{-3}n) \\ \qquad \text{and } z > Z_3 , \\ \left|\dfrac{K(\overline{z - Z_3})}{At}\right|^{1/n} \exp(Q/RT(z) \cdot 10^{-3}n) + (S_1^P - S_3^P), \text{ if} \\ \qquad \left|S_1^P - S_3^P\right| \leq \left|\dfrac{K(\overline{z - Z_3})}{At}\right|^{1/n} \exp(Q/RT \cdot 10^{-3}n), \text{ and } z > Z_3 ; \end{cases}$$

and,

$$(3.27) \qquad S_3^Y = - \left|\dfrac{K(\overline{z - Z_3})}{At}\right|^{1/n} \exp(Q/RT \cdot 10^{-3}n) + (S_1^P - S_3^P), \text{ if } z < Z_3 .$$

$S_3^Y(z)$ represents the value of the fibre stress at depth z, where a transition from purely elastic to plastic behavior takes place. In the elastic part of the plate the fibre stresses are given by,

$$(3.28) \qquad S_3^f = \begin{cases} -EK(z - Z_3) & \text{for } z > Z_2 \\ -E_cK(z - Z_3) & \text{for } Z_t \leq z \leq Z_2 , \end{cases}$$

where E is Young's modulus for the portion of the lithosphere beneath the moho, and E_c is the crustal Young's modulus. In the portion of the plate undergoing plastic deformation, the fibre stresses are given by (3.26) or (3.27), depending on the depth.

Considering the situation shown in Figure 3.4, P153, in which plastic yielding takes place in the plate only below the neutral axis, the value of Z_3 and the depth of transition from purely elastic to plastic behavior, Z_4, are determined by the requirement of stress continuity at Z_4, and the static force balance requirement (Timoshenko and Gere, 1972). These relations read,

$$(3.29) \qquad -K(Z_4 - Z_3)E = S_3^Y(Z_4) ,$$

and

$$(3.30) \qquad \int_{Z_1}^{Z_2} KE_c(Z - Z_3)dZ + \int_{Z_2}^{Z_4} KE(Z - Z_3)dZ - \int_{Z_4}^{Z_b} S_3^Y(Z)dZ = 0 .$$

After Z_3 and Z_4 have been determined, the moment acting on the cross section of the plate is given by,

$$(3.31) \qquad M = -KE_c \int_{Z_t}^{Z_2} (Z - Z_3)^2 \, dZ - KE \int_{Z_2}^{Z_4} (Z - Z_3)^2 \, dZ + \int_{Z_4}^{Z_b} S_3^Y (Z - Z_3) \, dZ \, .$$

The construction of moment curvature relations when yielding in the plate takes place above the neutral axis is analogous. A typical stress vs depth curve for negative plate curvature is shown in Figure 3.4 in the next section.

(B) Moment-curvature relation for positive plate curvature

According to the coordinate convention which was previously adopted, the plate is considered to have positive curvature when the upper part is under tension and the lower part is under compression.

In order for the lower portion of the plate to reach yield, elastic unloading must first take place and then the yielding will occur at a positive horizontal stress state. Following the same steps taken in the derivation for the negative curvature case, the flexural yield stress for positive plate curvature reads,

$$(3.32) \qquad S_3^Y = -\left|\frac{K(\overline{z - Z_3})}{tA}\right|^{1/n} \exp(Q/RT \cdot 10^{-3} n) + (S_1^P - S_3^P) \, , \quad \text{for } z > Z_3 \, ,$$

and

$$(3.33) \qquad S_3^Y = \left|\frac{K(\overline{z - Z_3})}{tA}\right|^{1/n} \exp(Q/RT \cdot 10^{-3} n) + (S_1^P - S_3^P) \, , \quad \text{for } z \le Z_3 \, .$$

The flexural stresses within the plate are given by (3.32) or (3.33) in the plastic region, and by,

$$S_3^f = -KE(z - Z_3) \qquad \text{for } z \geq Z_3$$

and

$$S_3^f = -KE_c(z - Z_3) \qquad \text{for } Z_t \leq z \leq Z_2 ,$$

in the elastic region.

As in the negative flexure case, when yielding occurs only in the bottom part of the plate, Z_3 and Z_6, the depth where yielding first occurs, are calculated from the equations,

$$\text{(3.34a)} \qquad -K(Z_6 - Z_3)E = S_3^Y(Z_6) ,$$

and

$$\text{(3.34b)} \qquad \int_{Z_1}^{Z_2} KE_c(Z - Z_3)dZ + \int_{Z_2}^{Z_6} KE(Z - Z_3)dZ - \int_{Z_6}^{Z_b} S_3^Y(Z)dZ = 0 .$$

A typical fibre stress vs depth curve for positive curvature is shown in Figure 3.5 in section 3.7. The moment is calculated from,

$$\text{(3.35)} \quad M = -KE_c \int_{Z_t}^{Z_2} (Z - Z_3)^2 \, dZ - KE \int_{Z_2}^{Z_6} (Z - Z_3)^2 \, dZ + \int_{Z_6}^{Z_b} S_3^Y(Z)(Z - Z_3)dZ.$$

Figure 3.6 section 3.7 shows a moment curvature relation for a model of the lithosphere in the vicinity of the Hawaiian islands.

3.6 The Plastic Hinge

When the material has a non-hardening plastic behavior, there is a finite limit to the bending moment which the plate can support. This limit is reached when a plane has its entire section under yield, except the neutral axis. The curvature of the plate at this cross section can become arbitrarily large so that unrestricted plastic flow may take place. The plate is then said to have developed a plastic hinge (e.g. Martin, 1975).

3.7 Application: Flexure of the Lithosphere Underneath The Hawaiian Island Chain

This section describes how the formulation developed in the previous sections is applied to the problem of the flexure of the lithosphere in the vicinity of the Hawaiian island chain. In the model which is adopted in this study, the Hawaiian island chain is considered as a two dimensional load on top of a semi-infinite lithospheric plate. The plate is assumed to be weakened along the axis of the island chain by volcanic activity, and a plastic hinge condition is assumed there. The model is therefore, of a semi infinite plate, subjected to a distributed normal load, with a plastic hinge with zero shear traction condition at the origin, and a condition of zero deflection and slope at infinity. The boundary conditions at the origin appear to be more satisfactory than the free end condition or the zero slope and shear traction condition (continuous symmetric plate), adopted by previous investigators (Walcott, 1970a; Watts and Cochran, 1974). This is because they have either extremely overestimated the plate weakening or have not accounted for it at all.

The example of this section attempts to fit gravity, bathymetry and depth to moho data in a profile between the islands of Oahu and Moluki. This profile was deduced by Woollard (1966),and was later used by Walcott (1970a) in his flexural model for the Hawaiian island chain.

The bathymetric features in the vicinity of the Hawaiian island chain which include the Hawaiian deep and the Hawaiian arch, or rise, have long been recognized as typical features of mathematical solutions of problems involving a plate overlying a buoyant fluid (e.g. Gunn, 1943; Walcott 1970a; Watts and Cochran, 1974). The prominent features of the profile considered in this study, as summarized by Walcott (1970a), are:

(1) the distance between the crest of the Hawaiian arch and the island axis is about 250 km;

(2) the amplitude of the rise is 600 ∓ 200 meters;

(3) the depth to the moho is about 21 km beneath the island axis, 12 km beneath the trench, and 10 km beneath the rise. The undisturbed moho depth away from the Hawaiian structure is 10.5 km;

(4) the change in free air gravity anomaly values are + 200 mgal, -100 mgal, and + 30 mgal over the ridge, the trench and the rise respectively. The positive anomaly over the rise reaches a maximum of + 50 mgals in some places. These features comprise the bathymetry and gravity data which the plate model has to match.

It must be emphasized at this point that the assumption of two dimensionality is an oversimplification, as bathymetry and depth to moho vary considerably between different profiles along the Hawaiian island chain (Watts and Cochran, 1974; Furamoto, 1966; Woollard,1966). In particular the depth to the moho of 21 Km under the ridge in the profile considered in this study is large in comparison with observations in the vicinity of the island of Hawaii (Woollard,1966; Furamoto and Woollard,1965). Thus, the flexural model presented in this section is not aimed at matching accurately all the features along the island chain, but rather it attempts to demonstrate the feasibility of the plastic plate model developed in the previous sections by showing that it can fit all the data along the chosen profile,and can avoid the shortcomings, listed in Section 3.1, of the elastic or viscoelastic plate models.

The first stage of the numerical simulation is of the construction of the input parameters in equation (3.15) and (3.16) in Section 3.2. The island load is approximated to be a distributed normal load on the plate top,which is equal to the weight of the material between the bathymetry and the position of the plate top plus the weight of ocean water between sea level and the bathymetry (See Figure 3.7). The bathymetry and the plate top position coincide outside of the trench sediments, but the plate top position is unknown inside the sediments and under the ridge. The unknown plate top location is constrained only at two places by the condition that the Moho displacement measured under the ridge axis and under the trench, is equal to the plate top displacements in the same places respectively.

To proceed to the solution for the deformed plate profile; first a deformed plate top profile is assumed under the trench sediments with the constraints that it pass through the two observed moho depths, and that it join smoothly the bathymetry profile outside the trench sediments. This profile is the zeroth order approximation to the solution. It is used for calculating a density structure for the crust and sediments which will fit the free air gravity anomaly data. The computed densities are then used to compute the vertical normal load on the plate top. von Karman's plate bending equation with the nonlinear moment-curvature relation developed previously, is then solved by the Finite Element technique using the Newton-Raphson iteration procedure (see Appendix B and Appendix E). The parameters in the solution, in addition to those which have been determined by matching gravity, are the magnitude of the horizontal prestress and the asthenosphere density below the lower boundary of the lithosphere. These parameters are chosen so that the solution fits closely the given data of lithospheric deformation. The first computed plate profile, constrained only to pass through the deflection at two places inside the trench sediments and to match bathymetry outside of the trench sediments, differs in detail from the assumed zeroth order approximation of the deformed plate profile. The first computed plate profile is then used as the input profile for the next series of computations. The process is then repeated iteratively until it converges to a state where the input profile equals the calculated profile to within a prescribed accuracy, and also where the gravity, depth to Moho, and the bathymetry data outside the trench region are matched.

The main steps in each iteration are as follows,

(A) Determination of island, crust and sediment density from the free air gravity anomaly.

The free air gravity anomaly is calculated by the polygon method of Talwani, Worzel and Landisman (1959). The density model and computed free air gravity anomaly are shown in Figures 3.3a and 3.3b respectively.

(B) Calculation of vertical loads from the computed densities.

The Kirchhoff stress tensor S_{ij}, is approximated to the first order by the Eulerian stress tensor σ_{ij}. The traction at the lower plate boundary arises from the buoyancy forces and is given by,

$$S_{zz}(Z_b) = -\rho_a g w ,$$

where ρ_a is the asthenosphere density immediately below the lithosphere and w is the plate deflection. The normal tractions on the top of the plate are given by,

$$S_{zz}(Z_t) = \ell_1(x)\,\rho_c g + \ell_2(x)\rho_s g + \rho_w g B(x) , \tag{3.36}$$

where ρ_c is the density of the island load, ρ_s is the density of the trench sediments, ρ_w is the ocean water density, $B(x)$ is the bathymetry, $\ell_1(x)$ is the vertical distance between the top of nonsediment crust and the point considered as the top of the plate, and $\ell_2(x)$ is the thickness of the sediments. The sum of $\ell_1(x)$ and $\ell_2(x)$ is equal to the vertical distance between the top of the plate and the bathymetry. The term which remains to be specified in equation (3.16) is the integral of the body forces over the plate thickness. However, as this is a constant term for all x, it causes a uniform displacement

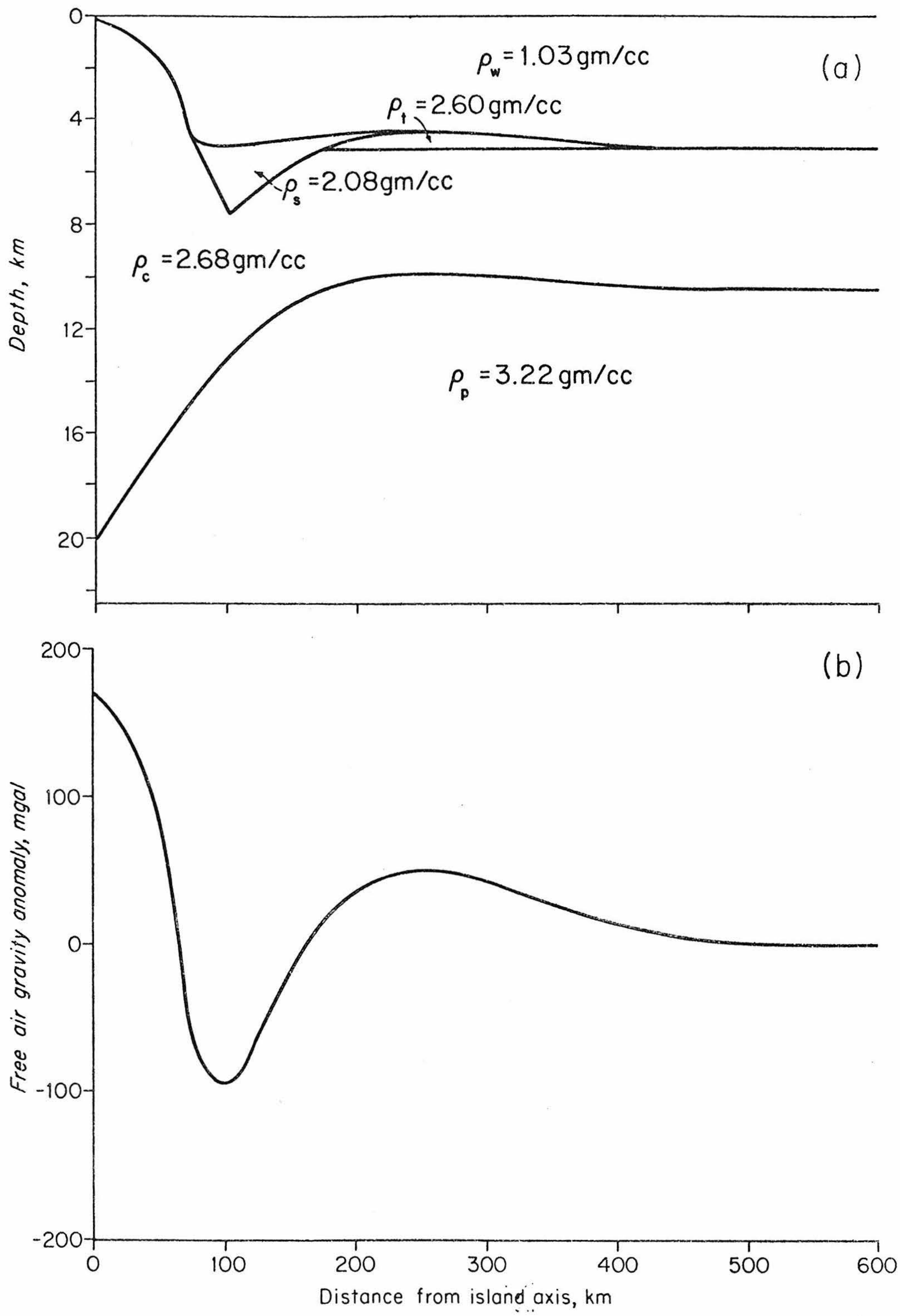

Figure 3.3 (a) Density model (input for the final iteration) for free air gravity computation. (b) Free air gravity anomalies computed from the density model shown in (a).

$w^{(0)}$ and therefore need not be considered.

(C) Calculation of thrust.

The thrust of N_x in (3.15) is given by,

$$N_x = \int_{Z_t}^{Z_b} (S_{30} + \beta(Z) \cdot S_1^{(P)} dZ \,, \tag{3.37}$$

where S_{30} is the horizontal prestress from tectonic origins, and $S_1^{(P)}$, the vertical prestress, is given by equation (3.20a) in section 3.3. The horizontal flexural stress S_3^f does not enter into (3.37), as the force balance conditions require that its integral over the plate thickness vanish (see equations 3.30 and 3.34b in section 3.5).

(D) Finite element solution of von Karman's plate equation with a nonlinear moment-curvature relation.

After all the input parameters have been specified, von Karman's plate equation is solved for the plate deflections, plate slopes, curvatures and moments. Details of the solution algorithm are given in Appendices B and E.

The parameters used in the final iteration of the plate deflection computation are;

(1) Elastic parameters; E_c = 0.8962 Mbar, is the crustal Youngs modulus, E = 1.7171 Mbar, is the average Young's modulus for the lithosphere below the Moho. These are 90% of the seismic values in Kanamori's (1969) oceanic surface wave model 5.08 M.

(2) Plastic yield stress parameters, (see equation 3.24); average distance from the yielded part of the lithosphere to the neutral axis during plate bending by the island load, $\overline{Z - Z_3}$, is taken to be 23 Km.

This value is arrived at after several trial solutions and it agrees with the final solution to within $\pm$ 5%. $A = 5.1 \cdot 10^{-9}\ K_b^{-3.3} s^{-1}$, $n = 3.3$, $Q = 113.2$ kcal/mole, are from dunite deformation data by Carter and Ave'Lallemant (1970). The temperature in the lower lithosphere is approximated by a linear function of depth,

$$T(z) = 178.86 + 17.868 \cdot 10^{-3} z \ ,$$

where T is in K° and z is in meters. This equation is constructed from the oceanic lithosphere temperature profile by Sclater and Francheteau (1970). The loading, time t, is taken to be 1.3 million years

(3) Density and undeformed plate parameters. The plate bottom depth is $Z_b = 60$ km, the plate top depth is $Z_t = 5.103$ km and the Moho depth is 10.5 km. The ocean water density is $\rho_w = 1.03$ gr/cm^3, the trench sediment density is $\rho_s = 2.08$ gr/cm^3, the crustal density is 2.68 gr/cm^3, the average plate density below the Moho is 3.22 gr/cm^3, and the asthenosphere density immediately below the lithosphere is 3.6 gr/cm^3.

(4) Prestress, thrust and moment parameters. The prestress parameters in equations (3.20b) are $\beta = 1/3$, $S_{30} = -2.9$ kb, the thrust N_x, is $-4.983 \cdot 10^{13}$ N/m. The plastic hinge per unit width, M_p, is $M_p = 4.3 \cdot 10^{16}$ N.

The variation of fibre stress with depth for specified curvatures, and the parameters used in the final calculation is shown in Figure 3.4 and Figure 3.5 . These figures show that the present model does not produce the excessive stresses which occur in elastic or viscoelastic

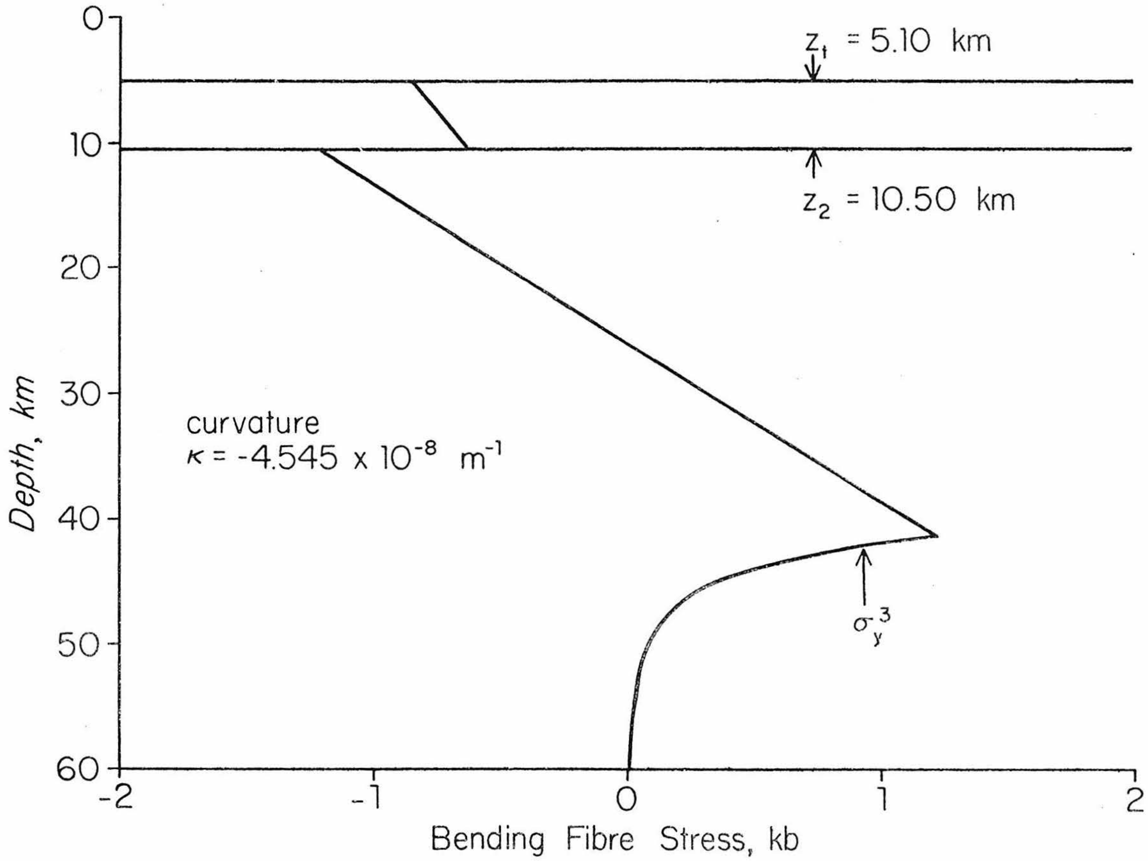

Figure 3.4 Stress distribution associated with bending in a plate cross section in negative curvature.

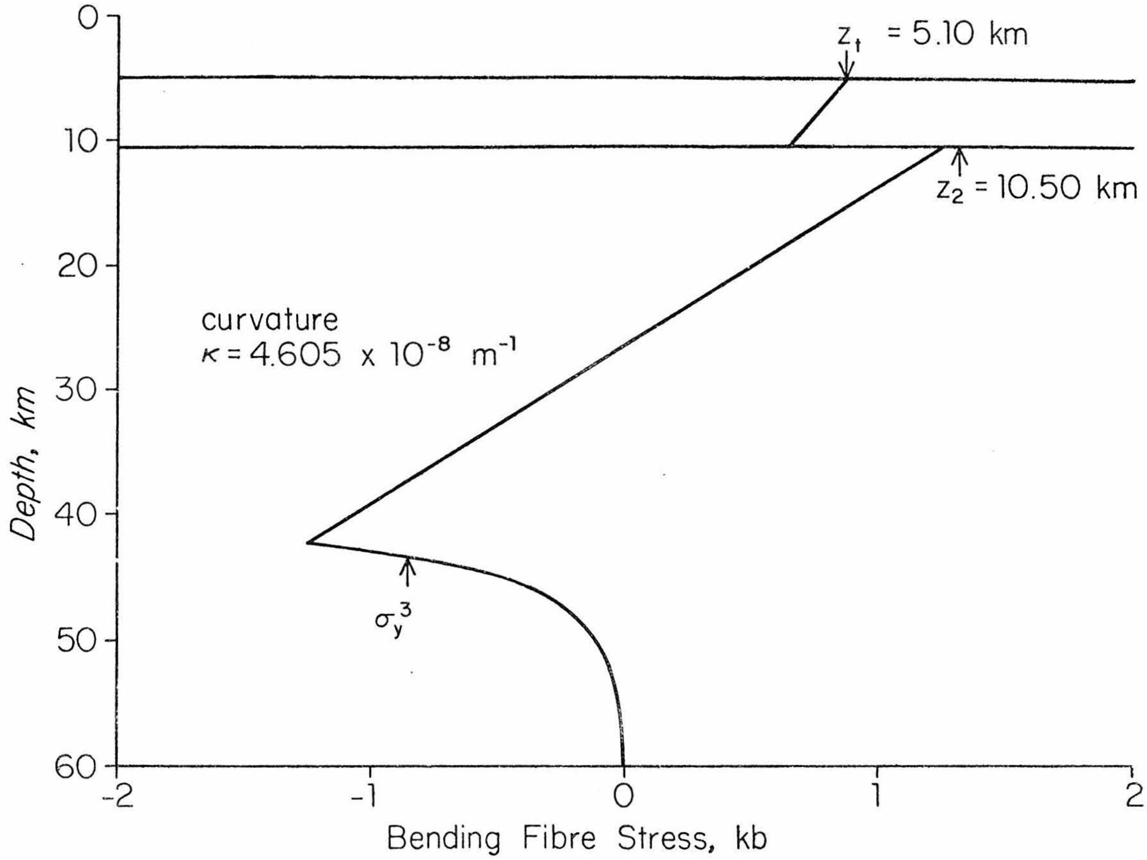

Figure 3.5 Stress distribution associated with bending in a plate cross section in positive curvature.

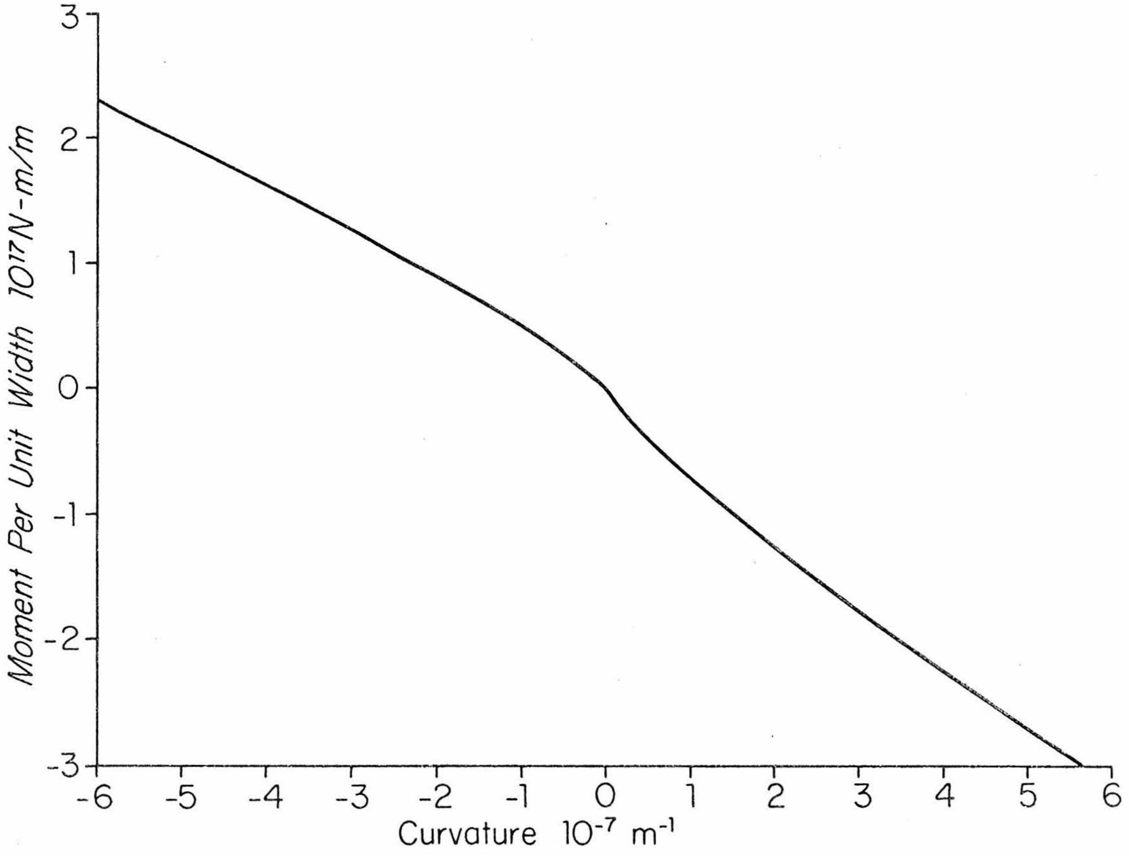

Figure 3.6 The moment curvature relation for the lithosphere bending used in the last iteration.

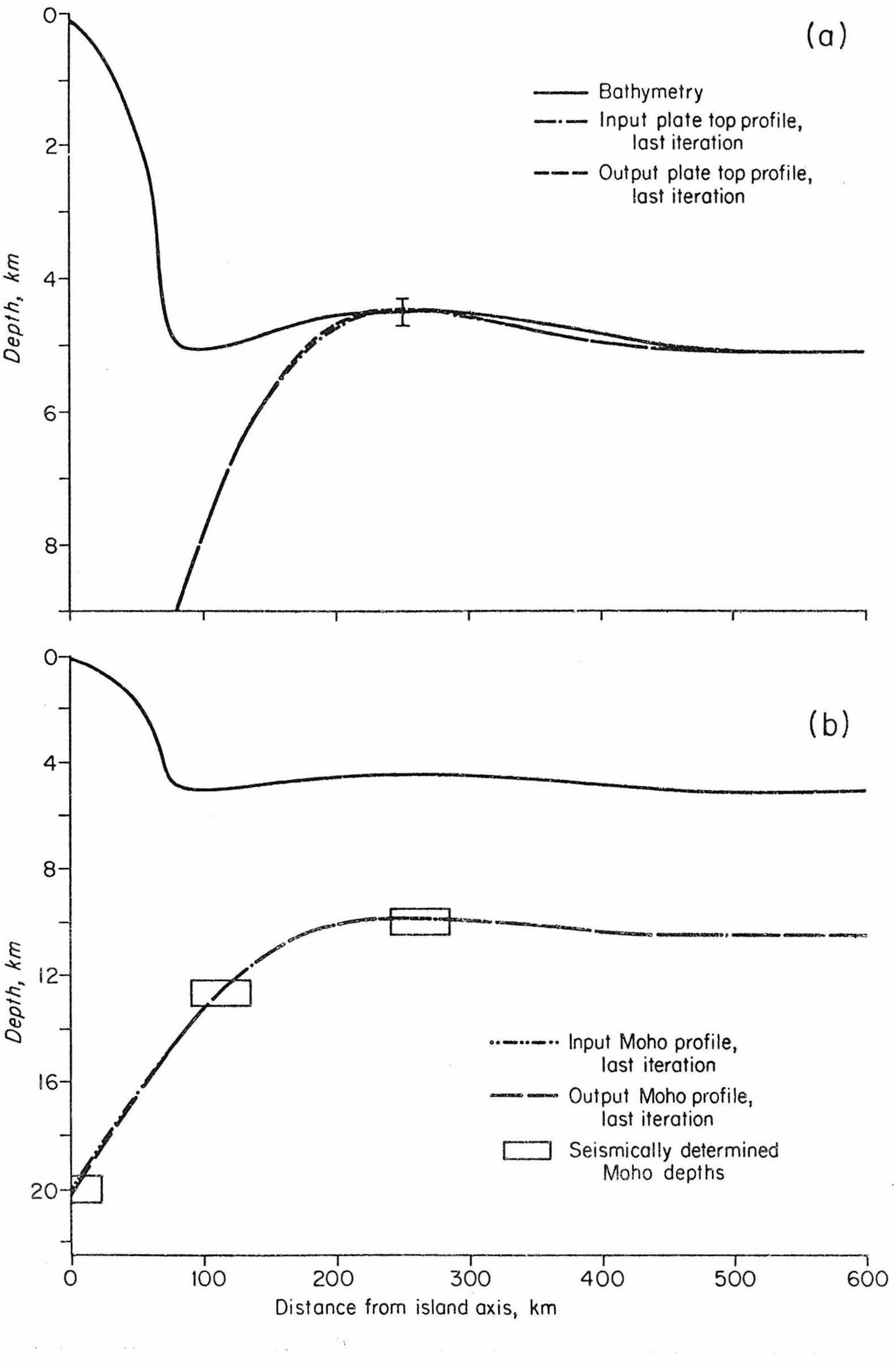

Figure 3.7 Input and output profiles in the last iteration of the Hawaiian deflection problem as compared with observational data; (a) bathymetry and plate top profile; (b) Moho displacement.

models. The complete moment-curvature relation is shown in Figure 3.6. The input and output profiles for the Hawaiian structure are shown in Figure 3.7. They practically coincide with each other.

3.8 Conclusion

A plate deformation model for the lithosphere with a material rheology based on rock mechanics data has been presented in this study. It is demonstrated that the model is capable of matching to within observational accuracy, bathymetry and gravity profiles in a profile in the vicinity of the Hawaiian island chain. The type of plate model which has been developed herein can be applied to a wide class of lithosphere deflection problems along plate margins and island arcs. Furthermore, the theory can be extended, if necessary, to solve problems involving two dimensional plate and load configurations. The considerations which are used in developing the plate rheology in this study should also apply to situations where a full continuum mechanics theory is more relevant to the problem than the plate theory approximation.

References

Anderson, D. L., 1962. The plastic layer of the Earth's mantle, Scientific American, 205, pp. 2-9.

Carter, N. L., 1976. Steady state flow of rocks; Rev. Geophys. Space Phys., 14, pp. 301-360.

Carter, N. L., and Ave'Lallemant, H. G., 1970. High temperature flow of Dunite and Periodotite, Geol. Soc. Amer. Bull., 81, pp. 2181-2202.

Fung, Y. C., 1965. Foundations of Solid mechanics, Prentice-Hall.

Furamoto, A. S., and Woolard, G. P., 1965. Seismic reflection studies of the crustal structure of the Hawaiian Archipelago; Pacific Science, Vol. 19, pp. 315-319.

Griggs, D. T., Turner, F. J., and Heard, H. C., 1960. Deformation of rocks at 500°C to 800°C; Rock Deformation, Chapter 4, Memoir 79, the Geological Society of America, New York.

Green, D. H., 1972. Magnetic activity as the major process in the chemical evolution of the Earth's crust and mantle; Tectonophysics, 13, pp. 47-71.

Gunn, R., 1943. A quantitative study of isobaric equilibrium and gravity anomalies in the Hawaiian islands; Journal Franklin Inst., 236, pp. 373-390.

Gutenberg, B., 1960. Low velocity layers in the Earth, ocean, and atmosphere; Science, 131, pp. 959-965.

Hanks, T. C., 1971. The Kuril Trench-Hokkaido Rise System; large shallow earthquakes and simple model of deformation; Geophys.

J. R. Astr. Soc., 23, 173-189.

Kanamori, H., and Press, F., 1970. How thick is the lithosphere? Nature, 226, pp. 330-331.

Le Pichon, X., Francheteau, J., Bonnin, J., 1973. Plate Tectonics, p. 220-227.

Liu, H.-P., Anderson, D. L., and Kanamori, H., 1976. Velocity dispersion due to anelasticity, implications for seismicity and mantle composition; Geophy. J. R. Astr. Soc., 47, pp. 41-58.

Martin, J. B., 1975. Plasticity: fundamentals and general results; M.I.T. Press.

O'Connell, R. J., 1971. Pleistocene glaciation and the viscosity of the lower mantle; Geophy. J. R. Astr. Soc., 23, pp. 299-327.

Parsons, B., Molnar, P., 1976. The origin of outer topographic rises associated with trenches, Geophys. J. R. Astr. Soc., 45, 707-712.

Sclater, J. G., and Francheteau, J., 1970. The implications of terrestial heat-flow observations on current tectonic and geochemical models of the crust and upper mantle of the earth, Geophys. J. R. Astr. Soc., 20, pp. 509-542.

Talwani, M., Worzel, L., and Landisman, M., 1959. Rapid gravity computations for two dimensional bodies with applications to the Mendocino submarine fracture zone, J. Geophys. Res., 64, pp. 49-54.

Timoshenko, S. P., and Gere, J. M., 1972. Mechanics of Materials, Van-Nostrand Reinhold Co., New-York.

Vening Meinesz, F. A., 1941. Gravity over the Hawaiian archipelago and over the Maderia area, Proc. Neth. Acad. Wetenschap., 44, pp. 1-12.

Walcott, R. I., 1970a. Flexure of the lithosphere at Hawaii, Tectonophysics, 9, pp. 435-446.

Walcott, R. I., 1970b. Flexure rigidity, thickness and viscosity of the lithosphere, J. Geophy. Res., 75, pp. 3941-3954.

Walcott, R. I., 1976. Lithospheric flexure, analysis of gravity anomalies, and the propagation of seamount chains; The Geophysics of the Pacific Ocean Basin and its Margin, Sutton, G. H., Manghnani, M. H., and Moberly, R., editors.

Watts, A. B., and Cochran, J. R., 1974. Gravity anomalies and flexure of the lithosphere along the Hawaiian-Emperor Seamount chain; Geophys. J. R. Astr. Soc., 38, 119-141.

Watts, A. B., and Talwani, M., 1974. Gravity anomalies seaward of deep sea trenches and their tectonic implications; Geophys. J. R. Astr. Soc., 36, 57-90.

Watts, A. B., Talwani, M., and Cochran, J. R., 1976. Gravity field of the Northwest Pacific Ocean basin and its margin, The Geophysics of the Pacific Ocean Basin and its Margin, Sutton, G. H., Manghnani, M. H., and Moberly, R., editors.

Woollard, G. P., 1966. Crust and Mantle relations in the Hawaiian area, Geol. Surv. Can. Paper, 66-15, pp. 294-310.

Appendix A: DERIVATION OF THE QUASISTATIC FINITE ELEMENT EQUATIONS

A.1 Equations of Balance of Forces for a Continuum

For a solid body occupying a volume V, bounded by a surface S, and undergoing infinitesimal deformations, the equations of static force balance are given by,

$$\text{(A1)} \qquad \frac{\partial \sigma ij}{\partial x_j} + f_i = 0 , \; i = 1 \ldots D ,$$

where D is the number of degrees of freedom, f_i are the body forces, x_j are a set of Cartesian coordinates, and σ_{ij} are the components of the stress tensor. The summation convention according to which repeated indices imply summation is used throughout this appendix.

Equation (A1) must be supplemented by a set of boundary conditions on the surface S which can either be specified displacements or specified tractions, $T_i = \sigma_{ij} n_j$, where $\underline{n}(x)$ is the normal vector to S. In the following derivations, S_u will denote the portion of S upon which displacements are specified and S_σ will denote the portion of S upon which tractions are specified.

A.2 Spatial Discretization

A spatial region is discretized by subdividing its volume V into a total of E elements containing N modal points. The displacement field $U_i(x)$, throughout V is interpolated from the displacements U_i^n,

$n = 1 \ldots N$, at the nodes of the elements. The spatial interpolation is achieved using piecewise smooth interpolation functions $P_n(x)$ according to,

$$U_i(\underline{x}) = \sum_{n=1}^{N} P_n(\underline{x})\, U_i^n \; . \tag{A2}$$

The interpolation functions satisfy the relation,

$$P_n(\underline{X}^m) = \delta_{nm} \; , \tag{A3}$$

where $\underline{X}^m$ is the coordinate of the m^{th} node.

Spatial derivatives of the displacement field are expressed in terms of nodal displacements by the differentiation of equation (A2),

$$\frac{\partial U_i}{\partial x_j} = \sum_{n=1}^{N} \frac{\partial P_n(x)}{\partial x_j}\, U_i^n \; . \tag{A4}$$

The variations of the material properties, throughout the volume V, are approximated by assigning each element uniform material properties which are close in value to the average material parameters in the region of the element.

A.3 The Galerkin Weak Form of the Force Balance Equations

For the derivation of the Finite Element equations, the equations of force equilibrium (A1) are replaced by the Galerkin weak form equations given by;

$$\int_V \frac{\partial P_n}{\partial x_j}(\underline{x})\, \sigma_{ij}\, d\tau = \int_V P_n(x) f_i\, d\tau + \int_S \sigma_{ij} n_j P_n(\underline{x})\, dS \qquad \begin{array}{l} n = 1 \ldots N_1 \\ i = 1 \ldots D \end{array} ,$$

or,

$$\text{(A5)} \qquad \int_V \frac{\partial P_n(\underline{x})}{\partial x_j} \sigma_{ij} d\tau = \int_V P^n(\underline{x}) f_i d\tau + \int_{S\sigma} T_i P_n(x) dS \qquad \begin{matrix} n = 1 \dots N_1 \\ i = 1 \dots D \end{matrix}$$

The nodes which lie on S_σ or in the interior of V are numbered from 1 to N_1, and the nodes which lie on S_u are numbered from $N_1 + 1$ to N. For interpolation functions which satisfy,

$$P_n(\underline{x}) = 0, \text{ for } x \in S_u,$$

equation (A5) is a less restrictive statement than (A1). This is because the solutions of (A1) also satisfy (A5), as becomes evident from integrating (A5) by parts.

The Finite Element equations are obtained from the Galerkin weak form (A5), after expressing the strains according to (A4), and incorporating a rheological prescription which relates stresses to strains. The derivation is carried out in the next section for the linear elastic case. The elastic-plastic case is discussed in Appendix E.

A.4 Finite Element Equilibrium Equations for a Linear Elastic Medium

For a linear elastic solid, the stress strain relations are given by;

$$\text{(A6a)} \qquad \sigma_{ij} = C_{ijk\ell} \frac{\partial U_k}{\partial x_\ell} , \qquad i,j = 1 \dots D$$

where $C_{ijk\ell}$ are the elastic coefficients. The symmetry of the $C_{ijk\ell}$ coefficients (there are at most 21 independent coefficients) allows the substitution of displacement gradients in (A6a) instead of the symmetric strain tensor. For an isotropic material there are two independent elastic coefficients and the relation (A6a) becomes;

$$\text{(A6b)} \qquad \sigma_{ij} = \lambda e_{kk} \delta_{ij} + 2\mu e_{ij} \;,$$

where λ and μ denote respectively Lame's constant and the shear modulus. The displacement gradients in (A6a) are expressed in terms of nodal displacements by (A4). Substituting in this manner (A5) and (A6) into (A5) results in,

$$\text{(A7)} \quad \left[\sum_{m=1}^{N} \int_V \frac{\partial P_n}{\partial x_j} C_{ijk\ell} \frac{\partial P_m}{\partial x_\ell} d\tau \right] U_K^m = \int_V P_n(x) f_i \, d\tau + \int_{S\sigma} T_i P_n(x) \, d\tau \qquad \begin{array}{l} n = 1 \ldots N_1 \\ i = 1 \ldots D \;. \end{array}$$

These equations can be written as a set of N_1 equations in N_1 unknowns,

$$\text{(A8)} \quad \sum_{m=1}^{N_1} K_{ik}^{nm} U_k^m = F_i^n \;,$$

where,

$$\text{(A9a)} \quad K_{ik}^{nm} = \int_V \frac{\partial P_n}{\partial x_j} C_{ijk\ell} \frac{\partial P_m}{\partial x_\ell} d\tau \;, \qquad \begin{array}{l} i,k = 1 \ldots D \\ n,m = 1 \ldots N_1 \end{array}$$

and

$$\text{(A9b)} \quad F_i^n = \int_V P_n(\underline{x}) f_i \, d\tau + \int_{S\sigma} T_i P_n(\underline{x}) \, dS - \sum_{m=N_1+1}^{N} \left[\int_V \frac{\partial P_n}{\partial x_j} C_{ijk\ell} \frac{\partial P_m}{\partial x_\ell} d\tau \right] U_K^m \;, \qquad \begin{array}{l} i = 1 \ldots D \\ n = 1 \ldots N_1 \,. \end{array}$$

The K_{ik}^{nm} coefficient matrix is termed the stiffness matrix, and the vector F_i^m , which is known a priori, is called the generalized force vector.

In most finite element schemes the integrations in (A9a) and (A9b) are carried out element by element and are often calculated by numerical quadrature. In the FE scheme which was used in this thesis for continuum mechanics calculations, a one quadrature point integration rule, combined with an additional bending term, was used. Further details on integration procedure and the solution method used for equations (A8) are described in Appendices C and D.

Appendix B: DERIVATION OF THE PLATE FINITE ELEMENT EQUATIONS

B.1 The One Dimensional Plate Equilibrium Equation

The equation of equilibrium for a plate which is being bent in one direction only is given by,

$$\frac{d^2M_X}{dX^2} = -q - N_X \frac{d^2w}{dX^2} \tag{3.13}$$

(see section 3.2 for the meaning of the variables). In order to completely define the solution, equation (3.13) must be supplied with appropriate boundary conditions at the ends of the plate which may include a fixed displacement or a prescribed shear traction, and a fixed slope or a prescribed moment. In the problem of the flexure of the lithosphere under the Hawaiian island chain, N_X is a constant and q is a sum of a constant term and a term proportional to the deflection w (see Section 3.7). Thus, the equation to be solved for the Hawaiian plate calculation in Section 3.7 is of the form,

$$\frac{d^2M_x}{dx^2} = -a - bw - c\frac{d^2w}{dx^2} , \tag{B1}$$

where a, b, c are constants.

B.2 Galerkin Weak Form of the Plate Equation

The plate deflection is approximated by a series,

$$w(x) = \sum_{n=1}^{N} A_n \phi_n(x) , \tag{B2}$$

where $\{A_n\}_{n=1}^{N}$ are expansion coefficients, and $\{\phi_n\}_{n=1}^{N}$ is a set of as yet unspecified interpolation functions. The Galerkin weak form is obtained by premultiplying equation (B1) by ϕ_n and integrating over the length of the plate. After integrating by parts and substituting values for w(x) from (B2), one obtains,

$$\text{(B3)} \quad \int_{X_1}^{X_2} \phi_n'' M_x \, dx + \int_{X_1}^{X_2} a\phi_n \, dx + b\int_{X_1}^{X_2} \phi_n \sum_{m=1}^{N} A_m \phi_m(x)\, dx$$

$$+ C\int_{X_1}^{X_2} \phi_n \sum_{m=1}^{N} A_m \phi_m'' \, dx + \phi_n \frac{dM_x}{dx}\Bigg|_{X_1}^{X_2} - \phi_n' M_x \Bigg|_{X_1}^{X_2} = 0 \;, \; n = 1, \ldots N$$

where X_1 and X_2 denote the limits of the plate.

B.3 Construction of Interpolation Functions

The plate is discretized by subdividing its length ℓ into elements containing a total of E + 1 nodes (Figure B.1a). For convenience, the interpolation functions are constructed element by element with a local coordinate system for each element, which from now on will be termed the Z system, extending from $z = -1$ to $z = 1$. The two nodes in each element are given local numbers from one to two as in Figure B.1b. The deflections at the interior of a given element E are approximated from the values of the nodal deflections $\{W^i\}_{i=1,2}$ and the nodal deflection derivatives $\left\{\frac{dw^i}{dz}\right\}_{i=1,2}$, according to (e.g. Zienkiewicz, 1971),

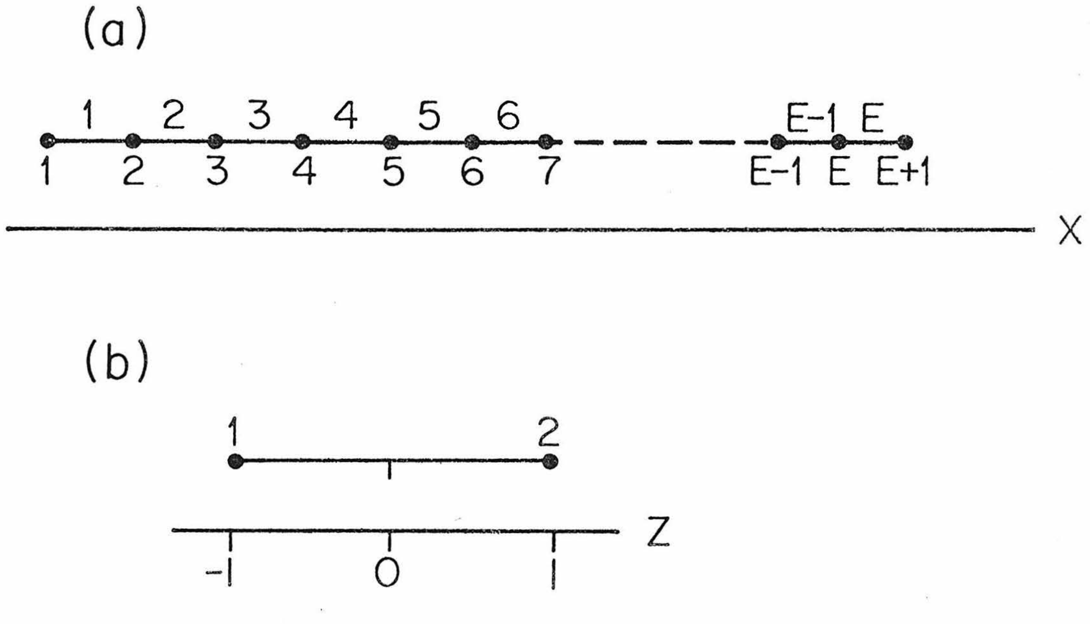

Figure B.1 (a) A Finite Element 1-D plate grid containing E elements and E+1 nodes. (b) The Z coordinate system for a plate element.

(B4) $$w(z) = \phi_1(z)\, W^1 + \phi_2(z)\, \frac{dW^1}{dz} + \phi_3(z)\, W^2 + \phi_4(z)\, \frac{dW^2}{dz},$$

where ϕ_i are given by,

(B5)
$$\phi_1 = \frac{1}{4}(2 - 3z + z^3),$$
$$\phi_2 = \frac{1}{4}(1 - z - z^2 + z^3),$$
$$\phi_3 = \frac{1}{4}(2 + 3z - z^3),$$
$$\phi_4 = \frac{1}{4}(1 - z + z^2 - z^3).$$

These interpolation functions satisfy the relations,

(B6)
$$\phi_i(Z^m) = \delta_i^{1+2(m-1)} \quad , \text{ when i is odd,}$$
$$\phi_i(Z^m) = 0 \quad , \text{ when i is even,}$$
$$\frac{d\phi_i}{dz}(Z^m) = 0 \quad , \text{ when i is odd,}$$
$$\frac{d\phi_i}{dz}(Z^m) = \delta_i^{2m} \quad , \text{ when i is even.}$$

Z^m is the Z coordinate of the m^{th} node in element E and can assume values of ∓ 1. In addition, the local interpolation functions are defined to be identically zero outside of the element E. The derivatives of the deflection with respect to z can be calculated from the nodal slopes by a chain rule according to,

(B7) $$\frac{dw}{dz} = \frac{dw}{dx} \cdot \frac{dx}{dz} = \frac{dw}{dx} \frac{(X^2 - X^1)}{2},$$

where X^i denote the global coordinates of the nodes surrounding element E.

After the interpolation functions have been defined in each element they are assembled globally by a summation over elements,

$$\phi_n = \sum_E \phi_n^E \; , \quad n=1, \ldots 2E \; ,$$

where,

$$\phi_n^E = \begin{cases} \phi_i & \text{for odd } n \text{ and } i \text{ which refer to the same node,} \\ \phi_i \cdot \dfrac{X^2 - X^1}{2} & \text{for even } n \text{ and } i \text{ which refer to the same node.} \end{cases}$$

The A_n coefficients in equation (B2) can now be written in terms of nodal deflections and slopes, and the equation can then be rewritten as,

$$\text{(B8)} \qquad w(x) = \sum_{n=1}^{E+1} w^n \, \phi_{2n-1}(x) + \sum_{n=1}^{E+1} \frac{dw^n}{dx} \, \phi_{2n}(x) \; .$$

B.4 The Finite Element Plate Equations

The Finite Element plate equations are obtained from the Galerkin weak form (B3) by interpreting the A_m coefficients according to (B8). After some algebra one obtains,

$$\int_{X_1}^{X_2} \phi_n'' \, M_x \, dx + \sum_{m=1}^{N_1} \left[\int_{X_1}^{X_2} (b \, \phi_n \, \phi_{2m-1} - C \, \phi_n' \, \phi_{2m-1}') \, dx \right] W^m$$

$$+ \sum_{m=1}^{N_2} \left[\int_{X_1}^{X_2} (b \, \phi_n \, \phi_{2m} - C \, \phi_n' \, \phi_{2m-1}') \, dx \right] \frac{dw^m}{dx} = - \int_{X_1}^{X_2} a \, \phi_n \, dx$$

(B9)

$$- \phi_n \frac{dM_x}{dx} \Big|_{X_1}^{X_2} + \phi_n' M_x \Big|_{X_1}^{X_2} - \sum_{m=N_1}^{E+1} \left[(b\, \phi_n\, \phi_{2m-1} - C\, \phi_n'\, \phi_{2m-1}')\, dx \right] W^m$$

$$- \sum_{m=N_2}^{E+1} \left[(b\, \phi_n\, \phi_{2m} - C\, \phi_n'\, \phi_{2m}')\, dx \right] \frac{dW^m}{dx} .$$

N_1 is the total number of nodes with free deflections, N_2 is the total number of nodes with free slopes, $E+1-N_1$ is the total number of nodes with prescribed displacements, and $E+1-N_2$ is the total number of nodes with prescribed slopes. All the terms on the right side of (B9) are known a priori and together they comprise the generalized force vector.

For an elastic plate the moment M_x is linearly related to the curvature or equivalently to the second derivative of the slope. In that case (B9) comprises a set of $N_1 + N_2$ non-homogeneous linear equations in the $N_1 + N_2$ unknowns. In the elastic-plastic case, (B9) becomes a set of $N_1 + N_2$ nonlinear equation which, as a rule, cannot be solved in one step. The procedure which is used in this thesis for solving (B9) in the non-linear case is outlined in Appendix E.

References

Zienkiewicz, O. C., 1971. The Finite Element Method in Engineering and Science, McGraw-Hill.

Appendix C: SOLUTION OF STATIC LINEAR ELASTIC FINITE ELEMENT EQUATIONS BY THE CONJUGATE GRADIENT METHOD

C.1 Introduction

The Conjugate Gradient method enables the solution of full 3-D continuum Finite Element problems involving 10^4 or more linear equations. It appears that such large systems cannot be feasibly solved, with the present day computer technology, by the often used direct factorization methods, because computing time and computer storage then become prohibitively large.

This appendix briefly reviews the Conjugate Gradient method and its implementation in solving the FE equations. It also presents a number of explanations to the apparent success of the method.

C.2 The Conjugate Gradient Method

The basic Conjugate Gradient method is designed to solve linear equations of the type,

$$A\underline{U} = \underline{b} , \tag{C1}$$

in which A is a square and positive definite symmetric matrix, $\underline{U}$ is a vector of unknowns, and $\underline{b}$ is the force vector. The solution procedure consists of a linear expansion of the solution by a set of A-orthogonal vectors which are generated one by one in a series of repeated steps. Let $\underline{U}^n$ denote the solution vector after the n^{th} step, $\underline{V}^n$ denote the n^{th} basis vector in the expansion of the solution, $\underline{r}^n$ denote the residual vector, $\underline{b} - A\underline{U}^n$, after n steps, and let $A\underline{V}^n$ denote the product of the A matrix by $\underline{V}^n$. A typical step of the CG method consists of the following calculations (e.g. Ralston, 1965),

(C2) $$\alpha_n = (\underline{V}^{n^T}, \underline{r}^n)/(\underline{V}^{n^T}, A\underline{V}^n) ,$$

(C3) $$\underline{U}^{n+1} = \underline{U}^n + \alpha_n \underline{V}^n$$

(C4) $$\underline{r}^{n+1} = \underline{b} - A\underline{U}^{n+1} = \underline{r}^n - \alpha_n A\underline{V}^n ,$$

(C5) $$\beta = -(\underline{r}^{n+1}, A\underline{V}^n)/(\underline{V}^{n^T}, A\underline{V}^n) ,$$

(C6) $$\underline{V}^{n+1} = \underline{r}^{n+1} + \beta\underline{V}^n .$$

Two vectors which are separated by a comma and enclosed within brackets denote the scalar product between the vectors, and a superscript T denotes the transpose. The method is initialized by setting,

$$\underline{V}^o = \underline{r}^o = \underline{b} ,$$

and

$$\underline{U}^o = 0 .$$

It can be shown that the expansion vectors, $\underline{V}^n$, fulfill the A orthogonality relation,

$$(\underline{V}^{i^T}, A\underline{V}^j) = 0, \text{for } i \neq j \quad \text{(e.g. Ralston, 1965).}$$

In applying the Conjugate Gradient method to solve the Finite Element equations, there is no need to store the stiffness matrix. Rather, the inner product of the stiffness matrix by the basis vectors is calculated by sequentially using (A4), (A6), and (A5), after replacing the nodal displacement vector, U_i^n, in (A4) by the expansion vector, V_i^n, (here, unlike in the rest of this appendix, the index n denotes the node number and not the step number). Although in effect this amounts to recalculating the stiffness matrix repeatedly in every step, a large savings in computer storage is encountered. Furthermore, the calculations in equations (C2)-(C6) can be performed efficiently by using the hourglass scheme described in Appendix D.

C.3 Convergence Properties of the Conjugate Gradient Method

Since the Conjugate Gradient method forms an expansion of the solution vector in terms of A-orthogonal basis vectors, it is not an iterative procedure in the strict sense. This is because the maximum number of A-orthogonal basis vectors which can be generated is equal to the number of linear equations. Therefore, in the absence of roundoff, the method will converge to the exact solution in at most that many steps.

Our experience has shown that for the type of three dimensional problems encountered in the first two chapters of this thesis the Conjugate Gradient method converged in a number of steps between five to ten times the number of elements in the grid dimension containing the largest number of elements. This number of steps is always much smaller than the bound placed by the number of equations. For example, the 3-D Long Beach subsidence simulations described in Chapter 2 used a 24 X 19 X 12 element grid with 6500 nodes and approximately 18000 degrees of freedom, and less than 200 steps were required to reach convergence.

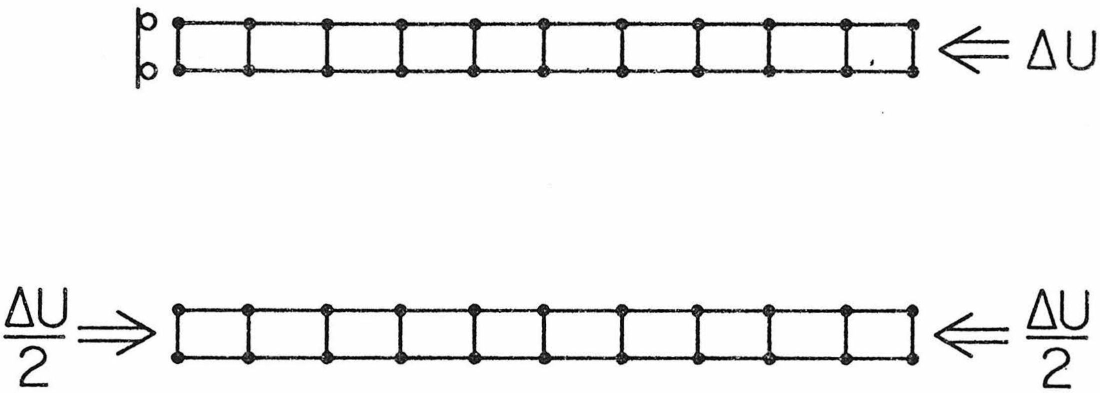

Figure C.1 Two statically equivalent beam problems.

Another observation is that for a given grid, the number of steps required for convergence varies according to the type of boundary conditions and element material parameters. This point is illustrated in the example of the two equivalent beam problems shown in Figure C.1. The second beam problem, in which the beam is displaced equally from both ends, converges in half the number of steps as the first problem, in which the beam is displaced from one side only with the other side held fixed. This observation has practical aspects; whenever possible it is advantageous to load a problem symmetrically, rather than from one side only.

In most problems roundoff has not been a problem with computers like the CDC 7600 which use a long word length. For computers which use a shorter word length, like the IBM 370, or for problems which involve materials with Poisson's ratios close to 0.5, the residuals sometimes lose accuracy. This obstacle can be remedied by calculating the residuals, after every certain number of steps, according to the central part of formula (C4) instead of according to the normally used right hand side of that equation.

The fast convergence of the CG method for 3-D problems can be explained by arguments on the dimensionality of the space spanned by the basis vectors. It is apparent from equations (C4) and (C6), that the set of expansion vectors (V^n) belongs to the vector space spanned by $\underline{b}$, $A\underline{b}$, $A^2\underline{b}$, ... $A^n\underline{b}$ ... which, from now on, will be termed the B space. The number of A-orthogonal expansion vectors which can be generated is equal to the dimension of the B space and is also, in the absence of roundoff, equal to the maximum number of steps which are required to achieve convergence. The dimension of the B space is bounded by the number of linear equations and obviously depends on the force vector b. When b is proportional to one of the eigenvectors of the A matrix, the dimension of the B space is one, and therefore the CG method will converge in one iteration only. In general, the dimension of the B space is less or equal to the smallest number of terms required to expand the b vector in terms of eigenvectors of A. This is a result of the fact that the space spanned by these eigenvectors is closed under a left hand multiplication by the A matrix.

In most problems, the load case vector b can be expanded with many fewer eigenvectors than the number of equations. Therefore, the Conjugate Gradient method will converge in many fewer iterations than this number. This also explains why, for a given grid, the number of required steps depends on the load case vector, since different vectors require a different number of terms in an eigenvector expansion.

References

Ralston, A., 1965. A first course in Numerical Analysis; McGraw-Hill.

Appendix D: A ONE QUADRATURE POINT INTEGRATION SCHEME WHICH ELIMINATES HOURGLASS IN LOW ORDER FINITE ELEMENT CODES

D.1 Introduction

In addition to the rigid body and constant strain degrees of freedom, the two dimensional four node quadrilateral element and the three dimensional hexahedral element possess degrees of freedom which correspond to non-constant strains in the element interior. The two dimensional quadrilateral possess two such degrees of freedom, and the three dimensional hexahedron possesses twelve (Figure D.1 (a), (b)) These degrees of freedom are often termed hourglass modes, because of their shape in plane strain or plane stress configurations.

The hourglass modes are often a nuisance in numerical codes in which the stiffness matrix is calculated by a one point quadrature integration rule. This is because the stiffness matrix is singular with respect to the hourglass patterns and is nonsingular only with respect to the constant strain modes. In dynamic codes this often leads to hourglass instability in which displacements become unbounded in the hourglass mode. The obvious way to overcome this problem is to use a two point quadrature rule. A large increase in computational effort is entailed, however, especially in codes in which the stiffness matrix is not stored but rather recalculated repeatedly, as is often the case in dynamic explicit codes and static iterative codes. In addition, it was pointed out by Wilson et al. (1973) that the

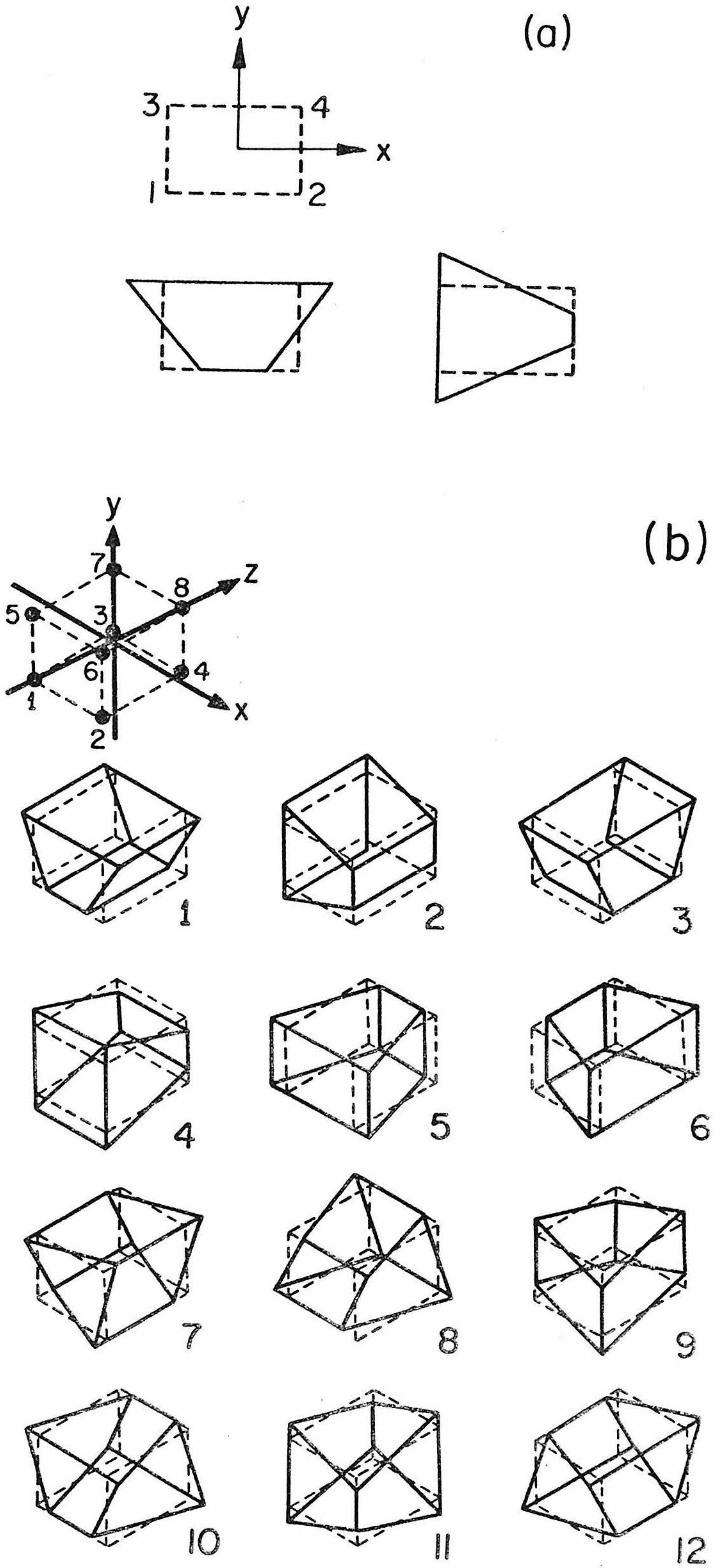

Figure D.1 (a) Hourglass patterns for 2-D quadrilateral elements. (b) Hourglass patterns for 3-D hexahedral elements.

isoparametric element with two point quadrature, does not accurately represent flexural modes of deformation.

In this appendix we describe a simple scheme to control hourglass instabilities by adding an hourglass response term to a one point quadrature stiffness matrix. Although the method of derivation is totally different, and at first this scheme does not appear to evolve from a variational principle, it is shown in Section D.3, that for two dimensional rectilinear elements the element is identical to the incompatible element introduced by Wilson et al. (1973). For non-rectilinear geometry the scheme has to be slightly modified, as was the case with the incompatible element (Taylor et al., 1976). This is to ensure that it will pass the patch test and not adversely affect rigid body and constant strain patterns.

Further details on the scheme and numerical examples can be found in Kosloff and Frazier (1977).

D.2 Derivation of the Scheme for Rectilinear Elements

For an isotropic elastic body occupying a volume V and bounded by surface S, the FE approximation to the equations of equilibrium are given by,

$$\text{(D1)} \qquad \left[K_{ij}\right] \left\{U_j\right\} + \left[M_{ij}\right] \left\{\ddot{U}_j\right\} = \left\{f_i\right\} \quad ;$$

where $\left\{U_j\right\}$ denotes the column vector of nodal displacements, $\left[K_{ij}\right]$ is the stiffness matrix, $\left[M_{ij}\right]$ is the mass matrix, $\left\{f_i\right\}$ is the column vector of nodal forces, dots above variables denote time differentiation and repeated indices imply summation from 1 to the number of degrees of freedom of the problem under consideration. In most explicit dynamic codes, the stiffness matrix is not stored, but rather the nodal restoring forces are calculated by an element by element integration (e.g. Frazier et al., 1974). Although the following derivations are written in terms of stiffness matrices, for dynamic explicit codes they should be interpreted in this sense. In static problems the second term on the left hand side of equation(D1) is omitted (e.g. Zienkiewicz, 1971, Gallagher, 1975).

The stiffness matrix is conveniently constructed element by element by a summation;

$$\left[K_{ij}\right] = \sum_{\text{elements}} \left[K_{ij}\right]^{e} .$$

For the quadrilateral plane strain element or the eight node hexahedral element,

$$\left[K_{ij}{}^{e}\right]^{nm} = \delta_{ij}\,\lambda_e \int_{V_e} \frac{\partial p^n}{\partial X_i}\,\frac{\partial p^m}{\partial X_i}\,dv + \mu_e \int_{V_e} \frac{\partial p^n}{\partial X_e}\,\frac{\partial p^m}{\partial X_e}\,dv$$

$$\text{(D2)} \qquad + \mu_e \int_{V_e} \frac{\partial p^m}{\partial X_i}\,\frac{\partial p^n}{\partial X_j}\,dv ,$$

where λ_e and μ_e denote respectively Lame's constant and the shear modulus of the element, p^n denotes the four or eight nodal interpolation functions of the element, X_i are the Cartesian coordinates used throughout the volume V. In plane stress λ_e is replaced by $\frac{2\mu_e\lambda_e}{\lambda_e+2\mu_e}$. The calculation of (D2) for isoparametric elements is done in the element

Table D.1. Stiffness matrix $[K_{ij}]^{nm}$ for a rectilinear 1 point quadrature plane strain element.

i1 j1	i1 j2	i2 j1	i2 j2	i3 j1	i3 j2	i4 j1	i4 j2
$(\lambda+2\mu)\left(\frac{\partial z_1}{\partial X_1}\right)^2+\mu\left(\frac{\partial z_2}{\partial X_2}\right)^2$							
$(\lambda+\mu)\ \frac{\partial z_1}{\partial X_1}\frac{\partial z_2}{\partial X_2}$	$(\lambda+2\mu)\left(\frac{\partial z_2}{\partial X_2}\right)^2+\mu\left(\frac{\partial z_1}{\partial X_1}\right)^2$						
$-(\lambda+2\mu)\left(\frac{\partial z_1}{\partial X_1}\right)^2+\mu\left(\frac{\partial z_2}{\partial X_2}\right)^2$	$(-\lambda+\mu)\ \frac{\partial z_1}{\partial X_1}\frac{\partial z_2}{\partial X_2}$	$(\lambda+2\mu)\left(\frac{\partial z_1}{\partial X_1}\right)^2+\mu\left(\frac{\partial z_2}{\partial X_2}\right)^2$			SYMMETRIX		
$(\lambda-\mu)\ \frac{\partial z_1}{\partial X_1}\frac{\partial z_2}{\partial X_2}$	$(\lambda+2\mu)\left(\frac{\partial z_2}{\partial X_2}\right)^2-\mu\left(\frac{\partial z_1}{\partial X_1}\right)^2$	$-(\lambda+\mu)\ \frac{\partial z_1}{\partial X_1}\frac{\partial z_2}{\partial X_2}$	$(\lambda+2\mu)\left(\frac{\partial z_2}{\partial X_2}\right)^2+\mu\left(\frac{\partial z_1}{\partial X_1}\right)^2$				
$(\lambda+2\mu)\left(\frac{\partial z_1}{\partial X_1}\right)^2-\mu\left(\frac{\partial z_2}{\partial X_2}\right)^2$	$(\lambda-\mu)\ \frac{\partial z_1}{\partial X_1}\frac{\partial z_2}{\partial X_2}$	$-(\lambda+2\mu)\left(\frac{\partial z_1}{\partial X_1}\right)^2-\mu\left(\frac{\partial z_2}{\partial X_2}\right)^2$	$(\lambda+\mu)\ \frac{\partial z_1}{\partial X_1}\frac{\partial z_2}{\partial X_2}$	$(\lambda+2\mu)\left(\frac{\partial z_1}{\partial X_1}\right)^2+\mu\left(\frac{\partial z_2}{\partial X_2}\right)^2$			
$(-\lambda+\mu)\ \frac{\partial z_1}{\partial X_1}\frac{\partial z_2}{\partial X_2}$	$-(\lambda+2\mu)\left(\frac{\partial z_2}{\partial X_2}\right)^2+\mu\left(\frac{\partial z_1}{\partial X_1}\right)^2$	$(\lambda+\mu)\ \frac{\partial z_1}{\partial X_1}\frac{\partial z_2}{\partial X_2}$	$-(\lambda+2\mu)\left(\frac{\partial z_2}{\partial X_2}\right)^2-\mu\left(\frac{\partial z_1}{\partial X_1}\right)^2$	$-(\lambda+\mu)\ \frac{\partial z_1}{\partial X_1}\frac{\partial z_2}{\partial X_2}$	$(\lambda+2\mu)\left(\frac{\partial z_2}{\partial X_2}\right)^2+\mu\left(\frac{\partial z_1}{\partial X_1}\right)^2$		
$-(\lambda+2\mu)\left(\frac{\partial z_1}{\partial X_1}\right)^2-\mu\left(\frac{\partial z_2}{\partial X_2}\right)^2$	$-(\lambda+\mu)\ \frac{\partial z_1}{\partial X_1}\frac{\partial z_2}{\partial X_2}$	$(\lambda+2\mu)\left(\frac{\partial z_1}{\partial X_1}\right)^2-\mu\left(\frac{\partial z_2}{\partial X_2}\right)^2$	$(-\lambda+\mu)\ \frac{\partial z_1}{\partial X_1}\frac{\partial z_2}{\partial X_2}$	$-(\lambda+2\mu)\left(\frac{\partial z_1}{\partial X_1}\right)^2+\mu\left(\frac{\partial z_2}{\partial X_2}\right)^2$	$(\lambda-\mu)\ \frac{\partial z_1}{\partial X_1}\frac{\partial z_2}{\partial X_2}$	$(\lambda+2\mu)\left(\frac{\partial z_1}{\partial X_1}\right)^2+\mu\left(\frac{\partial z_2}{\partial X_2}\right)^2$	
$-(\lambda+\mu)\ \frac{\partial z_1}{\partial X_1}\frac{\partial z_2}{\partial X_2}$	$-(\lambda+2\mu)\left(\frac{\partial z_2}{\partial X_2}\right)^2-\mu\left(\frac{\partial z_1}{\partial X_1}\right)^2$	$(\lambda-\mu)\ \frac{\partial z_1}{\partial X_1}\frac{\partial z_2}{\partial X_2}$	$-(\lambda+2\mu)\left(\frac{\partial z_2}{\partial X_2}\right)^2+\mu\left(\frac{\partial z_1}{\partial X_1}\right)^2$	$(-\lambda+\mu)\ \frac{\partial z_1}{\partial X_1}\frac{\partial z_2}{\partial X_2}$	$(\lambda+2\mu)\left(\frac{\partial z_2}{\partial X_2}\right)^2-\mu\left(\frac{\partial z_1}{\partial X_1}\right)^2$	$(\lambda+\mu)\ \frac{\partial z_1}{\partial X_1}\frac{\partial z_2}{\partial X_2}$	$(\lambda+2\mu)\left(\frac{\partial z_2}{\partial X_2}\right)^2+\mu\left(\frac{\partial z_1}{\partial X_1}\right)^2$

$\frac{\text{Vol}}{16}$.

"natural" coordinate system z_i $(-1 \leq z_i \leq 1 \quad i=1\ldots D)$ where D denotes the number of space dimensions of the problem and the coordinate values X_i are approximated by;

$$X_i = \sum_{\text{nodes}} p^m(\underline{z})\, X_i^m \quad , \tag{D3}$$

where X_i^m are the coordinates of the nodes of the element. In the natural coordinate system, the interpolation functions of the isoparametric element become,

$$p^m(\underline{z}) = \frac{1}{2^D} \sum_{i=1}^{D} (1 + z_i Z_i^m). \tag{D4}$$

When equations (D3) and (D4) are substituted in (D2) and the integrations are carried out exactly or by a 2 point Gaussian quadrature rule, the standard isoparametric element is obtained. In this case the element stiffness matrix is singular only with respect to rigid body displacements and its product by each of the displacement patterns of Figure D.1 is nonzero. However, when these integrations are performed by a one point quadrature rule, resulting for plane strain in the matrix shown in Table D.1, the stiffness matrix is singular with respect to all the patterns of Figure D.1. It is nonsingular only with respect to constant strain terms. In the scheme of this paper an hourglass stiffness matrix, which is nonsingular with respect to all the patterns of Figure D.1 but is singular with respect to rigid body and constant strain patterns, is added to the one point quadrature stiffness matrix.

Considering the 2-D rectilinear element of Figure D.2(a), with a linear varying fraction $\sigma_{11} = \sigma_0 y$ applied on its sides $x = \pm a$, the exact stress and displacement solutions are given by,

$$
\begin{aligned}
\sigma_{22} &= 0 , \\
\sigma_{11} &= \sigma_0 \cdot y , \\
\sigma_{12} &= 0 , \\
U_1 &= E^{-1} \sigma_0 \, x \cdot y , \\
U_2 &= \frac{1}{2} E^{-1} \sigma_0 \, (a^2 - x^2) ,
\end{aligned}
\tag{D5}
$$

where σ_{ij} denotes the components of the stress tensor, U_i denote the displacement components, E is equal to Young's modulus for plane stress and to $\frac{4\mu(\lambda+\mu)}{\lambda + 2\mu}$ for plane strain.

At the four nodes, the displacement in the X direction can be written as

$$U_1 = E^{-1} \cdot \sigma_0 \cdot ab \, \{1\} , \tag{D6}$$

where $\{1\}^T$ is the vector (1, -1, -1, 1).

Conversely σ_0 can be expressed as a function of nodal displacements by

$$\sigma_0 = \frac{E}{4ab} \{1\}^T \{U_1\} , \tag{D7}$$

and from now on the term $A_b = \{1\}^T \{U_1\}$, will be called the hourglass amplitude.

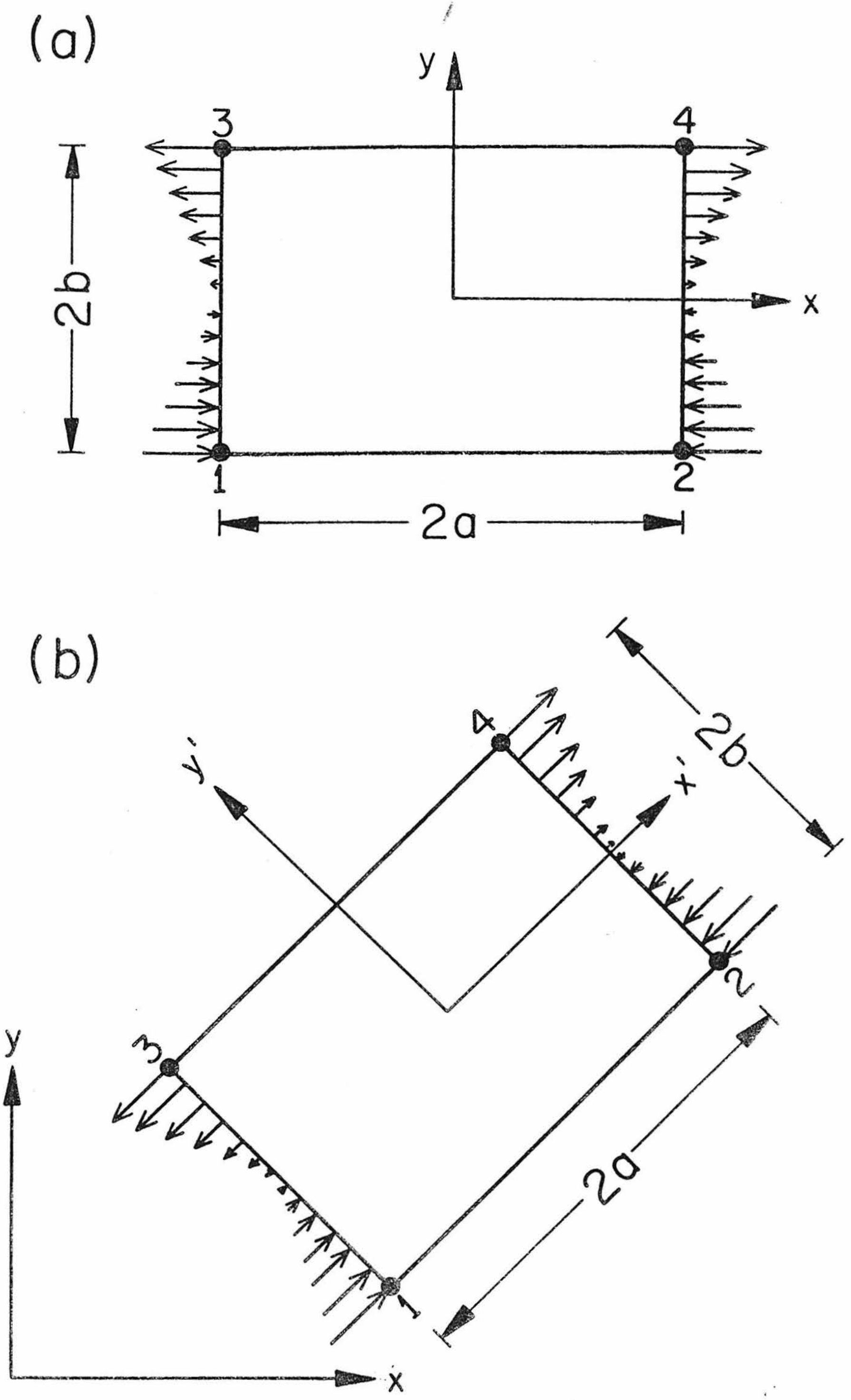

Figure D.2 (a) A 2-D rectilinear element oriented parallel to the coordinate axes with linear varying tractions applied at the sides X = ±a . (b) The same element as in Figure D.2(a) but oriented at an angle to the coordinate axes (X Y).

The nodal restoring forces for the element of Fig. D2(a), which define the product of the hourglass stiffness matrix by the displacements, is calculated by viewing the stresses in (D5) as tractions on the element sides $\mp a$, and calculating the restoring forces according to the formula for the nodal forces (Zienkiewicz, 1971),

$$\text{(D8)} \qquad f_i^m = \sum_e \int_{V_e} h_i P^m \, dv + \sum_e \int_{S_\delta} P^m T_i \, dS ,$$

$m = 1,\ldots 2^D$, $i = 1,\ldots D$;

where h_i are the body forces (in this case equal to zero), and S_δ is the portion of S on which the fractions T_i are specified. After substituting (D4), (D5), and (D7) into (D8) we obtain;

$$\text{(D9)} \qquad \{R_i\} = \frac{1}{12} A_b E \cdot \frac{b}{a} \cdot \{1\} ,$$

where $\{R_i\}$ denotes the column vector of the element restoring forces. By using the natural coordinate system and writing out A_b explicitly we obtain;

$$\text{(D10a)} \qquad \{R_1\} = \frac{E}{12} \cdot \text{Vol} \left(\frac{\partial Z_1}{\partial X_1}\right)^2 \{1\} \{1\}^T \{U_1\}$$

where Vol denotes the element area in 2-D, or volume in 3-D. The same derivation used to obtain (D10a) can be performed for displacements in the y direction to give;

$$\text{(D10b)} \qquad \{R_2\} = \frac{E}{12} \text{ Vol} \left(\frac{\partial Z_2}{\partial X_2}\right)^2 \{1\} \{1\}^T \{U_2\}$$

Equations (D10a) and (D10b) serve as the definition of the hourglass stiffness matrix for 2-D elements oriented parallel to the coordinate arises. It should be noted that when $\{U_i\}$ form a rigid body or constant strain displacement pattern, the hourglass amplitude $\{1\}^T \{U_i\}$ is zero and thus the hourglass matrix is singular with respect to these patterns as it should be.

When the rectilinear element is not oriented parallel to the coordinate system the stiffness matrix is derived by writing equations (D10a) and (D10b) in a primed coordinate system X_i' which is parallel to the element and has its origin at the element center (Figure D.2(b)) The relations are then translated and rotated to the unprimed system. After some algebra the following formula is obtained for an arbitrary element orientation,

$$\text{(D11)} \qquad \left\{R_i\right\} = \{1\}\left(\frac{\partial z}{\partial x_i}\ \frac{\partial z_j}{\partial x_\ell}\right)\left(\frac{E}{12} \cdot \text{Vol}\right)\{1\}^T \left\{U_\ell\right\}$$

and thus the hourglass stiffness matrix is given by,

$$\text{(D12)} \qquad \left[K_{ij}\right]^{hg} = \frac{E}{12} \cdot \text{Vol}\ \{1\}\{1\}^T \frac{\partial z_\ell}{\partial x_i}\ \frac{\partial z_\ell}{\partial x_j}$$

In practice, when the stiffness matrix is not stored, it usually is most economical to calculate (D11) from right to left. The entries of $\left[K_{ij}\right]^{hg}$ for the orientation of Figure D.2(a) in plane strain are listed in Table D.2.

In three dimensions there are four 8 component vector operators similar to the single $\{1\}$ operator of the 2-D case which are given by;

$$\{1\}^T_1 = (1, -1, -1, 1, 1, -1, -1, 1) ,$$

(D13)
$$\{1\}^T_2 = (1, 1, -1, -1, -1, -1, 1, 1) ,$$

$$\{1\}^T_3 = (1, -1, 1, -1, -1, 1, -1, 1) ,$$

$$\{1\}^T_4 = (1, -1, -1, 1, -1, 1, 1, -1) ;$$

and each operator is associated with a matrix which is calculated by (D12). The hourglass stiffness matrix is the sum of these four matrices. The choice of a value for the constant E depends on whether the problem to be solved is closer to a plane strain problem or a plane stress problem. For E, the difference between the two cases is usually not large. Whereas in the two dimensional case the hourglass modes are associated with bending, in the three dimensional cases this is true of only six of the twelve modes.

In summary, this scheme achieves the goal of controlling hourglass in all modes. It is also expected to give an accurate response for problems with a large amount of flexure.

D.3 Comparison with the Incompatible Modes Element for Rectilinear Element Geometry

In the two dimensional incompatible element formulation of Wilson et al. (1973), two interpolation functions are added to the four interpolation functions of the four node 2-D isoparametric quadrilateral element. In the natural coordinate system they are given by,

Table D.2. Flexural stiffness matrix for the rectilinear 2-D element of Figure 2a. $E = \frac{4\mu_e(\lambda_e+\mu_e)}{\lambda_e + 2\mu_e}$ for plane strain and equal to Young's modulus for plane stress.

$$\frac{E \cdot \mathrm{Vol}}{12}\left[\begin{array}{|c|c|c|c|c|c|c|c|}
\left(\frac{\partial Z_1}{\partial X_1}\right)^2 & & & & & & & \\
0 & \left(\frac{\partial Z_2}{\partial X_2}\right)^2 & & & & & & \\
-\left(\frac{\partial Z_1}{\partial X_1}\right)^2 & 0 & \left(\frac{\partial Z_1}{\partial X_1}\right)^2 & & & & & \\
0 & -\left(\frac{\partial Z_2}{\partial X_2}\right)^2 & 0 & \left(\frac{\partial Z_2}{\partial X_2}\right)^2 & & & & \\
-\left(\frac{\partial Z_1}{\partial X_1}\right)^2 & 0 & \left(\frac{\partial Z_1}{\partial X_1}\right)^2 & 0 & \left(\frac{\partial Z_1}{\partial X_1}\right)^2 & & & \\
0 & -\left(\frac{\partial Z_2}{\partial X_2}\right) & 0 & \left(\frac{\partial Z_2}{\partial X_2}\right) & 0 & \left(\frac{\partial Z_2}{\partial X_2}\right) & & \\
\left(\frac{\partial Z_1}{\partial X_1}\right)^2 & 0 & -\left(\frac{\partial Z_1}{\partial X_1}\right) & 0 & -\left(\frac{\partial Z_1}{\partial X_1}\right) & 0 & \left(\frac{\partial Z_1}{\partial X_1}\right) & \\
0 & \left(\frac{\partial Z_2}{\partial X_2}\right)^2 & 0 & -\left(\frac{\partial Z_2}{\partial X_2}\right) & 0 & -\left(\frac{\partial Z_2}{\partial X_2}\right) & 0 & \left(\frac{\partial Z_2}{\partial X_2}\right)
\end{array}\right]$$

(D14)
$$P^5 = 1 - z_1^2$$
$$P^6 = 1 - z_2^2 ,$$

the result is a 12 x 12 element stiffness matrix, $\left[K_{ij}\right]^{nm}$ (i, j=1, 2, n, m=1,... 6), the entries of which can be calculated from (D2). By a static condensation operation on the four additional element degrees of freedom, an 8 x 8 stiffness matrix is obtained and the interior degrees of freedom are eliminated from the system of FE equations.

The condensation is done after partitioning the 12 x 12 stiffness matrix in the form of,

$$\begin{bmatrix} K_{ij}^{bb} & K_{ij}^{ba} \\ K_{ij}^{ab} & K_{ij}^{aa} \end{bmatrix} .$$

In this stiffness matrix the superscript a refers to the four new degrees of freedom and b refers to the eight degrees of freedom of the quadrilateral isoparametric element. The 8 x 8 incompatible mode stiffness matrix is given by:

(D15)
$$\left[K_{ij}\right]^{bb'} = \left[K_{ij}\right]^{bb} - \left[K_{i\ell}^{ba}\right]\left[K_{\ell g}^{aa}\right]^{-1} \left[K_{gj}^{ab}\right] ,$$

(Wilson et al., 1973; Gallagher, 1975; Taylor et al. 1976).

When the entries of (D13) are calculated explicitly for a rectilinear element using (D2), (D3), (D4) and (D14), and compared to the sum of Tables D.1 and D.2, which comprises the stiffness matrix for the scheme of this thesis, it turns out that they are identical (e.g. see Gallagher, p. 277 for plane stress). Thus for 2-D, the scheme presented in this thesis is essentially an alternative method to derive the incompatible mode stiffness matrix. This fact is not surprising since it can be shown (Gallagher, 1975), that the incompatible element can be derived directly by requiring that the stress variation inside the element be of the form,

$$\sigma_{11} = C_0 + C_1 x_2$$

$$\sigma_{22} = C_2 + C_3 x_1$$

$$\sigma_{12} = C_4 ,$$

and then by calculating strains and displacements and by expressing displacements in the interior as a function of displacement values at the nodes. Similarly, in the presented scheme, the constant strain (stress) stiffness matrix is first calculated and the linear varying stress terms are added afterwards. The main point of the method derived here is the large savings in computational effort which can be encountered by constructing the stiffness matrix in two stages. Only a one point quadrature rule is needed, and the additional linear stress term can be calculated directly according to (D11).

D.4 Modification of the Scheme for Non-Rectilinear Element Geometry

As was pointed out by Taylor et al. (1976), the incompatible model scheme needs to be modified for nonrectilinear elements in order to pass the patch test. The same holds true for the scheme of this appendix since the inner product of the $\{1\}^T$ operator of Section D2 with a constant strain or rigid body displacement pattern is no longer always zero. The modification of the scheme consists of redefining the $\{1\}^T$ operator to make it orthogonal to constant strain and rigid body displacement patterns in the element, and of requiring that it degenerate to its previous definition in the case of rectilinear element geometry.

In two dimensions, the eight degrees of freedom of the quadrilateral element can be separated into two groups of four for each displacement component. Each group consists of one rigid body pattern, two constant displacement gradient patterns $\left(\frac{\partial u_i}{\partial x_1}, \frac{\partial u_i}{\partial x_2}\right)$ and one hourglass pattern (this separation was preferred to the more common division to three strains, two rigid body displacements, one rotation and two hourglass modes, because each of its members involves only one displacement component).

In order to satisfy the orthogonality relations stated above, the components of the new $\{1\}^T$ operator (a_1, a_2, a_3, a_4) must satisfy the following relations,

$$(a_1\ a_2\ a_3\ a_4)\begin{pmatrix}1\\1\\1\\1\end{pmatrix} = 0 \quad \text{(rigid body);}$$

$$(a_1\ a_2\ a_3\ a_4)\begin{pmatrix}X_1^1\\X_1^2\\X_1^3\\X_1^4\end{pmatrix} = 0 \quad \text{(displacement gradient in the } x_1 \text{ direction);}$$

and

$$(a_1\ a_2\ a_3\ a_4)\begin{pmatrix}1\\X_2\\X_2^2\\X_2^3\\X_2^4\end{pmatrix} = 0 \quad \text{(displacement gradient in the } x_2 \text{ direction)},$$

comprising a set of three homogeneous equations in four unknowns. The X_i are the global nodal coordinates of the quadrilateral element. Thus the ratio between each of the components of the $\{1\}^T$ operator can be calculated, and the $\{1\}^T$ operator is obtained by normalizing these components so that they become equal to their previous definition in the case of rectilinear element geometry. As was the case of rectilinear elements, the modified $\{1\}^T$ vector operator is the same for the two displacement components.

For the three dimensional hexahedral element, the twenty-four degrees of freedom can be divided into three groups corresponding to the three displacement components. Then each group will consist of one translation, three displacement gradients and four "hourglass" patterns. The $\{1\}_i^T$ operators consist of eight quantities $(a_i)^T$ ($i = 1 \ldots 8$) which must satisfy the relations,

$$(a_1\ a_2\ .\ .\ .\ a_8)\begin{pmatrix}1\\1\\1\\1\\1\\1\\1\\1\end{pmatrix} = 0$$

$$(a_1\ a_2\ \cdots\ a_8)\begin{pmatrix} X_1^1 \\ X_1^2 \\ \cdot \\ \cdot \\ \cdot \\ X_1^8 \end{pmatrix} = 0$$

$$(a_1\ a_2\ \cdots\ a_8)\begin{pmatrix} X_2^1 \\ X_2^2 \\ \cdot \\ \cdot \\ \cdot \\ X_2^8 \end{pmatrix} = 0 \tag{D17}$$

$$(a_1\ a_2\ \cdots\ a_8)\begin{pmatrix} X_3^1 \\ X_3^2 \\ \cdot \\ \cdot \\ \cdot \\ X_3^8 \end{pmatrix} = 0$$

Equations (D17) comprise a set of four homogeneous equations in eight unknowns $a_1 \ldots a_8$. The four $\{1\}_i^T$ vector operators span the remaining four dimensional solution space, and four basis vectors in this space (not necessarily orthogonal to each other) can be found which degenerate to the operators in Section D.2 for the rectilinear case.

References

Frazier, G. A., Petersen, C. M., 1974. Three dimensional stress wave code for Illiac Iv, Systems Science and Software, P. O. Box 1620, La Jolla, California 92037.

Gallagher, R. H., 1975. Finite Element Analysis, Fundamentals, Prentice-Hall, Inc., Englewood Cliffs, New Jersey.

Kosloff, D. D., and Frazier, G. A., 1977. Treatment of hourglass modes in low order Finite Element codes; the International Journal of Numerical and Analytical Methods in Geomechanics, in press.

Taylor, L. T., Beresford, P. J., Wilson, E. L., 1976. A nonconforming element for stress analysis, International Journal for Numerical Methods in Engineering, Vol 10, 1211-1219.

Timoshenko, S., 1934. Theory of Elasticity, McGraw-Hill.

Wilson, E. L., Taylor, R. L., Doherty, W. P., Ghabousi, J., 1973. Incompatible displacement models, in Numerical and Computer Methods in Structural Mechanics (Ed. S. J. Fenves et al.), Academic Press, New York, p. 43.

Zienkiewicz, O. C., 1971. The Finite Element Method in Engineering Science, McGraw-Hill.

Appendix E: SOLUTION OF THE FINITE ELEMENT EQUATIONS FOR AN ELASTIC-PLASTIC MEDIUM

E.1 Introduction

In both the continuum mechanics case and in the plate theory case, the Finite Element equilibrium equations have the form;

$$\text{(E1)} \qquad F_j\ (U_\ell) = b_j\ , \qquad j = 1 \ldots N$$

where U_ℓ is an unknown nodal vector, $F_j\ (U_\ell)$ is a set of nonlinear functions of U_ℓ, b_j is the load case vector, and N is the dimension of U_ℓ, F_j, and b_j, or equivalently, the number of unknowns (see equations (A5) and (B9)). The functional dependence of F_j on U_ℓ is not given in a closed form but rather the equilibrium equations are written in terms of stresses (or moments in the plate theory case), and the stresses (moments) are related to the nodal displacements (deflections and slopes) by a rheological prescription relating stresses to strains (moments to curvatures). This appendix describes the implementation of the Newton-Raphson method to the solution of equations of the type of (E1), which arose in the problems in Chapter 2 and Chapter 3 in this thesis. For the sake of brevity, from now on we will discuss the derivations in terms of stresses and strains, which for the plate theory equations should be interpreted as moments and curvatures respectively.

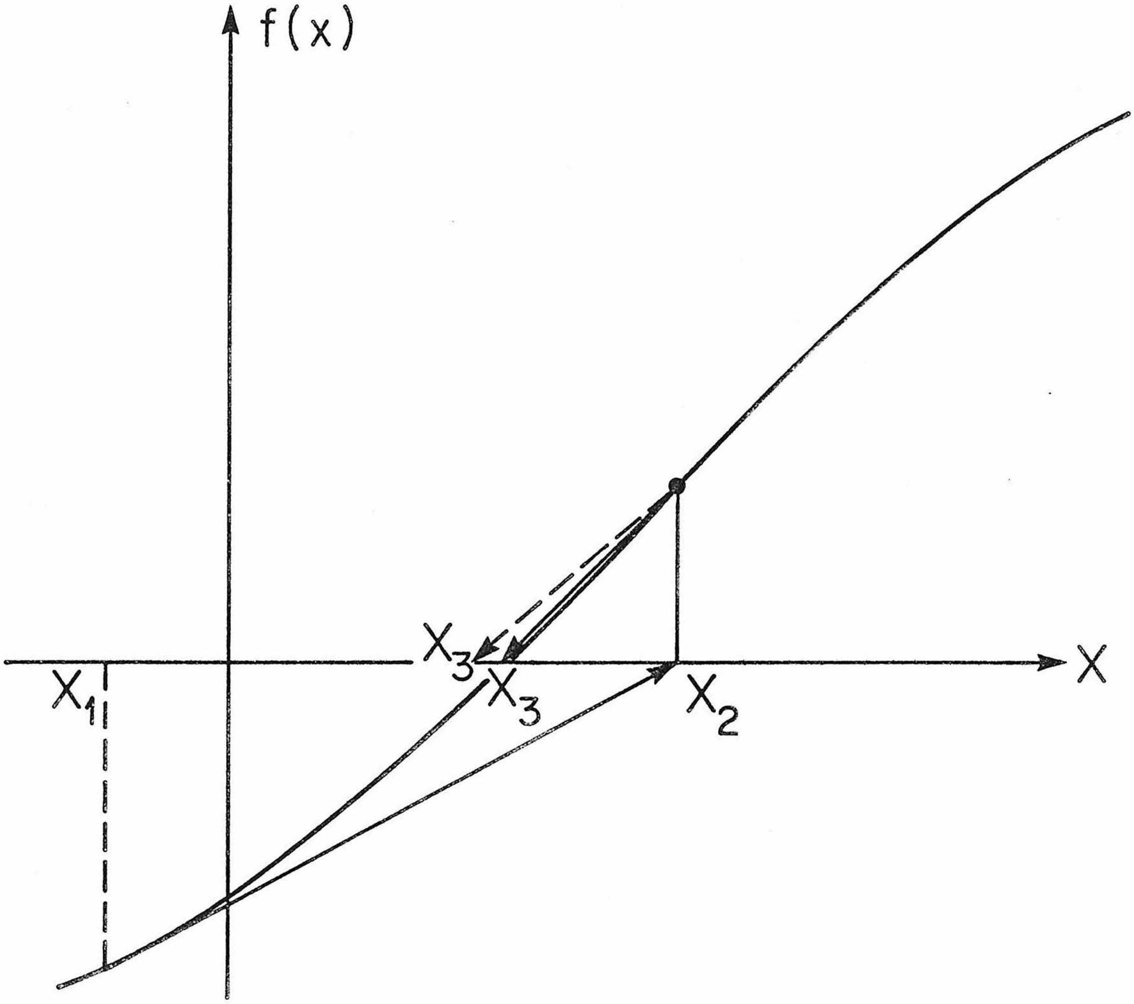

Figure E.1 Example of a one dimensional Newton-Raphson iteration. Solid lines denote the steps of the method with exact derivatives of F, whereas dashed lines denote the steps with approximate derivatives of F.

E.2 The Newton-Raphson Method

In each step of the Newton-Raphson procedure, an approximation to the solution of the nonlinear equation (E1) is obtained from the previous solution by a linear extrapolation along the slope of the equations at the previous approximation point. The procedure is illustrated for a single nonlinear equation in Figure E.1. Mathematically, each step can be written as a set of linear equations given by,

$$\text{(E2)} \qquad \left(\frac{\partial F_j}{\partial U_\ell}\right)^{\text{old}} \left[(U_\ell)^{\text{new}} - (U_\ell)^{\text{old}} \right] = - (F_j)^{\text{old}} + b_j \qquad j=1, \ldots N.$$

The superscripts (new) and (old) refer respectively to the values at the current and previous iteration. The term $\frac{\partial F_j}{\partial U_\ell}$ is often called the tangent stiffness matrix, and in the elastic case it reduces to the usual stiffness matrix (then the Newton-Raphson method converges in one iteration). In the type of problems which have been solved in this thesis, the tangent stiffness matrix cannot be obtained easily in closed form (if at all), and it is therefore approximated numerically at the end of each step according to (Figure E.1),

$$\frac{\partial F_j}{\partial U_\ell} = \frac{F_j^{(\text{new})} - F_j^{(\text{old})}}{U_\ell^{(\text{new})} - U_\ell^{(\text{old})}} \quad .$$

For continuum mechanics problems, equation (E2) is solved by the conjugate Gradient method. The tangent stiffness matrix does not need to be stored but rather, in effect, it is recalculated repeatedly in every iteration by performing the numerical integration in (A5) in combination with (A4) and the scheme described in Appendix D, with the elastic moduli replaced by the tangent bulk and shear moduli given respectively by,

$$K^{\tan} = \frac{1}{3} \cdot \frac{\sigma_{ii}^{(new)} - \sigma_{ii}^{(old)}}{e_{ii}^{(new)} - e_{ii}^{(old)}} ,$$

and,

$$(\mu^{\tan})^2 = \frac{1}{4} (\sigma_{ij}^{'(new)} - \sigma_{ij}^{'(old)})(\sigma_{ij}^{'(new)} - \sigma_{ij}^{'(old)}) /$$

$$(e_{ij}^{'(new)} - e_{ij}^{'(old)})(e_{ij}^{'(new)} - e_{ij}^{'(old)}) .$$

σ_{ij} denotes the stress tensor, $\sigma_{ij}^{'}$ denotes the stress deviator, e_{ij} denotes the strain and $e_{ij}^{'}$ denotes the strain deviator.

The problems which have been solved in this thesis by the Newton-Rapson solution scheme converged in at most six iterations.

Appendix F: STEREOGRAPHIC PROJECTION OF STRESSES

The Stereographic stress projection plot, displays the orientation in space of the principal stress axes, at given points in a horizontal cross section. The projection also gives the magnitudes of the differences between the maximum and minumum principal stresses (or alternatively of any other selected scalar function of the stress tensor).

The input data consist of the stresses σ_{ij}, $ij = 1,3$ at N selected points in a cross section, and a coordinate system XYZ, to which the stresses are referred.

The calculation sequence begins by calculating the first stress invariant at each point according to:

$$I_T = \sigma_{ii} , \tag{F1}$$

where the summation convention is used for repeated indices.

Then the second and third deviatovic stress invariants are calculated according to (Malvern, 1969);

$$II_T' = 1/2 \, \sigma_{ij}' \, \sigma_{ij}' , \tag{F2}$$

and,

$$III_T' = \det \sigma_{ij}' , \tag{F3}$$

where σ'_{ij} denotes the deviatovic stresses which are given by,

$$\sigma'_{ij} = \sigma_{ij} - 1/3\, \sigma_{kk}\, \delta_{ij}$$

In the next step the three roots of the equation,

(F4) $$\text{os}\ 3\alpha = \frac{III'_T}{2} \left(\frac{3}{II'_T}\right)^{3/2}$$

are found in order to calculate the three principal deviatoric stresses according to (Malvern, 1969),

(F5) $$\sigma'_\kappa = 2 \cos \alpha_\kappa \cdot \left(\frac{II_T}{3}\right)^{1/3}, \quad \kappa = 1 \ldots 3$$

After obtaining the three principal deviatoric stresses in (5), the axes of which coincide with the axes of the stress tensor σ_{ij}, the nine direction cosines $\eta_{\alpha\beta}$ of the angles between the XYZ coordinate system and the principal stress axes are calculated by solving the homogeneous system of equations;

(F6) $$a^\beta_j\, (\sigma'_{ij} - \delta_{ij}\, \sigma'_\beta) = 0 \quad i = 1 \ldots 3$$

for $\beta = 1 \ldots 3$, and normalizing the solution each time by,

$$\eta^\beta_\alpha = \frac{a^\beta_\alpha}{\left(a^\beta_\kappa\, a^\beta_\kappa\right)^{1/2}}$$

The direction cosines are then used to find the two normals $t_i^1\ t_i^2$ to the maximum shear planes of the stress tensor (which are parallel to the intermediate stress axis and inclined at 45° to the maximum stress axis) by a rotation operation;

$$(F7) \qquad t_i^1 = \eta_1^i \cdot \frac{\sqrt{2}}{2} + \eta_2^i \cdot \frac{\sqrt{2}}{2} \ ,$$

and

$$(F8) \qquad t_i^2 = \eta_1^i \frac{\sqrt{2}}{2} - \eta_2^i \frac{\sqrt{2}}{2} \ , \quad i = 1 \ldots 3 \ .$$

Next the dip and strike of the two maximum shear planes are calculated from their normals according to the formula,

$$(F9) \qquad \mathrm{dip}_\alpha = \arccos\,(t_3^\alpha) \quad \alpha = 1,2 \ ,$$

and,

$$(F10) \qquad \mathrm{strike}_\alpha = \arctan\left(\frac{t_2^\alpha}{t_1^\alpha}\right) \quad \alpha = 1,2 \ .$$

In the final stage, the maximum shear planes are projected stereographically (lower hemisphere) and plotted on the horizontal section in which the center of each projection circle is at the point to which the stress tensor is related. The radius is scaled according to;

$$(F11) \qquad R = C\left(\sigma'_{\mathrm{max}} - \sigma'_{\mathrm{min}}\right) \ ,$$

where C is a suitable constant scale factor for all points of the cross section.

References

Malvern, L. E. 1969. Introduction to the mechanics of a continuous medium, Prentice Hall, p. 89-93.

Appendix G: PROCEDURE FOR OBTAINING THE CAP MODEL PARAMETERS

This appendix briefly summarizes the equations arising in the cap model, and outlines the procedure which is used for assigning numerical values to its parameters. For completeness, basic elements of plasticity theory relevant to the derivations are included. A more complete presentation on this topic can be found in standard texts dealing with plasticity (e.g. Fung, 1965).

For a given volume of cap plastic material in a prestressed state, the change in strain Δe_{ij} during a deformation increment is separated into an elastic part Δe_{ij}^{e} and a plastic part Δe_{ij}^{P} which are related by;

(G1) $$\Delta e_{ij} = \Delta e_{ij}^{e} + \Delta e_{ij}^{P} .$$

In (G1), as well as in all the subsequent derivations, the strain increments and stress increments refer to the prestressed configuration of the given volume, and it is assumed that all strain increments from this state are infinitesimal. The stress increment $\Delta\sigma_{ij}$, which corresponds to the strain increment Δe_{ij}, is given by,

(G2) $$\Delta\sigma_{ij} = \lambda\Delta e_{KK}^{e}\,\delta_{ij} + 2\mu\Delta e_{ij}^{e} ,$$

where λ and μ respectively denote Lame's constant and the shear modulus of the cap material.

The cap material is characterized by two yield functions whose equations write,

$$F_1 = \sqrt{J_2'} + \alpha J_1 + \beta \ , \tag{G3}$$

and

$$F_2 = (J_1 - \ell)^2 + R^2 J_2' - (x - \ell)^2 \tag{G4}$$

where J_1 and J_2' respectively denote the first and second stress invariants, and α, β, and R are material parameters. The first yield surface, F_1, plots as a straight line in $J_1 - \sqrt{J_2'}$ space, whereas the second yield surface F_2 plots as an ellipse (Figure G.1). The F_1 yield surface does not change during the deformation of the cap material, but on the other hand, the second yield function F_2 moves during loading according to a hardening equation which writes,

$$x = \frac{1}{D} \ \ell n\left(\frac{e^P}{W} + 1\right) . \tag{G5}$$

W and D are material parameters and e^P is a measure of volumetric strain (e.g. section 2.12). For infinitesimal deformations, the change in e^P is equal to the change in volumetric strain,

$$\Delta e^P = \Delta e^P_{KK} \ . \tag{G6}$$

The relation between x and ℓ is obtained by noting that at the intersection of the two yield surfaces (point A in Figure G.1), the

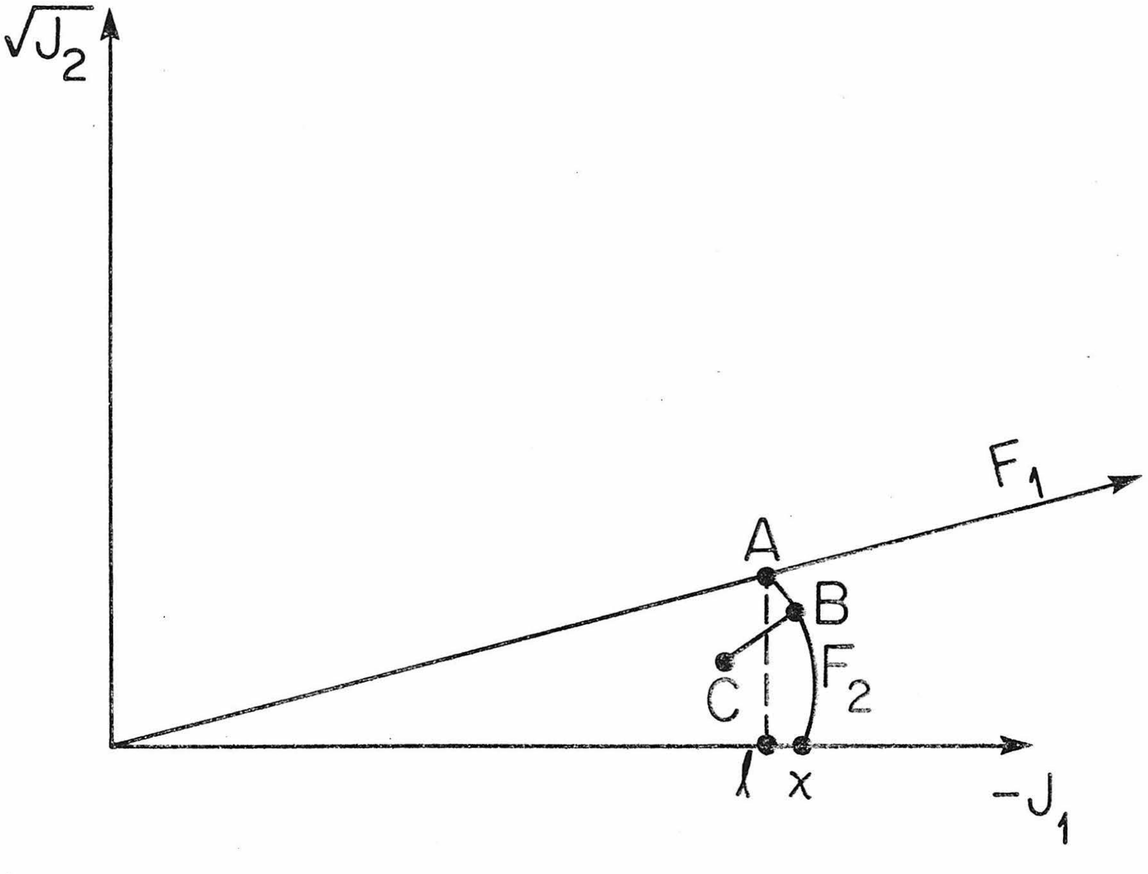

Figure G.1

following relations must hold,

$$J_1 = \ell ,$$

$$\sqrt{J_2'} + \alpha J_1 + \beta = 0 ,$$

$$R\sqrt{J_2'} = \ell - x ,$$

therefore,

(G7) $$\ell = \frac{x - R\beta}{1 + \alpha R} .$$

To complete the Cap rheological description, a relation for obtaining Δe_{ij}^{P} for a specified Δe_{ij} is required. When the final stress state of the material is within the elastic zone (line BC in Figure G.1), then the strain change is totally elastic and $\Delta e_{ij}^{P} = 0$. If the initial and final stress points lie on one of the two yield surfaces, the change in plastic strain is given by an associated flow rule which reads,

(G8) $$\Delta e_{ij}^{P} = \Lambda \frac{\partial F_\beta}{\partial \sigma_{ij}} ,$$

where Λ is a factor whose value is obtained from the requirement that during loading the initial and final stress points must lie on the yield surface (e.g. Fung, 1965). For the cap model, the relation for Λ reads, (G9) $$\Lambda = \frac{3\,\frac{\partial F}{\partial J_1}\,K de_{KK} + \mu\,\frac{\partial F}{\partial \sqrt{J_2'}}\,\frac{\sigma_{ij}}{\sqrt{J_2}}\,de_{ij}}{9K\left(\frac{\partial F}{\partial J_1}\right)^2 + \mu\left(\frac{\partial F}{\partial \sqrt{J_2'}}\right)^2 - 3\,\frac{\partial F}{\partial J_1}\,\frac{\partial F}{\partial e^P}}\ .$$

By means of equations (G1), (G2), (G3), (G4), (G5), (G6), (G7), (G8) and (G9) the stress increment $\Delta\sigma_{ij}$ can be calculated for a specified increment of strain Δe_{ij}, both for loading and unloading.

The first step in obtaining the parameters of the cap model involves the fitting of the elastic constants from the observed rebound. The results of section (2.14) indicate a value of 12 kbar for the shear modulus and a Poisson's ratio of 0.25.

The parameters of the F_1 yield function are obtained from the experimentally determined failure envelope. The results of Vesić et al. indicate a shear angle between 30°-40°, and very little cohesion (e.g. equation 2.13 in section 2.12). This translates in equation (G3) to values of $\beta \simeq 0$ and $\alpha \simeq 0.25$.

The remaining parameters are obtained by matching the experimentally determined tangent moduli. Considering first hydrostatic loading, equation (G2), in combination with (G8), can then be rewritten as,

(G10) $$\Delta\sigma_{KK} = 3K\left(\Delta e_{KK} - \Lambda\,\frac{\partial F}{\partial \sigma_{ij}}\,\delta_{ij}\right)\ .$$

For hydrostatic loading, $J_1 = x$; and Λ and $\frac{\partial F}{\partial \sigma_{ij}}$ are respectively given by,

(G11) $$\frac{\partial F}{\partial \sigma_{ij}} = \frac{\partial F_2}{\partial J_1}\,\delta_{ij} = 2(J_1 - \ell)\,\delta_{ij}\ ,$$

and,

(G12) $$\Lambda = \frac{(x - \ell)\ Kde_{KK}}{6K(x - \ell)^2 - (x - \ell)\dfrac{\partial F_2}{\partial e^P}} ,$$

where,

(G13) $$\frac{\partial F_2}{\partial e^P} = \frac{-2(x-\ell)}{D(e^P + W)} .$$

With the aid of (G11), equation (G10)can be rewritten in the form,

(G14) $$\Delta\sigma_{KK} = 3K(1 - 3Q\ \frac{\partial F}{\partial J_1})\ \Delta e_{kk} ,$$

where Q is defined by,

$$\Lambda = Q\ \Delta e_{kk} .$$

Equation (G14) can be recognized as a relation between volumetric stress change, and volumetric strain change. The two variables are connected by the tangent bulk modulus which is given by,

(G15) $$K_{eff} = K(1 - 3Q\ \frac{\partial F}{\partial J_1}) ,$$

or after substitution from (G5), (G11), (G12) and (G13),

(G16) $$K_{eff} = \frac{K}{1 + 3KDWe^{Dx}} .$$

This relation satisfies the condition that $K_{eff} \xrightarrow[+x \to -\infty]{} K$, which means that at large confining pressures after the pores have been collapsed out, the tangent modulus approaches the elastic modulus.

The parameters D and W are obtained from the data of Vesiĉ et. al (1968) as well as by comparison with core samples taken from the Wilmington field (Scranton, 1976, personal communications). The W parameter represents the maximum value of e^P which can be obtained, which occurs in a state of total pore collapse. It therefore can be related to the porosity n by,

$$\text{(G17)} \qquad W = \ell n(1 + n) .$$

The porosities of the dense samples of Vesiĉ et al., and in the upper layers in the Wilmington field are on the order of 30-40%, and therefore W is assigned values between 2.6 to 3.5. The value of D is obtained by noting the good agreement between the calculated maximum subsidence of the elastic simulation and the observed maximum subsidence, and thus requiring that the tangent bulk modulus of the cap model, at the depths of the producing zones, be similar to the tangent bulk modulus obtained by Vesiĉ et. al for that depth. This requires that the values of D be in the vicinity of 0.7. It must be emphasized that the hardening law (equation (G5)) used in this study appears oversimplified, and therefore the cap model is only capable of matching the data of Vesiĉ et. al. in the stress variation range which is relevant to the Wilmington subsidence. However, it is felt that introducing more parameters at this stage without further experimental data is premature considering the uncertainties in the observations and the non-uniformity of the material in the formations in the Wilmington field.

The next stage involves calculating the tangent shear modulus. Vesic et al. used the triaxial stress test for this purpose but, unfortunately, they did not specify the size of their loading increment, and since the tangent shear moduli is highly variable at different points in stress space, (primarily depending on the slope of the yield surface) their results cannot be used directly. Therefore, we have chosen to calculate the tangent modulus from uniaxial strain tests by requiring that the Poisson's ratio be between 1/4 and 1/3.

In a uniaxial strain test, only the uniaxial strain increment Δe_3 is present, and $\Delta e_1 = \Delta e_2 = 0$. Equation (G2), in combination with (G8), can then be rewritten in terms of the change in the axial stress deviator $\Delta\sigma_3'$ as,

$$\Delta\sigma_3' = 2\mu\left(\frac{2}{3}\,\Delta e_3 - \Lambda\,\frac{\partial F}{\partial J_2'}\,\sigma_3'\right) . \tag{G18}$$

The Λ factor takes the form (e.g. Sandler, et al., 1976),

$$\Lambda = \frac{\left(3K\,\frac{\partial F}{\partial J_1} + \mu\,\frac{\partial F}{\partial\sqrt{J_2}}\,\frac{2\sigma_3'}{\sqrt{3}\,|\sigma_3|}\right) de_3}{9K\left(\frac{\partial F}{\partial J_1}\right)^2 + \mu\left(\frac{\partial F}{\partial\sqrt{J_2'}}\right) - 3\,\frac{\partial F}{\partial J_1}\,\frac{\partial F}{\partial e^P}} \tag{G19}$$

By defining $\Lambda = Q\,de_3$ in (G19) and (G18), we obtain for the tangent shear modulus, (G20) $$\mu^*_{eff} = \mu\left(1 - \frac{3}{2} Q \frac{\partial F}{\partial J'_2} \sigma'_3\right) .$$

Substituting the cap model equations for Q results in,

(G21) $$Q = \frac{6K(J_1 - e) + 2\mu R^2 \sigma'_3}{36K(J_1 - \ell)^2 + 3\mu R^4 \sigma'^2_3 - 6(J_1 - \ell) \dfrac{\partial F}{\partial e^P}}$$

The material constant R is obtained by assigning a numerical value to μ^*_{eff} at a chosen point in stress space. It was found that with a value of R = 1 a Poisson's ratio between 0.25 and 0.3 is maintained during loading at all stress levels (Figure G.3(b)).

The volumetric strain vs confining pressure curves for hydrostatic and uniaxial loading are shown in Figure G.2 for the material parameters: $\upsilon = 0.25$, K = 20 Kbar, A = 0.25, D = 0.7143 Kbar^{-1}, R = 1.227, and W = 0.27. Figure G.3 (a) shows the relation between the tangent shear modulus and confining pressure in a uniaxial strain test, and Figure G.3 (b) shows the variation of the tangent Poisson's ratio with confining pressure.

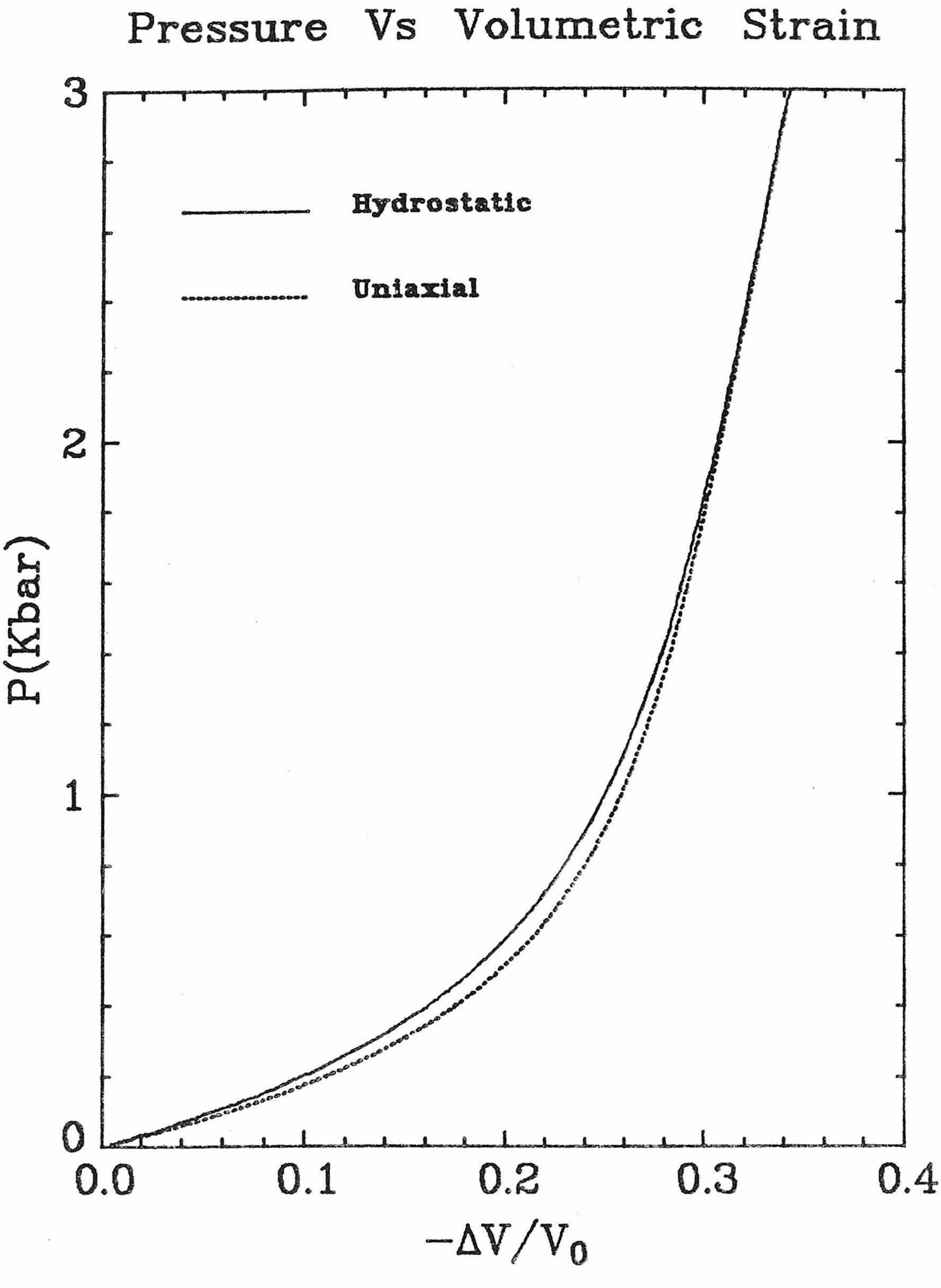

Figure G.2 Pressure vs volume change for hydrostatic compression and uniaxial strain tests on cap material.

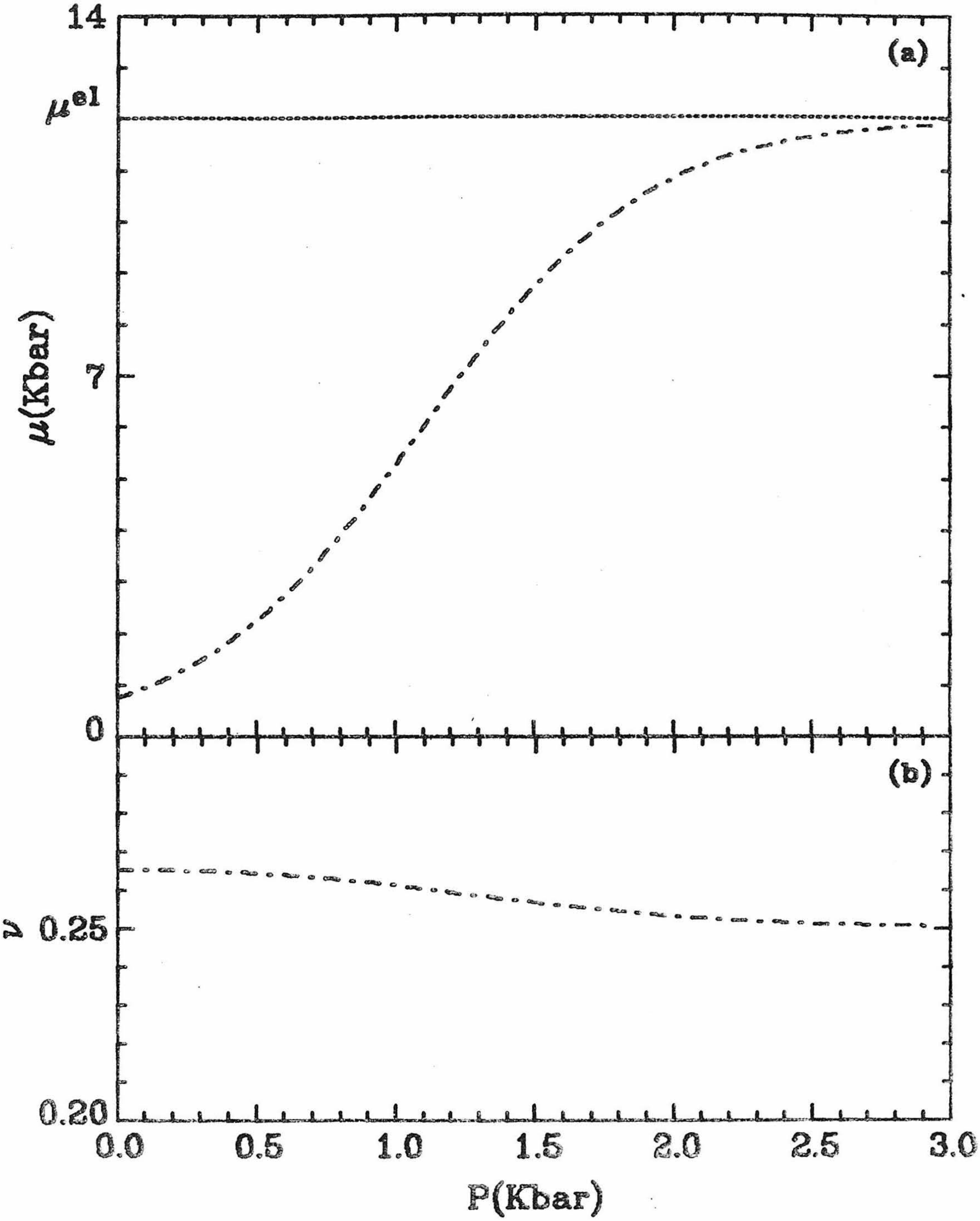

Figure G.3 (a) Bulk modulus vs confining pressure for a uniaxial strain test of cap model material. (b) Poisson's ratio vs confining pressure for uniaxial strain test of cap model material.

References

DiMaggio, F., and Sandler, I., 1971. Material model for granular soils, J. of Eng. Mech. Div., ASCE, Vol 97, pp. 935-950.

Fung, Y. C., 1965. Foundations of solid mechanics. Prentice-Hall.

Sandler, I., DiMaggio, I., and Baladi, G. Y., 1976. Generalized cap model for geological materials, J. Geotech. Engin. Div., ASCE, Vol 102, No GT7, pp. 683-700.

Vesiĉ, A. S., and Clough, G. W., 1968. Behaviour of granular soils under high stresses, ASCE, Soil Mech. and Foundation Div., pp. 661-687.